Interplay between magnetic quantum criticality, Fermi surface and unconventional superconductivity in UCoGe, URhGe and URu2Si2

Gaël Bastien

Communauté
UNIVERSITÉ Grenoble Alpes

THÈSE

Pour obtenir le grade de

DOCTEUR DE la Communauté UNIVERSITÉ GRENOBLE ALPES

Spécialité : **Physique**

Arrêté ministériel : 7 Août 2006

Présentée par

BASTIEN Gaël

Thèse dirigée par **KNEBEL Georg**

préparée au sein **Institut de nanoscience et cryogénie, UGA-CEA, Grenoble**
et de **École Doctorale de physique de Grenoble**

Interplay between magnetic quantum criticality, Fermi surface and unconventional superconductivity in UCoGe, URhGe and URu_2Si_2.

Thèse soutenue publiquement le **09/01/2017**,
devant le jury composé de :

Gilbert Lonzarich
Cavendish Laboratory, Université de Cambridge, Royaume-Uni, Rapporteur
Anne de Visser
Van der Waals-Zeeman Institute, Université d'Amsterdam, Pays Bas, Rapporteur
Claudine Lacroix
Institut Néel, Grenoble, France, Président
Bernd Büchner
Leibniz Insitute for Solid State and Materials Research, Dresde, Allemagne, Examinateur
Georg Knebel
Institut de nanoscience et cryogénie, UGA-CEA, Grenoble, France, Directeur de thèse

Acknowledgement

I would like to thank my Phd supervisor Georg Knebel for having trusted me during this three years. He helped me when I needed help and let me drive the experiment, when I was able to do it. I would like to thank Dai Aoki and Grd Lapertot for having grown high quality samples for my Phd project. I thank Daniel Braithwaite for his help to mount diamond anvil cell. I thank Ilya Sheikin and the technicians of the LNCMI Grenoble for our collaboration for high magnetic field measurements.

Jacques Flouquet, Jean Pascal Brison, Vladimir Mineev, Alexandre Pourret, Adrien Gourgout and Beilun Wu helped me for the understanding and interpretation of what I was measuring. We had interesting discussions together. I thank also Georg Knebel and Jacques Flouquet for careful reading of my articles and my manuscript.

I thank Jean Michel Martinod and Iulian Matei for their technical support for cryogenics and Frric Poletti for his help for computer science. I thank Marielle Perrier for the administrative work. She made things simpler, when they seemed very complicated. Finally I would thank the people, who clean our building, provide food at lunch time and take care of lights and elevators.

Abstract

This thesis is concentrated on the ferromagnetic superconductors UCoGe and URhGe and on the hidden order state in URu_2Si_2. In the first part the pressure–temperature phase diagram of UCoGe was studied up to 10.5 GPa. Ferromagnetism vanishes at the critical pressure $p_c \approx 1$ GPa. Unconventional superconductivity and non Fermi liquid behavior can be observed in a broad pressure range around p_c. The superconducting upper critical field properties were explained by the suppression of the magnetic fluctuations under field. In the second part the Fermi surfaces of UCoGe and URhGe were investigated by quantum oscillations. In UCoGe four Fermi surface pockets were observed. Under magnetic field successive Lifshitz transitions of the Fermi surface have been detected. The observed Fermi surface pockets in UCoGe evolve smoothly with pressure up to 2.5 GPa and do not show any Fermi surface reconstruction at the critical pressure p_c. In URhGe, three heavy Fermi surface pockets were detected by quantum oscillations. In the last part the quantum oscillation study in the hidden order state of URu_2Si_2 shows a strong g factor anisotropy for two Fermi surface pockets, which is compared to the macroscopic g factor anisotropy extracted from the upper critical field study.

Résumé

Cette thèse montre de nouveaux résultats sur les supraconducteurs ferromagnétiques UCoGe et URhGe et sur l'ordre caché dans URu_2Si_2. Le diagramme de phase pression température d'UCoGe a été étudié jusqu'à 10.5 GPa. L'ordre ferromagnétique subsiste jusqu'à la pression critique $p_c \approx 1$ GPa et la supraconductivité non conventionnelle jusqu'à $p = 4$ GPa. Les fluctuations magnétiques responsables de la supraconductivité peuvent être réduites par l'application d'un champ magnétique. Les surfaces de Fermi d'UCoGe et d'URhGe ont été mesurées grace aux oscillations quantiques. Quatre poches ont été détectées dans UCoGe, elles subissent une succession de transition de Lifshitz sous champ magnétique. Les poches détectées évoluent continument avec la pression jusqu'à 2.5 GPa, sans montrer de reconstruction de la surface de Fermi à la pression critique p_c. Dans URhGe, trois poches lourdes de la surface de Fermi ont aussi été découvertes. Enfin dans la phase d'ordre caché d'URu_2Si_2, les oscillations quantiques ont révélé une forte anisotropie du facteur gyromagnétique g pour deux poches de la surface de Fermi, qui est comparable à l'anisotropie macroscopique. Cette dernière a été étudiée à partir du champ critique supérieur de la supraconductivité.

Introduction

The study of strongly correlated electrons systems revealed various interesting phenomenon such as unconventional superconductivity, magnetic quantum criticality or frustrated magnetism. The strong interactions between the electrons can lead to different competitive orders. Quantum phase transitions between these orders and the associated fluctuations have attracted much attention during the past decades. An important discovery was the occurrence of unconventional superconductivity in $CeCu_2Si_2$ [Steglich et al. (1979)] and of pressure induced superconductivity in the vicinity of an antiferromagnetic quantum critical point in $CeCu_2Ge_2$ [Jaccard et al. (1992)], $CePd_2Si_2$ and $CeIn_3$ [Mathur et al. (1998)]. The coexistence of ferromagnetism and superconductivity was observed in UGe_2 under hydrostatic pressure [Saxena et al. (2000)] and at ambient pressure in two other ferromagnets URhGe and UCoGe [Aoki et al. (2001), Huy et al. (2007a)], which are both considered in this thesis. The attractive pairing interaction for the superconductivity is most likely due to ferromagnetic fluctuations. UCoGe and URhGe are heavy fermion systems with an orthorhombic unit cell and complex band structures. This thesis aims at the characterization of the magnetic fluctuations and the Fermi surface in URhGe and UCoGe. The interplay between the magnetic phase transition, the Fermi surface properties and the unconventional superconductivity is discussed in this thesis.

Another open question in heavy fermion physics is the nature of the so called hidden order state in URu_2Si_2. It has been investigated for more than thirty years and the nature of this order remains unclear [Mydosh and Oppeneer (2014)]. Unconventional superconductivity was observed inside the hidden order state of URu_2Si_2. The strong Ising behavior of URu_2Si_2 is a key element of the hidden order state. In this thesis, the g factor anisotropy in URu_2Si_2 was investigated microscopically by quantum oscillations. The aim is to study the role of the different Fermi surface pockets in URu_2Si_2 for a better understanding of both the hidden order state and the coexisting superconductivity.

The first chapter of this thesis introduces the magnetic quantum criticality, the unconventional superconductivity and the Fermi surface instabilities in heavy fermion systems. It discusses also the electrical resistivity, the Hall effect and the quantum oscillations, which

were used to study the magnetic fluctuations and the Fermi surface properties. Chapter 2 describes the experimental techniques for resistivity measurements at low temperature under high magnetic field and under high pressure. In chapter 3 the ferromagnetic quantum criticality in UCoGe was studied by resistivity measurements up to 10.5 GPa. The results about the Fermi surface of UCoGe and URhGe are reported in chapter 4 and 5. In chapter 6 the results of the microscopic measurements of the *g* factor anisotropy in URu_2Si_2 from the Shubnikov-de Haas effect are reported.

Introduction en français

L'étude des systèmes d'électrons fortement corrélés a révélé une grande variété de phénomènes physiques tels que la supraconductivité non conventionnelle, les points critiques magnétiques quantiques et le magnétisme frustré. Les fortes interactions entre les électrons peuvent mener à différents états de la matière. Les transitions de phase quantiques entre ces états et les fluctuations associées ont été étudiées pendant des décennies et ne sont encore que partiellement connus. Une découverte importante a été la supraconductivité non conventionnelle dans $CeCu_2Si_2$ [Steglich et al. (1979)], puis sous pression au voisinage de points critiques quantiques antiferromagnétiques dans $CeCu_2Ge_2$ [Jaccard et al. (1992)], $CePd_2Si_2$ et $CeIn_3$ [Mathur et al. (1998)]. La coexistence de la supraconductivité non conventionnelle et du ferromagnétisme a ensuite été observée sous pression hydrostatique dans UGe_2 [Saxena et al. (2000)] et à pression ambiante dans URhGe et UCoGe [Aoki et al. (2001), Huy et al. (2007a)], qui sont discutés dans cette thèse. Les fluctuations magnétiques sont surement à l'origine de l'appariement des électrons dans la phase supraconductrice. UCoGe et URhGe sont des composés à fermions lourds avec une maille orthorhombique et une structure de bandes complexe. Le but de cette thèse est la caractérisation des fluctuations magnétiques et de la surface de Fermi d'UCoGe et URhGe. Cette thèse vise à faire un lien entre la transition de phase magnétique, les propriétés de la surface de Fermi et la supraconductivité.

Une autre question ouverte dans la physique des électrons corrélés est la nature de l'ordre caché dans URu_2Si_2. Malgré trente année de recherche à ce sujet, l'ordre caché demeure mystérieux [Mydosh and Oppeneer (2014)]. A basse température URu_2Si_2 devient supraconducteur, et l'ordre caché coexiste avec la supraconductivité. Le fort caractère Ising est un élément clé de l'ordre caché. Dans cette thèse l'anisotropie du facteur g a été étudié microscopiquement à partir de mesure d'oscillations quantiques. Cette étude peut permettre d'identifier le rôle des différentes poches de la surface de Fermi dans l'apparition de l'ordre caché et de la supraconductivité.

Le premier chapitre de cette thèse introduit les transitions de phase magnétiques, la supraconductivité non conventionnelle et les instabilités de surface de Fermi dans les sys-

tèmes à fermions lourds. Les phénomènes physiques utilisés pour cette étude : la résistivité électrique, l'effet Hall et les oscillations quantiques sont aussi discutés dans ce chapitre. Le chapitre 2 décrit les méthodes expérimentales utilisées pour mesurer la résistivité électrique avec précision, à basse température, sous champ magnétique et sous pression hydrostatique. La mesure du diagramme de phase pression température d'UCoGe est discutée au chapitre 3. L'étude de la surface de Fermi d'UCoGe et d'URhGe sont présentées aux chapitres 4 et 5. Enfin le chapitre 6 porte sur l'étude microscopique de l'anisotropie du facteur gyromagnétique g d'URu_2Si_2.

Table of contents

Chapter 1

Introduction to heavy fermion physics, electrical resistivity and quantum oscillations

Résumé en français

Ce chapitre présente la physique des fermions lourds, les transitions de phase magnétiques quantiques, la supraconductivité non conventionnelle et les changements de topologie de surface de Fermi induits sous pression ou sous champ magnétique. Le magnétisme dans les composés ayant des fermions lourds est un intermédiaire entre un modèle de magnétisme localisé et un modèle de magnétisme itinérant. L'application de pression ou de champ magnétique peut réduire ce magnétisme. La transition de phase quantique qui en résulte induit dans certains matériaux par l'intermédiaire des fluctuations magnétiques une supraconductivité non conventionnelle. Les supraconducteurs ferromagnétiques UGe_2, URhGe et UCoGe deviennent supraconducteurs au voisinage d'une transition ferromagnétique quantique du premier ordre. Les propriétés microscopiques des fluctuations ferromagnétiques engendrant la supraconductivité et le role de la surface de Fermi à la transition de phase ferromagnétique constituent des questions ouvertes. Les phénomènes physiques utilisés pour étudier les propriétés de ces matériaux tels que la résistivité électrique, l'effet Hall et les oscillations quantiques sont également décrits dans ce chapitre. La résistivité nous renseigne sur les fluctuations magnétiques, l'effet Hall sur la surface de Fermi. Enfin les oscillations quantiques permettent de mesurer directement la surface de Fermi du matériau.

Abstract

This chapter introduces briefly heavy fermion systems, magnetic quantum criticality, unconventional superconductivity and topological changes of the Fermi surface induced by pressure or magnetic field. Magnetism in heavy fermion systems is at the border between a localized and an itinerant picture. The magnetic order can be suppressed by pressure or magnetic field. This quantum criticality may induce unconventional superconductivity mediated by the magnetic fluctuations. The ferromagnetic superconductors UGe_2, URhGe and UCoGe are heavy fermion systems showing superconductivity in the vicinity of a first order ferromagnetic quantum phase transition. The microscopic properties of the ferromagnetic fluctuations responsible for superconductivity and the role of the Fermi surface in ferromagnetic quantum criticality constitute open questions. The physical probes used to study the properties of these materials: resistivity, Hall effect and quantum oscillations are also introduced in this chapter. While the resistivity is influenced by the spin fluctuations, the Hall effect is sensitive to the Fermi surface properties. Quantum oscillations are used to measure directly the Fermi surface.

1.1 Magnetism

Magnetism in uranium based intermetallic compounds is due to magnetic moments carried by the $5f$ electrons of uranium atoms. These magnetic moments come both from the orbital moment and from the spin. These two moments are strongly coupled by the spin orbit interaction. Two models can describe magnetic ordering: the localized picture and the itinerant picture. More details on these models can be found in textbooks about magnetism in matter such as [Skomski (2008), Blundell (2001)].

In the localized picture each electron stays around the same nucleus, so the magnetic moments are carried by the atoms. The magnetic energy is given by the Hamiltonian:

$$H = -\sum_{i,j} J_{i,j} S_i . S_j \tag{1.1}$$

Where S_i is the magnetic moment on the i site and $J_{i,j}$ is the coupling constant representing the magnetic interaction between the i and j sites. Since interactions between spins are short range, the system can be described by considering mainly the nearest neighbor interactions. Within this approximation, the system will be ferromagnetic at zero temperature if the nearest neighbor interaction coupling constant J is positive and antiferromagnetic if J is negative.

In the itinerant picture the electrons responsible for the magnetism are delocalized in the crystal. In a paramagnet half of the electrons have up moments and the other half have down moments. On the contrary in an itinerant ferromagnet, the number of spin up electrons is higher than the number of spin down electrons. The behavior of magnetic moments in matter can follow either the localized picture, the itinerant picture or it can have an intermediate behavior. While the itinerant picture is necessary to describe iron, cobalt or nickel ferromagnetism, the localized picture is necessary to understand magnetism in insulators. The inter-metallic uranium compounds we are interested in are at the border between the localized and the itinerant picture. A crossover or phase transition between localized and itinerant behavior can be induced by tuning an external parameter [Hoshino and Kuramoto (2013), Kubo (2015)].

1.2 Landau Fermi liquid

Electrons in metals can be described by considering a Fermi surface, which separates the occupied state in k vector space from the empty states. In a free electron gas or non interacting Fermi liquid, the excitations are pairs of an electron above the Fermi energy and a hole below the Fermi energy. The Landau Fermi liquid theory was developed to treat an interacting Fermi liquid like the non interacting one [Landau (1957)]. Electrons are screened by the neighbors to become a quasiparticles and excitations are quasiparticles above the Fermi level or quasiholes below the Fermi level. The concept of quasiparticles is well explained in [Leggett (1975), Coleman (2012)]. The interactions modify the relation between the energy E_F and the wave vector k_F of the quasi-particle above the Fermi level. Thus an effective mass $m^\star$ should be considered to describe the quasiparticles instead of the bare electron mass. It is given by:

$$E_F = \hbar^2 k_F^2 / 2m^\star \tag{1.2}$$

the Fermi velocity v_F of the quasiparticles is defined by:

$$v_F = \hbar k_F / m^\star \tag{1.3}$$

The effective mass of the quasiparticles $m^\star$ is usually below the bare electron mass. For example the effective mass of the electrons in copper is $m^\star_{Cu} = 0.5\ m_0$. It can be extracted from specific heat C measurements. Indeed the Sommerfeld coefficient $\gamma = (C/T)_{T\to 0}$ in a Fermi liquid is given by:

$$\gamma = \frac{m^\star k_F k_B^2}{3\hbar^2} \tag{1.4}$$

1.3 Magnetic criticality in heavy fermion systems

1.3.1 Basic properties of heavy fermion systems

In this thesis we will discuss compounds with strongly enhanced effective masses giving rise to very small Fermi velocities (one hundred times smaller than in copper) and very low Fermi energies. This behavior was observed in metallic alloys containing a regular lattice of an inter-metallic compound with a partially filled $4f$ or $5f$ shell. It can be cerium (Ce), ytterbium (Yb) or uranium (U) atoms. $YbRh_2Si_2$ and UPt_3 are famous heavy fermion systems. The electronic specific heat coefficient γ of these compounds are respectively 1.6 J.mol^{-1}.K^{-2} and 1.6 J.mol^{-1}.K^{-2}. In the trivalent state Ce atoms have one electron on the $4f$ sheet, Yb atoms have 13 electrons on the $4f$ shell and thus one hole. However the physics of uranium based systems is more complex. Its valence can either be $U3+$ or $U4+$. Some valence transitions could occur between these two values. f orbitals have a small average radius of electron orbital motion. However a hybridization occurs between f states and the conduction electrons. It forms numerous nearly flat bands, which are responsible for the heavy masses of the electrons. As a consequence the Fermi energy is rather low and the hybridized f bands are close to the Fermi level. In heavy fermion materials the hybridized f electrons carry magnetic moments. Spin orbit coupling is strong and play an important role. More details on heavy fermion physics can be found in reference [Flouquet (2005), Bauer et al. (2007)].

1.3.2 Magnetic quantum criticality in heavy fermion systems

The origin of magnetic interactions in heavy fermion materials was explained by the Ruderman, Kittel, Kasuya and Yosida (RKKY) model. f electrons are assumed to be well localized in this model and there is no overlap between their wave functions. However the conduction electrons which are hybridized with a f electron can interact with other conduction electrons. The RKKY interaction between localized f electrons on neighboring sites is indirect via the conduction electrons. The coupling interaction J oscillates with the distance from the f electron site. This interaction may favor ferromagnetism $(J > 0)$ or antiferromagnetism $(J < 0)$, depending on the nearest neighbor distance. Another interaction between the magnetic moments and the conduction electrons should be considered: the Kondo effect. It competes with the RKKY interaction and acts for paramagnetism. This effect comes from the scattering processes between the conduction electrons and the magnetic ions. The localized spins are screened by the conduction electrons and a non magnetic state is favored.

Kondo physics in heavy fermion materials is discussed in details in reference [Bauer et al. (2007)].

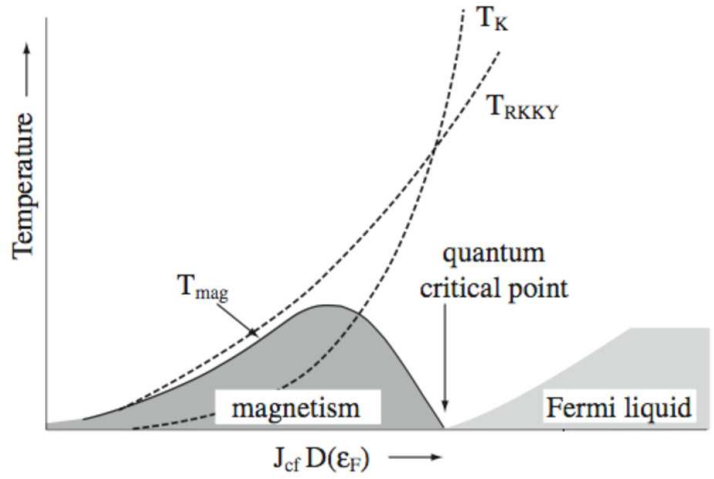

FIG. 1.1 Doniach phase diagram [Doniach (1977)]. Dashed lines represent the characteristic temperatures of the RKKY interaction and the Kondo screening as a function of the product of the coupling interaction and the density of states $JN(E_F)$ named "$JD(\varepsilon_F)$" in the figure. The resulting T–$JN(E_F)$ phase diagram is also represented. The annotation "'Magnetism"' and "'Fermi liquid"' correspond respectively to the magnetically ordered state and the disordered Fermi liquid state. A quantum critical point occurs where the magnetic transition temperature vanishes due to the equality of the RKKY and the Kondo temperature.

Doniach studied the competition between the RKKY interaction and the Kondo effect [Doniach (1977)]. The characteristic temperature of the RKKY interaction and the Kondo effect are plotted as a function of $JN(E_F)$ with the resulting T–$JN(E_F)$ phase diagram in figure 1.1. $N(E_F)$ is the density of states at the Fermi level and J is the exchange coupling. The quantity $JN(E_F)$ can be experimentally tuned by hydrostatic pressure, uniaxial stress, magnetic field or chemical substitution. At low values of $JN(E_F)$ the ground state is a magnetically ordered state. The magnetic transition here is assumed to be second order. When $JN(E_F)$ is increased, T_K increases faster than T_{RKKY} and the ordering temperature decreases. This temperature vanishes when $T_{RKKY} \approx T_K$ at the quantum critical point. Above this point the ground state is a paramagnetic state. The Doniach phase diagram describes well the properties of heavy fermion antiferromagnets, such as $CeCu_2Ge_2$ [Jaccard et al. (1992)], $YbNi_2Ge_2$ [Knebel et al. (2001)]. The situation in uranium based systems is more complicated. Other models were proposed to take into account the spin fluctuations in the vicinity of the quantum phase transition: the itinerant spin fluctuation theory [Moriya (1985)] and the Herz-Millis theory [Millis (1993)]. The different spin fluctuation models assume an

itinerant magnetism and a second order phase transition and they do not consider the Fermi surface. Thus an eventual feedback of Fermi surface changes at the transition is not taken into account. However some antiferromagnetic systems show strong deviations from the spin fluctuation theory in the quantum critical regime which lead to the development of a "local criticality", not only the fluctuations at a specific wave vector gets critical, but fluctuations on the whole Fermi surface [Si et al. (2003)]. This senario includes a change from a small Fermi surface in the magnetically ordered state to a large Fermi surface in the paramagnetic state [Coleman et al. (2001)].

1.3.3 Ferromagnetic quantum criticality

A model was proposed to describe ferromagnetic criticality considering a Fermi surface size changes for both spins at the magnetic phase transition [Kubo (2013)]. However in ferromagnets a decrease of the Curie temperature leads usually to a tricritical point (TCP) at finite temperature, where the magnetic transition becomes first order [Belitz et al. (1999)]. A typical temperature–coupling constant phase diagram of a ferromagnetic material is represented in figure 1.2(a). Above the tricritical point, the first order transition temperature also decreases with the external parameter and it is expected to reach zero temperature with a vertical slope [Mineev (2008)]. At zero temperature a first order quantum phase transition occurs. A theoretical model taken this first order behavior into account was proposed in reference [Imada et al. (2010)].

The pressure–temperature–magnetic field phase diagram of the heavy fermion ferromagnet UGe_2 [Taufour et al. (2010)], URhAl [Shimizu et al. (2015)] and U_3P_4 [Araki et al. (2015)] show a wing structure as represented in figure 1.2(b) [Belitz et al. (2005)]. Two first order-transition lines go from the TCP to the positive and negative field regions. They end up at zero temperature at two quantum critical end points. Theoretical studies show, that quantum order by disorder may induce other phase diagram for ferromagnetic quantum criticality [Karahasanovic et al. (2012)]. They predict the possible occurrence of spiral phase or nematic phase in the vicinity of the ferromagnetic quantum phase transition. A spiral phase was observed in PrPtAl [Abdul-Jabbar et al. (2015)] and a spin glass state was observed in $UNi_{1-x}Co_xSi_2$ [Pikul and Kaczorowski (2012)].The different types of ferromagnetic criticality and the different theoretical models to describe them are reported in the recent review paper [Brando et al. (2016)].

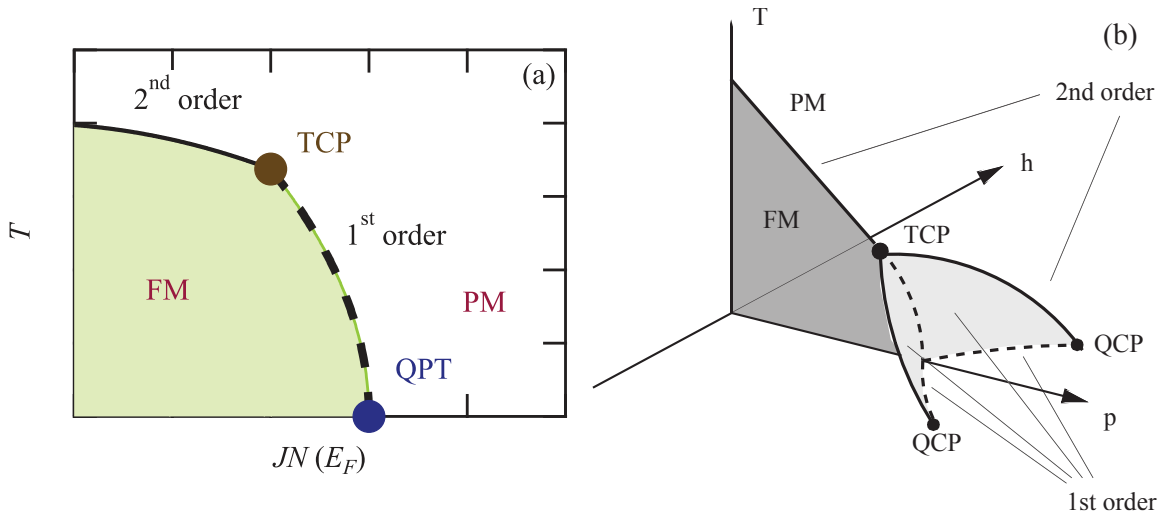

FIG. 1.2 (a) $T - JN(E_F)$ Schematic phase diagram of a ferromagnet. FM and PM represent respectively the ferromagnetic and paramagnetic state. TCP and QPT stand respectively for tricritical point and quantum phase transition. (b) Wing structure phase diagram from reference [Belitz et al. (2005)]. QCP stands for quantum critical point.

1.4 Superconductivity

1.4.1 Introduction to unconventional superconductivity

In the conventional superconductors, superconductivity is induced by the electron-phonon interaction and the it is well described by the Bardeen Cooper Schrieffer model (BCS). This theory is detailed in textbooks such as [Tinkham (1975)]. Unconventional superconductivity was observed in the vicinity of antiferromagnetic quantum critical point in heavy fermion systems such as $CeCu_2Si_2$ [Steglich et al. (1979)] and $CeIn_3$ [Mathur et al. (1998)], which let to the proposal that superconductivity is induced by magnetic fluctuations. Superconductivity in the vicinity of antiferromagnetic quantum critical point were observed more recently in iron pnictides such as $Ba(Fe_{1-x}Co_x)_2As_2$ [Pratt et al. (2009)]. The discovery of superconductivity in $CeCoIn_5$, $CeRhIn_5$ and $CeIrIn_5$ gave good examples to study magnetic fluctuations mediated unconventional superconductivity [Petrovic et al. (2001b), Hegger et al. (2000), Petrovic et al. (2001a)]. These compounds are easy to grow and have a quasi two dimensional structures and relatively high superconducting temperature up to 2.3 K in $CeCoIn_5$, so they have been widely studied. The superconducting gap in $CeCoIn_5$ was determined and is *d* wave [Izawa et al. (2001)]. For some other superconductors like cuprates, organic superconductors and uranium based heavy fermion systems superconductors such as UBe_{13} and UPt_3 [Ott et al. (1983), Stewart et al. (1984)], the pairing mechanism is still under debate [Bennemann and Ketterson (2014)].

The superconducting coupling constant is defined as the product of an average value of the attraction potential leading to electron pairing V and the density of states at the Fermi level: $\lambda = N(E_F)V$ [Leggett (1975)]. It measures the pairing strength. The limiting case $\lambda << 1$ and $\lambda > 1$ are respectively referred as weak coupling and strong coupling limits. The BCS theory describes the superconductivity in the weak coupling limit. In the strong coupling limit, superconductivity can be described by Éliashberg equations [Éliashberg (1960)]. Superconductivity in the strong coupling limit was observed in the uranium based superconductor UBe_{13} [Glémot et al. (1999)]. The Éliashberg equations can be solved numerically [McMillan (1968), Bulaevskii et al. (1988)]. The solution for a spherical Fermi surface in the normal state and an isotropic gap in the superconducting state can be fitted by the formula :

$$T_{sc}^0 = \Omega \exp(-\frac{1}{\lambda - \mu^\star}) \tag{1.5}$$

Ω is the typical phonon energy and $\mu^\star \approx 0.1$ is the average value of Coulomb repulsion multiplied by the density of states at the Fermi level. However a mean field resolution of the Éliashberg equation shows, that the superconducting transition temperature in the quantum critical region depends on the microscopic properties of the magnetic fluctuations and on the Fermi-surface properties [Monthoux and Lonzarich (2001)]. In particular an anisotropic Fermi surface could favor unconventional superconductivity [Monthoux and Lonzarich (2002)].

1.4.2 Upper critical field H_{c2}

Superconductivity is suppressed under magnetic field. The field where it vanishes is called upper critical field or H_{c2}. The main phenomena responsible for this suppression are the Pauli paramagnetic limitation and the orbital limitation. Their origin is explained below. More details can be found in reference [Mineev (1999)]. In the normal state a paramagnetic material can save energy thanks to the Pauli paramagnetism. If this energy gain becomes larger than the energy gain of Cooper pairs condensation $E_S = N(E_F)\Delta^2/2$, superconductivity becomes unfavorable [Clogston (1962)]. The Pauli limit is given by the equality of these two energies:

$$H_{c2}^P = \frac{\Delta\sqrt{2}}{g\mu_B} \tag{1.6}$$

The anisotropy of the paramagnetic limit shows the anisotropy of the gyromagnetic factor g. The Pauli limit is absent in superconductors with equal spin Cooper pairs.

However a second phenomenon leads to the suppression of superconductivity under magnetic field: the orbital limit. Under magnetic field a Lorentz force $F = ev_F \times B$ acts

on Cooper pair electrons. If this force gets bigger than the ratio Δ/ξ between the gap and correlation length, it breaks the pairs. The correlation length is related to the gap through the equation: $\Delta = \hbar v_F/\xi$. So H_{c2} in the orbital limit is given by :

$$H_{c2}^{orb} = \frac{\phi_0 \Delta^2}{\pi(\hbar v_F)^2} \tag{1.7}$$

ϕ_0 is the flux quantum.

In the vicinity of T_{sc} the gap Δ can be parametrized with the Bardeen Cooper Schrieffer expression:

$$\Delta = 1.78 k_B T_{sc} \sqrt{1 - T/Tsc} \tag{1.8}$$

So the initial slope of the upper critical field is given by the WHH theory [Werthamer et al. (1966)]:

$$\frac{dH_{c2}}{dT_{sc}}_{T_{sc}=T_{sc}^0} = -\frac{\phi_0 k_B^2 T_{sc}^0}{2\pi \cdot 0.016(\hbar v_F)^2} \tag{1.9}$$

This equation can be used to deduce the Fermi velocity from H_{c2}. It gives an average Fermi velocity in the plane perpendicular to the magnetic field. An anisotropy of Fermi velocity leads to the anisotropy of the upper critical field in the orbital limit. Since the heavy fermion materials have low Fermi velocities, the orbital limit of the upper critical field is higher in these materials than in other material with comparable critical temperatures.

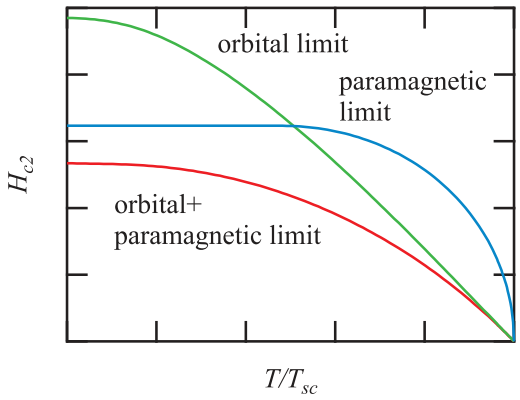

FIG. 1.3 Typical temperature dependence of upper critical in the Pauli limit, in the orbital limit and in the case, where both phenomenon have to be taken into account.

The temperature dependence of the upper critical field is represented in figure 1.3. The three different curves correspond to the orbital limit, the Pauli or paramagnetic limit and H_{c2} in the case, where both phenomenon have to be taken into account. In the pure Pauli limit the slope of the upper critical field at T_{sc} diverges. If H_{c2} is governed by both the orbital

and Pauli limits, the initial slope results from the orbital limit and Fermi velocity can be extracted from equation (1.9).

1.4.3 Ferromagnetic superconductors

Ferromagnetic and superconducting states are consider as antagonistic ground states, since in most superconductors electrons with opposite spins are coupled, whereas ferromagnetism induces a parallel orientation. The coexistence of ferromagnetism and superconductivity was first observed in $ErRh_4B_4$ [Sinha et al. (1982)]. The superconducting critical temperature of $ErRh_4B_4$ is $T_{sc} = 8.7$ K. It becomes ferromagnetic at 1.2 K and superconductivity is suppressed below 0.7 K. In this system ferromagnetism and superconductivity are competitive phenomenon. However the study of the superfluid state of ^{3}He shows, that it comes from the Bose Einstein condensation of equal spin pairs. Indeed ^{3}He shows two superfluid states: the A and B states. The spin part of the wave function of a pair in the A state is the combination of $\uparrow\uparrow$ and $\downarrow\downarrow$. In the B state it is the combination of $\uparrow\uparrow$, $\uparrow\downarrow + \downarrow\uparrow$ and $\downarrow\downarrow$. The superfluid phase in ^{3}He is discussed in [Leggett (1975), Mineev (1999)]. The study of ^{3}He suggests the possibility of superconductivity with equal spin Cooper pair in ferromagnetic materials.

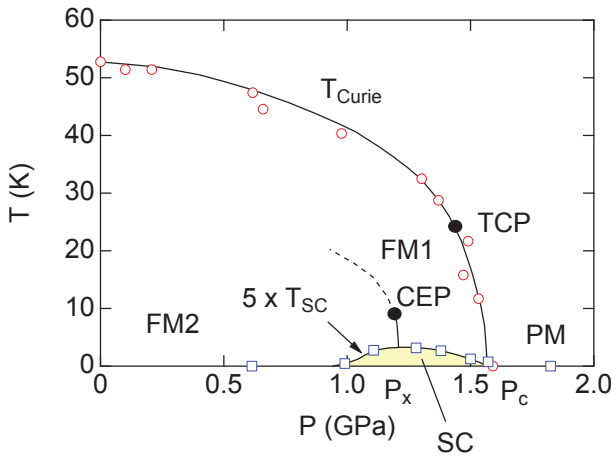

FIG. 1.4 Pressure temperature phase diagram of UGe_2 [Saxena et al. (2000), Pfleiderer and Huxley (2002), Taufour et al. (2010)]. TCP and CEP stand for tricritical point and critical end point.

Superconductivity mediated by ferromagnetic fluctuations in the vicinity of a ferromagnetic quantum critical point was proposed by a theoretical study [Fay and Appel (1980)]. The coexistence of superconductivity and ferromagnetism was observed in the vicinity of a first order ferromagnetic quantum phase transition under pressure in the heavy fermion system UGe_2 [Saxena et al. (2000)]. The pressure temperature phase diagram of UGe_2 is rep-

resented in figure 1.4. The Curie temperature T_C decreases with pressure and the magnetic transition becomes first order at a tricritical point around 1.4 GPa [Taufour et al. (2010)]. The Curie temperature reaches zero temperature at the critical pressure $p_c \approx 1.5$ GPa. This phase diagram shows another first order quantum phase transition between two ferromagnetic states FM2 and FM1 at $p_x \approx 1.2$ GPa [Pfleiderer and Huxley (2002)]. The transition at p_x may correspond to a change from a localized behavior to the itinerant behavior [Kubo (2015)]. A superconducting dome was observed around p_x and superconductivity seems to be excluded from the paramagnetic state above p_c. The appearance of superconductivity was explained from the magnetic fluctuations around these two transitions [Mineev (2002)]. Two ferromagnetic superconductors at ambient pressure were discovered later: URhGe and UCoGe [Aoki et al. (2001), Huy et al. (2007a)]. Magnetic quantum criticality can be induced in URhGe by the application of a magnetic field of $H_R = 12$ T along the hard axis b. A superconducting region was observed around this transition, it was named reentrant superconductivity [Lévy et al. (2005)]. Chapter 3 and 4 of this thesis will be devoted to the ferromagnetic superconductor UCoGe and chapter 5 to URhGe. These two compounds will be introduced in detail later. Table 1.1 gives the Curie temperature T_C, the spontaneous magnetization M_0, the critical pressure p_c, the superconducting transition temperature T_{sc} and the Sommerfeld coefficient γ of the ferromagnetic superconductor UGe_2, URhGe and UCoGe. The results on UGe_2 were taken from references: [Saxena et al. (2000), Tateiwa et al. (2001)]. It is important to notice the strong variation of the Curie temperature and the spontaneous magnetization between these three compounds. While UGe_2 is strongly ferromagnetic with the spontaneous magnetization $M_0 = 1.4\mu_B$/U, URhGe shows a much smaller spontaneous magnetization $M_0 = 0.4\mu_B$/U and UCoGe is weakly ferromagnetic with $M_0 = 0.03\mu_B$/U. The Sommerfeld coefficient values show that all of them are heavy fermion systems. Finally coexistence between ferromagnetism and superconductivity was also observed under pressure in the monoclinic system UIr [Akazawa et al. (2004)].

Compound	T_C(K)	$M_0(\mu_B/U)$	p_c(GPa)	$T_{sc}(K)(p=0)$	γ(mJ.mol^{-1}.K^{-2})
UGe2	52	1.4	1.5	-	30
URhGe	9	0.4	>12.5	0.22	160
UCoGe	2.7	0.03	1	0.6	55

Table 1.1 Properties of ferromagnetic superconductor UGe_2, URhGe and UCoGe.

Superconductivity in ferromagnetic superconductors comes from equal spin Cooper pairs. As a consequence the upper critical field of the ferromagnetic superconductors is in the pure orbital limit [Mineev (2010)]. The wave function of the Cooper pair consists in an orbital part and a spin part. It must be antisymmetric to obey the Pauli principle, so one

part is antisymmetric and the other one must be symmetric. As a consequence the orbital part of equal spin Cooper pairs is antisymmetric. The symmetry of the orbital part of equal spin Cooper pair may correspond to the spherical harmonic p. The symmetry of the superconducting gap in the density of states is given by the symmetry of the wave function of the Cooper pairs. So it would be also p wave. More experiments on ferromagnetic superconductors are needed to confirm, that magnetic fluctuations are responsible for superconductivity and for a better understanding of microscopic phenomena responsible for superconductivity.

1.5 Fermi surface instabilities

1.5.1 Fermi surface and quantum crticality

We focus now on the interplay between quantum criticality and the Fermi surface. We consider first a quantum phase transition between antiferromagnetic and paramagnetic states. The periodicity of the lattice changes at the transition, so the Brillouin zone is reduced. A folding of the Fermi surface is expected leading to a complete reconstruction of the Fermi surface. As a consequence transport and thermodynamic properties of the material are modified. Such Fermi surface reconstructions were observed at the quantum critical point of the heavy fermion superconductors such as $CeRh_2Si_2$ [Araki et al. (2002)] and $CeRhIn_5$ [Shishido et al. (2005)]. However no theoretical description of quantum criticality takes the details of the Fermi surface into account. These Fermi surface changes may influence the unconventional superconductivity.

An open question is the role played by the Fermi surface at a quantum phase transition between a ferromagnetic and a paramagnetic state. The Brillouin zone remains unchanged at these transitions and a splitting of the Fermi surface is induced by the spontaneous magnetization. In the ferromagnetic superconductor UGe_2 with a strong polarization in the ferromagnetic state it was shown that the quantum phase transitions at p_x and p_c are accompanied with drastic Fermi surface changes [Terashima et al. (2001), Settai et al. (2002)]. Then the absence of superconductivity in the paramagnetic state was explained from these Fermi surface changes [Sandeman et al. (2003)]. A Fermi surface change was also observed in the ferromagnetic superconductor URhGe, when ferromagnetism is suppressed by a transverse magnetic field [Yelland et al. (2011)]. The authors claim, that the Fermi surface change is responsible for the occurrence of the reentrant superconductivity [Yelland et al. (2011)]. This point is under debate, since the reentrant superconductivity can also be explained from magnetic fluctuations without taking the Fermi surface into account [Mineev (2011), Mineev (2015a)]. The interplay between quantum criticality, Fermi surface and

unconventional superconductivity in ferromagnetic materials is still unclear. More heavy fermion ferromagnets have to be studied to compare them with these two examples. In particular the Fermi surface change at the ferromagnetic transition of the weak ferromagnet UCoGe is discussed in this thesis.

1.5.2 Effect of a magnetic field on the Fermi surface

The three heavy fermion systems studied in this thesis UCoGe, URhGe and URu_2Si_2 shows negative g factor [Butchers et al. (2015), Shick (2002), Werwiński et al. (2014)]. This means that the magnetic moment on the uranium site coming both from the spin and orbital moment is opposite to the spin of the electrons. g in this thesis refers to the modulus of the g factor. Under magnetic field the Zeeman energy can be usually described by:

$$\Delta E_{\uparrow} = \frac{g\mu_B}{2}B \tag{1.10}$$

$$\Delta E_{\downarrow} = -\frac{g\mu_B}{2}B \tag{1.11}$$

As a consequence the up magnetic moment bands shrink under magnetic field, they constitute the minority bands. On the other hand the down magnetic moment bands expand with magnetic field and constitute the majority bands. In uranium based systems the bands may mix up and down moment due to hybridization. The bands will be considered as majority bands if they expand with magnetic field and minority bands if they shrink. k_F^2 measures the size of the Fermi surface, its evolution with magnetic field is given by:

$$\Delta k_F^2 = -\frac{2m^\star}{\hbar^2}\Delta E = \pm\frac{ge}{2\hbar}\frac{m^\star}{m_0} \tag{1.12}$$

It is important to notice that higher the effective mass $m^\star$, the stronger is the influence of the magnetic field on the Fermi surface. This continuous Fermi surface change may lead to changes of the Fermi-surface topology named Lifshitz transitions (see below).

The effective masses associated to the different bands of the Fermi surface in a heavy fermion system may also be affected by the magnetic field. A simple argument was proposed by considering the Hubbard model to describe the evolution of these masses under magnetic field [Korbel et al. (1995), Spałek (2006)]. The renormalization of the effective mass is expected to come mainly from the Coulomb interaction between opposite spin electrons. Since the majority band electrons interact with less and less opposite spin electrons under magnetic field, the effective mass associated to a majority band increases with magnetic field. On the other hand the effective mass associated to a minority band decreases

with magnetic field. Another theory based on a two band models was proposed to describe the field dependence of the effective mass under magnetic field [Edwards and Green (1997)]. At low magnetic field, the authors proposed an increase of the effective mass for the majority band and a decrease for the minority band in contradiction with the solution from the Hubbard model. However a Fermi surface change is predicted at higher magnetic field and would lead to a large effective mass for the minority band and a small effective mass for the majority band as proposed from the Hubbard model.

1.5.3 Lifshitz transitions

The Fermi surface of metallic compounds can be tuned by the modification of an external parameter such as hydrostatic pressure, magnetic field or chemical doping. This modification of the Fermi surface may induce changes of the topology of the Fermi surface. The transition occurring at a change of topology of the Fermi surface without any change of the magnetic order or crystal structure is called a Lifshitz transition [Lifshitz and Kaganov (1963)]. One possibility is the appearance or disappearance of Fermi surface pockets. This is represented in figure 1.5(a). A neck disruption or formation as represented in figure 1.5 (b) are other possibilities of Lifshitz transitions. The transition becomes a crossover for finite temperature. Contrary to magnetic phase transitions discussed previously, Lifshitz transition are transitions between two states with the same symmetry. The value of the external parameter where the transition occurs is not sensitive to temperature. The specific heat is continuous at the transition. However if a Lifshitz transition is induced by the modification of the external parameter x, the first derivative of the specific heat diverges at the Lifshitz transition in $1/\sqrt{x}$ [Blanter et al. (1994)]. Thus Lifshitz transitions are referred as 2.5 order transitions. Asymmetric peaks in the thermal expansion and the thermopower and a broad step-like anomaly were predicted at the Lifshitz transition [Blanter et al. (1994)]. However an other study predicts the possibility of peaks in the resistivity and succession of minimum and maximum in the Seebeck effect at a Lifshitz transition [Buhmann and Sigrist (2013)].

One of the first Lifshitz transitions was discovered in arsenic under hydrostatic pressure [Schirber and Van Dyke (1971)]. A simple example of a Lifshitz transition is the transition induced by chemical substitution in the system $Li_{1-x}Mg_x$ [Rajput et al. (1993)]. Lithium crystallizes in the body center lattice. Its Fermi surface is represented on figure 1.5(c). It consists of a closed pocket at the center of the Brillouin zone. It expands with the substitution and connects to itself at the Brillouin zone border for a Mg concentration x=0.18. This Lifshitz transition is a neck formation. Lifshitz transitions play an important role in topological insulators [Liu et al. (2016)]. Indeed transport properties are sensitive to the Fermi-surface topology. Lifshitz transitions induced by chemical substitution were also observed close

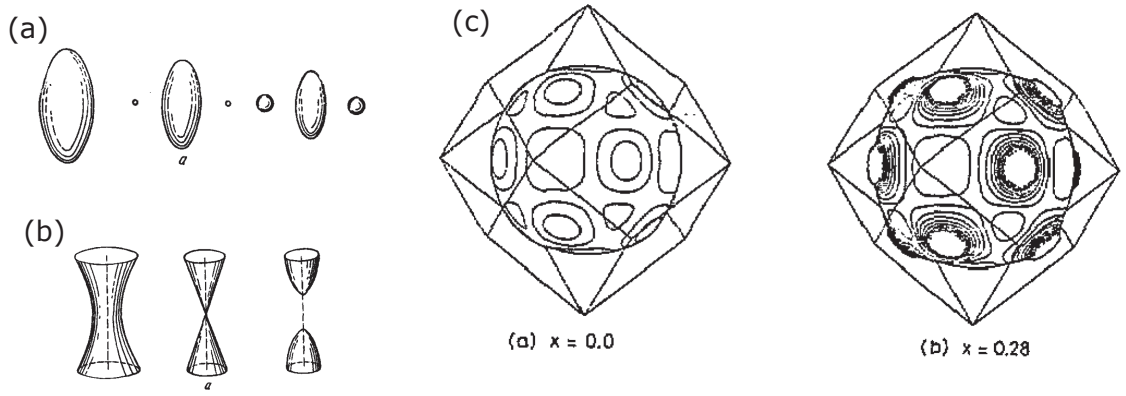

FIG. 1.5 Evolution of the Fermi surface through a Lifshitz transition. (a) and (b) represent respectively the void formation and the neck disruption of a Fermi surface pocket and are taken from reference [Lifshitz and Kaganov (1963)]. (c) Lifshitz transition in $Li_{1-x}Mg_x$ [Rajput et al. (1993)]. While the Fermi surface of Lithium on the left consists of a closed pocket, the Fermi surface of the x=0.28 alloy on the right is connected to itself through the Brillouin zone boundary. A Lifshitz transition consisting in a neck formation occurs at x=0.18.

to the edge of a superconducting dome in iron pnictides such as $Ba_{1-x}K_xFe_2As_2$ [Khan and Johnson (2014)] and in cuprates such as $YBa_2Cu_3O_y$ [LeBoeuf et al. (2011)]. Several hydrostatic pressure induced Lifshitz transitions were predicted by bandstructure calculations in the highest T_{sc} superconductor H_3S in the vicinity of the superconducting transition [Jarlborg and Bianconi (2016)]. The interplay between these Lifshitz transitions and superconductivity is still under debate.

Recently the expression Lifshitz transition was also used more generally for any transitions with Fermi-surface topology changes. Several Fermi-surface topology change coupled with a magnetic transition were also named Lifshitz transition. Lifshitz transitions would occur at the first order transitions on the wing structure of ferromagnets $ZrZn_2$ and UGe_2 [Yamaji et al. (2006)], at the first order magnetic moment reorientation of the ferromagnet URhGe [Yelland et al. (2011)] and at at the Néel temperature in $BaFe_2As_2$ [Wang et al. (2015)]. These three examples do not correspond to the definition of Lifshitz transition given in the previous paragraph, because the Fermi surface changes are accompanied with a change of the magnetic order. Several recent theoretical studies interpreted these cases in terms of an interplay between a magnetic transition and a Lifshitz transition [Bercx and Assaad (2012), Kubo (2015) and Yamaji et al. (2006)]. Finally the expression Lifshitz transition is not used only in solid state physics, other topological properties change were interpreted as Lifshitz transitions for example in ^{3}He [Silaev et al. (2015)] and in ultracold dipolar fermions [van Loon et al. (2016)].

As shown by equation 1.12 Lifshitz transitions can be easily induced by a magnetic field in heavy fermion systems. Since the magnetic field is easier to tune with precision than pressure or chemical substitution, heavy fermion compounds are good systems to study the Lifshitz transitions. Such field induced Lifshitz transitions were observed in many heavy fermion systems such as $CeRu_2Si_2$ [Aoki et al. (1993)], $CeIn_3$ [Sebastian et al. (2009)] and $YbRh_2Si_2$ [Pfau et al. (2013), Pourret et al. (2013a)]. A theoretical study based on the experimental results on $CeIn_3$ from reference [Sebastian et al. (2009)] shows, that Lifshitz transitions under magnetic field must have different properties from zero field Lifshitz transition due to the Landau level quantization [Schlottmann (2011)]. In particular the anomaly in resistivity at a Lifshitz transition would be more clear under high magnetic field [Schlottmann (2013)]. The discovery of a field induced Lifshitz transition in UCoGe is reported in chapter 4 and the comparison between the properties of the different field induced Lifshitz transitions in heavy fermion systems will be discussed in this chapter .

1.6 Electrical resistivity and Hall effect

1.6.1 Resistivity in a Fermi liquid

The resistivity ρ is an intrinsic property of the material. It is defined for a cylindrical sample of length l in current direction, section σ and resistance R with: $\rho = R\sigma/l$. The ratio σ/l is sometimes called the geometrical factor. The electrical current in metals is carried by the quasiparticles and the quasiholes and the resistivity comes from their scattering processes. For a simple picture scattering is usually described in terms of electrons and holes scattering. The uranium based heavy fermion systems, we are interested in, are compensated metals. It means, that the contribution of electrons and holes to the resistivity are equivalent. Only electrons and holes at the Fermi level contribute to the resistivity, so it is related to the geometry of the Fermi surface. The main contributions to the resistivity are electron impurity scattering, electron electron scattering, electron phonon scattering and electron magnon scattering. The electron magnon scattering comes from the interaction between ordered magnetic moments and electrons, it occurs only in magnetically ordered states. The electron phonon scattering contribution is proportional to T^5, so it is often negligible below liquid helium temperature and it will not be taken into account in this thesis. In a paramagnetic state within the Fermi liquid model the resistivity follows:

$$\rho = \rho_0 + AT^2 \tag{1.13}$$

ρ_0 is the residual resistivity, it comes from electron impurity scattering and depends only on sample quality. The residual resistivity ratio $RRR = \rho_{300K}/\rho_0$ is used as an indication of sample quality assuming, that ρ_{300K} is dominated by electron-phonon scattering processes and independent of sample quality. AT^2 is the inelastic scattering term. The A coefficient is related to the effective mass $m^\star$ of the quasiparticles by the Kadowaki Woods ratio, which is obeyed in many heavy fermion systems [Kadowaki and Woods (1986)]:

$$A \propto \gamma^2 \propto m^{\star 2} \tag{1.14}$$

1.6.2 Resistivity in the quantum critical region

The Kadowaki Woods ratio is not verified in the vicinity of a quantum critical point. Then the behavior of the resistivity and the specific heat can often be described by spin-fluctuation theory [Moriya (1985)]. They depend on the type of the magnetic order and on the dimensionality of the system [Moriya (2003), Flouquet (2005)]. A typical schematic phase diagram is represented in figure 1.6. At low temperature the Fermi liquid behavior $\rho = \rho_0 + AT^2$ is verified in the paramagnetic state in the entire pressure range. In a three dimensional ferromagnet, the Sommerfeld coefficient diverges as $\gamma \propto \log(p - p_c)$ in the vicinity of the critical pressure p_c and the A coefficient of resistivity diverges in $A \propto (p - p_c)^{-1}$. At the critical pressure and at positive temperature a non Fermi liquid state is predicted. The Fermi and non Fermi liquid states are separate by a crossover line, which starts at the quantum critical point and the crossover temperature increases when the system is tuned from the critical pressure to the paramagnetic state. The resistivity in the non Fermi liquid state is often fitted by a power law:

$$\rho = \rho_0 + AT^n \tag{1.15}$$

In the non Fermi liquid state, the exponent n is lower than 2 and it was predicted to be $n = 5/3$ for a three dimensional ferromagnet by the spin fluctuations theory [Moriya (1985)]. This prediction was confirmed by calculations based on the Hertz-Millis theory of the quantum fluctuations [Millis (1993)]. These two theories were developed for a second order phase transition, however first order quantum phase transitions in the itinerant ferromagnets $NiAl_3$, U_3P_4 and URhAl follow their predictions [Niklowitz et al. (2005), Araki et al. (2015), Shimizu et al. (2015)]. It means that the quantum phase transition in these systems is weakly first order: it shows some characteristics of second order phase transitions such as the violation of T^2 law for resistivity. On the contrary the ferromagnets CoS_2, UGe_2 shows T^2 resistivity in the whole pressure range around its quantum phase transition indicating a strong first order behavior [Sidorov et al. (2011), Kobayashi et al. (2002)]. Deviations from

the spin-fluctuaton theory have also been reported in the ferromagnets MnSi and $ZrZn_2$ with $n = 3/2$ over an extended pressure range above the critical pressure [Pfleiderer et al. (2001), Kabeya et al. (2012)].

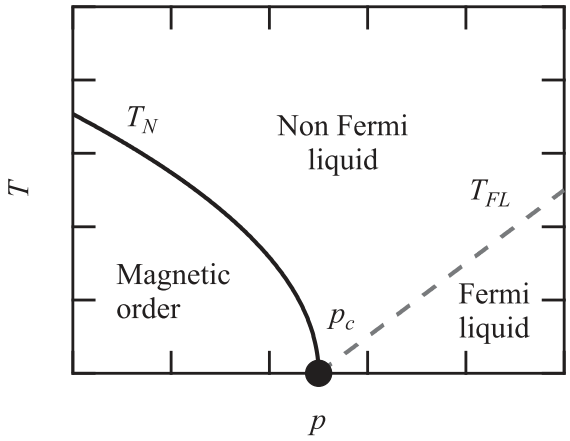

FIG. 1.6 Schematic pressure–temperature phase diagram of a heavy fermion system. The magnetic transition is assumed to be second order and reaches zero temperature at a quantum critical point at $p = p_c$.

1.6.3 Magnetoresistance

The resistivity under magnetic field is called magnetoresitance. It is discussed in detail in the textbook [Pippard (1989)]. An applied magnetic field induces an orbital motion of the electron in the plane perpendicular to the field direction. If the magnetic field and the electrical current are applied along the same direction, the resistivity is not affected by the orbital motion. In bad quality samples the resistivity decreases with field due to the reduction of disorder by the polarization. The magnetoresistance may also result from the modification of the Fermi surface or the magnetic correlations by the magnetic field. However if the magnetic field is transverse to the electrical current, the resistivity can be affected by the orbital motion of the electrons. The cyclotron frequency of this motion is:

$$\omega_c = eB/m^\star \tag{1.16}$$

The diffusion time τ is defined as the average time between two scattering processes. The cyclotron angle $\omega_c\tau$ is the average angle of the cyclotron motion between two scattering processes. In low quality samples $\omega_c\tau << 1$, the orbital effect is killed by disorder and the resistivity is not affected by the orbital motion. On the contrary in high quality crystals

$\omega_c\tau >> 1$, a strong magnetoresistance is expected due to the orbital effect. In a compensated metal with close Fermi surface pockets it is expected to be proportional to H^2. However if the Fermi surface shows an open orbit in the direction transverse to both current and magnetic field, the magnetoresistance saturates [Pippard (1989)]. Such a saturation was observed for example in the ferromagnetic superconductor UGe_2 [Ōnuki et al. (1991)].

1.6.4 Hall effect

When a magnetic field B and an electrical current I are applied in different directions, a non zero Hall voltage V_{xy} is induced along the direction $I \times B$. The Hall resistance is defined as the ratio between Hall voltage and electrical current: $R_{xy} = V_{xy}/I$. Finally, the Hall resistivity is the ratio between the Hall resistance and the thickness of an orthorhombic sample in magnetic field direction: $\rho_{xy} = R_{xy}/z$. The Hall resistivity is an intrinsic property of the material, it does not depend on the sample shape. It is the sum of the linear Hall effect and the anomalous Hall effect, which are respectively proportional to B and M:

$$\rho_{xy}(B) = R_0 B + R_A M(B) \tag{1.17}$$

The orbital motion of the electrons described in the previous paragraph is also responsible for the linear Hall effect. Its coefficient R_0 is directly related to the number of carrier in the metal:

$$R_0 = \frac{1}{(n_h - n_e)e} \tag{1.18}$$

n_h and n_e are respectively the number of hole type carriers and electron type carriers. In compensated metals this formula leads to a divergence and it is not valid anymore. It should be replaced by:

$$R_0 = \frac{1}{n_e e} \frac{\omega_{c,e}\tau_e - \omega_{c,h}\tau_h}{\omega_{c,e}\tau_e + \omega_{c,h}\tau_h} \tag{1.19}$$

The index e and h stand for electrons and holes. The linear Hall effect is well described in reference [Pippard (1989)].

The anomalous Hall effect plays an important role in ferromagnets. Up spin and down spin itinerant electrons give opposite contributions to the anomalous Hall effect and up spin and down spin magnetic impurities give also opposite contributions. The Anomalous Hall effect is proportional to the magnetization M. It occurs in presence of strong spin-orbit coupling. It comes from three contributions: the intrinsic Hall effect, the skew scattering and the side jump effect. They are described in details in [Nagaosa et al. (2010)]. The intrinsic Hall effect comes from the Berry curvature, so it depends on the topology of the

bandstructure. The skew scattering is an asymmetric scattering process of electrons on an impurity. If the anomalous Hall effect is dominated by the skew scattering, it is proportional to the scattering time τ and to the resistivity ρ of the material. Side jump contribution comes from the deflection of the electron velocities in the vicinity of an impurity. The analysis of the Hall effect in multiband systems is rather complicated. However both the linear and the anomalous Hall effect are very sensitive to the Fermi-surface properties. So the Hall effect is a good probe to detect Fermi surface changes in multiband systems.

1.7 Quantum oscillations

1.7.1 Simple picture

Under magnetic field electrons are on quantized levels called Landau levels [Pippard (1989)]. In the k vector space these levels are tubes along the magnetic field direction. The section of these tubes is proportional to the magnetic field B:

$$\sigma_n = \pi k_n^2 = \frac{2\pi e}{\hbar}(n+\frac{1}{2})B \tag{1.20}$$

n is the index of the Landau tube. For a simple picture we consider a spherical Fermi surface with the extremal cross section of area S_{ext}. If a tube has the same size as the Fermi surface: $\sigma_n = S_{ext}$, the density of states at the Fermi level is enhanced. When the magnetic field is swept, Landau tubes are extended and go successively through the Fermi surface edge. As a consequence oscillations of the density of states at the Fermi level can be observed. It can be easily shown from equation (1.20), that they are periodic in $1/B$ and their frequency is proportional to the extremal cross section of the Fermi surface through the Onsager formula:

$$F = \frac{\hbar S_{ext}}{2\pi e} \tag{1.21}$$

This equation is valid for any Fermi surface geometry, the demonstration is detailed in [Schoenberg (1984)]. For a more complicated Fermi surface each extremal area of the Fermi surface will give a contribution to the oscillations of the density of states at the Fermi level. These oscillations induce oscillations of the free energy and of many measurable quantities: magnetization (de Haas-Van Alphen effect), resistivity (Shubnikov-de Haas effect), specific heat, thermopower, skin depth, sound velocity and others. Quantum oscillations can be used to probe the Fermi surface as shown by the example in figure 1.7. The Fermi surface in figure 1.7(a) has one extremal cross section perpendicular to the magnetic field, oscillations can be detected in the resistivity with a frequency proportional to this area (c). The Fermi

surface after the neck formation 1.7(b) shows a second extremal area. As a consequence a lower frequency oscillation is added on the resistivity signal (d). This figure shows, that a Lifshitz transition resulting from a neck formation leads to the appearance of a new quantum oscillation frequency.

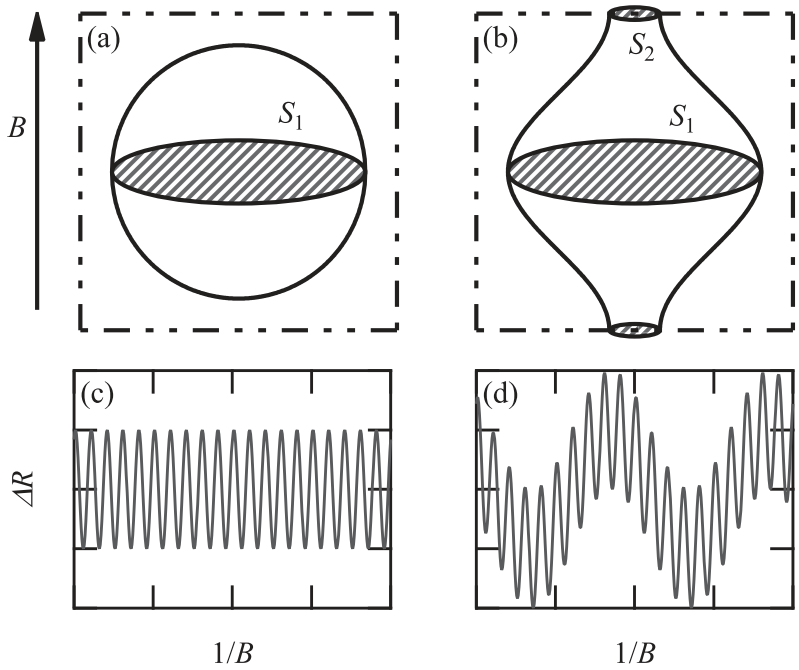

FIG. 1.7 (a) Nearly spherical Fermi surface with an extremal area S_1 in a plane perpendicular to the applied magnetic field. (b) Fermi surface after a neck formation on the top of the Brillouin zone. A second extremal area S_2 appears. (c), (d) Shubnikov-de Haas signal as a function of inverse magnetic field corresponding respectively to the Fermi surfaces represented in (a) and (b). The amplitudes of quantum oscillations were chosen arbitrary.

1.7.2 The role of the Zeeman effect

In the previous paragraph the Zeeman effect was not taken into account. If we consider first a minority spin electron pocket, its size is reduced under magnetic field by the Zeeman effect. While the Landau tubes are expanded under magnetic field, the edge of the Fermi surface moves in the opposite direction. As a consequence the quantum oscillation frequency is increased by an additional contribution from the Zeeman effect. The Onsager formula can be derived taking this effect into account:

$$F = F_{true} - B\frac{F_{true}}{dB} \tag{1.22}$$

$$F_{true} = \frac{\hbar}{2\pi e} S_{ext} \tag{1.23}$$

Equation (1.22) can be interpreted geometrically: the frequency of quantum oscillations is the linear back projection of the true frequency as a function of the magnetic field down to zero field as illustrated in figure 1.8. The phase of the quantum oscillations is also affected by the Zeeman effect:

$$\phi = \phi_0 + 2\pi \frac{dF_{true}}{dB} \tag{1.24}$$

ϕ_0 is the intrinsic phase, it is related to the Berry curvature. The phase of quantum oscillations will be discussed in detail later.

The Zeeman effect is usually linear in field and follow equations (1.10) and (1.12). In this case for a circular orbit on the Fermi surface, we can easily show:

$$S_{ext} = S_{ext}(B = 0) + \frac{m^\star g \mu_B B}{\hbar^2} \tag{1.25}$$

This equation is also valid for other shapes of extremal cross section on the Fermi surface [Schoenberg (1984)]. The frequency of quantum oscillations is given by:

$$F = \frac{\hbar}{2\pi e}(S_{ext}(B = 0)) \tag{1.26}$$

Thus the Quantum oscillation frequency depends only on the extremal cross section of the Fermi surface at zero field. The true and observed frequencies as a function of magnetic field are represented in figure 1.8(a) for a paramagnetic material in the case of a linear Zeeman effect. The frequency of the quantum oscillations is the same for both spins and it is constant with field. On the contrary in a ferromagnetic material spin up and spin down Fermi surfaces give two different oscillations frequencies according to equation (1.26).

In some particular cases the Zeeman effect shows non linearity. An example is given in figure 1.8(b). In this example the minority band collapses faster and faster leading to an increase of the quantum oscillation frequency of the minority band. The majority bands expands faster and faster, so its quantum oscillation frequency decreases with magnetic field. In this case the quantum oscillation frequency depends on the magnetic field. Magnetic field dependence of the extremal cross section of the Fermi surface can be deduced from the field dependence of the quantum oscillation frequency by integrating equation (1.22). However this integration leaves an unknown term in $F_{true}(B)$. It is linear in magnetic field.

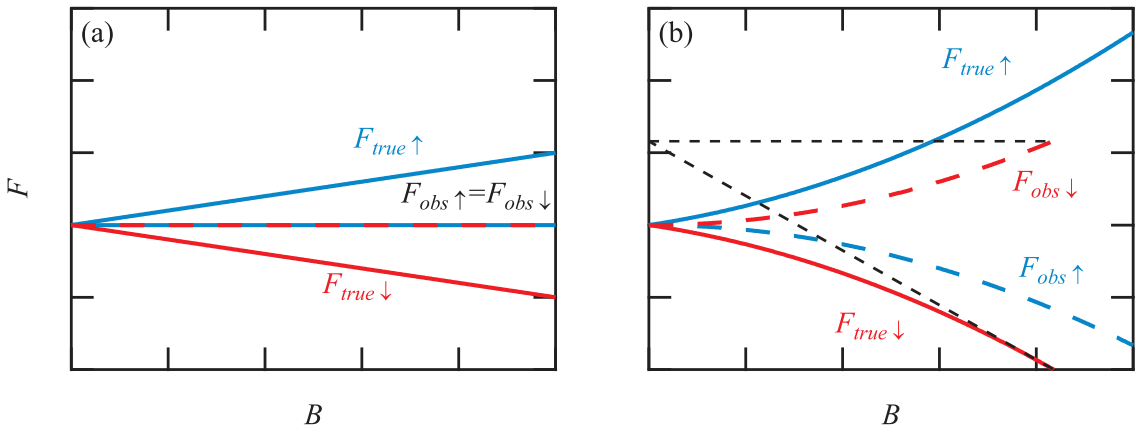

FIG. 1.8 Magnetic field dependence of the true frequencies F_{true} defined from equation (1.23) and of the quantum oscillations frequency F_{obs} calculated with equation (1.22) for both spins. (a) The left panel corresponds to the case of a linear Zeeman effect in a paramagnetic material. (b) The right panel corresponds to the case of a non linear Zeeman effect in a paramagnetic material with the suppression of the spin down-Fermi surface and an increase of the spin up-Fermi surface. The dashed lines show the geometrical interpretation of equation (1.22): $F_{obs}(B)$ is the back projection of $F_{true}(B)$ down to zero field.

1.7.3 Analysis of a quantum oscillation signal

If the quantum oscillation signal comes from a single extremal orbit on the Fermi surface, the oscillation frequency can be deduced from a sinusoidal fit or from the interval in 1/B between successive extrema. However in multiband systems, fast Fourier transform (FFT) algorithm is needed to extract the numerous quantum oscillation frequencies. This algorithm is performed on the oscillation signal $\Delta R(1/B)$ on a finite interval from $1/B_{max}$ to $1/B_{min}$. To avoid satellite peaks in the FFT due to the finite size of the field interval, the FFT is performed on the product of the oscillation signal and the Hanning window. This window is given by:

$$W(1/B) = (cos(\pi \frac{1/B - 1/2B_{min} - 1/2B_{max}}{1/Bmin - 1/B_{max}}))^2 \tag{1.27}$$

For FFT on small intervals, the number of points in the FFT can be artificially increased by adding points with the value zero at the end of the oscillations signal before the application of the FFT algorithm. This trick is called the zero padding. The FFT algorithm, the effect of the Hanning window and of the zero padding are discussed in reference [Press et al. (1986)]. The effective magnetic field of the FFT interval is defined with $1/B_{eff} = (1/B_{min} + 1/B_{max})/2$.

1.7.4 Amplitude of the dHvA oscillations

The oscillations of the magnetization as a function of inverse magnetic field are named de Haas-van Alphen (dHvA) effect. These oscillations are described by the Lifshitz-Kosevic formula. The demonstration of this formula can be found in [Schoenberg (1984)].

$$\Delta M = \sum_i \sum_p \frac{a_{i,p}}{p^{3/2}} sin(\frac{2p\pi F_i}{B} + \phi_{ip}) \tag{1.28}$$

$$a_{i,p} = \frac{B^{1/2}}{\kappa^{1/2}} R_{T,i,p} R_{D,i,p} R_{S,i,p} \tag{1.29}$$

$$R_{T,i,p} = \frac{\alpha p m_i^* T/B}{sh(\alpha p m_i^* T/B)} \tag{1.30}$$

$$R_{D,i,p} = exp(-\frac{\alpha p m_i^* T_{D,i}}{B}) \tag{1.31}$$

$$R_{S,i,p} = \frac{1}{2}, \ \ (F_{i\uparrow} \neq F_{i\downarrow}) \tag{1.32}$$

$$R_{S,i,p} = cos(\frac{p\pi g m_i^\star}{2m_0}), \ \ (F_{i\uparrow} = F_{i\downarrow}) \tag{1.33}$$

$$\alpha = 2\pi^2 k_B / e\hbar \tag{1.34}$$

The dHvA signal is decomposed in a Fourier series where p is the harmonic index and the index i stands for the different extremal cross sections of the Fermi surface. The quantum oscillation amplitude depends on the average curvature of the Fermi surface along the extremal orbit κ. As a consequence a cigar shape Fermi surface along the field direction gives higher amplitude quantum oscillations than a pancake shape Fermi surface. R_T, R_D and R_S are the temperature damping factor, the impurity damping factor and the spin interference factor. They will be discussed in details in the three following paragraphs.

Quantum oscillations are smeared out by finite temperature as described by equation (1.30). A higher effective mass of the quasiparticles gives a stronger suppression of quantum oscillations amplitude with the temperature. The effective mass of the orbit responsible for the observed quantum oscillations can be extracted from this equation. The amplitude of the first harmonic of quantum oscillations is extracted with FFT and fitted by the equation:

$$a(T) = a(T=0) \frac{\alpha m^\star T/B_{eff}}{sinh(\alpha m^\star T/B_{eff})} \tag{1.35}$$

B_{eff} is the effective field of the FFT interval. The two fitting parameters are the zero temperature amplitude $A(T=0)$ and the effective mass $m^\star$. This fitting procedure gives an average

value of the effective mass in the plane perpendicular to the applied magnetic field for the Fermi-surface pocket giving the quantum oscillations.

Landau levels are smeared out if the mean free path l is not much bigger than the radius of the cyclotron motion $r_c = \hbar k_F / eB$. This effect leads to the impurity damping factor R_D of the oscillation amplitude:

$$R_{D,i,p} = exp(-p\frac{\pi r_{c,i}}{l_i}) \tag{1.36}$$

When temperature is high compared to $\alpha m^\star / B$, the impurity damping acts like an additional temperature. This additional temperature T_D is named Dingle temperature and it is defined by:

$$R_{D,i,p} = exp(-\frac{\alpha p m_i^* T_{D,i}}{l}) \tag{1.37}$$

$$T_{D,i} = \frac{\hbar}{2\pi k_B \tau_i} \tag{1.38}$$

The increase of the quantum oscillations amplitude with magnetic field is mainly due to the impurity damping factor. The lower the sample quality, the higher is the magnetic field needed to resolve quantum oscillations. The Dingle temperature T_D is an indication of the sample quality. The field dependence of the first harmonic of the dHvA oscillation amplitude can be extracted by performing FFT on a sliding window.

1.7.5 Spin interferences and g factor anisotropy

The phase of spin up and spin down quantum oscillations can be calculated from equation (1.24). In the case of a linear Zeeman effect, these phases are:

$$\phi_\uparrow = \phi_0 + \pi\frac{m_\uparrow^\star g}{2m_0} \tag{1.39}$$

$$\phi_\downarrow = \phi_0 - \pi\frac{m_\downarrow^\star g}{2m_0} \tag{1.40}$$

Two cases will be treated separately: (i) quantum oscillations from spin up and spin down have different frequencies: $F_\uparrow \neq F_\downarrow$ and (ii) they have the same frequency: $F_\uparrow = F_\downarrow$.

(i) If $F_\uparrow \neq F_\downarrow$, the oscillations amplitude for each spin is reduced by $R_S = 1/2$. It happens in ferromagnets or in paramagnets with a non linear Zeeman effect according to equation (1.22). The information of the spin and g factor can be extracted from the phase of quantum oscillations. If the g factor or the effective mass $m^\star$ are anisotropic, the phase will depend on the field angle:

$$\phi(\theta) = \phi_0(\theta) \pm \pi\frac{m^\star(\theta)g(\theta)}{2m_0} \tag{1.41}$$

In a heavy fermion system $m^\star/m_0$ is much bigger than 1, so the angular dependence of ϕ_0 can be neglected and the angular dependence of the product $m^\star g$ can be deduced from the angular dependence of the phase of the quantum oscillations.

(ii) We consider now the second case $F_\uparrow = F_\downarrow$. It occurs in paramagnets with a linear Zeeman effect. In this case the quantum oscillations from spin up and spin down bands interfere. If the effective mass and the mean free path of spin up and spin down quasiparticles are equal, then these oscillations have the same amplitude. The amplitude of the resulting quantum oscillation signal is reduced by the interference factor given by equation (1.33). If the g factor or the effective mass $m^\star$ are anisotropic the interference factor can be observed by rotating the sample with respect to the magnetic field direction. The amplitude and the phase of the first harmonic of quantum oscillations follow:

$$a(\theta) = a_0(\theta)\,|cos(\pi g(\theta) m^\star(\theta)/2m_0)| \tag{1.42}$$

$$\phi(\theta) = \phi_0(\theta),\ \ (cos(\pi g(\theta) m^\star(\theta)/2m_0) > 0) \tag{1.43}$$

$$\phi(\theta) = \phi_0(\theta) + \pi,\ \ (cos(\pi g(\theta) m^\star(\theta)/2m_0) < 0) \tag{1.44}$$

$a_0(\theta)$ contains the other factors of the Lifshitz Kosevic formula and is expected to vary slowly with angle. Quantum oscillations vanish when $gm^\star/m_0$ is an odd integer, this phenomenon is called spin zero. Their amplitude is maximum when $gm^\star/m_0$ is an even integer. A phase shift of π occurs at each spin zero. A spin zero was observed for example in copper [Joseph and Thorsen (1964)]. The amplitude of quantum oscillations from a torque measurement in copper is represented as a function of the field direction in figure 1.9. It vanishes at 13° from [111] to [110] or [001]. The g factor in copper is expected to be constant at $g = 2$. The angular dependence of the effective mass is also represented in figure 1.9. It increases with angle from 0.45 m_0 at [111]. At 13° it reaches 0.5 m_0 , so the product $m^\star g = 1$ is an odd integer and it explains the suppression of the quantum oscillations at this angle. In heavy fermion systems, the effective mass is much higher than in copper, so the quantity $m^\star g$ may show much bigger variations and successive spin zero are expected. They can be used to measure quantitatively the microscopic anisotropy of $m^\star g$.

In both cases the anisotropy of the g factor can be extracted for each Fermi-surface pocket. These two methods are used to study the g factor anisotropy of the different Fermi-surface pockets in URu_2Si_2, the results are reported in chapter 6. However they give the anisotropy of the product $gm^\star/m_0$, so the anisotropy of $m^\star$ must be measured separately. It can be extracted from the angular and temperature dependence of the quantum oscillation amplitude from equation (1.35).

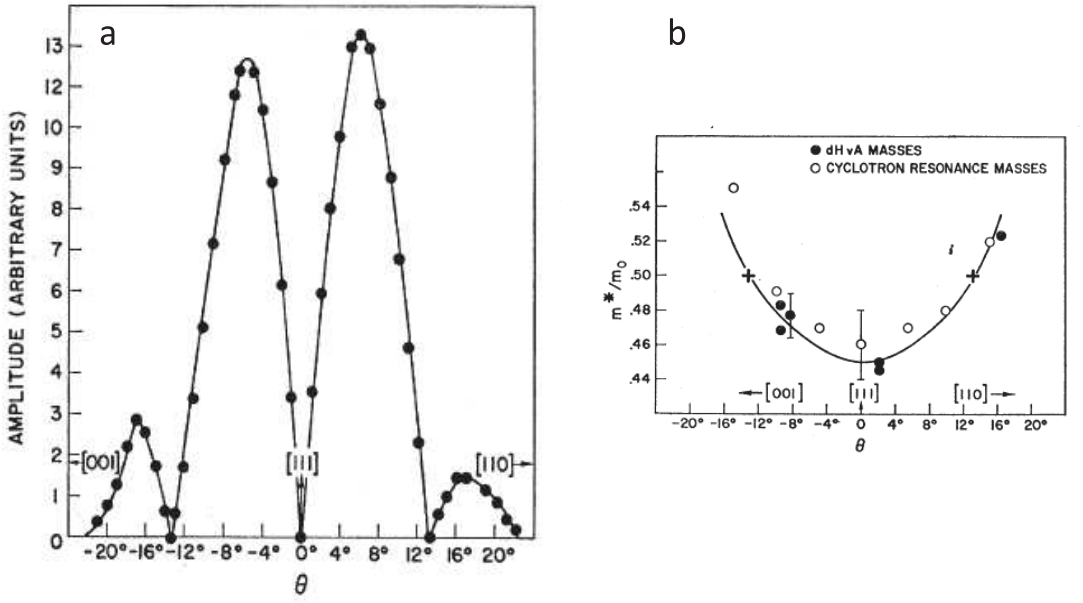

FIG. 1.9 (a) Amplitude of the quantum oscillations from a torque measurement in copper as a function of the magnetic field direction [Joseph and Thorsen (1964)]. (b) Angular dependence of the effective mass of electrons in copper. With g=2, the quantity $m^{\star}g$ reaches 1 at 13° leading to a spin zero in the quantum oscillation signal in (a).

1.7.6 Amplitude of the SdH oscillations

The oscillations of the resistivity cannot be calculated analytically from the quantum oscillations of the density of states at the Fermi level. Many scattering processes contribute to the Shubnikov-de Haas oscillations. In good metals Shubnikov-de Haas oscillations are too small to be detected. However in low carrier number system such as semiconductors, semimetals, topological insulator or Weyl semi-metals their amplitude is much bigger and they can easily be detected. According to Pippard's argument the amplitude of Shubnikov-de Haas oscillations in conductivity $\Delta\sigma$ should follow:

$$\frac{\Delta\sigma}{\sigma} \propto \frac{\Delta N(E_F)}{N(E_F)} \tag{1.45}$$

$N(E_F)$ and $\Delta N(E_F)$ are the density of states at the Fermi level and quantum oscillations of this density of states. If we consider this assumption and study quantum oscillations in the

limit $\Delta\sigma << \sigma$, we can show that the Shubnikov-de Haas oscillations follow the Lifshitz Kosevic formula: $\Delta\rho \propto \Delta M$ [Schoenberg (1984)]. Several Shubnikov-de Haas experiments show a very good agreement with the Lifshitz Kosevic formula as illustrated in chapters 4 and 5.

1.7.7 Microscopic measurement of the Sommerfeld coefficient

The contribution of the different Fermi-surface pockets to the Sommerfeld coefficient or reduced specific heat: $\gamma = (C/T)_{T\to 0}$ can be computed from quantum oscillations measurements [Aoki et al. (2000)]. Indeed the contribution γ_i of the Fermi surface pocket i is proportional to its density of states at the Fermi level $N_i(E_F)$:

$$\gamma_i = \frac{\pi^2}{3} k_B^2 N_i(E_F) \tag{1.46}$$

For a spherical Fermi-surface pocket this density is given by:

$$N(E_F) = \frac{V}{2\pi^2}\left(\frac{2m^\star}{\hbar^2}\right)^{3/2} E_F^{1/2} = \frac{V}{2\pi^2}\frac{2\sqrt{2}m^\star\sqrt{e}\sqrt{F}}{\hbar^{5/2}} \tag{1.47}$$

V is the molar volume. For a cylindrical pocket, this density of states at the Fermi level is given by:

$$N(E_F) = \frac{V}{2\pi^2 z}\left(\frac{2\pi m^\star}{\hbar^2}\right) \tag{1.48}$$

z is the unit cell length along the cylinder direction. This calculation can be used to evaluate the ratio of the Fermi surface detected in the quantum oscillation experiments. Good agreements were observed in heavy fermion systems between the Sommerfeld coefficient deduced from specific heat measurements and its expectation from the contribution of the different pockets observed in quantum oscillations studies. This agreement is discussed for example for UPt_3 [McMullan et al. (2008)]. It shows the itinerant behavior of these heavy fermion systems.

To conclude quantum oscillations are a powerful tool to probe the Fermi surface and to determine the microscopic properties of its different pockets: effective mass, Sommerfeld coefficient, diffusion time, g factor.

Chapter 2

Experimental techniques

Résumé en français

Ce chapitre décrit les différentes techniques expérimentales qui ont été utilisées au cours de la thèse : la croissance cristalline, les basses températures, les champs magnétiques intenses, les mesures de résistivité et la haute pression. La méthode de Czochralski a été utilisée pour faire croître des monocristaux d'UCoGe, URhGe et URu_2Si_2. Un autre échantillon d'URu_2Si_2 a été fait avec la méthode de flux. Ces échantillons ont été refroidis dans des réfrigérateurs à dilution jusqu'à 25 mK. Ils ont été placés dans des bobines supraconductrices pour leur appliquer des champs magnétiques allant jusqu'à 15 T et dans des bobines résistives au laboratoire des champs magnétiques intenses de Grenoble délivrant des champs magnétiques allant jusqu'à 34 T. La résistivité électrique de ces échantillons a été mesurée avec une grande précision par la méthode quatre fils en courant alternatif grâce à des transformateurs maintenus à basse température, afin d'étudier les oscillations quantiques dans la résistivité. Les échantillons ont été tournés par rapport à la direction du champ magnétiques avec des rotateurs mécaniques ou piézoélectriques. Enfin la résistivité d'UCoGe a été mesurée sous pression hydrostatique avec une cellule diamant jusqu'à 10.5 GPa et avec une cellule piston cylindre jusqu'à 2.5 GPa.

Abstract

This chapter describes the experimental techniques used during this thesis : sample growth, low temperature techniques, high magnetic field, electrical resistivity measurements and high pressure techniques. UCoGe, URhGe and URu_2Si_2 single crystals were grown by the Czochralski method and another URu_2Si_2 sample was grown by the flux method. Measure-

ments were performed in dilution refrigerators down to 25 mK. Magnetic field was applied with superconducting magnets up to 15 T and with resistive magnets up to 34 T in the high magnetic field laboratory (LNCMI) of Grenoble. High resolution resistivity measurements were performed using the ac current four probe technique with low temperature transformers to study the quantum oscillations. Mechanical and piezoelectric rotators were used to turn the samples with respect to the applied magnetic field. Finally resistivity in UCoGe was measured under hydrostatic pressure both in a diamond anvil cell up to 10.5 GPa and in a piston cylinder cell up to 2.5 GPa.

2.1 Sample growth and preparation

UCoGe, URhGe and URu_2Si_2 single crystals were grown by Dai Aoki by the Czochralski pulling method in a tetra arc furnace [Aoki et al. (2010)]. The raw elements are melted together with stoichiometric amounts. The single crystals were pulled at a speed of 15 mm/hr under pure argon atmosphere. The single crystals were oriented by Laue diffraction and cut by a spark erosion saw to achieve bar shape samples for resistivity measurements or plate shape samples for Hall effect measurements with a sample length around 1 mm. The samples are annealed during several days under ultrahigh vacuum. Their quality was estimated from low temperature resistivity measurements. The residual resistivity ratio $RRR = R(300\ \mathrm{K})/R(0\ \mathrm{K})$ of URhGe, UCoGe and URu_2Si_2 samples grown by the Czochralski pulling method and measured in this thesis goes respectively up to 50, 105 and 275.

URu_2Si_2 samples were also grown in indium flux by Gérard Lapertot. The sample growth procedure was taken from reference [Baumbach et al. (2014)]. The elements were melted together with the ratio 1(U):2(Ru):2(Si):22(In) and heated up to 1400°C at 70°C/hr. It was held at this temperature for 10 hr and quickly cooled to room temperature at a rate of 100°C/hr. One of the numerous single crystals was selected. Its $RRR = R(300\ \mathrm{K})/R(0\ \mathrm{K})$=350 is higher than the one of the Czochralski sample. However the flux sample is relatively small with a length in the basal plane of the tetragonal unit cell of 0.5 mm and a thickness of few tens of microns along the c axis.

2.2 Low temperature and high magnetic field

Low temperature resistivity and Hall effect measurements reported in this thesis were performed in conventional dilution refrigerator or in a top loading dilution refrigerator. A dilution refrigerator developed in the laboratory Ecce with the possibility to change pressure in situ at low temperature is used to measure resistivity in diamond anvil cell. Its lowest

temperature is 40 mK. A superconducting magnet can apply field up to 7 T on the pressure cell. A Kelvinox dilution from Oxford Instrument with a superconducting magnet was used to measure the resistivity in UCoGe and URhGe at ambient pressure or in a piston cylinder pressure cell. Its maximum field and lowest temperature are 13.4 T and 25 mK. In these two dilutions the temperature of the mixing chamber is measured by a germanium thermometer installed in a magnetic field compensated area. A RuO_2 thermometer is mounted close to the sample or pressure cell. The small magnetoresistance of RuO_2 was neglected below 7 T in Ecce and corrected from a calibration under magnetic field for measurements up to 13.4 T in the Kelvinox dilution. The superconducting magnet in the Kelvinox dilution shows an hysteresis of about 0.04 T, which was taken into account. For precise measurements at low temperature, the magnetic field was swept at 0.03 T/min.

The magnetoresistance measurements in URu_2Si_2 were performed down to 22 mK in a top loading dilution from Oxford instruments with a 15 T superconducting magnet. In this top loading dilution, the sample is inside the mixing chamber allowing a very good thermalization of the sample and also faster sample changes. Thus the magnetic field can be swept faster at 0.15 T/min and the base temperature is rapidly recovered after the rotation of the sample. However the resolution of resistivity measurement in the top loading dilution is lower as discussed in the following paragraph.

Resistivity measurements in UCoGe and URhGe were performed under high magnetic field up to 34 T in the Laboratoire National des Champs Magnétiques Intenses (LNCMI) in Grenoble. The magnetic field is produced by a resistive magnet made of an alloy of copper and silver and cooled down by pressurized water. The field was swept at a rate of 0.6 T/min. The samples were cooled down in a top loading dilution from Oxford instruments.

2.3 Resistivity and Hall effect measurements

Resistivity and Hall effect measurements are performed with the four probe lock-in method. The resistivity and Hall effect set up for high magnetic field measurements is represented in figure 2.1. Six 15 μm gold wires were connected to an URhGe sample to measure simultaneously resistivity and Hall effect. They are soldered by the spot welding technique with a voltage pulse of 6 V during 10 μs. The gold wires are connected to 80 μm copper wires by tin soldering. The copper wires for current, voltage and Hall voltage are twisted by pairs to avoid current induction in the wires under magnetic field. The samples are glued to the sample holder with GE varnish. The sample holder for top loading dilution is made of plastic to avoid heating by induced current during magnetic field sweeps. On the contrary

the sample holder in the Kelvinox dilution is made of copper for a better thermal conduction from the mixing chamber to the sample.

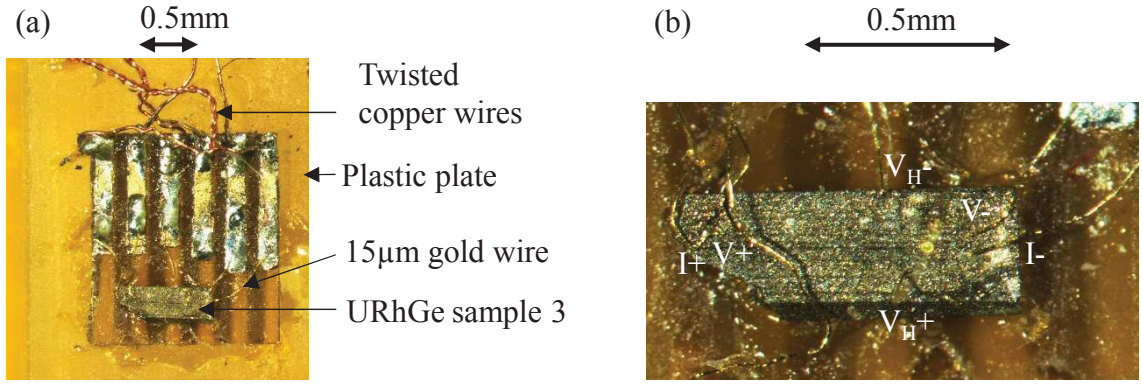

FIG. 2.1 (a) Resistivity and Hall effect measurements in URhGe in the LNCMI Grenoble. This sample is referred as sample 3 in chapter 5. (b) Zoom on the sample. $I+$ and $I-$ design the contacts used to send electrical current, $V+$ and $V-$ are used for voltage measurement and V_H+, V_H- are used for Hall voltage measurements.

The wiring for precise low temperature resistivity measurement in the Kelvinox dilution or in Ecce is represented in figure 2.2. A low noise level in the resistivity measurements is needed to detect Shubnikov-de Haas oscillations. An alternative voltage source is connected to a resistance of 10 kΩ to send an alternative current below 100 μA through the sample. The voltage wires are plugged into a transformer. It is installed on the 1.4 K plate of the dilution to amplify the measured voltage before the addition of thermal noise. Superconducting wires are used between the sample and the transformer to ensure a low impedance. The transformers in the Kelvinox dilution and in Ecce amplify respectively by 30 and 100 and their optimal frequency are around 80 Hz. The signal from the transformer is amplified by 1000 in a low noise amplifier at room temperature and measured with a Lock-in amplifier. This wiring gives a resolution on voltage measurement of about 0.03 nV in the Kelvinox dilution and 0.2 nV in Ecce for measurements in a diamond anvil cell.

In the top loading dilutions, the low temperature transformer was replaced by a room temperature transformer. Its amplification factor and optimal frequency are 100 and 30 Hz. The noise level for resistivity measurements in the LNCMI Grenoble is about 1 nV. Low impedance superconducting and copper wires in the top loading dilution used to measure URu_2Si_2 gives a noise level of 0.3 nV. However the top loading system gives a stronger cooling power and the electric current was increased in top loading dilution up to 200 μA for the measurement of quantum oscillations.

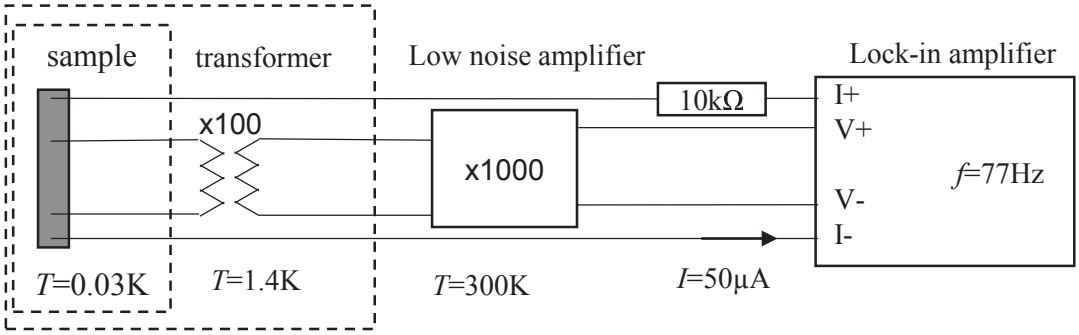

FIG. 2.2 Wiring for precise resistivity measurements in the Kelvinox dilution.

Sample geometry is measured with a camera installed on a microscope to deduce the resistivity and Hall effect from resistance measurements. If the electrical contacts for Hall voltage measurements are slightly misaligned, a contribution from the resistivity is added to the Hall effect signal. To avoid it, the Hall resistance R_{xy} was extracting by taking the antisymmetric part of the Hall signal $R_{xy,raw}$:

$$R_{xy}(B) = \frac{(R_{xy,raw}(B) - R_{xy,raw}(-B))}{2} \tag{2.1}$$

2.4 Sample rotation

The sample can be rotated with respect to the magnetic field in the high magnetic field laboratory with a manual Swedish rotator. In the top loading dilution used to measure URu_2Si_2 a Swedish rotator with a stepping motor allows fine tuning of the field angle in small steps. In the Kelvinox dilution a mechanical rotator was used to measure the angular dependence of the quantum oscillations in UCoGe reported in chapter 4. It was replaced by a piezoelectric rotator from Attocube before the measurement of the angular dependence of the magnetoresistance in URhGe reported in chapter 5.

Figure 2.3 shows a picture of the rotating system. The sample holder consists in a copper plate which is screwed on the rotating part. A silver foil is used to ensure a good thermal conduction between the rotating part and the fixed part. Copper wires for resistivity measurements are glued on the silver foil. This foil was designed to reduce its mechanical torque on the rotator. A plastic cup contains the silver foil. The temperature of the sample has been measured with a RuO_2 thermometer on the rotator. The rotation is induced by voltage pulses of 60 V at the frequency of 10 Hz. The angle between the sample and the field is measured with a Hall sensor glued on the sample holder. Its Hall effect is linear with

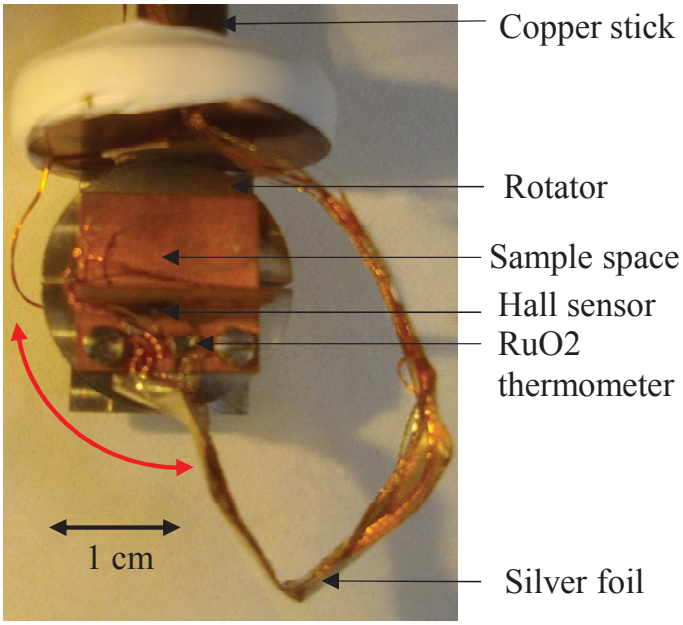

FIG. 2.3 Rotating system installed on the Kelvinox dilution. This set up is encapsulated in a plastic cup which was removed for the picture. The red arrow shows the rotating direction.

field up to 2 T: $R_{xy} = R_0 H$. If electrical current is applied along $\hat{x}$ direction, the Hall voltage is measured along $\hat{y}$ direction and is given by :

$$V_{xy} = R_0 (i \times H).\hat{y} = R_0 iH \cos(\theta) \tag{2.2}$$

It is directly related to the angle θ between $\hat{z}$ axis and magnetic field H. $H = 1$ T was chosen as magnetic field value and special care was taken to take into account the hysteresis of the superconducting magnet.

2.5 High pressure techniques

The pressure–temperature phase diagram of UCoGe was studied with two types of pressure cell : a diamond anvil cell and a piston cylinder cell. The diamond anvil cell was used to measure up to 10.5 GPa and the results are reported in chapter 3. The piston cylinder cell has a lowest maximum pressure of 2.5 GPa. However a bigger sample space in the piston cylinder cell allows us to measure resistivity with a better sample geometry to reach a much higher precision than in the diamond anvil cell. This precision is needed to detect quantum oscillations under hydrostatic pressure as shown in chapter 4.

2.5.1 Piston cylinder pressure cell

Figure 2.4 shows a scheme of the piston-cylinder pressure cell. Its body consists in a NiCrAl cylinder inside a CuBe cylinder. It is closed by a CuBe screw at the bottom. The sample chamber is filled with Daphnee 7373 oil as pressure transmitting medium. The sample is installed on a CuBe plug. A tungsten carbide cylindrical piston is placed on top of the sample chamber. To increase pressure, the piston is pushed with a mechanical press. It can be blocked by the upper screw to keep the pressure. A hole through the lower screw and the plug allows us to install wires for resistivity measurements. Black stycast is used to glue the wire in this hole and close it.

Figure 2.4(b) and (c) show both sides of the sample holder. A resistivity measurement set up similar to the ambient pressure set up shown in figure 2.1 is installed on one side. A piece of lead inside two copper coils is glued on the other side. It was used to determine the pressure by the superconducting transition temperature of lead. Indeed the critical temperature of lead is linear with pressure at least up to 2.5 GPa :

$$T_{sc} = T_{sc}^0 - \beta p \tag{2.3}$$

The parameters $T_{sc}^0 = 7.20$ K and $\beta = 0.347$ K/GPa are taken from reference [Bireckoven and Wittig (1988)]. The pressure was determined in a PPMS. Since the lead critical temperature is very sensitive to magnetic field, the residual field in the magnet was carefully suppressed. The pressure changes between 0 K and 7 K due to thermal expansion was neglected. Pressure was also measured during pressure changes with a manganin resistivity measurement at room temperature. This measurement is only indicative, since pressure changes between room temperature and low temperature due to thermal expansion. Manganin resistance at ambient temperature is linear with pressure [Dmowski and Litwin-Staszewska (1999)] :

$$\frac{1}{R}\frac{dR}{dp} = 0.029 \text{ GPa}^{-1}. \tag{2.4}$$

2.5.2 Diamond anvil cell

The phase diagram of UCoGe was studied up to 10.5 GPa with a diamond anvil cell and the results are reported in chapter 3. The pressure cell is shown in figure 2.5. It consists in two diamond anvils. While the lower diamond is fixed to the pressure cell body, the upper diamond is on a piston that can move vertically to apply pressure to the sample space between the two diamonds. The diamonds were carefully aligned, and their parallelism checked by the light interferences from multiple reflexion between the two diamonds. Figure 2.5(b) is

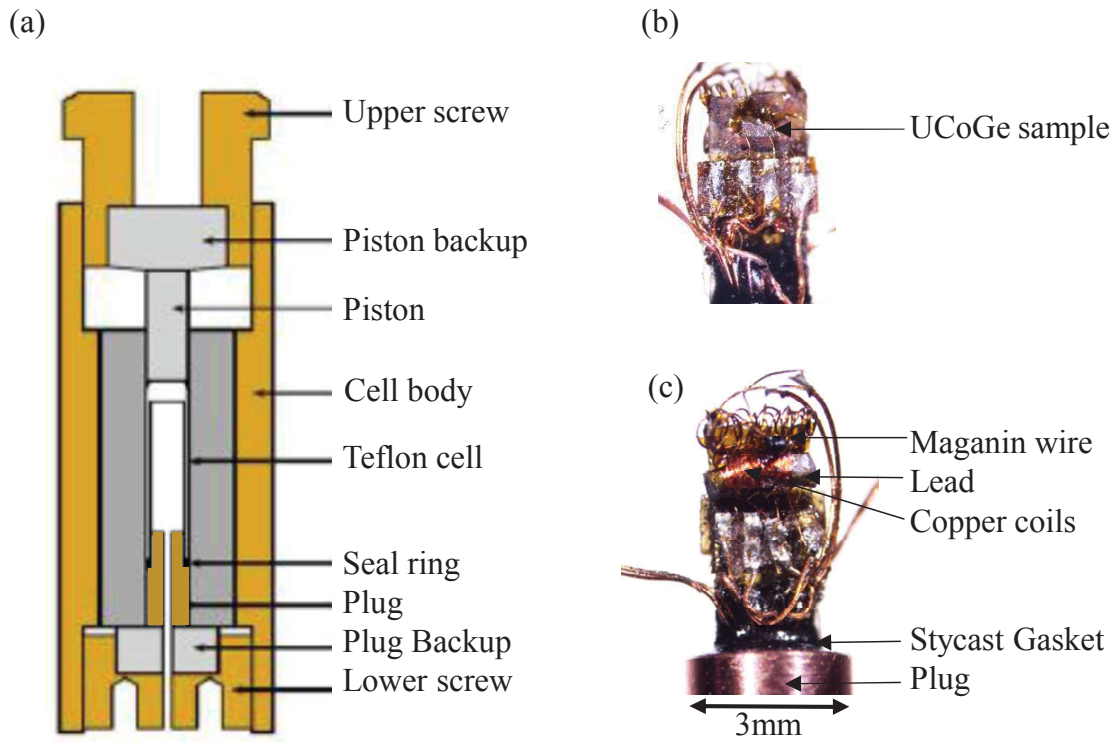

FIG. 2.4 (a) Piston cylinder pressure cell. Orange, dark gray and light gray represent respectively CuBe, NiCrAl and WC. (b) Sample holder picture with a resistivity measurement set up. The UCoGe sample is referred as sample 2 in chapter 3 and 4 (c) Back side of the sample holder. The bottom scale is valid for both (b) and (c) picture.

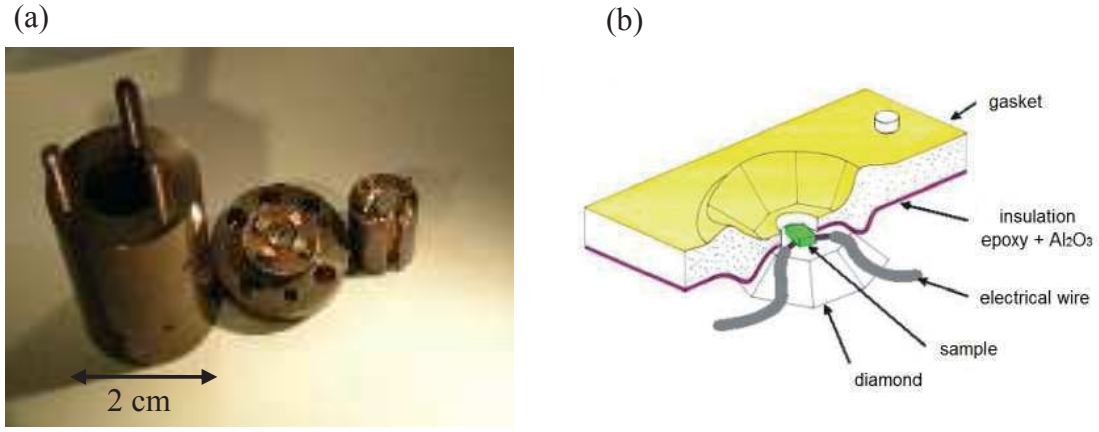

FIG. 2.5 (a) The diamond anvil cell used in this study. It shows from left to right the body, the lower diamond and the upper diamond. (b) Scheme of the lower diamond with the sample, electrical contacts and the insulated gasket.

a schematic of the lower diamond with the sample space. The diamond culet diameter is 1 mm. The sample space is closed by a stainless steel gasket. It consists in a plate with a 0.5 mm hole. The maximal sample size is about 0.2 mm. The sample is polished to reduce its thickness below 0.05 mm. To measure resistivity, 10 μm gold wires were attached to the sample with spot welding. Gold strips are glued to the lower diamond. When pressure is applied, they are mechanically connected to the 10 μm wires. The metallic gasket is insulated electrically with a mixture of white Stycast and alumina powder. As pressure transmitting medium Argon is used. It ensures good hydrostatic conditions [Tateiwa and Haga (2009)].

This pressure cell was installed in the home-built dilution refrigerator with a special system to change the pressure at low temperature. This dilution has been built up during the PhD of A. Fernandez Pañella and the details can be found in reference [Fernandez Pañella (2012)]. A helium gas bottle under pressure is connected with a capillary to the bellows on the mixing chamber, which can apply a force by levers to the pressure cell. More details on in situ pressure tuning systems can be found in reference [Salce et al. (2000)]. Thus argon is kept solid during all the measurement. The pressure is measured with ruby fluorescence. Ruby powder is put on top of a diamond anvil and optical measurements are performed through the diamond. Optical fibers go from a laser at room temperature to the pressure cell in the dilution and from the pressure cell to a spectrometer at room temperature. At ambient pressure and low temperature ruby emits at the wavelength : $\lambda_0 = 693.40$ nm. This ray is linearly shifted to higher wavelength under pressure:

$$\lambda(p) = \lambda_0 + \lambda_1 p \tag{2.5}$$

The shift rate is $\lambda_1 \approx 0.361$ nm/GPa. Ruby phosphorescence spectra are represented in figure 2.6 for different pressures up to 10.3 GPa. The peak coming from the ruby phosphorescence is shifted to higher wavelength under pressure. It gets smaller and broader under pressure. Its full width half maximum is multiplied by two between ambient pressure and 10.3 GPa. This broadening was previously reported and interpreted as the consequence of non hydrostatic effects [Tateiwa and Haga (2009)]. This non hydrostaticity may lead to pressure inhomogeneities in the sample chamber and uniaxial strain on the sample.

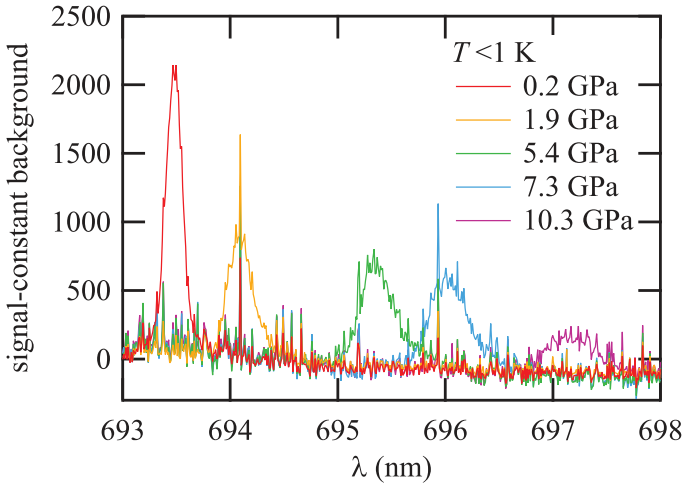

FIG. 2.6 Ruby fluorescence spectrum for different pressures. The temperature was below 1 K.

Chapter 3

Pressure–temperature–magnetic field phase diagram of UCoGe

Résumé en français

Ce chapitre reporte la mesure du diagramme de phase pression température d'UCoGe jusqu'à 10 GPa. La température de Curie T_C diminue sous pression et s'annule à la pression critique $p_c \approx 0.9$ GPa. UCoGe est supraconducteur jusqu'à 4 GPa. Les quasi-particules forment un liquide de non Fermi sur une grande gamme de pression autour de la pression critique et jusqu'à 5.5 GPa avec une résistivité linéaire en température à la pression critique. L'application d'un champ magnétique selon l'axe facile d'aimantation c restaure le comportement de liquide de Fermi. La résistivité extrapolée à zero température est maximale à $p^\star = 7.2$ GPa et décroît rapidement avec la pression au delà de cette valeur. Le champ critique supérieur H_{c2} selon l'axe c a été mesuré et comparé avec le champ critique supérieur H_{c2} selon l'axe b. Il est fortement anisotropique et sa dépendance en température est inhabituelle sur toute la gamme de pression. Tandis que a pente initiale peut être expliquée par un modèle analytique, le comportement général du champ critique H_{c2} est décrit à partir de la résolution numérique des équations d'Éliashberg. Ce calcul a permis de déterminer la dépendance en champ et en pression de l'interaction d'appariement dans UCoGe.

Abstract

The temperature–pressure phase diagram of UCoGe was studied up to 10.5 GPa. The Curie temperature T_C decreases with pressure and vanishes at the critical pressure $p_c \approx 0.9$ GPa. Superconductivity was observed up to 4 GPa. Non-Fermi liquid behavior was found in a

broad pressure range around the critical pressure up to 5.5 GPa with a resistivity linear in temperature around the critical pressure. The Fermi-liquid behavior can be recovered by the application of a magnetic field along the easy magnetization axis c. The residual resistivity shows a maximum at higher pressure at $p^\star = 7.2$ GPa and drops strongly for higher pressures. The upper critical field H_{c2} along the c axis was measured under hydrostatic pressure and is compared to H_{c2} along the b axis. It shows a strong anisotropy and an unusual temperature dependence in the entire pressure range. The upper critical field shows also a sample dependence. An analytical model is proposed to characterize the initial slope of the upper critical field. A model based on numerical resolution of the Éliashberg equations were used to explain the behavior of the upper critical field and to deduce the field and pressure dependence of the pairing strength in UCoGe.

3.1 Introduction to the ferromagnetic superconductor UCoGe

3.1.1 Unit cell and ferromagnetic order

UCoGe crystallizes in the orthorhombic TiNiSi structure. It is centrosymmetric and its symmetry space group is Pnma. The unit cell is represented in figure 3.1. Uranium atoms build zig-zag chains in the ac plane. The chains are along the a axis and the nearest neighbor uranium bounds are along these chains. This unit cell contains four formula units.

UCoGe is a moderate heavy fermion material with $\gamma = 55$ mJ.mol^{-1}.K^{-2} [Huy et al. (2007a)]. The inset of figure 3.2 shows the magnetization as a function of temperature measured at low field $B = 0.01$ T. A strong enhancement of the magnetization at $T_C = 3$ K indicates a transition to a ferromagnetic order. The field dependence of the magnetization at 2 K is represented for magnetic field applied along the three crystallographic axis in figure 3.2. The spontaneous magnetization can be observed only along the c axis and it is relatively small $M = 0.04\mu_B$/U at 2 K. bandstructure calculations, x-ray dichroism and magnetic Compton scattering show that this small magnetic moments on uranium atoms result from orbital moments opposite to the spin moments and slightly larger than the spin moments [Diviš (2008), Taupin et al. (2015), Butchers et al. (2015)]. The magnetic moment on cobalt atoms are much smaller than the moment on the uranium atoms and must be induced by the uranium moment [Taupin et al. (2015)]. A magnetic field of a few Tesla applied along the c axis induces a bigger magnetization underlying a large additional Pauli component. Thus UCoGe is considered as a weak ferromagnet. The magnetic susceptibility along the a and the b axis shows a much smaller magnetic susceptibility than under magnetic

field along the *c* axis. So UCoGe at low temperature has a strong Ising behavior, with the easy magnetization axis *c*. The hardest axis is the *a* axis.

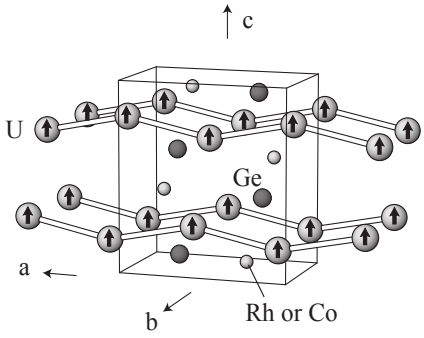

URhGe, UCoGe

FIG. 3.1 Orthorhombic unit cell of the ferromagnetic superconductors UCoGe and URhGe. The arrows represent the magnetic moments carried by the uranium atoms. The bounds between uranium atoms represent the nearest neighbor bounds.

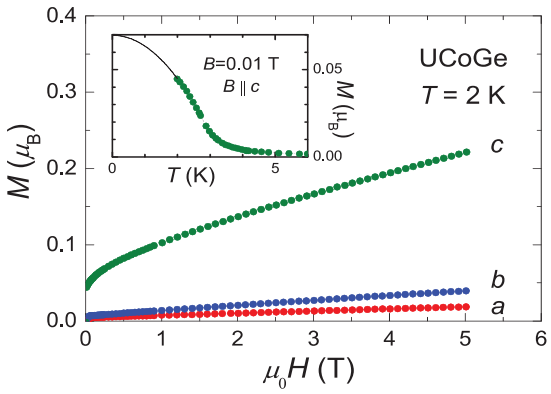

FIG. 3.2 Magnetization at 2 K in UCoGe for magnetic field applied along the three crystallographic directions [Huy et al. (2008)]. The inset shows the temperature dependence of the magnetization along the *c* axis under a magnetic field of 0.01 T.

3.1.2 Microscopic coexistence of ferromagnetsim and unconventional superconductivity

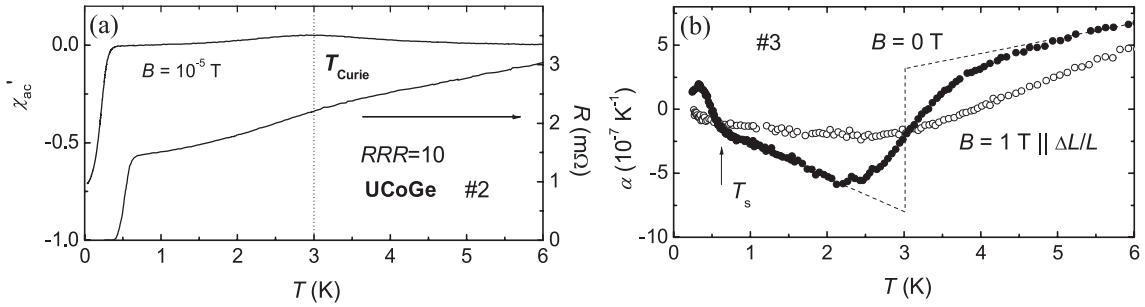

FIG. 3.3 (a) ac magnetic susceptibility (left axis) and resistance (right) axis of an UCoGe polycrystal as a function of temperature [Huy et al. (2007a)]. (b) Thermal expansion measurement of an UCoGe polycrystal at zero field and under a magnetic field of 1 T. T_{Curie} and T_s stands for Curie temperature and superconducting critical temperature respectively. They are called respectively T_C and T_{sc} in this thesis.

Figure 3.3 shows the ac magnetic susceptibility, the resistance and the thermal expansion of UCoGe polycrystals as a function of temperature [Huy et al. (2007a)]. The ac magnetic

susceptibility shows a peak at $T_C = 3$ K and decreases abruptly around $T_{sc} = 0.5$ K. The resistivity shows a change of slope at $T_C = 3$ K and zero resistivity below $T_{sc} = 0.5$ K. UCoGe shows superconductivity coexisting with ferromagnetic order below $T_{sc} = 0.5$ K. Thermal expansion exhibits a broad jump downwards around $T_C = 3$ K and a jump upwards at $T_{sc} = 0.5$ K. It follows that ferromagnetism and superconductivity are both bulk properties of UCoGe. This result was confirmed by specific heat and magnetization measurements [Huy et al. (2007a), Deguchi et al. (2010), Paulsen et al. (2012)]. Under a magnetic field of $B = 1$ T, the anomaly at T_{sc} and T_C are smeared out. Thus the ferromagnetic transition becomes a crossover at $B = 1$ T and superconductivity is suppressed.

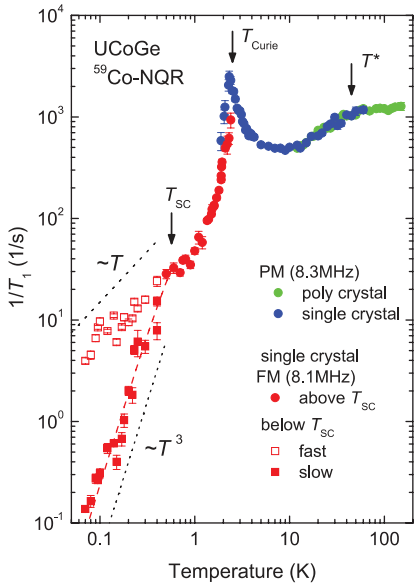

FIG. 3.4 Inverse relaxation time $1/T_1$ of ^{59}Co NQR as a function of temperature [Ohta et al. (2010)]. The red broken curve below T_{sc} represents the temperature dependence calculated assuming a line-node gap.

The coexistence of ferromagnetism and superconductivity was proved by microscopic experiments such as muon spectroscopy (μSR) nuclear magnetic resonance (NMR) and x-ray magnetic circular dichroism (XMCD) [de Visser et al. (2009), Ohta et al. (2010), Taupin et al. (2015)]. The ^{59}Co NQR inverse relaxation time $1/T_1$ is represented as a function of temperature in figure 3.4 [Ohta et al. (2010)]. It shows a broad peak at the Curie temperature corresponding to the enhancement of magnetic fluctuations in the vicinity of the magnetic transition. Below the critical temperature, two characteristic inverse times $1/T_1$ are observed. One of them follows a T^3 law indicating superconductivity with a line node in the gap. The second may come from a non superconducting part of the crystal suggesting a bad sample quality or a first order phase transition. This measurement shows the microscopic coexistence of ferromagnetism and superconductivity and that the $5f$ electrons of uranium atoms are responsible for both phenomena. Low field magnetization measurements indicate that vortices are induced in UCoGe by the spontaneous magnetization even in absence of

external magnetic field [Deguchi et al. (2010), Paulsen et al. (2012)]. Thus, the critical field H_{c1} is smaller than the internal field $B_{int} \approx 0.01$ T. The superconductivity in UCoGe was interpreted as unconventional superconductivity with triplet equal spin Cooper pairs induced by ferromagnetic fluctuations [Mineev (2008), Aoki et al. (2011a)]. The strong dependence of T_{sc} on sample quality and the T^3 behavior of $1/T_1$ [Ohta et al. (2010)] are indications of a p wave superconductivity.

3.1.3 Magnetic quantum criticality in UCoGe

The pressure–temperature phase diagram of UCoGe was first investigated by [Hassinger et al. (2010b)] and [Slooten et al. (2009)]. It was determined by resistivity and ac magnetic susceptibility measurements. It is represented in figure 3.5. The Curie temperature decreases almost linearly with pressure from $T_C = 2.7$ K at ambient pressure, and reaches T_{sc} at $p = 1.2$ GPa. The ferromagnetic transition was theoretically predicted to be first order at low temperature [Mineev (2008)]. NQR measurements show a phase separation at the ferromagnetic transition at ambient pressure[Ohta et al. (2010)]. It may come from sample inhomogeneity and from a first order behavior of the phase transition. In the second case the tricritical point would be at negative pressure. Superconductivity can be observed in both the ferromagnetic and the paramagnetic state at least up to 2.5 GPa with a maximum of the critical temperature where it crosses the Curie temperature. A strong enhancement of the inelastic scattering term $\rho(T) - \rho(T = 0\text{K})$ was observed around the critical pressure $p_c = 1.2$ GPa like in the vicinity of a second order transition [Hassinger et al. (2008a)]. So the quantum phase transition of UCoGe is considered as a weakly first order transition. The resistivity in the normal state is linear in temperature around the critical pressure [Hassinger et al. (2008a)]. This behavior is unusual, since a T^2 behavior and a $T^{5/3}$ would be respectively expected at a first order and at a second order ferromagnetic quantum phase transition (see section 1.6.2). Quantum criticality in UCoGe can also be induced by the substitution of Ge by Si [de Nijs et al. (2008)]. Ferromagnetism and superconductivity are both suppressed for the critical Si concentration $x = 0.12$. The suppression of superconductivity must be due to the disorder entering in the dirty limit for superconductivity. $UCoGe_{0.88}Si_{0.12}$ show also a resistivity linear in temperature.

3.1.4 Upper critical field in UCoGe

The upper critical field in UCoGe determined by resistivity as a function of temperature for magnetic field applied along each crystallographic axis is represented in figure 3.6 [Aoki et al. (2009)]. A recent thermal conductivity experiment shows that the bulk H_{c2} and the

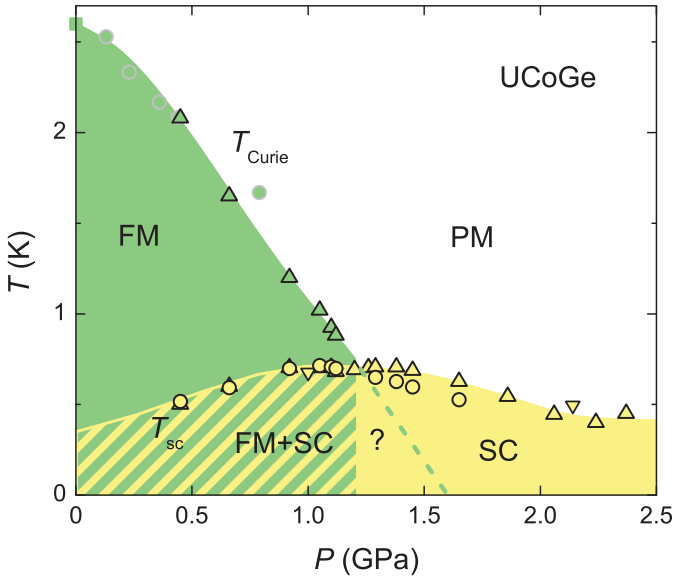

FIG. 3.5 Pressure temperature phase diagram of UCoGe Hassinger et al. (2010b). Circles and triangles were respectively obtained from resistivity and ac magnetic susceptibility measurements.

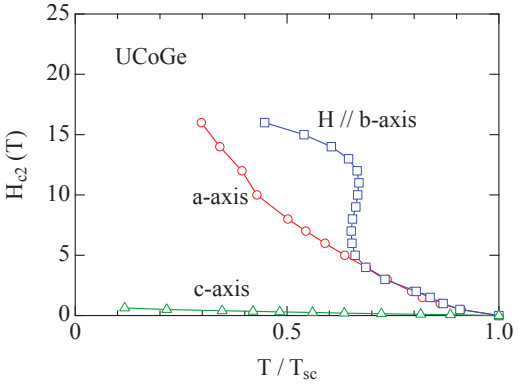

FIG. 3.6 Temperature dependence of the upper critical field in UCoGe for magnetic field applied along the three crystallographic directions [Aoki et al. (2009)]. Midpoint of the resistivity drop was chosen as a criteria for superconductivity.

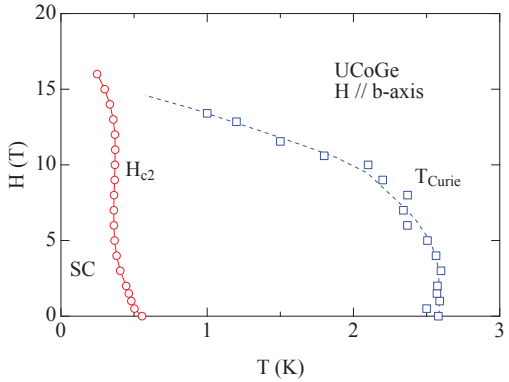

FIG. 3.7 Temperature–magnetic field phase diagram of UCoGe under magnetic field along the *b* axis [Aoki et al. (2009)]. The blue line corresponds to a crossover or a second order transition line which starts at the ferromagnetic transition.

resistive $H_{c2}(T)$ have qualitatively the same behavior [Wu et al. (2016)]. The anisotropy of H_{c2} is remarkably strong with a $H_{c2}(T=0)$ below 1 T for magnetic field along the *c* axis and above 20 T at low temperature for magnetic field along the hard magnetization axis *a* and *b*. The temperature dependence of H_{c2} shows a slight upward curvature in the whole temperature range for magnetic field along the *a* and the *c* axis. Under magnetic

field along the b axis H_{c2} as a function of temperature shows a "'S"' shape: the transition temperature decreases with magnetic field up to 6 T, however, it increases slightly with magnetic field up to 12 T and decreases finally for higher fields. Figure 3.7 shows the field-temperature phase diagram of UCoGe for $H//b$. The Curie temperature is continuously suppresses with increasing field. This phase diagram has been determined from resistivity measurement [Aoki et al. (2009)]. It would reach zero temperature around 15 T, so few Tesla above the region where the superconducting transition is enhanced by the magnetic field. ^{59}Co NMR measurements showed that a reinforcement of the magnetic fluctuations can be observed along this second order transition or crossover line [Hattori et al. (2014)]. The similar NMR experiment was performed for a magnetic field applied along the a axis [Hattori et al. (2014)]. The ferromagnetic transition is nearly independent of the magnetic field along the a axis.

The superconductivity in UCoGe is expected to be due to equal spin Cooper pairs, so there would be no Pauli limit for magnetic field along the c axis. The absence of Pauli limit for magnetic field along the hard axis a and b comes from the band splitting [Mineev (2010)]. The anisotropy of the orbital limited upper critical field usually comes from the anisotropy of the Fermi velocity. However, the anisotropy of the Fermi velocity in UCoGe was estimated from electrical resistivity measurements [Hattori et al. (2012)] and it is far too small to explain the anisotropy of the upper critical field. Moreover the temperature dependence of the upper critical field does not correspond to the usual temperature dependence of an orbital limited upper critical field, which was discussed in section 1.4.2. Indeed a downward curvature was expected for the temperature dependence of the upper critical field.

A theoretical model was proposed to explain the upper critical field of UCoGe [Mineev (2011)]. This model assumes that superconductivity in UCoGe is induced by ferromagnetic fluctuations. In this model the pairing strength depends on the strength of these fluctuations. Since the ferromagnetic fluctuations are strongly affected by the magnetic field, the coupling constant representing the pairing interaction would depend on the magnetic field. The reinforcement of the magnetic fluctuations under magnetic field along the hard axis b along the crossover line in figure 3.7 explains the S shape of the upper critical field [Aoki et al. (2009), Hattori et al. (2014)]. This phenomenological model explains also well qualitatively the reentrant superconductivity in the other ferromagnetic superconductor URhGe [Mineev (2015a), Miyake et al. (2008)], however, it does not give a microscopic picture.

Under magnetic field applied along the easy magnetization axis c, magnetic fluctuations are suppressed by the field as has been shown microscopically by NMR experiments. The inverse NMR relaxation time $1/T_1$ as a function of the c axis component of the magnetic field is represented in figure 3.8 [Hattori et al. (2012)]. The sample was rotated with respect

to a constant magnetic field applied in the *bc* plane. The results seems to be independent of the magnetic field value. $1/T_1$ decreases abruptly with the *c* axis component of the magnetic field below 1 T. This measurement confirms that the magnetic fluctuations are strongly reduced under magnetic field applied along the easy magnetization axis *c*. The same conclusion was given from measurements of the *A* coefficient of resistivity [Aoki et al. (2011a)], from a thermal transport study [Taupin et al. (2014b)] and from specific heat measurements [Aoki et al. (2011a); Wu et al. (2016)]. The anisotropy of the upper critical field of UCoGe was explained by this suppression of the magnetic fluctuations [Hattori et al. (2012)]. Indeed while the upper critical field for $H//a$ and $H//b$ corresponds to the orbital limit, for $H//c$ the upper critical field is dominated by the suppression of pair building magnetic fluctuations by the field. A theoretical model based on numerical solution of the Éliashberg equations explained the upward curvature of the upper critical field for $H//c$ in UCoGe by NMR results [Tada et al. (2013)]. These calculations show a better agreement with experiments assuming superconductivity in UCoGe similar to A state of ^{3}He, than assuming it mimics the B state. Finally, another calculation was performed to extract the field dependence of the coupling constant for superconductivity from H_{c2} temperature dependence [Wu et al. (2016)]. It describes both the enhancement of the coupling constant under magnetic field along the *b* axis and its suppression under magnetic field along the *c* axis.

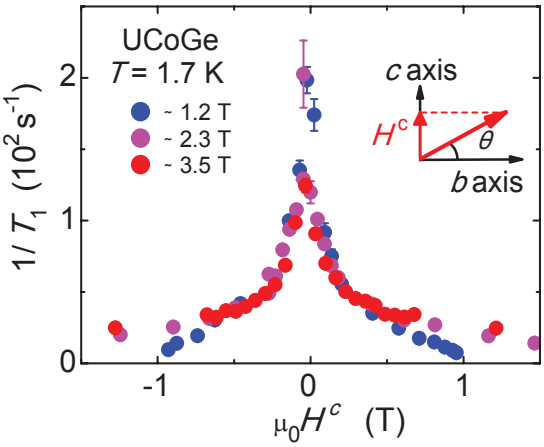

FIG. 3.8 Inverse relaxation time $1/T_1$ at $T = 1.7$ K as a function of the *c* axis component of the magnetic field for different values of the modulus of the magnetic field [Hattori et al. (2012)]. NMR was performed on ^{59}Co atoms.

3.1.5 Aim of this chapter

Our aim in this chapter is to study the ferromagnetic fluctuations responsible for superconductivity. The evolution from the critical region to the Fermi-liquid regime is studied. The upper critical field in UCoGe is measured under hydrostatic pressure. It allows us to verify the explanation of UCoGe H_{c2} behavior given in previous paragraph and to extract the pressure and field dependence of the coupling constant of the superconducting pairing.

3.2 Pressure temperature phase diagram of UCoGe

3.2.1 Determination of this phase diagram

The resistivity in a RRR=28 UCoGe sample was measured in the diamond anvil cell in a dilution refrigerator (see Chapter 2 for experimental details). Its resistivity as a function of temperature and pressure and the phase diagram extracted from these measurements are represented in figure 3.9. The resistivity shows a kink at T_C, as indicated in figure 3.9(a) for $p = 0.4$ GPa. T_C decreases with pressure from $T_C \approx 2.5$ K at ambient pressure and coincides with the superconducting transition temperature at $p \approx 0.8$ GPa and $T_{sc} \approx 0.8$ K. The extrapolation of the pressure dependence of T_C down to zero temperature determines $p_c \approx 0.9$ GPa. Above this pressure resistivity is nearly linear in temperature. At ambient pressure the superconducting transition is relatively broad. T_{sc} is maximal at 0.65 GPa, slightly below p_c with a sharp transition ($\Delta T_{sc} = 40$ mK). It broadens with increasing pressure in the paramagnetic phase. Zero resistivity can be observed up to 3.5 GPa. Taking the midpoint or the onset of the transition criteria superconductivity vanishes around 4 or 4.5 GPa, respectively. Thus, superconductivity survives in the paramagnetic regime far above the critical pressure p_c.

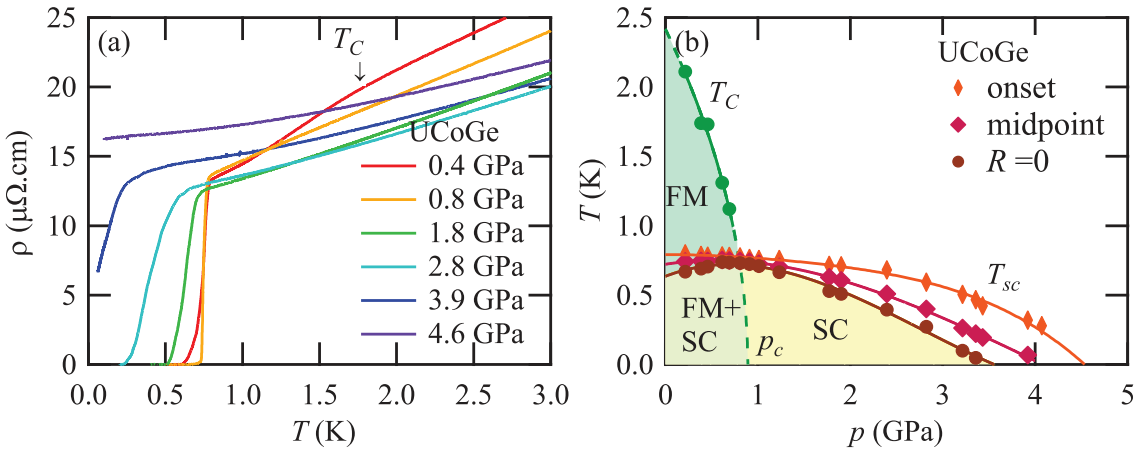

FIG. 3.9 (a) Temperature dependence of the resistivity in UCoGe for different pressures in the diamond anvil cell. For $p = 0.4$ GPa the Curie temperature T_C is denoted by the arrow. (b) Pressure–temperature phase diagram of UCoGe. T_C vanishes at $p_c \approx 0.9$ GPa. FM, PM, FM+SC and PM design the ferromagnetic state, the paramagnetic state, the ferromagnetic and superconducting state and the superconducting state.

These results are qualitatively in good agreement with previous studies [Slooten et al. (2009), Hassinger et al. (2010b)]. The value of the Curie temperature T_C and the critical pressure p_c in these two previous studies were higher with $T_C = 3$ K and $p_c = 1.2$ GPa. However, each study shows that T_{sc} is maximum at or slightly below the pressure where it

reaches T_C. The broadening of the superconducting transition under pressure is independent of sample quality and high pressure conditions and it is clearly related with the strength of dT_{sc}/dp. The exact pressure dependence of T_C in the superconducting dome is still unclear but from symmetry arguments the transition line should be first order and end up at zero temperature with a vertical slope [Mineev (2008)]. Several theoretical studies suggest that ferromagnetism is reinforced by superconductivity, so the Curie temperature would decrease slower with pressure when it is just below T_{sc} than when it is just above T_{sc} [Mineev (2008), Jian et al. (2009)].

3.2.2 Non Fermi liquid behavior

Figure 3.9 shows, that the resistivity in the vicinity of the critical pressure is linear in temperature corresponding to a non-Fermi-liquid behavior. To study how Fermi-liquid behavior T^2 dependence of the resistivity is recovered under pressure, the resistivity was measured up to 10.5 GPa and is represented in figure 3.10 as a function of the square temperature T^2. The residual resistivity as a function of pressure is represented in figure 3.11(a). It increases with pressure up to $\rho_0 \approx 22$ $\mu\Omega$cm at $p^\star \approx 7.2$ GPa and then decreases strongly. Finally it saturates around 9.5 GPa at $\rho_0 = 10$ $\mu\Omega$cm. The pressure of the maximum of the residual resistivity $p^\star$ is independent of magnetic field at least up to 7 T. The T^2 behavior of the resistivity is recovered around 5.5 GPa. At $p = 7.3$ GPa in figure 3.10 it can be observed below $T_{FL} \approx 1.5$ K and then the resistivity increases slower than a T^2 behavior. At $p = 9.7$ GPa the T^2 behavior is verified in a broader temperature range. Small deviations from the T^2 behavior were noticed above 2 K. The A_2 coefficient corresponding to the slope of the curve in figure 3.10 is represented in red as a function of pressure in figure 3.11(b). It decreases strongly with pressure and this decrease gets stronger above $p^\star = 7.2$ GPa.

The temperature dependence of the resistivity has been parametrized by fitting a power law $\rho = \rho_0 + A_n T^n$ in the normal state as proposed in section 1.6.2. The residual resistivity ρ_0 and prefactor A_n coefficient as a function of pressure are represented in figure 3.11(a) and 3.11(b). While the residual resistivity shows a shallow minimum at $p_c \approx 0.9$ GPa, the low temperature inelastic scattering term $A_n = \rho(1\text{K}) - \rho_0$ shows a clear maximum at p_c. To evaluate the pressure and temperature dependence of the exponent n we performed fits with the power law on a sliding window of 0.3 K in the normal state. This allows one to plot the exponent n as a function of pressure and temperature in figure 3.11(c). The resistivity follows a T^2 behavior at ambient pressure and low temperature in the ferromagnetic state. Remarkably, the resistivity is linear in temperature around p_c above the superconducting transition T_{sc}. The T^2 behavior of the Fermi-liquid regime is recovered only above 5 GPa

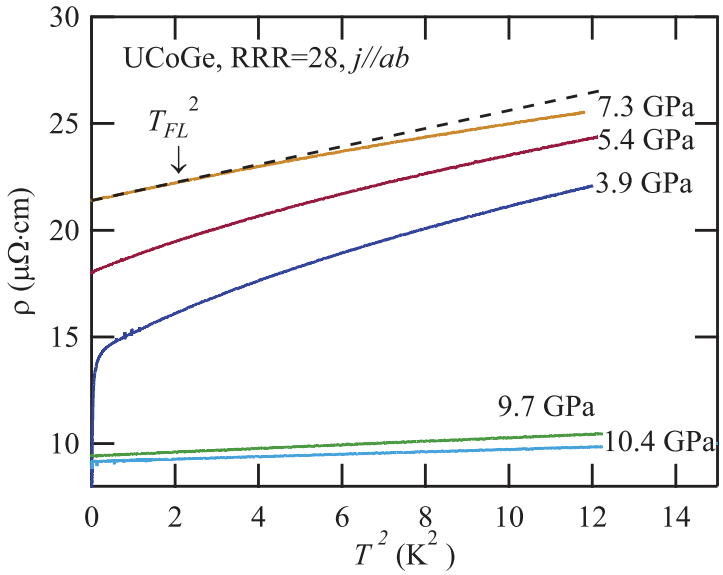

FIG. 3.10 (a) Residual resistivity ρ_0 as a function of pressure. ρ_0 shows a minimum at $p_c \approx 0.9$ GPa and a maximum at $p^\star = 7.2$ GPa. (b) $A_n = \rho(1\text{K}) - \rho_0$ on a logarithmic scale as a function of pressure. (c) Field dependence of n slightly above p_c obtained from fits in the normal state for $T < 1.5$ K. (d) $A_n = \rho(1\text{K}) - \rho_0$ for different magnetic fields as a function of pressure.

in the paramagnetic state far above p_c. The temperature T_{FL} where the Fermi liquid is recovered increases with pressure.

The compressibility of UCoGe was computed by DFT [Yu et al. (2011)] and experimentally determined by an x-ray scattering experiment under hydrostatic pressure up to 30 GPa [Adamska et al. (2010)]. At $p = 10$ GPa the volume of the unit cell is reduced by 3%. No structural transition was observed in the x-ray scattering and only tiny anomalies in the lattice parameters as a function of pressure around $p^\star$ [Adamska et al. (2010)]. In the ferromagnetic state at $p = 0$ the valence of UCoGe is close to the U^{3+} configuration [Fujimori et al. (2011)]. It was estimated at 3.2 by LDA calculations for ambient pressure [Samsel-Czekała et al. (2010)] and it is expected to be closer to the U^{4+} under pressure. Thus the anomaly at $p^\star$ may be related to a weak valence crossover as observed in various Ce or Yb based heavy fermion systems under pressure [Holmes et al. (2004), Rueff et al. (2011), Miyake and Watanabe (2014)].

As explained in section 1.6.2, the expected value of the n exponent in the vicinity of a ferromagnetic quantum phase transition is $n = 2$, if the transition has a strong first order behavior like in UGe_2 or $n = 5/3$ from spin fluctuation theory, if it is weakly first order like in URhAl and in U_3P_4. So the temperature linear resistivity in UCoGe is an unusual non Fermi liquid behavior. Non Fermi liquid behavior can be observed in a broad pressure range

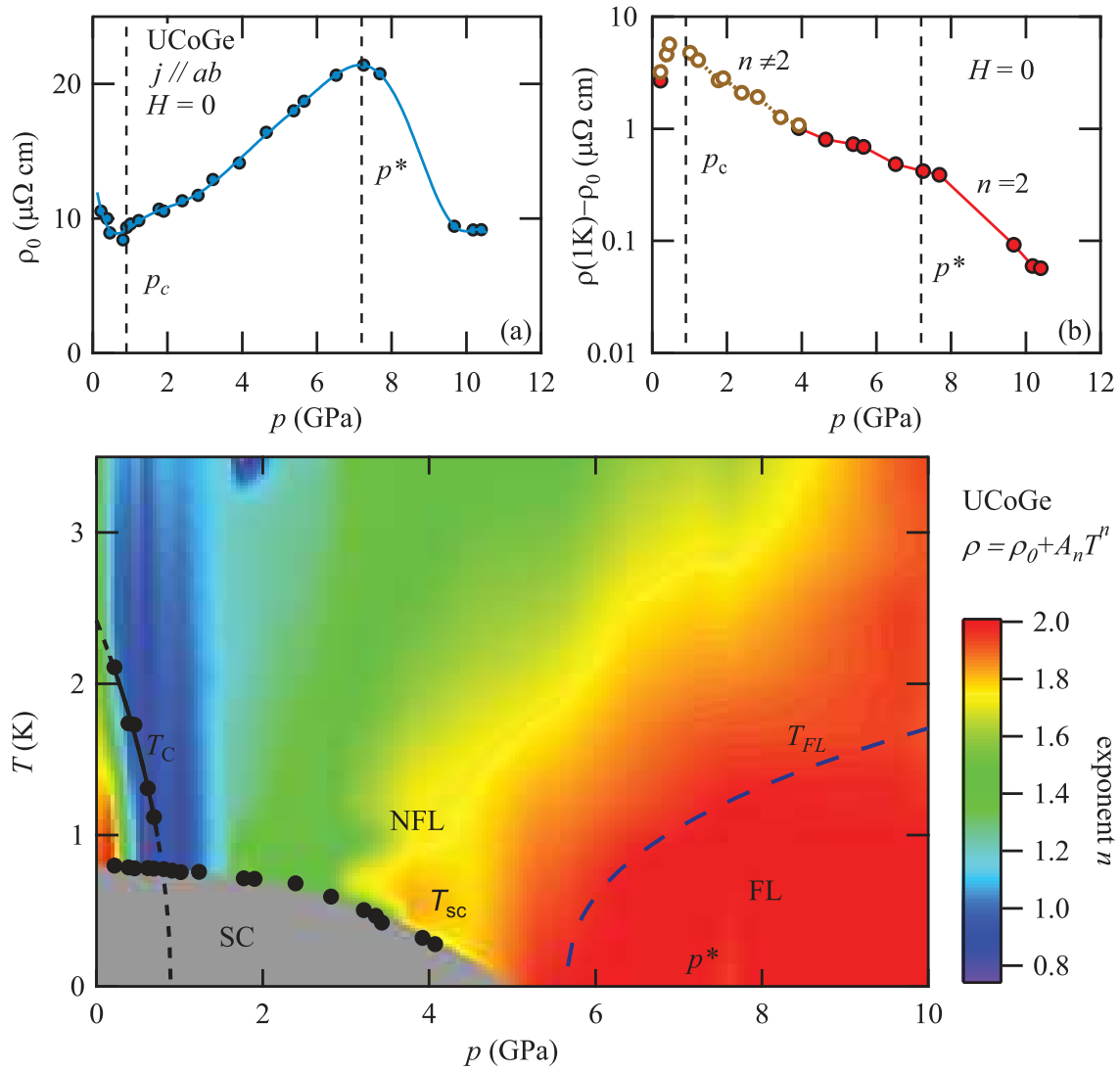

FIG. 3.11 (a) Residual resistivity ρ_0 as a function of pressure. ρ_0 shows a minimum at $p_c \approx 0.9$ GPa and a maximum at $p^\star = 7.2$ GPa. (b) $\rho(1\mathrm{K}) - \rho_0$ on a logarithmic scale as a function of pressure. (c) Color plot of the resistivity exponent n as a function of temperature and pressure from fitting $\rho = \rho_0 + A_n T^n$ over a sliding window of 300 mK. T_C and the onset of the superconducting transition as a function of pressure are represented by solid circles and diamonds, respectively. Linear resistivity is observed around p_c. At high pressure Fermi-liquid behavior is recovered and the upper limit of the Fermi-liquid regime T_{FL} is indicated by the dashed line.

above p_c like superconductivity. The same magnetic fluctuations may be responsible for this unusual non Fermi liquid behavior and for the unconventional superconductivity. A T linear resistivity was also observed in the vicinity of the critical substitution in $UCoGe_{1-x}Si_x$ and in $URh_{1-x}Ru_xGe$ [de Nijs et al. (2008),Huy et al. (2007b)]. Contrary to UCoGe under hy-

drostatic pressure, $UCoGe_{1-x}Si_x$ shows a T-linear resistivity only in a narrow range around the critical substitution.

A T-linear resistance has been observed in different strongly correlated electron systems, like high-T_{sc} cuprate or iron-pnictide superconductors close to the optimal doping [Cooper et al. (2009); Daou et al. (2009); Lee et al. (2006)], in organic superconductors [Doiron-Leyraud et al. (2009)], in ruthenates [Bruin et al. (2013)], and also in several heavy fermion systems, when these are close to quantum criticality such as $CeCoIn_5$ [Sidorov et al. (2002)], $CeRhIn_5$ [Knebel et al. (2008); Park et al. (2008)], or $YbRh_2Si_2$ [Gegenwart et al. (2002)]. For the antiferromagnetic heavy fermions, different theoretical scenarii have emerged to explain the unusual T dependence, such as a reduced dimensionality of the magnetic fluctuations [Millis (1993); Moriya (2003); Rosch et al. (1997)], critical valence fluctuations [Holmes et al. (2004); Miyake and Watanabe (2014)], or fluctuations associated with the change of the electronic structure from the ordered to the paramagnetic state [Paul et al. (2013); Pfau et al. (2012); Senthil (2008)]. The specific case of ferromagnetic fluctuations remains to be treated. The T-linear resistance in UCoGe may come from strong magnetic fluctuations.

The exponent n of the resistivity was also measured under magnetic field. It is represented as a function of magnetic field for a pressure slightly above the critical pressure : $p \approx 1.1$ GPa in figure 3.12(a). The exponent increases with magnetic field from 1 at zero field to 2 around 1 T. For a small magnetic field of 1 T along the c axis , the Fermi-liquid behavior appears in the entire pressure range. The low temperature electronic scattering, determined by $\rho(1\mathrm{K}) - \rho_0$, is plotted for different magnetic fields as a function of pressure in figure 3.12(b). Its acute enhancement at p_c is suppressed under magnetic field and a rather smooth pressure dependence is achieved. This indicates that the behavior of UCoGe in the critical region at zero field is determined by magnetic fluctuations which are rapidly suppressed by magnetic field applied along the c axis. So the suppression of magnetic fluctuations by magnetic field which was observed at zero pressure by NMR (figure3.8) [Hattori et al. (2012)], thermal transport [Taupin et al. (2014b)], and specific heat experiments [Aoki et al. (2011b), Wu et al. (2016)], would persist under pressure in the paramagnetic state. However the field attenuation will become weaker on escaping from p_c at high pressure.

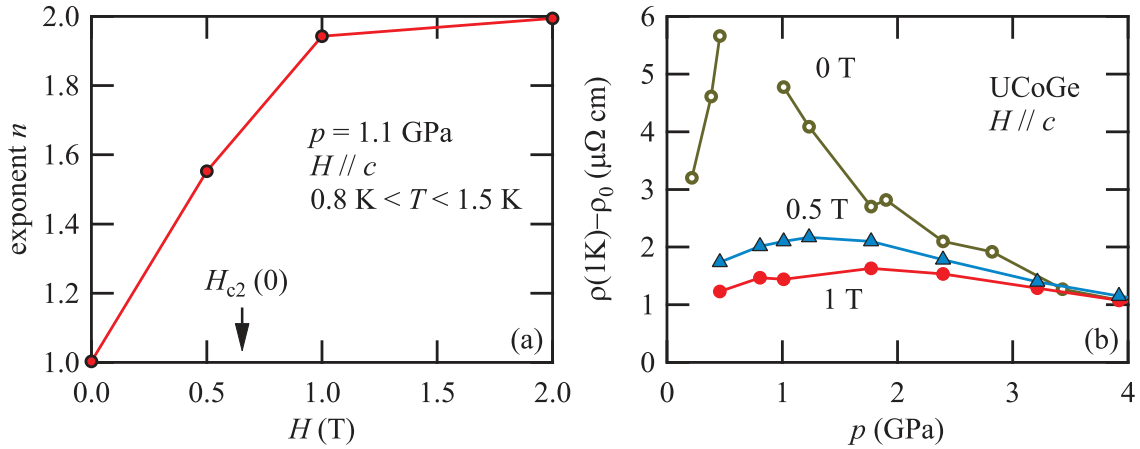

FIG. 3.12 (a) Field dependence of n slightly above p_c obtained from fits in the normal state for $T < 1.5$ K. (b) $\rho(1\text{K}) - \rho_0$ for different magnetic fields as a function of pressure.

3.3 Upper critical field in UCoGe under hydrostatic pressure

3.3.1 Experimental results

The upper critical field in UCoGe for magnetic field applied along the easy magnetization axis c was measured on five different samples. Two samples: UCoGe-d1 and UCoGe-d2 were measured in diamond anvil. UCoGe-d2 is the sample used to determine the pressure–temperature phase diagram. UCoGe-S2 was measured in a piston cylinder pressure cell in the Kelvinox dilution. UCoGe-Aoki and UCoGe-Araki were measured respectively by Dai Aoki in a piston cylinder cell and by Shingo Araki in an indenter cylinder cell in the Kelvinox dilution. The two last results have not been published. The difference between hydrostatic measurement in diamond-anvil cells and in piston-cylinder cells are discussed in details in chapter 2. These five samples are compared in table 3.1. They have similar RRR, superconducting transition and critical pressure $p_c \approx 1$ GPa. The superconducting transition was taken at zero resistivity.

The temperature and pressure dependence of H_{c2} in these five samples are represented in figure 3.13. At ambient pressure H_{c2} decreases with temperature with a slight upward curvature which has been observed in all the samples. While the zero field critical temperature T_{sc}^0 shows a relatively small sample dependence, the H_{c2} value at low temperature shows a strong sample dependence varying from 0.5 T to 1 T. This sample dependence cannot be explained by a misalignment of some samples, since the angular dependence of H_{c2} is relatively flat around $H//c$ [Aoki et al. (2009)]. Around the critical pressure H_{c2} is enhanced in

Sample name	d1	d2	S2	Aoki	Araki
pressure cell type	diamond anvil		piston cylinder		
RRR	38	28	36	30	15
T_{sc}(K)	0.56	0.64	0.55	0.61	0.6
p_c (GPa)	0.8	0.9	0.8	1	≈1

Table 3.1 UCoGe samples comparison. The pressure–temperature-magnetic field phase diagram of these five samples was measured under magnetic field along the c axis.

the five samples. The upward curvature and the sample dependence of $H_{c2}(T=0)$ are still there. A downturn can be observed around 0.08 K. In the paramagnetic state at $p \approx 1.8$ GPa, the three measured samples show a reinforcement of the upward curvature and an enhancement of H_{c2}. Finally at higher pressure $p \approx 2.4$ GPa the value of H_{c2} and the upward curvature are reduced. It can also be noticed that the sample dependence of the upper critical field seems to be reduced. This measurement shows that the unusual behavior of H_{c2} of UCoGe for $H//c$: its upward curvature is present both in the ferromagnetic and in the paramagnetic state under pressure. It is the strongest slightly above the critical pressure.

The H_{c2} of UCoGe-d2 was measured up to the end of the superconducting dome : $p \approx 4$ GPa. The results are represented in figure 3.14(a). When the pressure is increased above the critical pressure, both the superconducting transition temperature and the upper critical field decrease with pressure and are suppressed at $p \approx 4$ GPa. The curvature evolves continuously from an upward curvature at the critical pressure to a T-linear behavior at $p \approx 3.4$ GPa. At this pressure the n exponent gets close to the Fermi liquid value $n = 2$. These results suggest that the non Fermi liquid behavior and the superconductivity are both induced by the same ferromagnetic fluctuations. Their strength is maximum at the critical pressure and they would exist in a broad pressure range around the critical pressure. The upward curvature would come from their suppression under magnetic field.The usual behavior of $H_{c2}(T_{sc})$: the negative curvature is not recovered before the end of the superconducting dome.

The temperature dependence of H_{c2} under magnetic field along the b axis for different pressures is represented in figure 3.14(c). It was measured by D. Aoki and published in reference [Bastien et al. (2016)]. At ambient pressure $H_{c2}(T)$ shows a strong upward curvature with decreasing temperature. This measurement does not show the S shape of H_{c2} reported in figure 3.6 [Aoki et al. (2009)]. It may be due to a small misalignment along the a axis of the sample inside the pressure cell. The strong anisotropy of the upper critical field reported in figure 3.6 at ambient pressure survives under pressure in the paramagnetic state up to $p = 2.28$ GPa. The upward curvature of $H_{c2}(T)$ is reduced under pressure and vanishes around $p_c \approx 1$ GPa. At the highest pressure $p = 2.28$ GPa, H_{c2} is linear in temper-

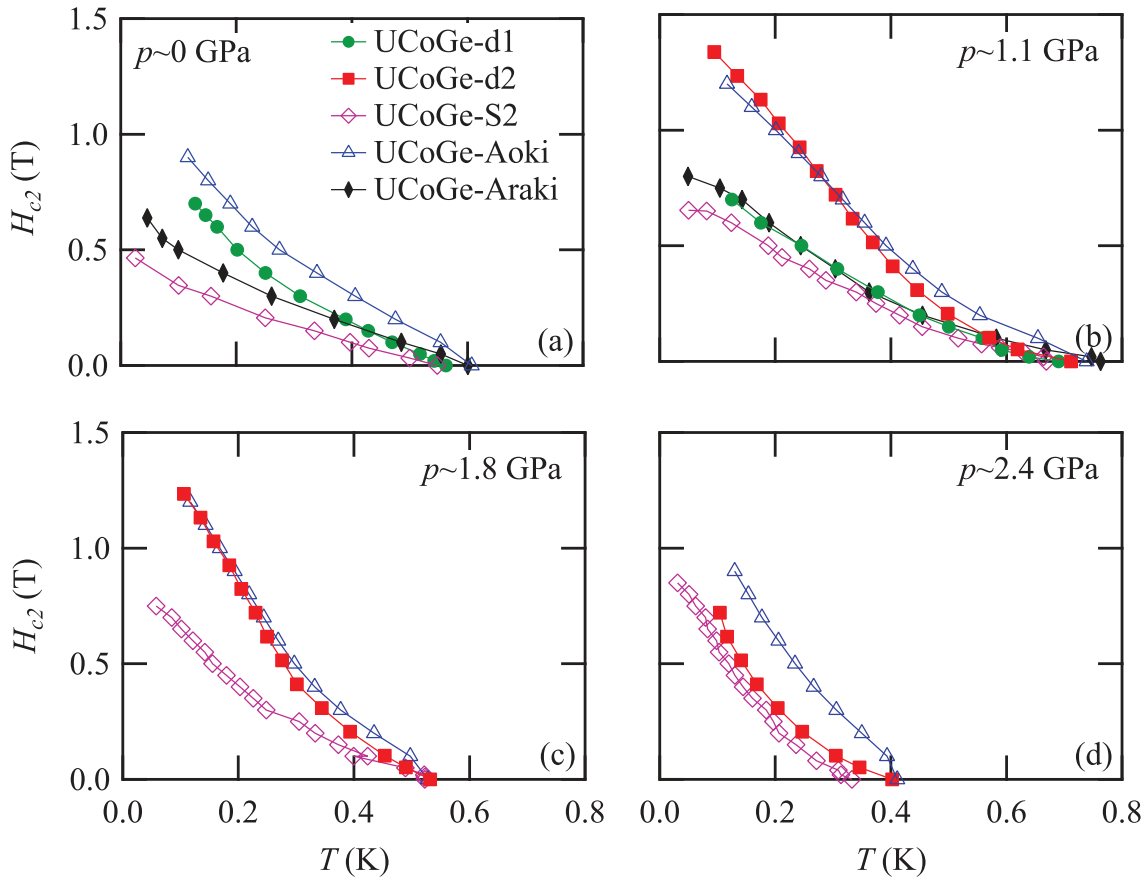

FIG. 3.13 Temperature dependence of UCoGe upper critical field under magnetic field applied along the easy magnetization axis c at ambient pressure (a) around the critical pressure $p \approx 1.1$ GPa (b), in the paramagnetic state at $p \approx 1.8$ GPa (c) and $p \approx 2.4$ GPa (d). The five different colors and symbols correspond to five different samples as indicated in figure (a). More details on the samples and the different high pressure techniques can be found in table 3.1.

ature. The suppression of the upward curvature of the upper critical field under magnetic field along the b axis is in good agreement with the assumption, that this unusual curvature comes from magnetic fluctuations induced by a magnetic field transverse to the spontaneous magnetization [Mineev (2011)]. The pressure dependence of the upper critical field along the a axis was previously reported in reference [Slooten et al. (2009)]. It evolves slightly with pressure through the critical pressure and the upward curvature of $H_{c2}(T)$ remains up to 1.66 GPa. However the sample seems to be misaligned toward the c axis and its quality may be low. The upper critical field pressure dependence for the three field directions shows the similarity of superconductivity in the ferromagnetic and in the paramagnetic state. In both states, it would be induced by ferromagnetic fluctuations.

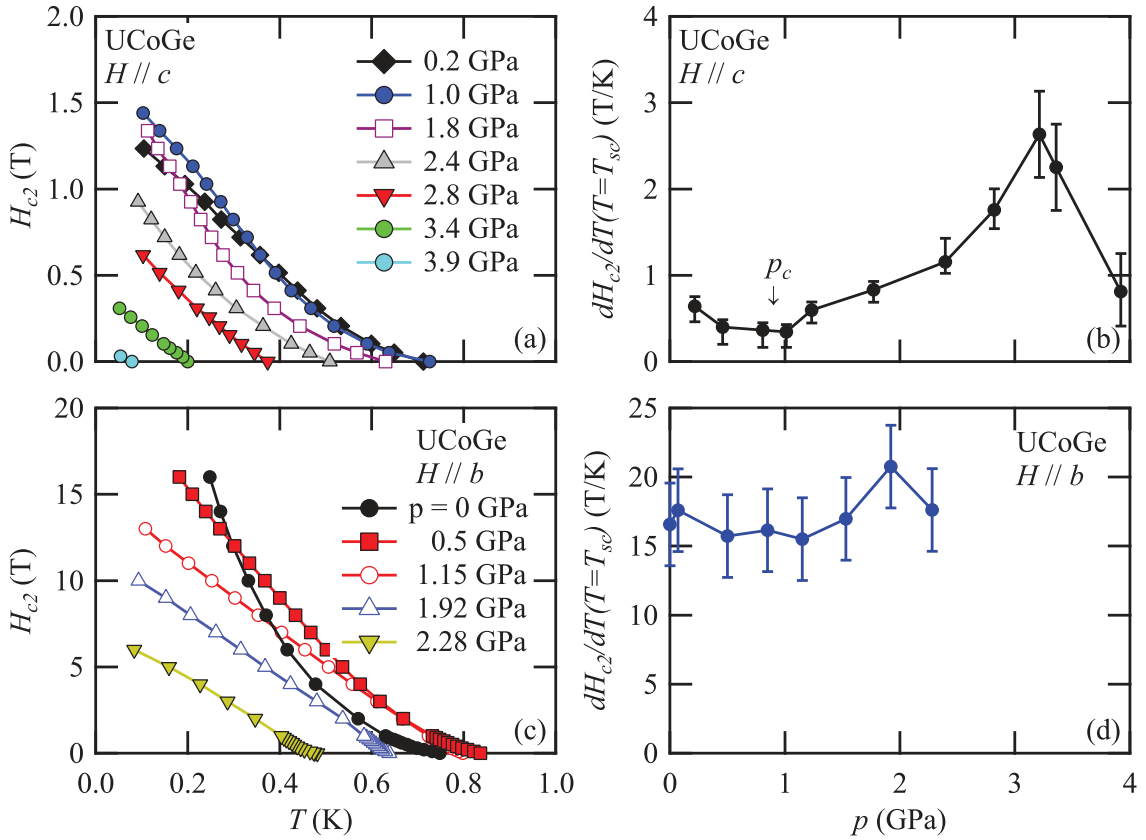

FIG. 3.14 (a) Temperature and pressure dependence of UCoGe-d2 upper critical field under magnetic field applied along the easy magnetization axis c. The measurements were performed up to 4 GPa. (b) Pressure dependence of the initial slope of the upper critical field along the c axis : $-dH_{c2}/dT_{sc}|_{T_{sc}=T_{sc}^0}$. (c) Temperature and pressure dependence of the upper critical field along the b axis published in reference [Bastien et al. (2016)]. (d) Pressure dependence of the initial slope of the upper critical field along the b axis : $-dH_{c2}/dT_{sc}|_{T_{sc}=T_{sc}^0}$.

The initial slope of the upper critical field : $-dH_{c2}/dT_{sc}|_{T_{sc}=T_{sc}^0}$ as a function of pressure is represented in figure 3.14(b) for $H//c$ and in figure 3.14(d) for $H//b$. T_{sc}^0 is the superconducting transition in zero field. The initial slope for $H//c$ is minimum at the critical pressure with $-dH_{c2}/dT_{sc}|_{T_{sc}=T_{sc}^0} = 0.4$ T/K and it undergoes a maximum around 3.2 GPa with $-dH_{c2}/dT_{sc}|_{T_{sc}=T_{sc}^0} = 2.6$ GPa. The initial slope for $H//b$ is roughly constant around $-dH_{c2}/dT_{sc}|_{T_{sc}=T_{sc}^0} = 18$ T/K and stays more than one order of magnitude above the initial slope for $H//c$ up to $p = 2.28$ GPa. In the usual orbital limit, this initial slope follows the WHH formula introduced and discussed in section 1.4.2. This formula can be written :

$$\left.\frac{dH_{c2}}{dT_{sc}}\right|_{T_{sc}=T_{sc}^0} = -\frac{\phi_0 k_B^2 T_{sc}^0}{2\pi \cdot 0.016(\hbar v_F)^2} \tag{3.1}$$

The superconducting transition temperature $T_{sc}^0(p)$ undergoes a maximum at the critical pressure and the Fermi velocity v_F is expected to have a minimum at the critical pressure, so the WHH formula (3.1) predicts a broad maximum of the absolute value of the initial slope at the critical pressure. This prediction is opposite to the experimental results for $H//c$ represented in figure 3.14(b). It confirms the idea that H_{c2} along the c axis in UCoGe does not follow the usual orbital limit as shown by the strong anisotropy of the H_{c2} and by its upward curvature. To understand the anisotropy and the pressure dependence of the initial slope $-dH_{c2}/dT_{sc}|_{T_{sc}=T_{sc}^0}$, we should refine the WHH formula to take into account the influence of the magnetic field on the pairing interaction.

3.3.2 Analytical model to describe the initial slope of the upper critical field

The WHH formula (3.1) can be written differently to express the superconducting transition temperature as a function of the magnetic field:

$$T_{sc}(H) = T_{sc}^0 - \frac{2\pi \cdot 0.016(\hbar v_F)^2}{\phi_0 k_B^2 T_{sc}^0} \cdot H \tag{3.2}$$

This equation is only valid in the low field limit, when the second term is small compared to T_{sc}^0. For a simple model the Fermi-surface properties, the superconducting gap properties and the microscopic properties of the magnetic fluctuations are not taken into account. UCoGe is considered as a single band superconductor, although spin up and spin own bands are expected to have different superconducting transition temperatures and effective masses [Fay and Appel (1980)]. The superconductivity of UCoGe is in the clean limit: the superconducting coherence length ξ_0 is much bigger than the mean free path l [Huy et al. (2008)]. The pairing strength is represented by a dimensionless quantity: the coupling constant λ. It was introduced in chapter 1 and defined as the product of an average value of the attraction potential leading to electron pairing V and the density of states at the Fermi level: $\lambda = N(E_F)V$ [Leggett (1975)]. The magnetic fluctuations are also responsible for an enhancement of the effective mass, which can be assumed to be proportional to the coupling constant λ. The effective mass is given by $m^\star(H,p) = m_B(1+\lambda(H,p))$, where the band mass m_B is related to the bandstructure. While the coupling constant depends strongly on magnetic field and pressure, the band mass m_B may evolve slowly with pressure and field. It will be assumed to be a constant in this model. The Fermi velocity satisfies $v_F(H,p) = v_{FB}/(1+\lambda(H,p))$, where the band Fermi velocity v_{FB} is constant.

The superconducting temperature in zero field T_{sc}^0 can be related to the coupling constant λ using the formula (see section 1.4.1):

$$T_{sc}^0 = \Omega \exp(-\frac{1}{\lambda - \mu^\star}) \tag{3.3}$$

Where Ω corresponds to the integral of the fluctuations over the whole spectrum, it is analog to the Debye frequency for BCS superconductors. $\mu^\star \approx 0.1$ to the Coulomb repulsion term. This formula is a fit of a numerical solution of the Éliashberg equations for an isotropic Fermi surface and an isotropic gap. According to this formula T_{sc}^0 is more affected by a change of the coupling constant λ than by a change Ω. So we assume Ω to be independent of field and pressure. Both λ and Ω are considered as independent of temperature.

This formula is extended to positive field to define $T_{sc}^0(H)$ by:

$$T_{sc}^0(H) = \Omega \exp(-\frac{1}{\lambda(H) - \mu^\star}) \tag{3.4}$$

To obtain the equivalent of the WHH formula (3.2) in case of a field dependent pairing interaction, the superconducting transition in (3.2) must be replaced by the value given by equation (3.4). Then the field dependence of the superconducting temperature can be described with:

$$T_{sc}(H) = T_{sc}^0(H) - \frac{2\pi \cdot 0.016(\hbar v_F(H))^2}{\phi_0 k_B^2 T_{sc}^0(H)} \cdot H \tag{3.5}$$

The calculation of the initial slope of the upper critical field from this equation gives the extension of the WHH formula for field dependent coupling constant :

$$\frac{dH_{c2}}{dT_{sc}}_{T_{sc}=T_{sc}^0} = \frac{1}{-\frac{2\pi \cdot 0.016(\hbar v_F)^2}{\phi_0 k_B^2 T_{sc}^0} + \frac{dT_{sc}^0(H)}{dH}_{H=0}} \tag{3.6}$$

This formula contains an additional term in the denominator $\frac{dT_{sc}^0(H)}{dH}_{H=0}$ compared to the usual WHH formula (3.1). It describes the initial field dependence of the pairing interaction. The unusual anisotropy of the upper critical field in UCoGe was explained by the strong suppression of the magnetic fluctuations under magnetic field applied along the easy magnetization axis c [Hattori et al. (2012)]. Indeed a small magnetic field applied in the hard plane does not change the coupling constant $\lambda(H)$. Thus it does not modify T_{sc}^0 and the second term in the denominator of equation (3.6) is small leading to a large initial slope of $H_{c2}(T)$. However, if the magnetic field is applied along the easy magnetization axis c, the magnetic fluctuations are damped and $T_{sc}^0(H)$ is strongly reduced under field. The second

term in the denominator of equation (3.6) would dominate and explain the low value of the initial slope of the upper critical field $(dH_{c2}/dT_{sc})_{T=T_{sc}^0} \approx 1$ T/K. So the strong anisotropy of the upper critical field of UCoGe can be explained within this model by the field dependence of the coupling constant λ for field along the c axis.

We consider now the pressure dependence of H_{c2} for $H//c$. In the vicinity of the critical pressure, the pair breaking from the orbital effect is negligible and the initial slope $(dH_{c2}/dT_{sc})_{T=T_{sc}^0}$ could be approximated by:

$$(dH_{c2}/dT_{sc})_{T=T_{sc}^0} \approx (\frac{dT_{sc}^0}{dH}_{H=0})^{-1} = \frac{(\lambda-\mu^\star)^2}{T_{sc}^0}(\frac{d\lambda}{dH}_{H=0})^{-1} \tag{3.7}$$

The initial slope of the upper critical field along the c axis $-(dH_{c2}/dT_{sc})_{T=T_{sc}^0}$ is represented in figure 3.14(b), it undergoes a minimum at the critical pressure. Since the maximum of $T_{sc}^0(p)$ at the critical pressure is relatively broad, this minimum shows that the suppression of the coupling constant $\frac{d\lambda}{dH}_{H=0}$ by the field is stronger at the critical pressure. Far above the critical pressure, the enhancement of the initial slope up to 3.2 GPa can be explained by a slower suppression of the coupling constant under magnetic field. However the depairing from the orbital effect represented by the first term in the denominator of equation (3.6) would be reinforced far above p_c by the suppression of T_{sc} and the enhancement of v_F. The maximum of the initial slope $-(dH_{c2}/dT_{sc})_{T=T_{sc}^0}$ around 3.2 GPa suggests a change of dominant term in the denominator of equation (3.6). Finally the suppression of the initial slope between 3.2 GPa and 3.9 GPa can be explained by the depairing due to the orbital effect.

Thus, the analytical model presented here describes the initial slope of the upper critical field of the ferromagnetic superconductor UCoGe, while the usual orbital limit with a field independent coupling could not describe it. This model is a refinement of the WHH formula (3.1), taking into account the field dependence of the pairing strength. Moreover it describes only the initial slope of the upper critical field. Numerical methods are needed to study the upper critical field in the entire field range. We aim to explain the upward curvature of the upper critical field in the vicinity of the critical pressure from the variation of the coupling constant $\lambda(H)$ under field.

3.3.3 Field and pressure dependence of the coupling constant λ extracted from numerical calculations.

The pressure and field dependence of the coupling constant corresponding to the measured H_{c2} curves was extracted from numerical calculations. The band Fermi velocity $v_{FB} = v_F(1+\lambda)$ is still considered as independent of field and pressure. Assuming that its anisotropy is small, its value is estimated at $v_{FB} = 5.1$ km/s by the WHH formula (3.1)

from the initial slope of $H//a$ upper critical field in reference [Wu et al. (2016)]. The value of $\lambda(H=0,p=0)$ was estimated from specific heat measurements at ambient pressure at $\lambda(H=0,p=0)$=0.6 [Wu et al. (2016)].

Calculations were performed to solve the Éliashberg equations in a one-phonon mode model [Bulaevskii et al. (1988)]. An *s*-wave gap was considered for simplification. An additional anisotropy may come from the anisotropy of the *p*-wave gap. The upper critical field for different constant values of the coupling constant λ are computed numerically and plotted on the same graph as our experimental $H_{c2}(T)$ curves in figure 3.15(a). When the experimental curve intersects one of the numerically computed curve, it gives the value of coupling constant for the experimental results at the field of the intersection.

This method was used to extract the field and pressure dependence of the coupling constant λ, which is represented in figure 3.15(b). λ decreases strongly with magnetic field. At zero field λ as a function of pressure shows a maximum at the critical pressure as T_{sc}^0 and its suppression under field is also stronger around the critical pressure. After its strong suppression at low field, the coupling constant decreases less strong for higher fields. The upward curvature of upper critical field curves can be explained by the upward curvature of the field dependence of the coupling constant $\lambda(H)$. According to this calculation the reduction of the coupling constant by the field gets much weaker above 3 GPa and the upper critical field gets closer to its value in the field independent pairing case, as a result H_{c2} is linear with temperature.

While the coupling constant λ gives the effective mass $m^\star = m_B(1+\lambda)$ in the superconducting state, the effective mass in the normal state can be deduced from the A coefficient of resistivity from the Kadowaki-Woods formula: $m^\star \propto \sqrt{A}$. Since the T^2 behavior is not verified in the vicinity of the critical pressure, the comparison between $1+\lambda$ and the A_n coefficient can only be qualitative. The A_n coefficient represented in figure 3.12(b) shows a stronger reduction under magnetic field around p_c, than deep inside the paramagnetic state $p \approx 3$ GPa like $m^\star = m_B(1+\lambda)$ extracted from the analysis of the upper critical field. However the A coefficient as a function of pressure shows a sharpest maximum around the critical pressure than λ. A such difference between A coefficient and the effective mass $m^\star$ is expected in the vicinity of a quantum phase transition [Flouquet (2005)].

This model shows that the different features of the H_{c2} of the ferromagnetic superconductor UCoGe can be explained by the strong magnetic field dependence of the pair building magnetic fluctuations. It confirms the idea that in the ferromagnetic and the paramagnetic state of UCoGe spin triplet superconductivity appears in the equal pairing state and is induced by the ferromagnetic fluctuations. This study shows that the pairing strength in fer-

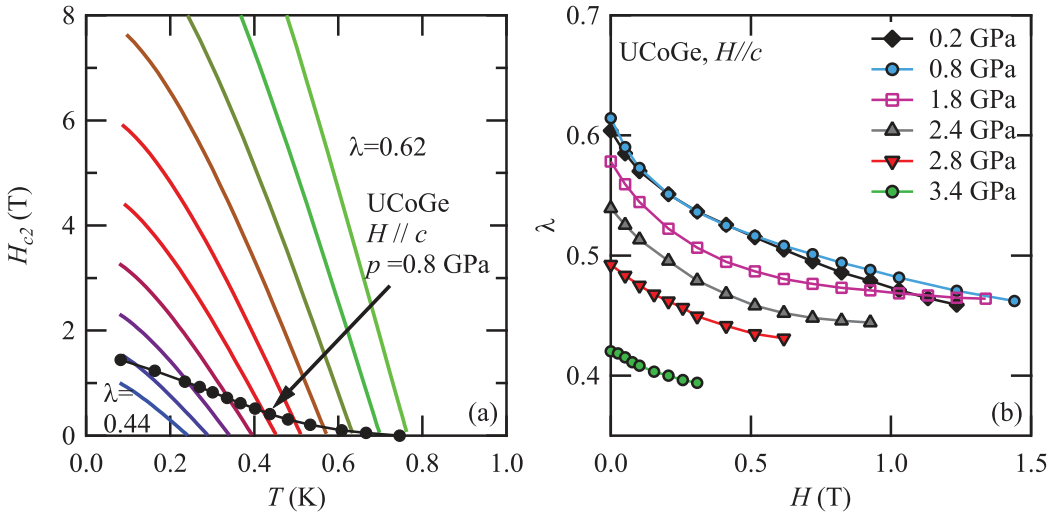

FIG. 3.15 (a) Lines represent the calculated orbital limited upper critical field for values of the coupling constant λ from 0.44 to 0.62 with a curve every 0.04. Black points correspond to experimental results for UCoGe for H//c and close to the critical pressure $p = 0.8$ GPa$\approx p_c$. The variation of the coupling parameter along the H_{c2} curve can be extracted from this graph. (b) Field and pressure variation of the coupling constant λ extracted from the experimental results presented in figure 3.14 and these numerically computed H_{c2} curves.

romagnetic superconductors can be modified by the application of hydrostatic pressure or a magnetic field.

However a numerical study of Éliashberg equations in the vicinity of a quantum phase transition showed that in the critical region the superconducting transition temperature is very sensitive to the Fermi surface properties [Monthoux and Lonzarich (2002)]. Their model could explain the pressure dependence of the superconducting transition temperature in UGe_2 [Sandeman et al. (2003)]. Both the analytical model and the numerical model used in this study do not take into account Fermi surface and gap properties. In particular the band mass m_B was assumed to be constant and it may change at the critical pressure, if a Fermi-surface change occurs. So the numerical calculations should be refined after the study of Fermi-surface properties of UCoGe under hydrostatic pressure.

A calculation of UCoGe upper critical field was performed for the ambient pressure by taking into account equal spin pairing and gap symmetry [Tada et al. (2013)]. The authors consider a square root field dependence for the coupling parameter $\lambda = \lambda_0/(1+\sqrt{H/H_0})$. This model was motivated by a fit of NMR results of figure 3.8 [Hattori et al. (2012)]. Their results reproduces well the upward curvature. However the initial slope given by this model $(dH^0_{c2}/dT_{sc})_{T_{sc}=T^0_{sc}} = 0$ is not finite. This point is in contradiction with experimental results. A new calculation is needed. It should take Fermi surface and gap properties into account

and verify that the results reported here do not depend on assumptions about the magnetic fluctuation spectrum. It could also take into account the multiband behavior of UCoGe superconductivity, which was predicted theoretically [Fay and Appel (1980)] and revealed by thermal conductivity measurements [Taupin et al. (2014a)].

3.4 Conclusion on the pressure–temperature– magnetic field phase diagram of UCoGe

The pressure temperature phase diagram of UCoGe was drawn up to 10.5 GPa. The magnetic quantum phase transition between the ferromagnetic state at low pressure and the paramagnetic state occurs at $p_c = 0.9$ GPa. Superconductivity is observed in a broad range around p_c up to 4 GPa. The non Fermi liquid behavior is observed in a broader range than superconductivity up to 5.5 GPa. It also shows an unusual $T-$linear behavior at the critical pressure and it should be related to the presence of strong magnetic fluctuations, which are also responsible for superconductivity. The suppression of these fluctuations under magnetic field leads to the recovery of Fermi liquid behavior and to an unusual temperature dependence of the upper critical field. The behavior of the upper critical field under temperature and pressure was explained successfully by a simple analytical model and by numerical calculations. It confirms that superconductivity in UCoGe is triplet superconductivity induced by ferromagnetic fluctuations both in the ferromagnetic and in the paramagnetic state. It shows that the pairing interaction in ferromagnetic superconductors can be tuned by magnetic field and hydrostatic pressure. Fermi-surface properties must also play an important role in ferromagnetic criticality and have an interplay with unconventional superconductivity. They are discussed in the next chapter.

Chapter 4

Fermi surface instabilities in the ferromagnetic superconductor UCoGe

Résumé en français

La surface de Fermi d'UCoGe a été étudiée par des mesures de magnétorésistance, effet Hall et d'oscillations quantiques dans des champs magnétiques allant jusqu'à 34 T. Les oscillations quantiques ont révélé quatre orbites sur la surface de Fermi α, β, γ et ω. Les mesures de transport et d'oscillations quantiques ont permis la découverte et la caractérisation de deux transitions de Lifshitz à $H_4 = 16$ T et $H_5 = 21$ T et des deux autres modifications de la surface de Fermi à $H_1 = 4$ T et $H_2 = 9$ T. Ces transitions sont comparées aux transitions de Lifshitz observées précédemment dans d'autres composés à fermions lourds. La mesure d'oscillations quantiques sous pression jusqu'à 2.5 GPa montre une faible évolution de la surface de Fermi. Quelques points communs ont pu être trouvés entre la surface de Fermi mesurées par les oscillations quantiues et les calculs de structure de bandes effectués précédemment pour décrire la phase paramagnétique d'UCoGe.

Abstract

The Fermi surface properties of UCoGe were studied by magnetoresistance, Hall effect and quantum oscillations under high magnetic field up to 34 T. Four orbits α, β, γ and ω on the Fermi surface were detected in quantum oscillations experiments. Both, the transport measurement and the quantum oscillations revealed and characterized two Lifshitz transitions at $H_4 = 16$ T and $H_5 = 21$ T and two further Fermi surface changes at $H_1 = 4$ T and $H_2 = 9$ T. They are compared to field induced Lifshitz transitions previously reported in

other heavy fermion systems. The Shubnikov-de Haas oscillations were also measured under hydrostatic pressure up to 2.5 GPa and evolves slowly with pressure through the critical pressure $p_c = 0.9$ GPa. The observed quantum oscillations show some correspondence with the predictions from bandstructure calculations performed for the paramagnetic state.

4.1 Previous Fermi surface studies on UCoGe

4.1.1 Bandstructure calculations and photo-emission spectroscopy

In this section we will first discuss different bandstructure calculations for UCoGe, compare them with each other and discuss the angular resolved photoemission spectroscopy experiment on UCoGe. Several bandstructure calculations were performed on the ferromagnetic superconductor UCoGe even before the first Fermi surface measurements. Two different method were used: the Density Functional Theory (DFT) and the fully relativistic self-consistent resolution of Kohn-Sham-Dirac equation. All the studies assume the local density approximation. The first study combined both techniques with a relatively good agreement [Diviš (2008)]. Here stronger magnetic moments on the cobalt sites than on the uranium sites have been predicted in contradiction with experimental results [de Visser et al. (2009), Taupin et al. (2015)]. The density of states as a function of the energy has been calculated and it shows strong differences in the paramagnetic and ferromagnetic state. A second DFT study shows similar results for the density of states as a function of the energy [de la Mora and Navarro (2009)]. However, again the calculated ferromagnetic moment $M = 1.35\mu_B$/U is far above the experimental value $M = 0.03\mu_B$/U [Huy et al. (2007a)].

A third band calculations was performed from the resolution of Kohn-Sham-Dirac equation [Samsel-Czekała et al. (2010)]. The results for the density of states are in relatively good agreement with the previous studies reported in [Diviš (2008), de la Mora and Navarro (2009)] and with the x-ray photoelectron spectroscopy (XPS) measurements reported in [Samsel-Czekała et al. (2010)]. The ferromagnetic moment predicted by this calculation $M = 0.47\mu_B$/U is still far above its experimental value $M = 0.03\mu_B$/U. The resulting bandstructure is represented in figure 4.1 for the paramagnetic state (a) and for the ferromagnetic state (b). In the paramagnetic state, UCoGe would be a compensated metal with three nearly flat bands close to the Fermi level. They are spin degenerated and their numbers are 251-252, 253-254 and 255-256. The bands 253-254 and 255-256 would give two small electron pockets around the S point. The band 251-252 would give a hole Fermi surface pocket around the T point. The bandstructure calculated in the ferromagnetic state is shown in figure 4.1(b). The band 252,253 and 254 leads respectively to a hole pocket between the Γ point and the

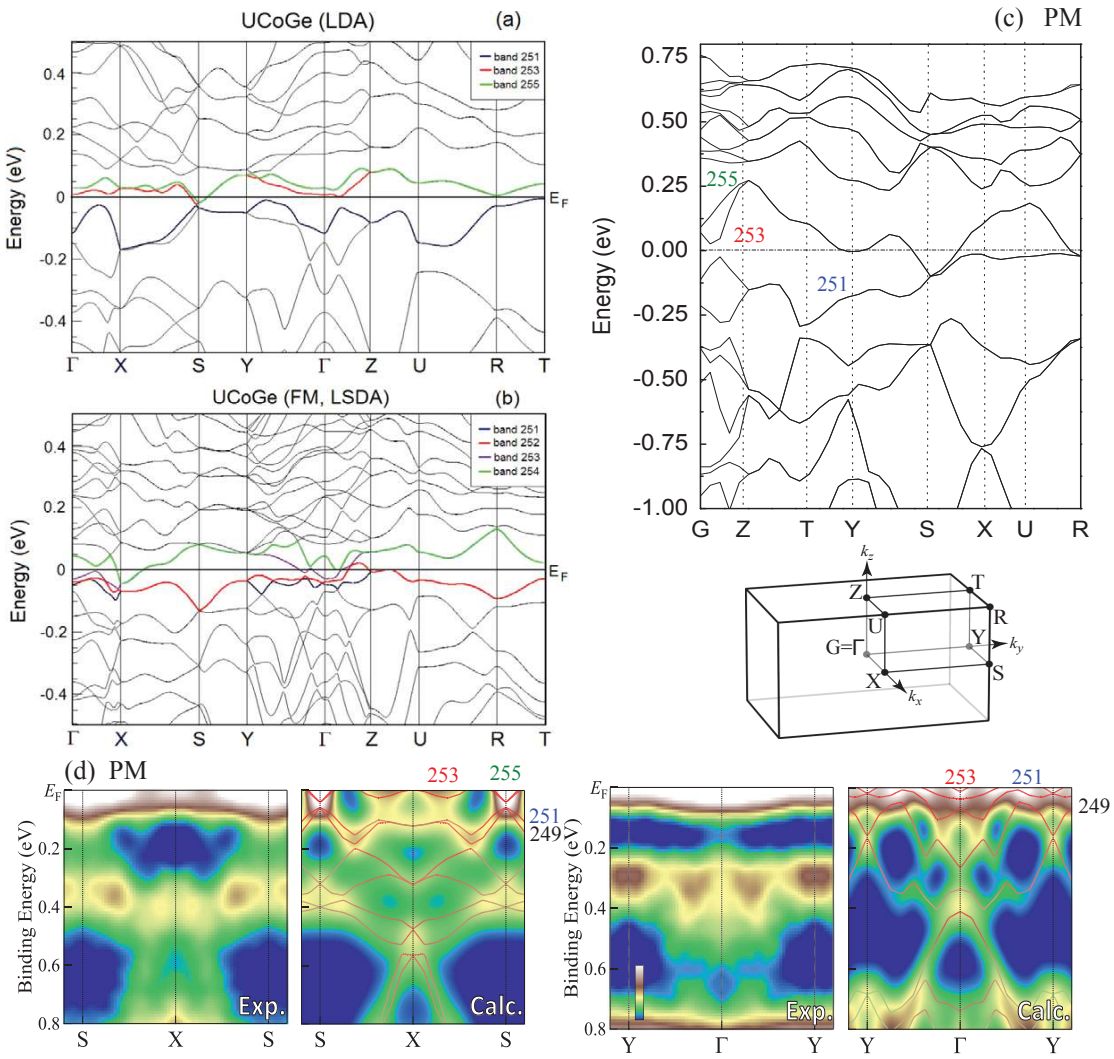

FIG. 4.1 (a) Electronic bandstructure of UCoGe in the paramagnetic state (a) and in the ferromagnetic state (b) calculated in reference [Samsel-Czekała et al. (2010)]. (c) bandstructure of UCoGe in the paramagnetic state taken from reference [Yu et al. (2011)]. The numbers of bands were added to the figure to correspond to (a). (d) The first and third panel are ARPES spectra of UCoGe in the paramagnetic state at $T = 20$ K [Fujimori et al. (2015)]. The color scale and the red lines on the second and fourth panels represents the calculated density of states as function of k vector and energy and the bandstructure of UCoGe in the paramagnetic state [Fujimori et al. (2015)]. The band numbers were modified from the original figure to be in good agreement with figure (a).

Z point, an electrons pocket around the X point and two electron pockets around the X and Γ points. The Fermi surface pockets predicted in the paramagnetic state around the S and the T point would not appear in the ferromagnetic state for any spin. Thus this calculation predicts a complete reconstruction of the Fermi surface at the magnetic transition. However

this result is obtained with a predicted spontaneous magnetization $M = 0.47\mu_B/\mathrm{U}$ much higher than the experimental value $M = 0.03\mu_B/\mathrm{U}$.

A fourth study for the paramagnetic state is based on non relativistic DFT calculations. The calculated bandstructure is reported in figure 4.1(c) [Yu et al. (2011)]. Finally a fifth band calculation was performed by relativistic DFT calculations by H. Yamagami and published in [Fujimori et al. (2015)]. The bandstructure and the computed density of states are reported in figure 4.1(d). The three studies agree about the occurrence of two electron Fermi surface pocket around the S point from the bands 253 and 255. However they show strong disagreement about the other pockets of the Fermi surface. For example the band 251 leads to a hole Fermi surface pocket around the T point in figure 4.1(a), stays below the Fermi level in figure 4.1(c) and leads only to two holes pocket between the Γ and the Y points in figure 4.1(d). These discrepancies point out the difficulty of the bandstructure calculations in UCoGe. This difficulty is related to the occurrence of nearly flat bands resulting from the heavy fermion behavior and to the low symmetry of the orthorhombic unit cell, where all uranium atoms are not on equivalent lattice sites (see figure 3.1). A much better agreement can be observed about the bands far below the Fermi level coming from *d* electrons of the cobalt atoms.

These bandstructure-calculation results can be compared with ARPES measurements [Fujimori et al. (2015)]. ARPES scans, bandstructure and computed density of states along the S-X-S and the Y-Γ-Y directions are represented in figure 4.1(d). They show a high density of states at the Fermi level, confirming the heavy fermion behavior of UCoGe. The S-X-S scan show a good agreement between the calculation and the experiment for the bands far below the Fermi level. The experiment suggests Fermi surface pockets around the S point and the X point, while the calculations predicts only a Fermi surface pocket around the S point. The ARPES scan along the Y-Γ-Y direction shows less agreement with band calculations and the bands in the vicinity of the Fermi surface could not be resolved.

The Fermi surface drawn by Samsel Czekała et al. in the ferromagnetic and paramagnetic states and by Fujimori et al. in the paramagnetic state are represented respectively in figure 4.2(a) and 4.2(b). The Fermi surface volume is rather small, indicating a low carrier or semimetallic system. The two electron Fermi surface pockets predicted in the paramagnetic state around the S point would be ellipsoids along the *c* axis according to Samsel Czekała et al. and cylinders along the *c* axis in the two other studies. They show discrepancies about all the other parts of the Fermi surface. The Fermi surface calculated by Samsel Czekała et al in the paramagnetic state contains also four closed electrons pockets and two hole pockets in the center of the Brillouin zone. On the contrary the Fermi surface calculated by H. Yamagami shows a small electrons pocket at the center of the Brillouin zone,

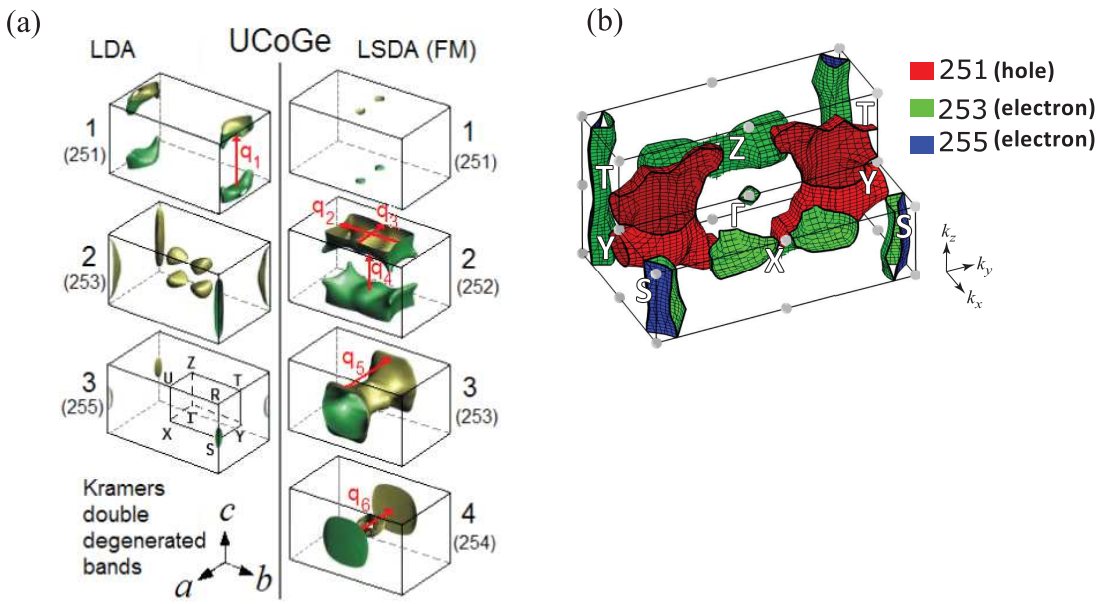

FIG. 4.2 (a) Fermi surface of UCoGe in the paramagnetic state on the left and in the ferromagnetic state on the right from reference [Samsel-Czekała et al. (2010)]. (b) Fermi surface of UCoGe in the paramagnetic state calculated by H. Yamagami and published in [Fujimori et al. (2015)]. The band numbers were modified from the original figure to coincide with figure (a).

two others around the X point and a big hole pocket around the Y point. The Fermi surface of the ferromagnetic state for a spontaneous magnetization of $M = 0.47\mu_B$/U calculated by M. Samsel Czekała et al. contains two small and two big closed hole Fermi surface pockets and two cylindrical Fermi surface pockets along the a axis.

To conclude, the different bandstructure calculations show a strong density of states around the Fermi level and two electron like Fermi surface pockets around the S point. However they show discrepancies about the other Fermi surface pockets and they fail to predict the spontaneous magnetization.

4.1.2 Anomalies in transport and thermodynamic properties in UCoGe under magnetic field

Transport properties in UCoGe revealed Fermi surface instabilities under magnetic field. A Seebeck effect measurement in UCoGe under magnetic field applied along the hard magnetization axis b is reported on figure 4.3 [Malone et al. (2012)]. The thermal gradient was applied along the a axis. The Seebeck effect shows a large peak at $H^\star = 11.1$ T and a second anomaly at $H^{\star\star} = 14.6$ T. They are not shifted under temperature and can be observed both below and above the Curie temperature, so these anomalies would not be correspond

to magnetic transitions. They were interpreted in terms of Fermi surface reconstructions. Thus the Fermi surface of in UCoGe is modified by a magnetic field applied along the hard magnetization axis *b*.

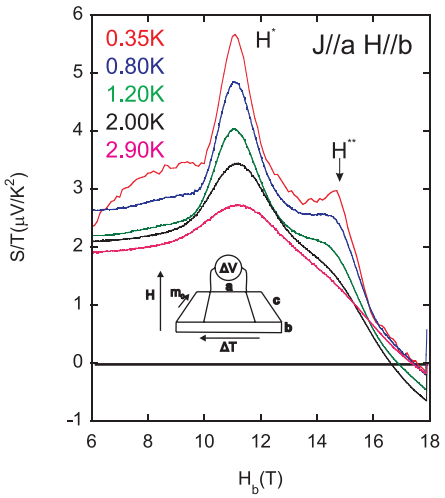

FIG. 4.3 Seebeck effect in UCoGe as a function of magnetic field applied along the hard magnetization axis *b* [Malone et al. (2012)]. Thermal gradient was applied along the *a* axis.

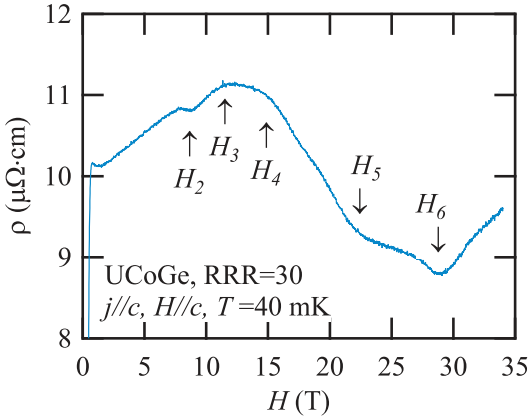

FIG. 4.4 Resistivity at 40 mK in UCoGe as a function of magnetic field applied along the easy magnetization axis *c*. These results were published in reference [Aoki et al. (2011c)].

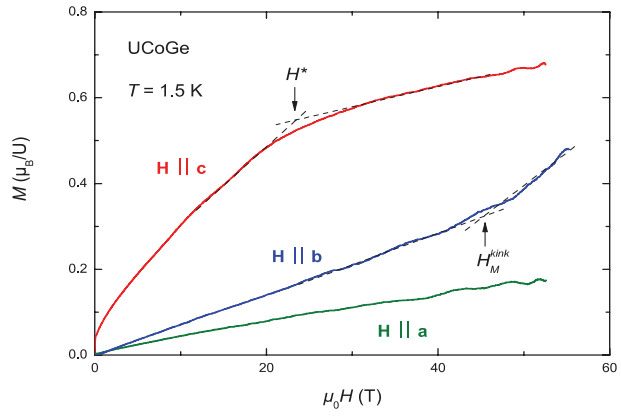

FIG. 4.5 Magnetization of UCoGe at 1.5 K as a function of magnetic field applied along the three crystallographic axis [Knafo et al. (2012)].

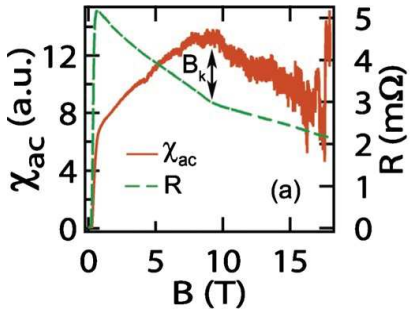

FIG. 4.6 ac magnetic susceptibility as a function of magnetic field applied along the easy magnetization axis *c* at 40 mK. [Steven et al. (2011)].

The longitudinal magnetoresistance of UCoGe with current and magnetic field applied along the easy magnetization axis *c* is reported in figure 4.4 [Aoki et al. (2011c)]. Above $H_{c2} \approx 1$ T it increases slightly with magnetic field, it shows a shoulder at $H_2 \approx 9$ T and

becomes constant above $H_3 \approx 12$ T. It starts to decrease with field at $H_4 \approx 15$ T and shows a kink at $H_5 \approx 22$ T and a minimum at $H_6 \approx 29$ T. It suggests that a magnetic field applied along the easy magnetization axis c would also induce Fermi surface instabilities. Measurements of the angular dependence of the magnetoresistance followed the anomaly at $H_2 \approx 9$ T in the ac and bc planes [Steven et al. (2011), Bay et al. (2014)]. It obeys a $1/\cos$ law, so it occurs always at the same value of the c axis component of the magnetic field. A measurement of the temperature and pressure dependence of the magnetoresistance of UCoGe shows that the anomaly at H_2 is nearly temperature independent and it is shifted to higher magnetic field under hydrostatic pressure [Bay et al. (2014)].

The magnetization measured at 1.5 K under pulsed magnetic field up to 60 T applied along each crystallographic axis [Knafo et al. (2012)] is reported in figure 4.5(a). The magnetization for field along the easy magnetization axis c increases strongly under magnetic field indicating a strong Fermi surface polarization under magnetic field. The increase gets weaker after a broad crossover around 24 T. For magnetic field along the b axis, the magnetization is much lower and shows an upturn around 45 T. The a axis is the hardest axis with a tiny magnetization. Tiny anomalies were observed in the derivative of the magnetization under magnetic field along the c axis at the same field values as in transport measurement [W. Knafo, private communication]. Thus these anomalies do not correspond to magnetic phase transitions at least above 1.5 K and may be related to Fermi surface transitions. An ac magnetic susceptibility measurement at 40 mK for magnetic field applied along the easy magnetization axis c is reported in figure 4.5(b). It shows a maximum at $H_2 \approx 9$ T and a jump at $H_4 \approx 16$ T. A recent magnetization study at dilution refrigerator temperatures shows a tiny anomaly at H_2 [Nakamura (2016)]. These results suggest small changes of the magnetic properties at these anomalies. A recent specific heat measurement under magnetic field shows also a slope change at H_2 [Wu (2016)].

4.1.3 Previous quantum oscillation experiments in UCoGe.

A Shubnikov-de Haas study was performed under high magnetic field from 20 T to 33 T and it is reported in figure 4.7(c). A big and heavy nearly spherical pocket was observed with $F_\alpha \approx 1000$ T and $m^\star_\alpha = 25\ m_0$ at the b axis. Later a de Haas-van Alphen experiment was performed on UCoGe [Aoki et al. (2014a)] up to 15 T. The dHvA signal was divided in two by a sharp peak at the anomaly $H_2 \approx 9$ T. A small Fermi surface pocket was observed below the anomaly at H_2 with $F \approx 250$ T. Its angular dependence suggests a cylindrical Fermi surface pocket. Above the anomaly H_2 two quantum-oscillations frequencies close to each other are observed with: $F \approx 250$ T and $F \approx 300$ T. Thus the two results of these two quantum-oscillation experiments performed on different field intervals on UCoGe are very

different. No correspondence has been found between these quantum-oscillations results and the bandstructure-calculation results for the ferromagnetic state [Samsel-Czekała et al. (2010)].

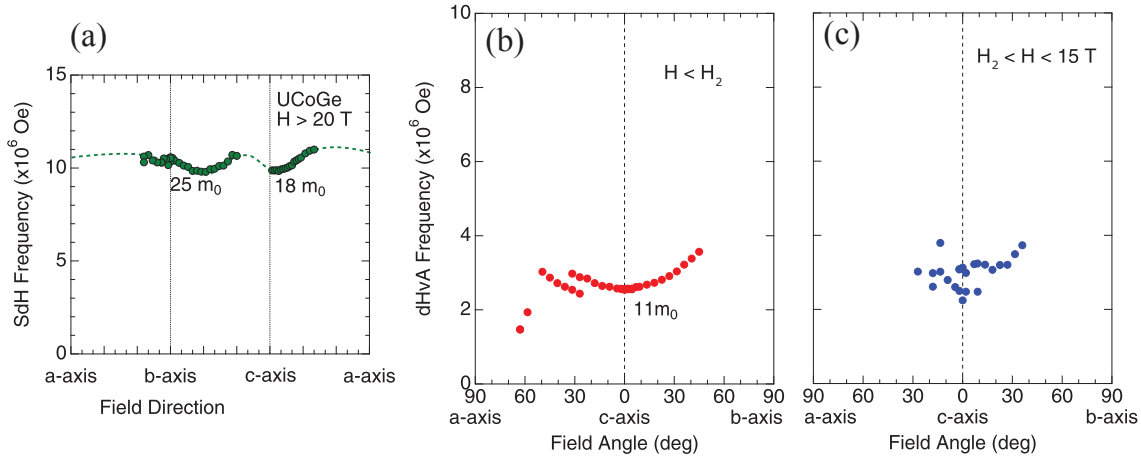

FIG. 4.7 (a)Angular dependence of Shubnikov-de Haas oscillations in UCoGe above 20 T [Aoki et al. (2014a)]. (b) Angular dependence of de Haas-van Alphen oscillations in UCoGe below the anomaly at H_2. (c) Angular dependence of de Haas-van Alphen oscillations between H_2 anomaly and 15 T.

4.1.4 Aim of this chapter

The first aim is to determine the Fermi surface of the ferromagnetic superconductor UCoGe. A second issue is the study of Fermi surface changes at the anomalies observed under magnetic field in the transport measurements. Finally the Shubnikov-de Haas effect is measured under hydrostatic pressure to discuss Fermi surface changes between the ferromagnetic and paramagnetic states.

4.2 Field induced Lifshitz transition in UCoGe

4.2.1 Hall effect and thermopower in UCoGe

The Hall effect in UCoGe was measured under magnetic field applied along the easy magnetization axis *c* in a high quality sample with RRR=105, which will be referred as UCoGe S1. Electrical current was applied along the *b* axis. The measurements were performed in a PPMS, in the Kelvinox dilution and in the top loading dilution in LNCMI (see chapter 2 for experimental details). The results obtained in the PPMS and in the Kelvinox dilution

are reported in figure 4.8. At room temperature the Hall effect is negative, linear up to 1 T. It gets much stronger under cooling down to 30 K. This enhancement must come from the reinforcement of anomalous Hall effect under cooling due to the enhancement of the magnetic susceptibility (see section 1.6.4. for Hall effect interpretation). For lower temperature the Hall effect gets smaller under cooling, it can be explained by the reduction of disorder under cooling in this high quality sample (RRR=105). Indeed it implies a reduction of the skew scattering contribution to anomalous Hall effect. At the Curie temperature $T_C = 2.6$ K determined by a simultaneous resistivity measurement on the same sample, the Hall effect shows a broad minimum around $H = 0.5$ T. In the ferromagnetic state at 1.5 K, it becomes positive. Thus a change of sign of the Hall effect occurs at the ferromagnetic transition, however no abrupt change in the Hall effect is observed at this transition. At 4 K in the paramagnetic state the Hall effect represented in figure 4.8(b) is negative at low magnetic field and it becomes positive above 2.5 T applied along the easy magnetization axis c like in the ferromagnetic state. It suggests the similarity between the Fermi surface of the ferromagnetic state and the Fermi surface of the polarized paramagnetic state under a magnetic field of few Tesla along the c axis.

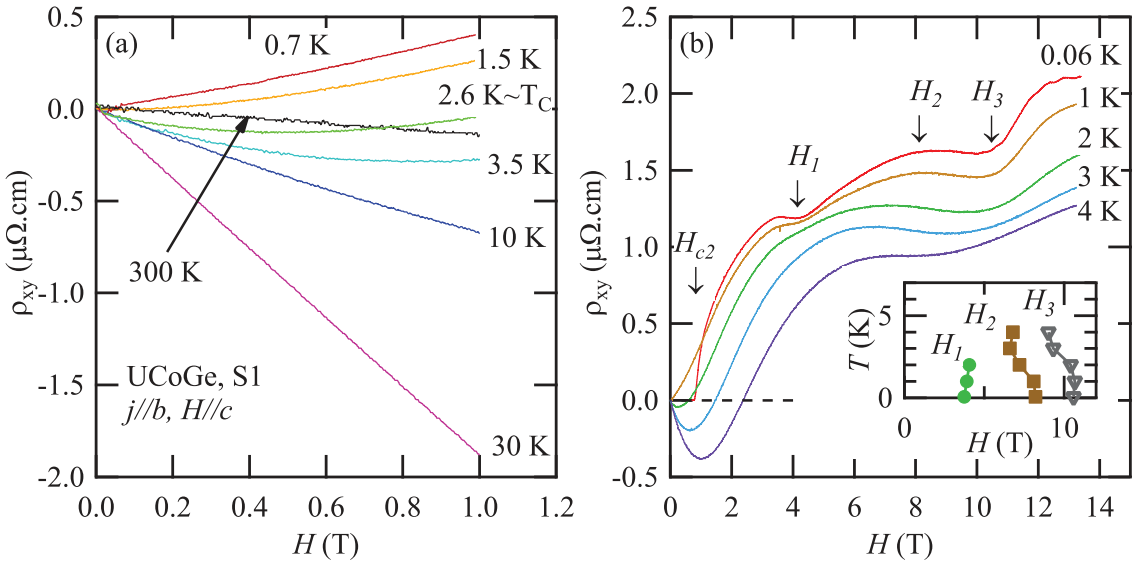

FIG. 4.8 (a) Hall effect in UCoGe S1 as a function of magnetic field applied along the easy magnetization axis c for different temperatures. (b) Same experiment up to 13.4 T. Three anomalies at H_1, H_2 and H_3 are indicated by arrows. The inset shows the temperature dependence of these anomalies.

The Hall effect at 0.06 K as a function of magnetic field shows several anomalies above its upper critical field H_{c2}. It shows a shoulder at $H_1 \approx 4$ T, it becomes constant at $H_2 \approx 8$ T and increases strongly at $H_3 \approx 11$ T. The anomaly at H_1 can be followed up to $T =$

2 K. The anomalies at H_2 and H_3 become a clear maximum and a clear minimum with higher temperature and they are both slightly shifted to lower field with temperature. The temperature dependence of H_2 is in good agreement with a previous study [Bay et al. (2014)]. The anomaly at H_1 have not been reported in the literature, but it has been observed in an other sample by resistivity measurements [M. Taupin, private communication]. The Hall effect in UCoGe was also measured under high magnetic field up to 34 T along the c axis. It is represented in figure 4.9 at 40 mK with the thermopower at 900 mK and 450 mK on the same sample S1 measured by A. Gourgout, A. Pourret and G. Seyfarth and published in [**?**]. The thermopower experiment is described in reference [Gourgout (2017)]. The Seebeck effect exhibits successive marked minima at $H_1 \approx 3.7$ T, $H_2 \approx 9.2$ T. At $H_4 = 16$ T the Hall effect decreases abruptly whereas the Seebeck effect has a marked minimum and increases for higher fields. A small kink appears at $H_5 = 21$ T in the Seebeck effect but no clear anomaly in the Hall effect. At 450 mK, in addition, large quantum oscillations occur in the thermopower. In the whole field range the Hall effect and the Seebeck effect have opposite sign, which changes around 22 T suggesting a change of the dominant carrier type. However in a compensated metal like UCoGe, the dominant carrier type is difficult to determine. The sign of Seebeck effect may depend on the current direction as observed in URhGe [Gourgout et al. (2016)]. The temperature dependence of the anomalies observed in the Seebeck effect is shown in the inset of figure 4.9. It does not show any change in the field position of the anomaly under temperature, while the Hall effect suggests a small temperature dependence for H_2 and H_3. However it may be due to the different criteria in determining the position of the characteristics fields by the different probes. The study of the Hall effect in compensated metals is rather complex, however a one band model is proposed to analyze the Hall effect in UCoGe. The Hall effect is the sum of the linear Hall effect and the anomalous Hall effect as described in section 1.6.4. Assuming that the anomalous Hall effect under high magnetic field comes mainly from skew scattering, the anomalous Hall effect ρ_{xy}^a would be proportional to the resistivity ρ. So the Hall effect should satisfy:

$$\frac{\rho_{xy}}{H} = \rho_{xy}^0 + \alpha \frac{\rho M}{H} \tag{4.1}$$

α is a constant coefficient. The quantity ρ_{xy}/H is plotted versus $\rho M/H$ in figure 4.10. The magnetization was taken from reference [Knafo et al. (2012)]. While the Hall effect and the resistivity were measured at 40 mK, the magnetization was measured at 1.5 K. The temperature dependence of the magnetization below 1.5 K is neglected. On each interval between the anomalies, the Hall effect can be fitted by a line. So the experimental results are in good agreement with this model. An effective number of carriers is defined by $\rho_{xy}^0 = 1/n_{\text{eff}}e$. Its field dependence determined from this simplified approach is represented in the

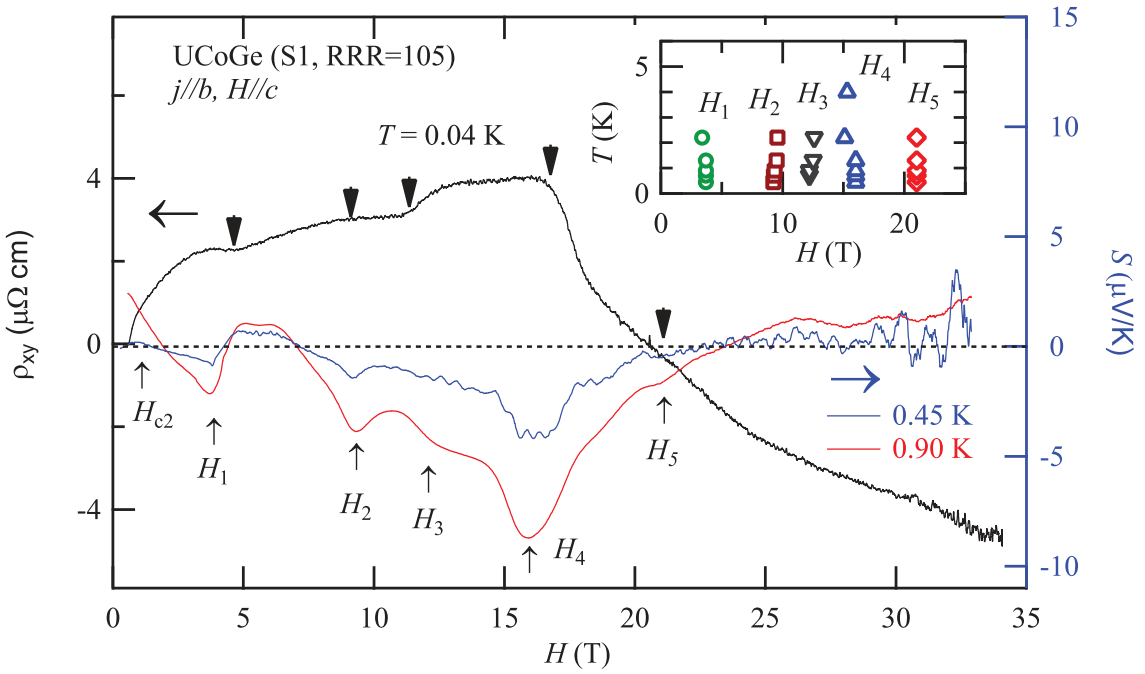

FIG. 4.9 Hall effect ρ_{xy} at 40 mK (left scale) and thermopower S at 900 mK and 450 mK (right scale) of UCoGe as a function of magnetic field applied along the easy magnetization axis c. A series of transitions can be observed as a function of field. The inset shows the temperature dependence of the anomalies in the thermopower.

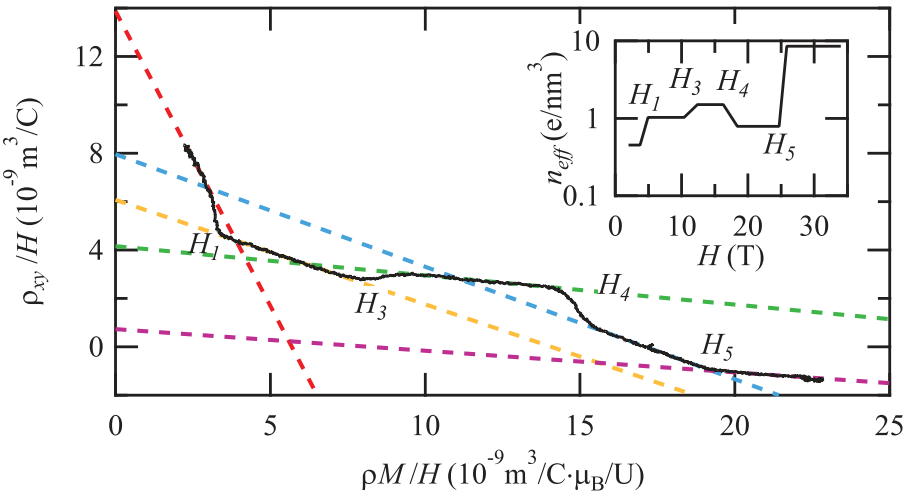

FIG. 4.10 The quantity $\frac{\rho_{xy}}{H}$ is plotted versus $\frac{\rho M}{H}$ for the Hall effect measurement reported in figure 4.9. The dashed lines are linear fits from equation (4.1). They were performed on the intervals delimited by the anomalies in the Hall effect. The inset is a scheme of the field dependence on the effective carrier number n_{eff} extracted from these fits.

inset of figure 4.10. It changes at the anomalies H_1, H_3, H_4 and H_5. So at each anomaly, the Hall effect suggests a change of the effective number of light carriers. The clear signatures of these transitions in transport properties $\rho_{xy}(H)$ and $S(H)$ and the absence of any marked phase transition in thermodynamic properties [Knafo et al. (2012); Wu et al. (2016)] suggest that they are related to topological Fermi surface changes.

4.2.2 Transverse magnetoresistance in UCoGe

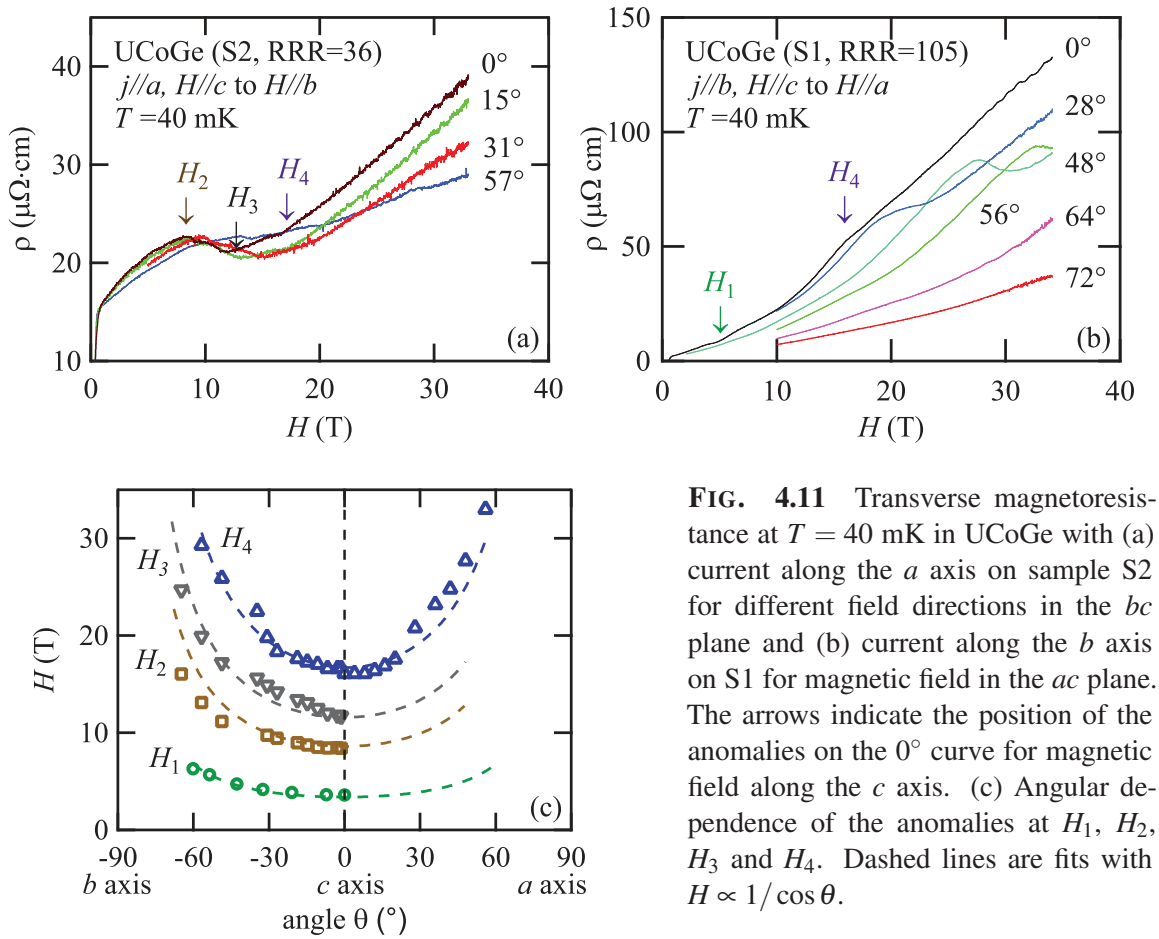

FIG. 4.11 Transverse magnetoresistance at $T = 40$ mK in UCoGe with (a) current along the a axis on sample S2 for different field directions in the bc plane and (b) current along the b axis on S1 for magnetic field in the ac plane. The arrows indicate the position of the anomalies on the 0° curve for magnetic field along the c axis. (c) Angular dependence of the anomalies at H_1, H_2, H_3 and H_4. Dashed lines are fits with $H \propto 1/\cos\theta$.

Figure 4.11 shows the transverse magnetoresistance in UCoGe up to 34 T (a) in the bc plane with current along the a axis in sample S2 and (b) in the ac plane with current along b in sample S1. The magnetoresistance values in the two samples are very different with $\rho(H = 34\text{ T})/\rho(H = 0) \approx 75$ in S1 and $\rho(H = 34\text{ T})/\rho(H = 0) \approx 3$ in S2. As discussed in section 1.6.3, this difference indicates a sample quality difference in good agreement with the RRR values : RRR(S1)=105 and RRR(S2)=36. Previously the magnetoresistance under magnetic field along the c axis and current along the b axis has been reported in reference

[Bay et al. (2014)] on a sample with $RRR = 30$. Their results are similar to that found on S2 with the current along the a axis and similar RRR. Its magnetoresistance is $\rho(H = 34\ \mathrm{T})/\rho(H = 0) \approx 4$. It shows that the magnetoresistance in UCoGe depends strongly on sample quality. The magnetoresistance shows in both configurations several anomalies and at high field quantum oscillations can be resolved. For current along the a axis in sample S2 in figure 4.11(a) the resistivity shows a broad maximum around $H_2 \approx 9$ T and a minimum at $H_3 \approx 12$ T. A tiny kink can also be observed at $H_4 = 16$ T.

In order to investigate the anisotropy of the detected anomalies we turned the samples in the bc and in the ac plane, while keeping the transverse configuration $j \perp H$ in both cases. The rotation of S2 in the bc plane shows a shift of the anomalies H_2 and H_4 to higher fields which can be followed up to a field angle of $\theta \approx 60^\circ$. In the ac plane $\rho(H)$ is strongly reduced when the field is rotated from the easy c axis to the hard a axis and H_3 increases with angle from the c axis. While the anomaly at H_4 smears out by rotating the field from the c axis toward the b axis, it gets more pronounced by rotating field towards the a axis and at 48° a broad maximum in $\rho(H)$ appears at H_4. Figure 4.11(c) shows the angular dependence of the anomalies in the bc and ac planes. The angular dependence of H_1 in the bc plane was determined by thermopower [Gourgout (2017)]. The anomalies follow quite well $1/\cos\theta$ dependence for both rotation axes and thus depend mainly on the c axis component of the magnetic field. For H_2 good agreement with previous reports is observed [Aoki and Flouquet (2014); Bay et al. (2014); Steven et al. (2011)]. While the anomalies under magnetic field are less clear in the transverse magnetoresistance than in the longitudinal magnetoresistance reported in figure 4.4, the transverse magnetoresistance shows Shubnikov-de Haas oscillations for both samples.

4.2.3 Lifshitz transitions revealed by quantum oscillation experiments

Figure 4.12 shows the oscillatory part after subtraction of a non-oscillatory background of (a) the thermopower and (b) of the magnetoresistance of S1 for different angles in the ac plane. For a magnetic field $H < H_4 = 16$ T along the c axis slow oscillations were observed with two very close frequencies at 240 T and 310 T in both probes. These low frequencies vanish at $H_4 = 16$ T and faster oscillations with a frequency of $F_\omega = 600$ T appear above H_4 but disappear again at $H_5 = 21$ T in the thermopower. No oscillations were observed between H_4 and H_5 in SdH. Above H_5 a higher frequency F_α=970 T called α branch occurs in both probes. The frequencies of the quantum oscillations measured in the different field intervals delimited by the anomalies are reported in table 4.1. This measurement is in good agreement with previous measurements reported in figure 4.7 [Aoki et al. (2014a)]. However it shows the occurrence of two Fermi surface reconstructions at

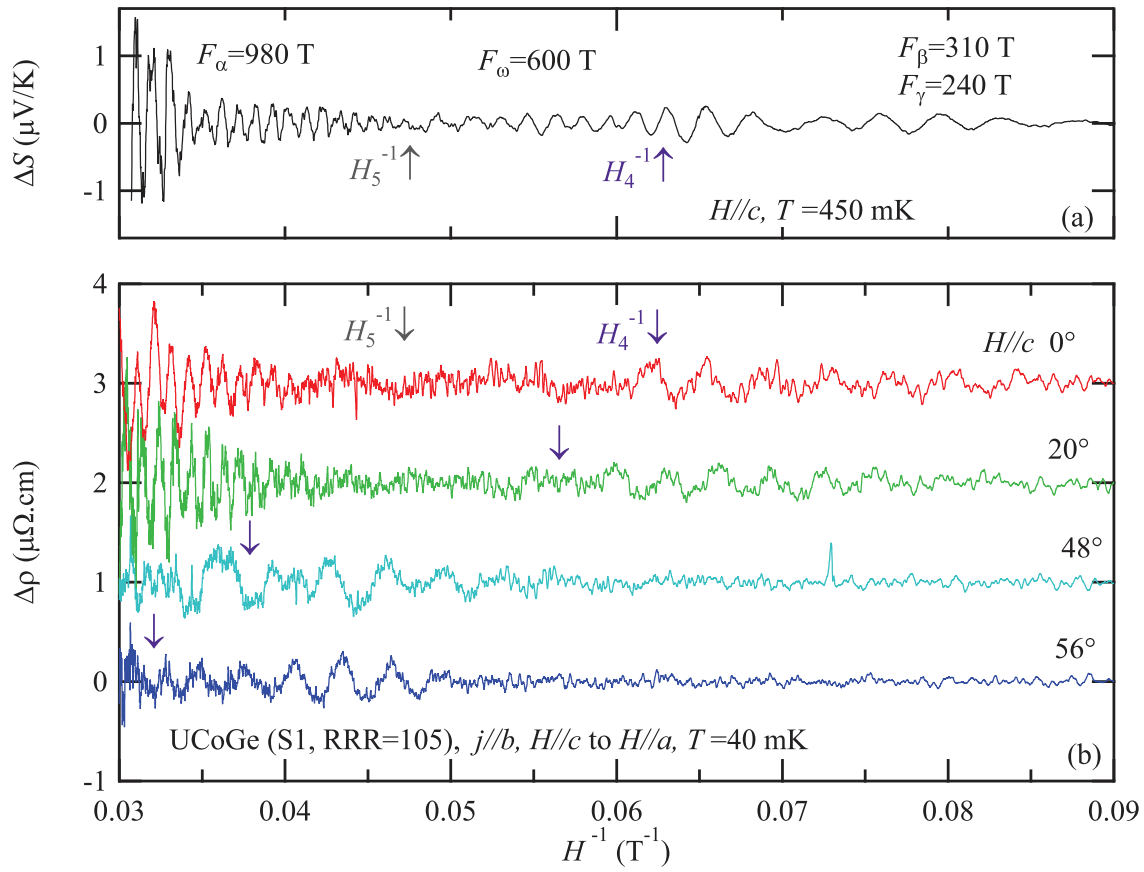

FIG. 4.12 Quantum oscillations in UCoGe extracted from (a) thermopower at 450 mK [Gourgout (2017)] and (b) resistivity at 40 mK measured on the same sample S1 as a function of inverse magnetic field. The arrows show the positions of H_4 and H_5 anomalies detected in thermopower. The lower panel (b) shows also quantum oscillations in the *ac* plane measured by resistivity.

$H_4 = 16$ T and $H_5 = 21$ T, which were not identified by previous quantum oscillation studies. Moreover the ω branch observed in the thermopower had not been detected before.

The Fermi surface reconstruction at H_4 was followed in the *ac* plane. While H_4 increases to higher field when approaching the *a* axis, the oscillations at F_γ and F_β are suppressed at H_4 at each angle. At 56° a continuous increase of F_γ with field can be observed, when field gets close to the anomaly $H_4(56°) = 33$ T. Indeed while a three period sinusoidal fit centered at $1/B = 0.043$ T$^{-1} = 1/(23.3$ T) gives $F_\gamma(56°) = 340$ T, a such fit centered at $1/B = 0.035$ T$^{-1} = 1/(28.6$ T) gives $F_\gamma(56°) = 430$ T. If the suppression of a Fermi surface pocket under magnetic field gets faster and faster, a such increase of the quantum oscillation frequency is observed, as illustrated in section 1 in figure 1.8. Thus the field dependence of the quantum oscillation frequency suggests that the Fermi surface pocket of the γ branch shrinks continuously, when the field gets close to the Fermi surface reconstruction

at $H_4(56°) = 33$ T. Such a continuous change of a quantum oscillation frequency could not be observed clearly for the other field directions. Since the γ and β orbits are much smaller than the Brillouin zone, the possibility of a neck formation under magnetic field at a edge of these orbits is ruled out. The Fermi surface change at H_4 corresponds to the collapse of the orbits on the Fermi surface γ and β in a Lifshitz transition.

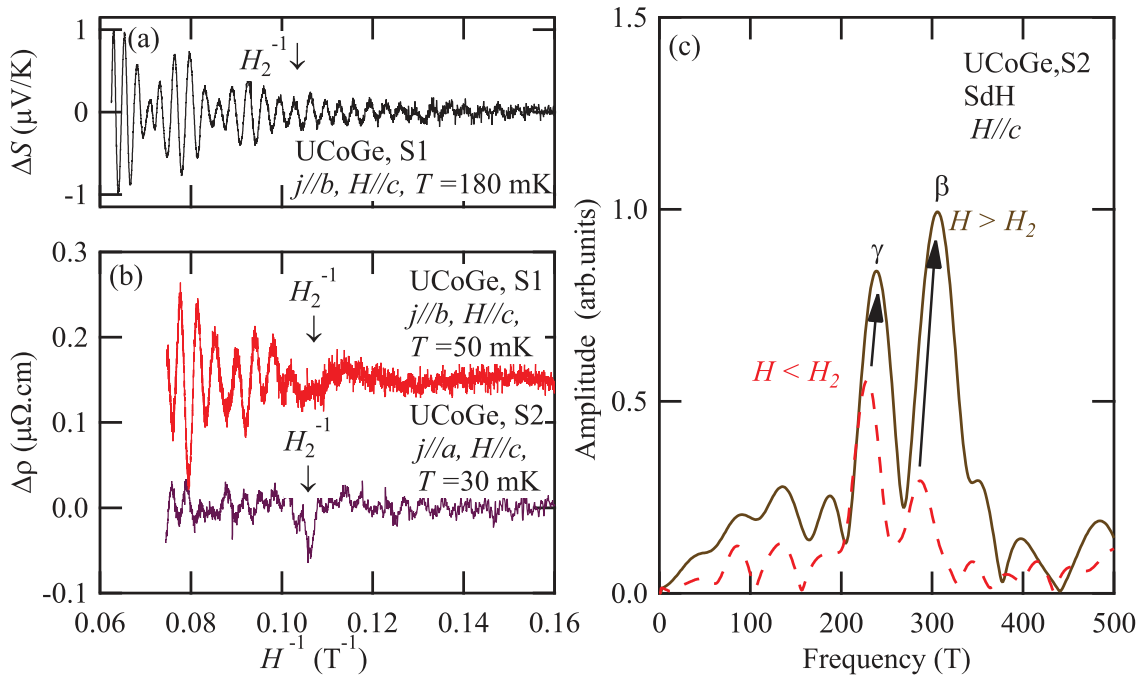

FIG. 4.13 Quantum oscillations below 16 T as a function of inverse magnetic field for (a) thermopower and (b) resistivity measured more precisely in a superconducting magnet. (c) FFT spectrum of quantum oscillations in the resistivity of sample S2 for field along the c axis below and above $H_2 \approx 9$ T.

Quantum oscillations below H_4=16 T were measured more precisely in the resistivity in the Kelvinox dilution with a superconducting magnet of 13 T and in the thermoelectric power using a dilution refrigerator with a 16 T superconducting magnet. The oscillations are represented in figure 4.13 after subtracting a non-oscillatory background. Above H_2, a modulation of the amplitude of the oscillations in the thermopower can be observed due to beating of two close quantum oscillation frequencies F_β and F_γ. While S1 shows large oscillations above H_2, the SdH oscillations below 10 T are more visible on S2. The fast Fourier transformation (FFT) spectra of the oscillations for S2 are represented in figure 4.13(c), both for field below and above H_2. Two frequencies can be observed below H_2 at 230 T and 280 T. For $H > H_2$ these two frequencies are slightly shifted to 240 T and 310 T. The previous dHvA study reported in figure 4.7 suggested a splitting of one frequency from

below to above H_2 [Aoki et al. (2014a)]. On the contrary, our measurements show that both quantum-oscillation frequencies survive below H_2 and a small change in the β frequency occurs at H_2. As discussed in section 1.7.2 the frequency of the quantum oscillation is related to the extreme area of the Fermi surface S_{ext} by the formula:

$$F = \frac{\hbar}{2\pi e}(S_{ext} - B\frac{dS_{ext}}{dB}) \tag{4.2}$$

Thus the change in β frequency can either correspond to a small increase in the size of the Fermi surface section S_{ext} or to a strong increase of the Zeeman effect term $-BdS_{ext}/dB$. The Fermi surface pocket β may come from the minority band, since it vanishes at $H_4 = 16$ T. So the second case would correspond to a reinforcement of the Zeeman effect of the minority band, which would become non linear.

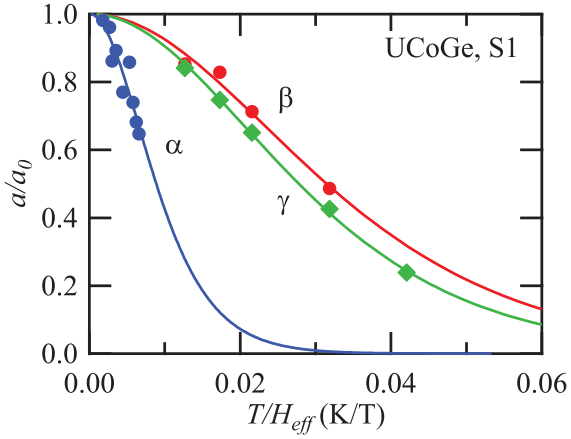

FIG. 4.14 Renormalized Shubnikov-de Haas oscillation amplitude in sample S1 as a function of temperature renormalized by the effective magnetic field H_{eff} of the field interval. The magnetic field is applied along the c axis and it is between $H_2 \approx 9$ T and 13.4 T for the γ and β branches and between 24 T and 34 T for the α branch. The results are $m^\star_\alpha = 17m_0$, $m^\star_\beta = 10m_0$, $m^\star_\gamma = 11m_0$.

The temperature dependence of the quantum-oscillation amplitude in S1 is represented in figure 4.14 for magnetic field along the c axis. The temperature was renormalized by the effective magnetic field H_{eff} and the amplitude was renormalized to its extrapolation down to zero temperature. It was fitted by the Lifshitz-Kosevich formula introduced in section 1.7.4:

$$a = a_0 \frac{\alpha m^\star T/B_{eff}}{sinh(\alpha m^\star T/B_{eff})} \tag{4.3}$$

with $\alpha m_0 = 14.69$ K/T. The fits show a good agreement with experimental results and give the effective mass values : $m^\star_\alpha = 17m_0$, $m^\star_\beta = 10m_0$ and $m^\star_\gamma = 11m_0$. These values are reported in table 4.1 with the results of the same study on sample S2 and the effective mass values extracted from the temperature dependence of thermopower quantum oscillations [Pantsulaya and Varlamov (1989), Palacio Morales et al. (2016)]. A relatively good agreement is observed between these different experiments on values of the effective masses.

	SdH(sample1)		SdH(sample2)		Seebeck(sample1)	
orbit	F(T)	$m^*(m_0)$	F(T)	$m^*(m_0)$	F(T)	$m^*(m_0)$
$H_1 < H < H_2$						
γ			225	7		
β	269		279		285	
$H_2 < H < H_3$						
γ	240	11	238	9	240	12
β	310	10	306	10	310	13
$H_3 < H < H_4$						
ω					604	14
$H_4 < H$						
α	969	17	954		983	14

Table 4.1 Quantum-oscillation frequencies and effective masses in UCoGe from resistivity and Seebeck effect measurements. The different field intervals are delimited by the anomalies observed in transport measurements.

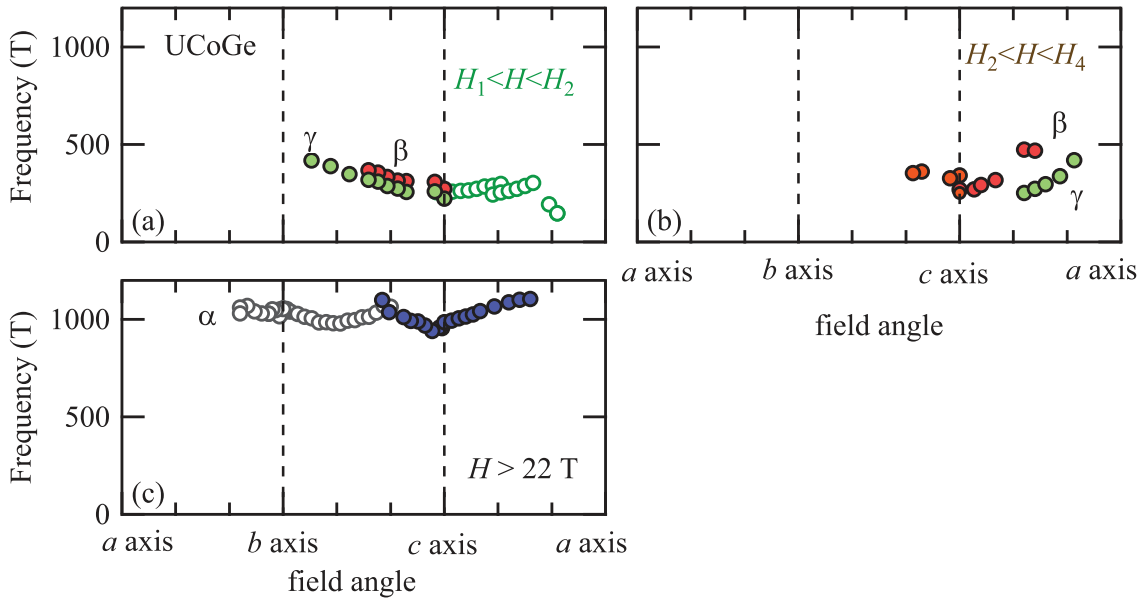

FIG. 4.15 Angular dependence of quantum-oscillation frequencies in UCoGe (a) below the anomaly at H_2, (b) between H_2 and H_4 anomaly field, (c) above 22 T. Open circles in (a) and (c) have been taken from reference [Aoki et al. (2014a)].

The angular dependence of the oscillation frequencies for the different field intervals are represented in figure 4.15. Data in the vicinity of the b axis are taken from reference [Aoki et al. (2014a)] and connect perfectly to those presented here. At low field $H < H_2$, the γ and β branches correspond to two small Fermi surface pockets elongated along the c axis. The γ pocket seems closed and nearly ellipsoidal. Both pockets change in size at H_2, but

disappear abruptly above H_4. The angular dependence of the frequency at $F_\omega = 600$ T has not been measured. The pocket α in figure 4.15(c) is experimentally observed above 22 T, independent of the field angle in the *bc* plane. Thus it may exist in the all field range even below the anomalies, which are evolving with angle according to a $1/\cos(\theta)$ law. It seems to be nearly spherical with a frequency around $F_\alpha \approx 1000$ T. Its effective mass is anisotropic with $m^\star_\alpha = 17\ m_0$ at *c* axis and $m^\star_\alpha = 25\ m_0$ at *b* axis in reference [Aoki et al. (2011c)].

The contribution to the specific heat of the different Fermi surface pockets can be calculated assuming spherical Fermi-surface pockets coming from one spin projection as explained in section 1.7.7. Assuming spherical pockets with the average frequencies $F_\gamma \approx F_\beta \approx 300$ T, $F_\omega \approx 600$ T and $F_\alpha \approx 1000$ T and the average effective masses $m^\star_\gamma \approx m^\star_\beta \approx 10\ m_0$, $m^\star_\omega \approx 14\ m_0$ and $m^\star_\alpha \approx 20\ m_0$ the contribution to the specific heat are $\gamma_\gamma \approx \gamma_\beta \approx 0.8$ mJ.mol^{-1}.K^{-2}, $\gamma_\omega \approx 1.5$ mJ.mol^{-1}.K^{-2} and $\gamma_\alpha \approx 3$ mJ.mol^{-1}.K^{-2}. These values are small compared to the total Sommerfeld coefficient in UCoGe is $\gamma \approx 55$ mJ.mol^{-1}.K^{-2} [Huy et al. (2007a)]. Thus the Fermi surface of UCoGe contents bigger or heavier Fermi surface pockets, which were not detected by this experiment.

The main observation is that most anomalies observed in the field dependence of the transport properties in figure 4.9 and 4.11 coincide with distinct changes in the quantum oscillation frequencies and effective masses. They are related to modifications of the Fermi surface topology with the most drastic change occurring at H_4, where the Hall effect collapses and the Seebeck effect has a pronounced minimum. The Fermi surface in a heavy fermion system can be easily modified by applying a magnetic field and this modification may lead to field induced Lifshitz transitions as explained in section 1.5.3. Since γ and β orbits are much smaller than the Brillouin zone, the possibility of a neck formation under magnetic field at an edge of these orbits is ruled out. The Fermi surface change at H_4 may correspond to the disappearance of minority spin Fermi surface pockets in a Lifshitz transition. We can estimate the characteristic energy of each detected pocket with $\varepsilon_i = \hbar^2 k^2_{F,i}/2m^\star_i \approx \hbar e F_i/m^\star_i c$ and we find $\varepsilon_\gamma \approx 2.5$ meV, $\varepsilon_\omega \approx 5$ meV and $\varepsilon_\alpha \approx 6.6$ meV. These energies can be compared to the Zeeman energy scale of a free electron divided by the magnetic field, $\varepsilon_Z/\mu_0 H = g\mu_B \approx 0.12$ meV/T for $g = 2$. As UCoGe is a weak ferromagnet this effect will even be strengthened by the internal field. Hence, an important polarization of the bands can be achieved by easily accessible magnetic fields, and thus several magnetic field-induced Lifshitz transitions appear.

The magnetization up to 50 T [Knafo et al. (2012)] has a strongly non-linear field dependence suggesting that the electronic magnetic response must vary strongly with the magnetic field while the ferromagnetic fluctuations are already fully suppressed for $H > 1$ T along the *c* axis as discussed in chapter 3 [Aoki et al. (2011b), Hattori et al. (2012)]. Thus the elec-

tronic instabilities seem to occur in the paramagnetic regime without any additional phase transitions and far above the field where the ferromagnetic inter-site magnetic correlations collapse. While the spontaneous magnetization is about $M \approx 0.05\ \mu_B$ per Uranium atom, a magnetic field of $H_1 = 4$ T applied along the easy magnetization axis c induces a much bigger magnetization $M \approx 0.2\ \mu_B$ per uranium atom. The other transitions H_2, H_4 and H_5 occur respectively for $M \approx 0.3\ \mu_B$, $M \approx 0.4\ \mu_B$ and $M \approx 0.5\ \mu_B$ [Knafo et al. (2012)]. The key phenomenon is that Fermi surface changes are induced by crossing some critical values of magnetic polarization.

4.2.4 Discussion of field induced Lifshitz transitions in heavy fermion systems

Field-induced Lifshitz transition have been invoked in different heavy-fermion systems, however they have different characteristics. They can be associate to pseudo-metamagnetic transitions such as the transition at $H_m = 7.8$ T in $CeRu_2Si_2$ [Aoki et al. (1993)] and the transition between the III and V phase in UPt_2Si_2 [Schulze Grachtrup et al. (2012)]. In these two compounds, the magnetization shows a jump at the Lifshitz transition and a change of magnetic correlations may occur. In case of $CeRu_2Si_2$ the pseudometamagnetic transition is accompanied by a reconstruction of the Fermi surface. It has been explicitly shown by dHvA measurements [Aoki et al. (1993), Daou et al. (2006)]. It has been demonstrated that a minority spin Fermi surface pocket is continuously suppressed at H_m. In UPt_2Si_2 no quantum oscillations have been reported but the Lifshitz transition is documented by electronic structure calculations under magnetic field. On the contrary Lifshitz transition without any metagnetic transition are observed in UCoGe under magnetic field along the c axis. It can be compared to the field induced Lifshitz transition observed in the paramagnet $CeIrIn_5$ at 28 T [Aoki et al. (2016)]. While the magnetization evolves rather smoothly through this transition, thermopower and torque measurements show an anomaly and quantum oscillations reveals the suppression of a Fermi surface pocket.

The case of UCoGe can also be compared to the series of Fermi-surface reconstructions observed under magnetic field inside the hidden order state in URu_2Si_2. The transitions in URu_2Si_2 are related to the polarization of the small Fermi surface pockets [Hassinger et al. (2010c), Altarawneh et al. (2011), Malone et al. (2011)]. They occur without any metamagnetic transition and depends only on the c axis component of the magnetic field like in UCoGe [Scheerer et al. (2012), Scheerer et al. (2014)]. However contrary to the transition in UCoGe, these transitions are strongly temperature dependent [Pourret et al. (2013b)]. The Fermi surface reconstruction in URu_2Si_2 might be related to changes of hidden order prop-

erties. Lifshitz transitions were also proposed inside the antiferromagnetic state in $CeIn_3$ [Sebastian et al. (2009)] and $CeRhIn_5$[Jiao et al. (2015)]. They occur respectively at 42 T and 30 T much lower than the critical field to suppress the antiferromagnetic order, which are respectively 60 T and 50 T in $CeIn_3$ and $CeRhIn_5$. These two examples differ also from the basic picture of Lifshitz transition, since the transitions occur in an ordered state. They were both associated to a change from localized magnetism to itinerant magnetism.

A cascade of field-induced Lifshitz transitions was observed in $YbRh_2Si_2$ far above the suppression of the antiferromagnetic state by the magnetic field [Rourke et al. (2008), Pfau et al. (2013), Pourret et al. (2013a)]. It goes along with a suppression of the local Kondo effect as has been demonstrated by renormalized bandstructure calculations under magnetic field [Zwicknagl (2011)]. The Fermi-surface reconstruction under a magnetic field along the hard axis b in UCoGe reported in figure 4.3 could be related to the collapse of the ferromagnetic correlations [Malone et al. (2012)]. Thus the origin of this Fermi surface reconstruction would be different from the origin of the ones observed in the same compound under magnetic field along the easy magnetization axis c reported in this thesis. Finally the first order magnetic moment reorientation under magnetic field along the hard magnetization axis b in URhGe becomes a Lifshitz transition, when the magnetic field is tilted toward the c axis [Yelland et al. (2011)]. This last example will be discussed in chapter 5.

4.3 Fermi surface properties of UCoGe under hydrostatic pressure

4.3.1 Pressure dependence of the Fermi surface instabilities

The magnetoresistance and the Shubnikov-de Haas effect were studied in UCoGe under hydrostatic pressure. The measurements were performed on sample UCoGe S2 and the electrical current and the magnetic field were respectively applied along the a and the c axis. They were performed both below the critical pressure $p_c = 1$ GPa and above up to 2.5 GPa. The magnetoresistance at $T \approx 80$ mK as a function of field is represented for the different pressures in figure 4.16. Above the upper critical field H_{c2} the resistivity increases with magnetic field. The measurement at $p = 0.06$ GPa shows a small kink at $H_1 \approx 4$ T and a shoulder at $H_2 \approx 9$ T like previously observed at zero pressure. The pressure dependence of these two anomalies is represented in figure 4.16(b). The anomaly at H_1 becomes more and more clear under pressure. It is shifted linearly to higher field under pressure up to 10 T at 2.5 GPa. The anomaly at H_2 is shifted faster to higher field under pressure. Its pressure

dependence was measured previously with more pressure steps [Bay et al. (2014)]. So these anomalies can be induced either by magnetic field or by hydrostatic pressure at constant magnetic field.

While a magnetic field along the c axis in UCoGe induces Fermi surface instabilities, the effect of hydrostatic pressure seems opposite, since the Fermi surface instabilities are shifted to higher magnetic field under pressure. At the critical pressure, the spontaneous magnetization is suppressed. When the pressure is increased above the critical pressure, the induced magnetization should be reduced. So the strong polarization of the Fermi surface of UCoGe is expected to become weaker and weaker under pressure. There is no measurement of magnetization under pressure in UCoGe to confirm this prediction, however such a behavior of the magnetization was observed through the quantum phase transition induced by Si substitution of Ge [de Nijs et al. (2008)]. The shift of the Fermi instabilities at H_1 and at H_2 to higher magnetic field under hydrostatic pressure can be explained by the reduction of the polarization under pressure. It confirms the idea that Fermi surface instabilities at H_1 and at H_2 are induced by the polarization of the Fermi surface under magnetic field. A measurement of UCoGe magnetization under pressure is needed for a better identification of the leading force of these Fermi surface instabilities.

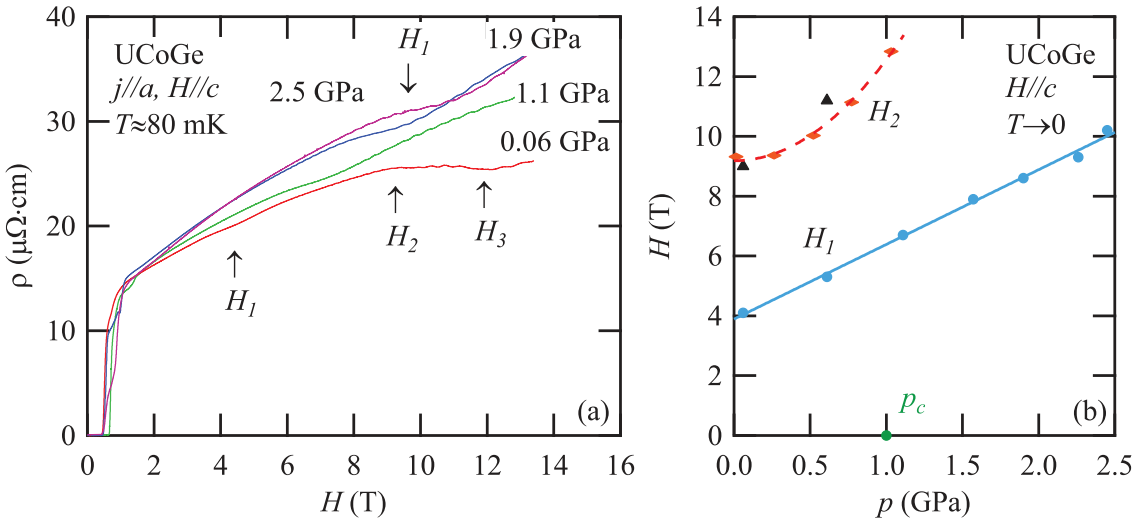

FIG. 4.16 (a) Field dependence of the magnetoresistance in UCoGe as a function of magnetic field for various pressures at T≈ 80 mK. The curves are shifted vertically for clarity. (b) Pressure dependence of the anomalies at H_1 and H_2. The orange points were taken from reference [Bay et al. (2014)]. The solid and the dashed lines are a linear fit for H_1 field and a parabolic fit for H_2.

4.3.2 Quantum oscillations under pressure

Quantum oscillations were detected in the entire investigated pressure range up to 2.5 GPa. They are represented as a function of inverse magnetic field in figure 4.17. They were observed down to 6 T at the lowest pressure $p = 0.06$ GPa and 5 T at $p = 1.9$ GPa. At 0.06 GPa a slight change of the quantum oscillations is observed at $H_2 = 9$ T comparable to the Fermi-surface change at ambient pressure, which was reported in figure 4.13. The quantum oscillation signal seems unchanged at the critical pressure $p_c = 1$ GPa. The FFT spectrum of quantum oscillations slightly above the expected critical pressure at $p = 1.1$ GPa is represented in figure 4.18 (a) for different magnetic field intervals. It shows the same two pockets γ and β as the ambient pressure spectrum in figure 4.13(c). The quantum oscillations at this pressure are observed between the anomalies $H_1(p = 1.1 \text{ GPa}) = 6.5$ T and $H_2(p = 1.1 \text{ GPa}) > 13.4$ T. The magnetic field dependence of these quantum oscillations frequencies is smaller than the peak widths. While the amplitude of β branch oscillations increases with magnetic field as expected from the Lifshitz-Kosevich formula (see section 1.7.4), an unusual field dependence of the amplitude of the γ branch oscillations can be observed. Figure 4.18(b) shows the FFT spectrum of quantum oscillations deep inside the paramagnetic state at $p = 2.5$ GPa. It shows the same two peaks as γ and β at ambient pressure (see figure 4.13(c)) and around the critical pressure $p = 1.1$ GPa. So the observed quantum oscillation signal is nearly unchanged from ambient pressure to the paramagnetic state at 2.5 GPa. After the first observation of the γ and β branches by dHvA, the authors proposed that these two peaks could come from the spin splitting of a single band [Aoki et al. (2014a)]. However under this assumption a decrease of the difference between the two frequencies would be expected when magnetism is tuned by the application of hydrostatic pressure. Thus this assumption is ruled out and the γ and β branches must come from two different orbits.

The FFT spectrum of quantum oscillations below and above $H_1(p = 2.5 \text{ GPa}) = 10$ T are both represented on figure 4.18(b). A slight increase of the β frequency is observed at $H_1(p = 2.5 \text{ GPa}) = 10$ T from 245 T to 275 T. No frequency change is observed for the γ branch. The change in the β frequency confirms that the anomaly at H_1 corresponds also to a Fermi surface instabilities. The two Fermi surface changes H_1 and H_2 seems similar, since an increase of β frequency of about 10% occurs at both anomalies. Since quantum oscillations are measured on relatively broad intervals, these Fermi surface changes may be either smooth or continuous.

The pressure dependence of the quantum oscillations frequencies is plotted for the three field intervals delimited by these Fermi surface changes $H < H_1$, $H_1 < H < H_2$ and $H_2 < H$ in figure 4.17. A slow decrease of the quantum oscillation frequency of γ orbit with pressure

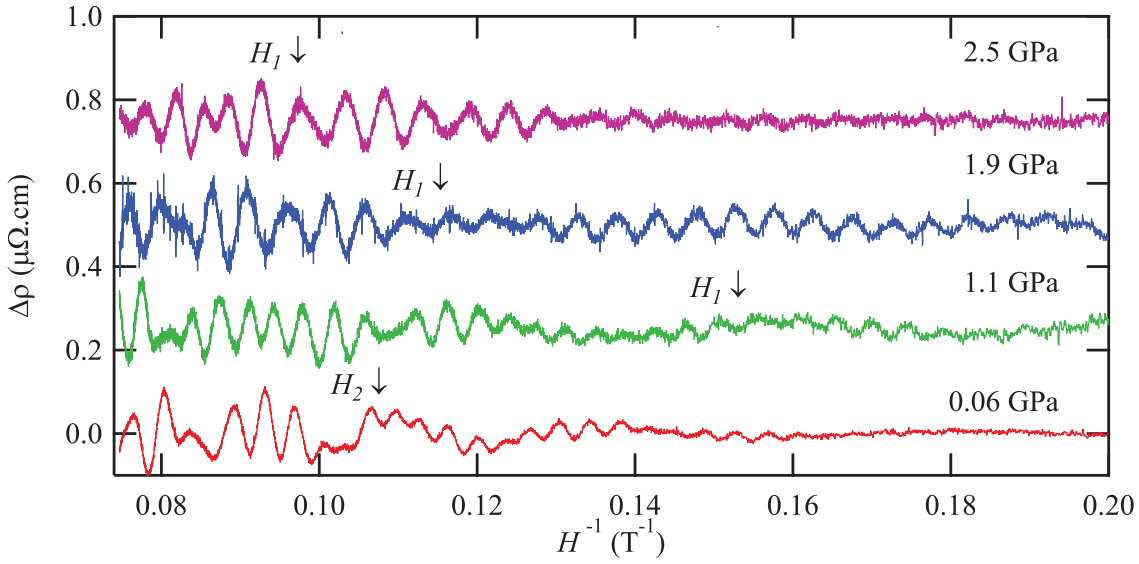

FIG. 4.17 Shubnikov-de Haas oscillations as a function of inverse magnetic field for various pressure. Temperature was around 60 mK. The arrows indicate the position of anomalies in the resistivity.

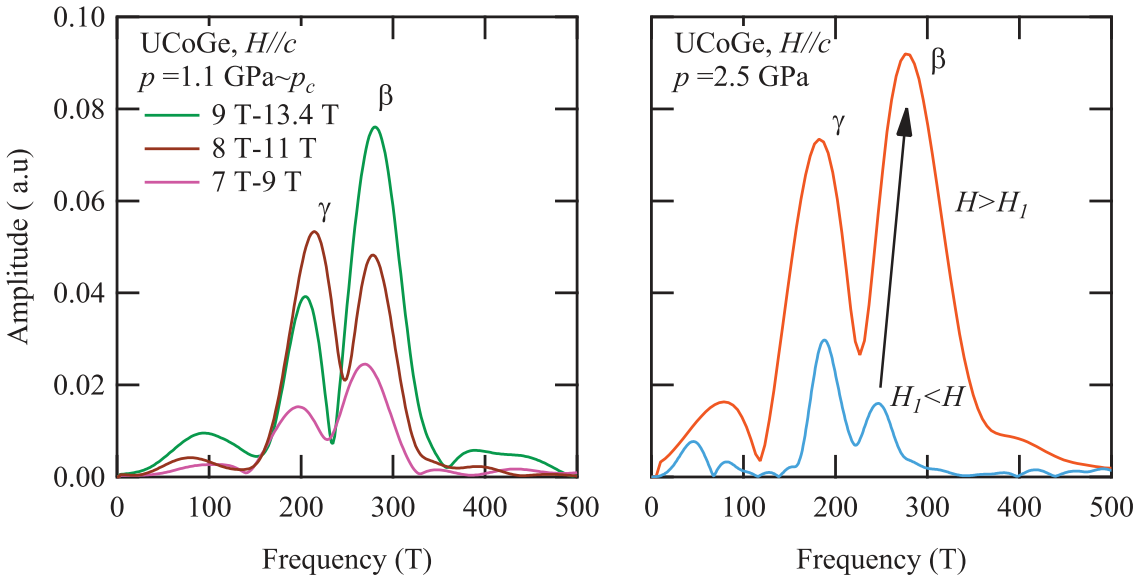

FIG. 4.18 FFT spectrum of UCoGe quantum oscillations slightly above the critical pressure at $p = 1.1$ GPa. They are represented for three different field intervals. These intervals are above the anomaly in resistivity at $H_1(p = 1.1\ \text{GPa}) = 6.5$ T and below the anomaly at $H_2(p = 1.1\ \text{GPa}) > 13.4$ T.

is observed both for the field intervals $H < H_1$ and $H_1 < H < H_2$. No change in the β frequency with pressure is observed for both field intervals $H < H_1$ and $H_1 < H < H_2$. No abrupt change of the SdH frequencies has been observed through the critical pressure. An

increase of the β frequency can be observed at H_2 at ambient pressure and at H_1 under pressure above 1 GPa.

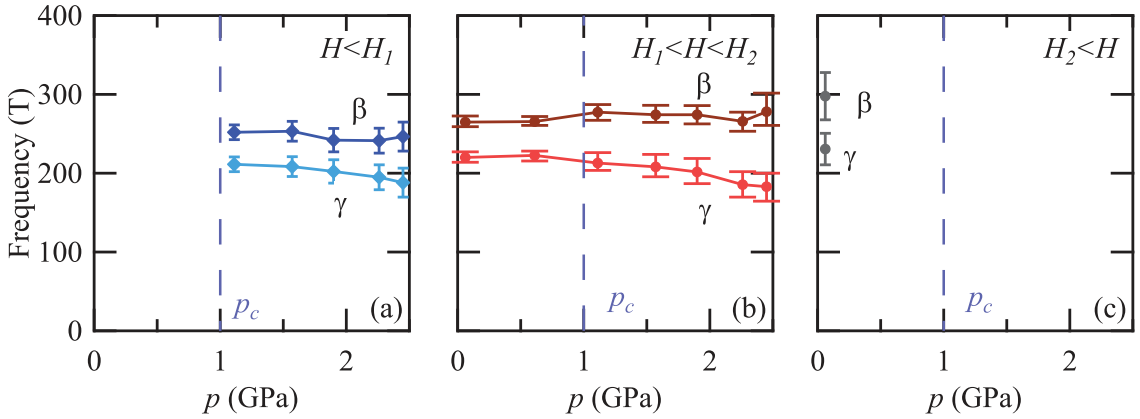

FIG. 4.19 (a) Pressure dependence of quantum oscillations frequencies under for the different field intervals delimited by the anomalies H_1 and H_2 reported in transport measurements. The results obtained in the interval below H_1, between H_1 and H_2 and above H_2 anomaly are respectively represented in (a), (b) and (c).

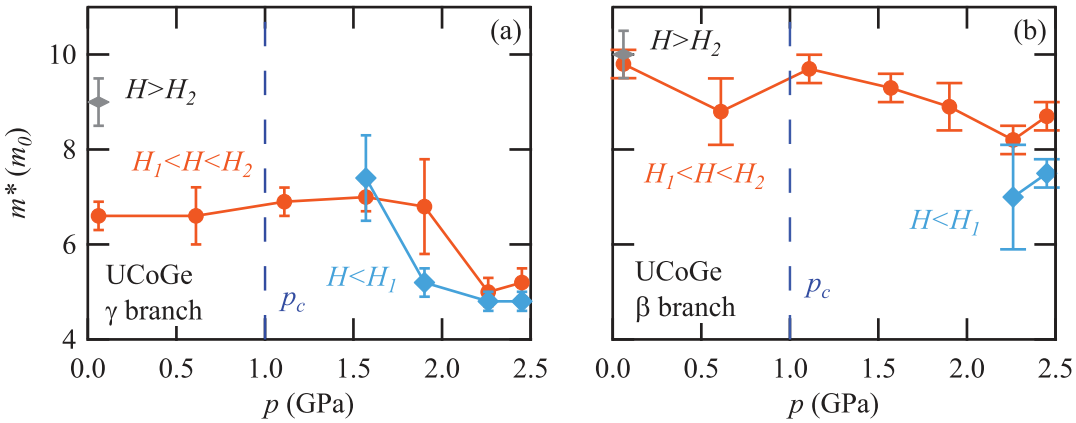

FIG. 4.20 (a) Pressure dependence of the effective mass of γ orbit for the different field intervals delimited by the anomalies H_1 and H_2 reported in transport measurements. (b) Same figure for the β orbit.

The pressure dependence of the effective mass is represented in figure 4.20 for the field intervals delimited by the anomalies at $H1$ and H_2. It was extracted from the temperature dependence of quantum oscillation amplitude, as discussed in the ambient pressure case and reported in figure 1.2. The effective mass of the γ branch at ambient pressure seems to be lower below the anomaly at H_2 with $m^\star_\gamma(p = 0.06$ GPa)$\approx 7\ m_0$ than above with $m^\star_\gamma(p =$

0.06 GPa)$\approx 9\ m_0$. In the interval between H_1 and H_2, it is constant up to the critical pressure and decreases with pressure in the paramagnetic state down to $m^\star_\gamma(p = 2.5\text{ GPa})\approx 5\ m_0$. No significant change in $m^\star_\gamma$ was observed at H_1. The effective mass of the β branch in the interval $H_1 < H < H_2$ is relatively constant with pressure. At 2.5 GPa, it increases with magnetic field around $H_1(p = 2.5\text{ GPa}) = 10$ T from $m^\star_\beta(p = 2.5\text{ GPa})\approx 7.5\ m_0$ to $m^\star_\beta(p = 2.5\text{ GPa})\approx 9\ m_0$. Thus, the effective mass of the γ and the β branches evolve smoothly from ambient pressure to 2.5 GPa and they do not show any abrupt change at the critical pressure.

4.3.3 Correspondence between bandstructure calculations and quantum oscillations

The experimental results can be compared to the band calculation prediction for the ferromagnetic and the paramagnetic state reported in figure 4.1 and 4.2 [Samsel-Czekała et al. (2010), Yu et al. (2011), Fujimori et al. (2015)]. No correspondence can be found with the bandstructure calculation in the ferromagnetic state. The two orbits of the Fermi surface γ and β must correspond to the two orbits around the S point predicted in the paramagnetic state by the three bandstructure-calculation studies. The Fermi surface pocket α observed under high magnetic field could correspond to the four nearly spherical pockets predicted inside of the Brillouin zone in the paramagnetic state in figure 4.2(a) [Samsel-Czekała et al. (2010)] or to the two pockets around the X point in figure 4.2(b) [Fujimori et al. (2015)]. Thus the observed Fermi surface under a magnetic field above 5 T below or above the critical pressure shows clear similarities with the Fermi surface predicted in the paramagnetic state. Since the angular dependence of quantum oscillations at ambient pressure represented in figure 4.15(a) suggests an ellipsoidal pocket for the γ branch like in the band calculation from [Samsel-Czekała et al. (2010)], whereas the two other band calculations proposed cylindrical pockets [Yu et al. (2011), Fujimori et al. (2015)]. In a weakly ferromagnetic state a spin splitting of the Fermi surface is expected. It could also be observed in the paramagnetic state, since non linearity in the Zeeman effect could occur in the vicinity of the critical pressure. The observed quantum oscillation signal must come from single spin bands. The two pockets γ and β must belong to the minority band since they vanish under magnetic field at $H_4 = 16$ T.

While only a small amount of the Fermi surface have been observed in quantum-oscillation experiment, the different bandstructure-calculation studies show agreement only on few pockets of the Fermi surface. It points out the difficulty of both high quality sample growth and band calculations for the ferromagnetic superconductor UCoGe. A key challenge in the-

ory is now to take into account the feedback between the polarization and the Fermi surface to model the influence of the magnetic field on the electronic structure.

4.3.4 Discussion on Fermi surface evolution through the critical pressure

At zero field a spin splitting of the band occurs in the ferromagnetic state and is absent in the paramagnetic state. The ferromagnetic correlations vanish under a magnetic field of $H_S \approx 1$ T along the easy magnetization axis c as discussed in section 3.2.2. The Hall effect as a function of field at 1 K at ambient pressure in figure 4.8 does not show any anomaly around H_S, suggesting a continuous evolution of the Fermi surface from the ferromagnetic state to the polarized paramagnetic state. The measurement reported in this thesis shows a smooth and small evolution of the Fermi surface through this crossover under a magnetic field of 5 T applied along the easy magnetization axis c. The comparison with bandstructure calculations shows the similarity of the observed Fermi surface above 5 T and the Fermi surface in the paramagnetic state. A recent Hall effect study under hydrostatic pressure suggests that the Fermi surface evolves also continuously from the paramagnetic state to the polarized paramagnetic state under a magnetic field 5 T applied along the easy magnetization axis c [S. Araki, private communication]. So our measurement shows that the Fermi surface pocket γ and β of UCoGe are slightly affected by the spontaneous polarization at the ferromagnetic transition. So it rules out the possibility of a drastic change in the bandstructure at this transition at it was predicted by [Samsel-Czekała et al. (2010)].

The A coefficient as a function of pressure reported in figure 3.12(b) shows that the enhancement of the effective mass at the critical pressure can be observed only below $H_S = 1$ T. As a consequence the evolution of the effective masses measured in the quantum oscillations experiment above 5 T would not be affected by the variation of magnetic correlations. The two small Fermi surface pockets detected in the quantum oscillations experiment show a small decrease of their average effective mass in the *ab* plane through the critical pressure. Moreover the initial slope of the upper critical field in UCoGe for magnetic field applied along the hard axis a and b do not show any change of the average Fermi velocity in the *bc* and *ac* planes (see chapter3) [Slooten et al. (2009)]. Thus the effective mass study suggests also a continuity through the critical pressure from the ferromagnetic state to the paramagnetic state.

While the Fermi-surface change at an antiferromagnetic transition is due to the change of the magnetic-Brillouin zone, no Brillouin-zone change is expected at a ferromagnetic transition. Thus the Fermi surface change at the ferromagnetic transition comes only from

the splitting of the bands in the ferromagnetic state. The two other ferromagnetic superconductors UGe_2 and URhGe show a Fermi surface reconstruction at the magnetic quantum phase transition. In UGe_2 criticality is also induced by pressure and the Fermi surface reconstruction was observed with dHvA [Terashima et al. (2001)Settai et al. (2002)]. In URhGe the quantum criticality is induced by magnetic field applied along the hard magnetization axis b. A Fermi surface reconstruction occurs at the quantum phase transition as detailed in chapter 5 [Yelland et al. (2011), Aoki et al. (2014b), Gourgout et al. (2016)]. Contrary to the two other ferromagnetic superconductors, UCoGe would show a rather small Fermi surface change at the magnetic transition, which affects slightly the γ and β pockets. This difference must be related to the strong difference in the spontaneous magnetization between these compounds. Indeed $M_0(\text{UCoGe}) = 0.05\ \mu_B/\text{U}$ is much smaller than $M_0(\text{URhGe}) = 0.4\ \mu_B/\text{U}$ and $M_0(\text{UGe}_2\text{-FM1}) = 1\ \mu_B/\text{U}$ [Huy et al. (2008),Aoki et al. (2001),Pfleiderer and Huxley (2002)], so the polarization of the bandstructure in UCoGe is less strong than in the two other ferromagnetic superconductors. An important difference can be noticed between the phase diagram of UGe_2 and UCoGe. While the superconducting temperature in UCoGe is continuous at p_c, superconductivity is excluded from the paramagnetic state in UGe_2 [Saxena et al. (2000)]. This properties of UGe_2 was explained by the Fermi surface reconstruction at the transition [Sandeman et al. (2003)]. So the absence of discontinuity in the superconducting temperature in UCoGe at the critical pressure suggests also that the Fermi surface in UCoGe is slightly affected by the magnetic transition.

4.4 Conclusion on the Fermi surface of UCoGe

UCoGe is a heavy fermion system with nearly flat bands close to the Fermi level. The polarization of its Fermi surface under magnetic field along the easy magnetization axis c leads to Fermi-surface instabilities. Four small and heavy Fermi-surface pockets α, β, γ and ω were detected at zero pressure. The pockets β and γ are affected by Fermi-surface instabilities at $H_1 = 4$ T and $H_2 = 9$ T and vanish in a Lifshitz transition at $H_4 = 16$ T. The pocket ω vanishes at a second Lifshitz transition at $H_5 = 21$ T. the β and γ Fermi surface pockets show a smooth evolution with hydrostatic pressure through the critical pressure $p_c \approx 1$ GPa under magnetic field above 5 T. This results suggests that the Fermi surface change at the critical pressure $p_c \approx 1$ GPa would be a small band splitting without a major Fermi surface reconstruction. It would explain the continuity of the superconducting transition temperature and the upper critical field behavior through the critical pressure discussed in chapter 3.

New bandstructure calculation studies are needed for a better understanding of the electronic structure in UCoGe. A challenge would be to calculate its Fermi surface evolution under magnetic field. Further quantum oscillations experiment are needed to detect the other pockets of the Fermi surface and characterize more precisely the Fermi surface transitions. The direct observation of the bandstructure change in UCoGe at the Curie temperature at ambient pressure in ARPES would be interesting for the study of the interplay between the Fermi surface and the ferromagnetic transition. The observation of quantum oscillations under a magnetic field along the hard magnetization axis *a* and their study under hydrostatic pressure through the critical pressure could also be interesting. While UCoGe is famous for the microscopic coexistence of ferromagnetism and superconductivity, this study shows that it is also an interesting compound to study field induced Lifshitz transitions.

Chapter 5

Fermi surface study of the ferromagnetic superconductor URhGe

Résumé en français

URhGe est ferromagnétique en dessous de $T_C = 9$ K et il est un supraconducteur ferromagnétique en dessous de $T_{sc} = 0.25$ K. Des mesures de magnétorésistance avec différentes directions de champ magnétiques ont permis l'obtention de nouveaux résultats sur les fluctuations magnétiques et la surface de Fermi. Les oscillations Shubnikov-de Haas ont révélé trois poches lourdes de la surface de Fermi α, β et γ. Les mesures de magnétorésistance ont monté qu'un champ magnétique supérieur à $H_S = 5$ T selon l'axe facile d'aimantation c fait disparaître les fluctuations magnétique et que la polarisation des bandes peur entrainer des changements de comportement de la résistivité. Lorsque le champ magnétique est orienté selon l'axe b, il entraîne une transition de phase quantique du premier ordre à $H_R \approx 12$ T. Elle consiste en une réorientation des moments magnétiques et une reconstruction de la surface de Fermi. Cette transition devient une évolution continue, lorsque le champ est écarté de l'axe c vers l'axe b, qui a été caractérisée par des mesures de magnétorésistance dans le plan bc. Enfin la surface de Fermi au-delà de la transition à $H_R \approx 12$ T a été caractérisée par des mesures d'oscillations quantiques.

Abstract

URhGe is a ferromagnetic superconductor with a ferromagnetic transition $T_C = 9$ K and a superconducting transition $T_{sc} = 0.25$ K. Its magnetic fluctuations and Fermi surface properties were studied with magnetoresistance measurements for various field directions up to

34 T. Three heavy Fermi-surface pockets α, β and γ were detected by Shubnikov-de Haas oscillations. The magnetoresistance along the easy magnetization axis c shows the suppression of magnetic fluctuations at $H_S = 5$ T and anomalies due to the polarization of the bands. Under magnetic field along the b axis, a first order magnetic moment reorientation with a Fermi surface reconstruction was previously reported at $H_R \approx 12$ T. The crossover line starting from this first order transition is followed under magnetic field in the bc plane in this chapter. The Fermi surface above the transition at $H_R \approx 12$ T is characterized from quantum oscillations.

5.1 Introduction to the ferromagnetic superconductor URhGe

5.1.1 Magnetic properties

Only two heavy fermion systems show the microscopic coexistence of ferromagnetism and superconductivity at ambient pressure : URhGe and UCoGe. UCoGe was discussed in detail in the two previous chapters. Both compounds have the same orthorhombic TiNiSi structure as discussed in chapter 3 and shown in figure 3.1. The Curie temperature, spontaneous magnetization and superconducting transition temperature of URhGe are $T_C = 9$ K, $M = 0.4\mu_B$/U and $T_{sc} = 0.25$ K [Aoki et al. (2001)]. URhGe seems to be located further away from the quantum criticality than UCoGe. However URhGe shows a strong heavy fermion behavior with the Sommerfeld coefficient value : $\gamma = 160$ mJ.mol^{-1}.K^{-2}.

The magnetization of URhGe is represented in figure 5.2 for magnetic field applied along the three crystallographic axis [Hardy et al. (2011)]. The spontaneous magnetization $M = 0.4\mu_B/U$ is along the c axis. a is a hard magnetization axis with a low magnetic susceptibility. Under magnetic field applied along the b axis the magnetic susceptibility is much bigger than for magnetic field along the a or the c axis and the increase of magnetization with field gets faster around $H_R = 12$ T. Neutron scattering experiments were performed on URhGe under magnetic field applied along b axis [Lévy et al. (2005)]. The total magnetization and the magnetization component along the b axis are represented as a function of magnetic field in figure 5.3. It shows the reorientation of magnetic moment from the c axis toward the b axis at H_R. Thus the spontaneous magnetization along the c axis is suppressed at H_R. Torque and Hall effect measurements show an hysteresis at this transition [Lévy et al. (2009), Aoki et al. (2014b)] indicating a first order behavior. It can be noticed, that this reorientation occurs, when the induced magnetization along the b axis is comparable to the spontaneous magnetization along the c axis. The field temperature phase diagram of URhGe for magnetic field applied along the b axis was drawn by magnetization measurements and

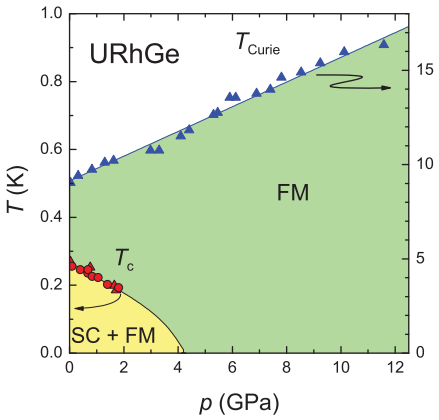

FIG. 5.1 Pressure-temperature phase diagram of URhGe. T_{Curie} and T_c stand for the Curie temperature and the superconducting transtition temperature, which are called T_C and T_{sc} in this thesis. This phase diagram was determined from ac calorimetry and resistivity measurements [Hardy et al. (2005), Miyake et al. (2009)].

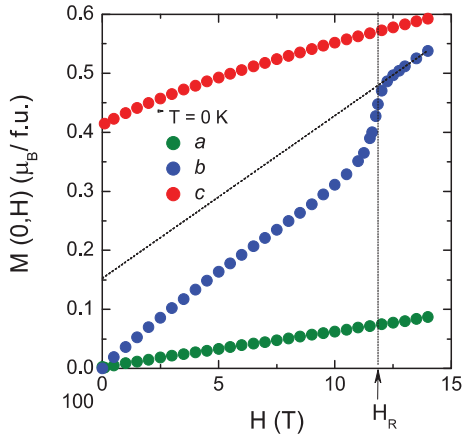

FIG. 5.2 Magnetization of URhGe extrapolated down to zero temperature as a function of magnetic field applied along the three crystallographic axis [Hardy et al. (2011)].

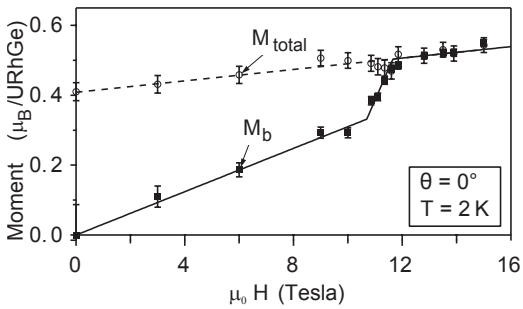

FIG. 5.3 Magnetization along the *b* axis and the total magnetization as a function of magnetic field applied along the *b* axis [Lévy et al. (2005)].

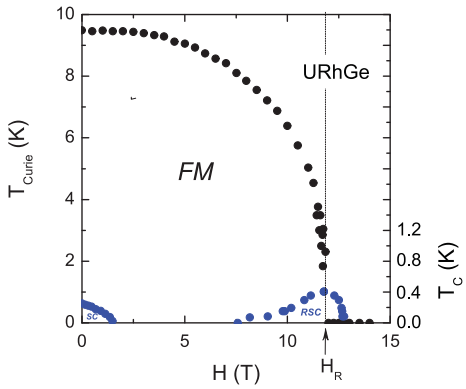

FIG. 5.4 Field temperature phase diagram of URhGe for magnetic field applied along the *b* axis [Hardy et al. (2011)]. H_R, *SC* and *RSC* stand respectively for reorientation field, superconductivity and reentrant superconductivity.

is reported in figure 5.4[Hardy et al. (2011)]. The Curie temperature T_C decreases with magnetic field and vanishes at $H_R = 12$ T. This phase diagram was also determined by resistivity and ac calorimetry [Aoki et al. (2011b)], ^{73}Ge NMR [Kotegawa et al. (2015)] and recently by thermopower [Gourgout et al. (2016)]. The tricritical point, where the transition changes from second to first order was localized around 4 K by NMR and 2 K by thermopower. The

microscopic origin for the first order magnetic moment reorientation is still under debate. It may be due to a change of the magneto-crystalline energy linked to the action of the exterior field on the crystal field. Another possibility is a Fermi surface change, which induces a drastic change in the inter-site ferromagnetic interactions.

5.1.2 Reentrant superconductivity

One of the most surprising property of URhGe is the reentrance of superconductivity under magnetic field around the magnetic moment reorientation H_R. The superconducting temperature T_{sc} as a function of magnetic field applied along the hard axis b is represented in figure (5.4). Superconductivity is suppressed at $H_{c2} \approx 1.5$ T and reappears between 8 T and 13 T. The critical temperature is maximum at $H_R \approx 12$ T : $T_{sc}(H_R) = 0.4$ K and it is even higher than at zero field $T_{sc}(H = 0) = 0.25$ K. An enhancement of the effective mass $m^\star$ at H_R was observed from resistivity [Miyake et al. (2008)] and specific heat measurements [Hardy et al. (2011)]. It suggests an enhancement of the magnetic fluctuations around the reorientation at H_R. This enhancement was directly observed by a ^{73}Ge NMR study on URhGe [Kotegawa et al. (2015)] and by a ^{59}Co NMR study performed on $URh_{0.9}Co_{0.1}Ge$ [Tokunaga et al. (2015)]. The reentrant superconductivity was explained qualitatively by this enhancement of magnetic fluctuations [Miyake et al. (2008)]. Recently a phenomenological description of the field temperature phase diagram has been given on the basis of a Landau theory [Mineev (2015a)].

The magnetic moment reorientation was followed in the *ab* and *bc* planes by resistivity measurements as reported in figure 5.5 [Lévy et al. (2009)]. The reorientation occurs at a constant value of the b axis component of the magnetic field. Superconductivity can still be observed around H_R, when H_R is shifted to 28 T. Torque measurements confirmed, that the transition stay first order in the *ab* plane [Lévy et al. (2009)]. On the contrary for magnetic field in the *bc* plane, torque, Hall effect and NMR measurements showed that the first order transition becomes a crossover when the magnetic field is tilted of few degrees from the b axis toward the c axis [Lévy et al. (2005), Aoki et al. (2014b), Tokunaga et al. (2015)]. While torque and Hall effect measurements suggest, that the transition is already a crossover at 3°, a quantum critical end point where the transition changes from first order to a crossover was localized at 5° by NMR [Tokunaga et al. (2015)]. When a magnetic component is added along the easy magnetization axis c, the b axis component at the magnetic moment reorientation is enhanced. Superconductivity can be observed in the *bc* plane up to 6° from the b axis.

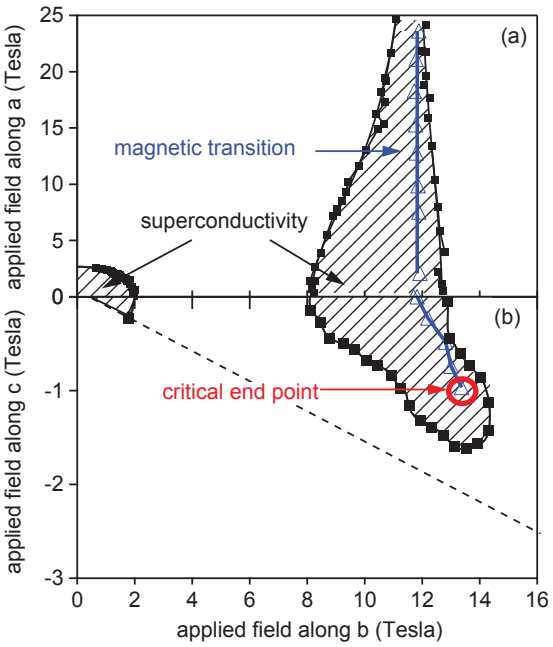

FIG. 5.5 Superconductivity and magnetic transition for magnetic field applied in the (ab) and (bc) planes [Lévy et al. (2009)]. The hatched ares correspond to the superconducting state at 40 mK. The blue line with triangles is the reorientation field at T=500 mK. The red circle is the expected quantum critical end point. These results were obtained by resistivity measurements.

5.1.3 Fermi-surface investigation

The bandstructure in the ferromagnetic state of URhGe was first calculated within the local spin density approximation (LSDA) [Shick (2002)]. The authors predicted the ferromagnetic component along the c axis and an additional antiferromagnetic component along the a axis, which was not observed in neutron scattering [Lévy et al. (2005)]. The Fermi surface of URhGe in the paramagnetic state was calculated by H. Yamagami and published in [Fujimori et al. (2014)]. The bandstructure was calculated from relativistic linear augmented-plane-wave within the local density approximation (LDA). U $5f$ electrons were treated as itinerant electrons. The bandstructure of URhGe was also measured with APRES technique [Fujimori et al. (2014)]. The bandstructure, the calculated density of states and the ARPES signal are represented as a function k vector along S-Y-S direction and energy in figure 5.6(a). The bandstructure calculation and the ARPES experiments show some agreement. The bandstructure contains four bands close to the Fermi level. The main contribution to these bands comes from $5f$ electrons. This result confirms the heavy fermion behavior of URhGe. While the bandstructure calculation show two electron pockets around the S point coming from the bands FS71 and FS72, at least one of them was confirmed by ARPES experiment. The Fermi surface predicted by the calculation is represented in figure 5.6(b).

The electron pocket FS72 is a cylinder along c axis. The other electron pocket FS71 is connected to itself at the Brillouin zone edge both along the a and c directions. The calculated bandstructure in figure 5.6(a) shows also a hole pocket around the Y point from the band FS69 and FS70. However the ARPES scan along Y-S-Y suggests, that this band stays below the Fermi level along this line. According to the calculations FS70 would give a large hole pocket in the center of the Brillouin zone and connected to itself along the b axis. ARPES measurements were also performed along U-Z-U and Γ-X-Γ directions, however they could not resolve the bands in the vicinity of the Fermi level.

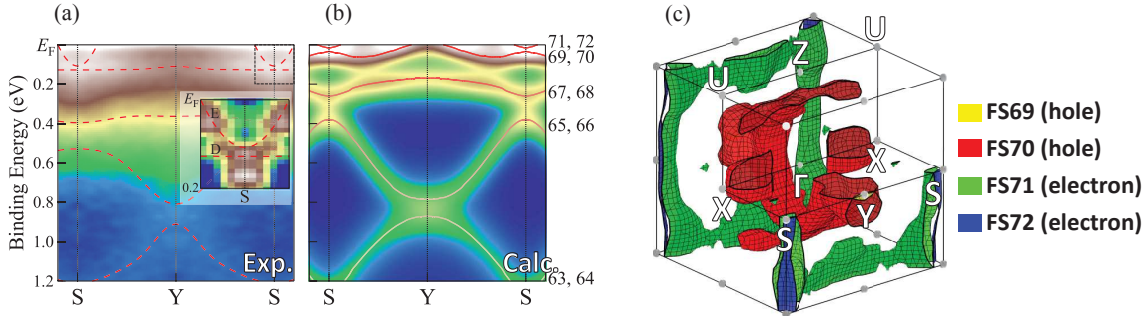

FIG. 5.6 (a) ARPES scan of URhGe at 20 K along the S-Y-S line [Fujimori et al. (2014)]. The inset is a zoom on the area delimited by the black square. (b) Calculated bandstructure and density of states along the S-Y-S direction. (c) Calculated Fermi surface of URhGe.

To study the change in the bandstructure at the ferromagnetic transition Fujimori et al. measured ARPES above Curie temperature at 20 K and below at 6 K. The difference between the two ARPES scans suggests a small change in the bandstructure between the ferromagnetic and the paramagnetic state.

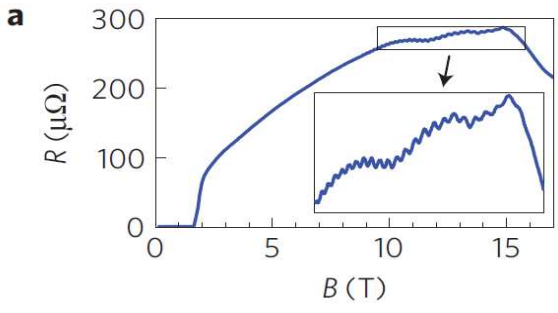

FIG. 5.7 URhGe resistivity at 20 mK as a function of the magnetic field applied at 10° from the b axis toward the c axis. Quantum oscillations vanish at $H_R(10°) = 15.5$ T.

No detailed quantum-oscillation study in URhGe has been reported up to now. Only one Shubnikov-de Haas experiment was performed on URhGe [Yelland et al. (2011)]. Quantum oscillations were observed under magnetic field along the b axis below the magnetic-moment reorientation with the frequency $F \approx 600$ T. The magnetoresistance in URhGe

under magnetic field at 10° from the c axis toward the b axis are represented in figure 5.7. These oscillations vanish at the crossover $H_{co}(10^\circ) = 15.5$ T. This result suggests that a Fermi surface reconstruction occurs at $H_R = 12$ T under magnetic field along the b axis. E. Yelland et al. claim that, that the suppression of this Fermi surface pocket would be responsible for reentrant superconductivity. The orbital limit for the upper critical field would be enhanced by the reduction of the Fermi velocity of the electrons on this Fermi surface pocket. However it should be noted, that this Fermi surface pocket corresponds only to a small part of the Fermi surface, and it is hard to believe, that such a small band alone can count for superconductivity.

A Hall effect measurement with electrical current along the a axis and magnetic field along the b axis shows a sharp peak at H_R suggesting a Fermi surface change [Aoki et al. (2014b)]. Finally Seebeck effect measurements with electrical current along each crystallographic axis and magnetic field along the b axis show also clear anomalies at H_R indicating a Fermi surface change [Gourgout et al. (2016)].

5.1.4 Aim of this chapter

The aim of this study was to determine and characterize the Fermi surface of URhGe. Another issue was to study the effect on the Fermi surface of URhGe of magnetic polarization under magnetic field along the easy magnetization axis c and the effect of the magnetic moment reorientation H_R induced by a magnetic field along the hard magnetization axis b.

5.2 URhGe samples

The electrical resistivity was measured on three different URhGe samples, they will be referred as S1, S2 and S3 in the following. Their RRR, current direction, magnetic field direction and geometrical factor S/l are given in table 5.1. These samples were chosen for their high RRR indicating large mean free path. However their superconducting transitions show sample inhomogeneities and S3 does even not any show superconductivity at zero magnetic field. S2 and S3 were also used for a thermopower study on URhGe [Gourgout et al. (2016)].

Sample name	S1	S2	S3
RRR	50	36	36
T_{sc}(K)(R=0)	0.21	0.09	<0.02
current direction	b	b	a
field direction	c → a	c → b	c → b
S/l(cm)	0.027	0.014	0.0042

Table 5.1 Characteristics of the three URhGe samples measured in this study.

5.3 Effect of a magnetic field on URhGe

5.3.1 Magnetic polarization and the suppression of the ferromagnetic correlations

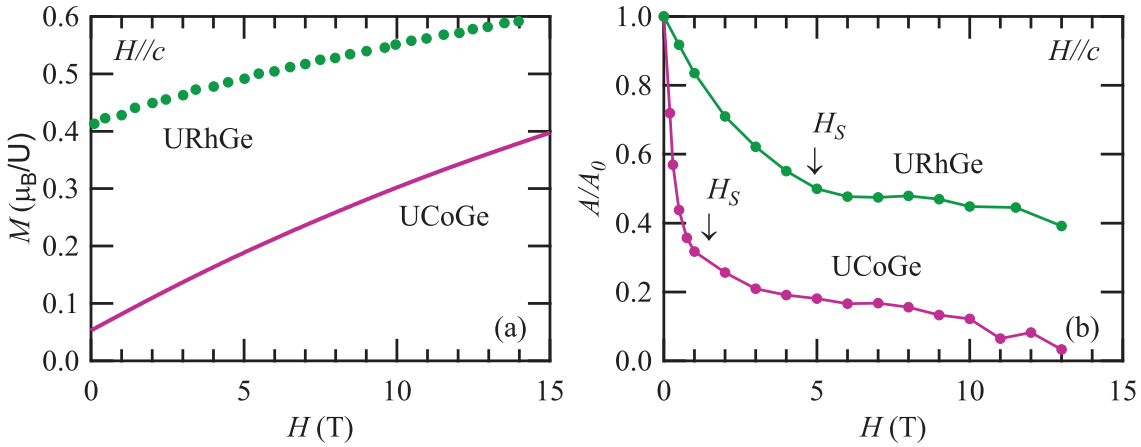

FIG. 5.8 (a) Magnetization as a function of magnetic field applied along the easy magnetization axis c in URhGe and UCoGe. The data were taken from [Hardy et al. (2011)] and Knafo et al. (2012)]. (b) A coefficient of resistivity renormalized by its value at zero field as a function of magnetic field applied along the c axis in URhGe S2 and UCoGe S2. The fits were performed just above the onset of superconductivity below 0.8 K for URhGe and below 1.2 K for UCoGe.

The magnetization of URhGe and UCoGe as a function of magnetic field for field along the c axis are represented in figure 5.8(a). The data were taken from references [Hardy et al. (2011)] and [Knafo et al. (2012)]. While the spontaneous magnetization in URhGe $M_0 = 0.4\mu_B/U$ is much bigger than in UCoGe $M_0 = 0.05\mu_B/U$, the magnetic susceptibility in URhGe$\chi = dM/dH \approx 0.015\mu_B/U/\mathrm{T}$ is smaller than in UCoGe with $\chi \approx 0.025\mu_B/U/\mathrm{T}$. As a consequence the effect of magnetic polarization on the Fermi surface in URhGe is expected to be weaker than in UCoGe. Figure 5.8(b) shows the field dependence of the A coefficient of the resistivity in URhGe and UCoGe for field along the easy magnetization

axis c normalized to the value at $H = 0$. The measurements were performed respectively on sample URhGe S2 and UCoGe S2. The A coefficient is strongly suppressed at low field and then decreases slower. The field, where the slope changes H_S is expected to correspond to the field where ferromagnetic fluctuations and ferromagnetic correlations are suppressed as discussed for UCoGe in section 3.2.2. This field is much higher in URhGe ($H_S \approx 5$ T) than in UCoGe ($H_S \approx 1$ T). Similar results for URhGe were obtained previously from specific heat calculation based on magnetization measurements and Maxwell relations [Hardy et al. (2011)]. The temperature dependence of the upper critical field for magnetic field along the c axis can be well fitted within the pure orbital limit with $H_{c2}(0) = 0.6$ T [Hardy and Huxley (2005)] . It confirms, that magnetic fluctuations in URhGe survive far above $H_{c2}(0) =$ 0.6 T. These results show that ferromagnetic fluctuations in URhGe are more robust under magnetic field that in the other ferromagnetic superconductor UCoGe.

5.3.2 Anomalies in the magnetoresistance of URhGe induced by a magnetic field along the easy magnetization axis c.

The magnetoresistance of URhGe at $T = 30$ mK for current along the b axis and magnetic field along the easy magnetization axis c in sample 1 and 2 is represented in figure 5.9(a) and 5.9(b) respectively. Both samples show superconductivity below 0.6 T. Above the superconducting transition, the resistivity increases with magnetic field up to a shoulder at $H_k \approx 5.5$ T. This shoulder ends up at $H'_k = 7.5$ T and above the magnetoresistance increases with magnetic field. This increase gets faster after a kink at $H^\star \approx 12$ T. The temperature dependence of magnetoresistance in sample S2 under magnetic field along the c axis is represented in figure 5.9(c). It shows that both anomalies vanish around 1 K without any shift in field.

The magnetoresistance in the ac plane in sample 1 and in the bc plane in sample 2 are represented in figure 5.9(a) and 5.9(b) respectively. The angular dependence of the anomalies in ac and bc planes is represented in figure 5.9(d). In the ac plane the transverse magnetoresistance as a function of angle θ shows a broad maximum around 50°. The anomaly at H_k is shifted to higher field following a $1/\cos\theta$ law and thus H_k depends only on the c axis component of the magnetic field. In the bc plane the magnetoresistance increases with the angle from the transverse configuration at c axis to the longitudinal configuration at b axis. Reentrant superconductivity is observed for magnetic field along the b axis between 9 T and 13 T. H_k becomes more and more marked with clear maximum and minimum at 25°. This anomaly is shifted to higher magnetic field much faster than a $1/\cos$ law. $H^\star$ was followed only in the bc plane and it is shifted to lower field with the rotation in the bc plane. At 64°

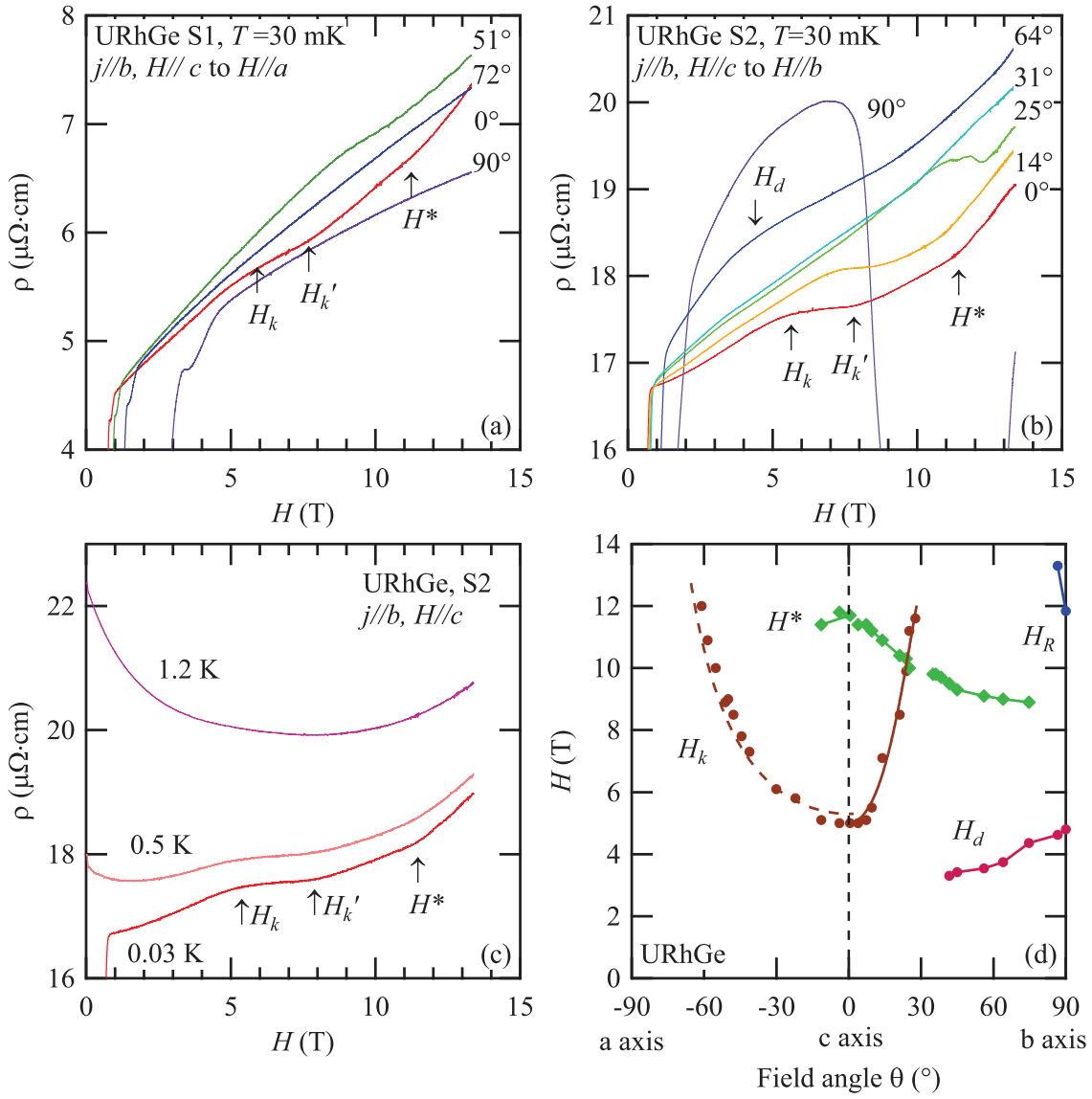

FIG. 5.9 (a) Magnetoresistance at 30 mK of URhGe S1 with current along the *b* axis and magnetic field in the *ac* plane. The arrows indicate anomalies on the $H//c$ curve : $H_k \approx 5.5$ T, $H_{k'} \approx 7.5$ T and $H^\star \approx 12$ T. (b) Magnetoresistance of URhGe S2 with current along the *b* axis and magnetic field in the *bc* plane. A change of slope at $H_d \approx 4$ T is reported on the 64° curve.(c) Temperature dependence of URhGe S2 magnetoresistance for H//c.(d) Angular dependence of the anomalies H_k and $H^\star$, H_d and the magnetic moment reorientation field H_R. The dashed line in *ac* plane is a fit with a $1/\cos\theta$ law. Solid lines are guides for the eye. The reorientation field H_R was defined as the maximum of the resistivity at 0.5 K as discussed in reference [Lévy et al. (2005)].

from the *c* axis toward the *b* axis, the resistivity shows another kink with a reduction of its slope at $H_d \approx 4$ T. It is shifted to higher magnetic field, when the field is rotated toward the *b* axis.

No anomaly in the magnetization at H_k or $H^\star$ are reported in figure 5.2. The Hall effect at 2 K does not show any anomaly at H_k and $H^\star$[Aoki et al. (2014b)]. The anomalies in the magnetoresistance may correspond to Fermi surface instabilities without magnetic phase transition like the anomalies at H_1 and H_2 in UCoGe reported in chapter 4. Like the anomalies in UCoGe, H_k vanishes with temperature and is shifted to higher field with a $1/\cos\theta$ law when the magnetic field is tilted toward the hard a axis. The H_k and $H^\star$ anomalies would be induced by the magnetic polarization. They occur at $M = 0.5\ \mu_B$/U and $M = 0.55\ \mu_B$/U. However it is important to notice that the first anomaly H_k in URhGe occurs just above H_S the field where ferromagnetic fluctuations and correlations collapse (figure 5.8). So the anomaly at H_k may be related to the change from the ferromagnetic state to a polarized paramagnetic state. While in UCoGe the effect of the collapse of ferromagnetic fluctuations and of changes due to the increases of the magnetic polarization are well separate (see chapter 3 and 4), they could occur in the same field range in URhGe.

5.3.3 Crossover between the ferromagnetic and the polarized paramagnetic state in the bc plane.

The magnetoresistance of URhGe was measured under high magnetic field up to 34 T in the LNCMI Grenoble. The magnetoresistance of sample S3 with current along the a axis and magnetic field in the bc plane is represented in figure 5.10. For a magnetic field applied along the b axis zero resistivity has been observed between 10.5 T and 12.5 T. The first order transition at $H_R = 12$ T is hidden by the reentrant superconductivity (RSC). At 4° from the b axis toward the c axis the RSC is fully suppressed and the magnetoresistance increases steeply at $H_{co} = 13$ T indicating a crossover. This crossover was defined at the maximum of $d\rho/dH$ and its angular dependence is represented in figure 5.10(b). It is shifted to higher field with angle faster than a $1/\cos$ law and it was followed up to 48° from the b axis. This crossover becomes broader by rotating the sample from the b axis toward the c axis. The Shubnikov-de Haas measurement reported in figure 5.7 shows, that at 10° this crossover is also a Fermi surface change and it was described in term of a Lifshitz transition [Yelland et al. (2011)]. So this crossover line may correspond to the Fermi surface change from the Fermi surface of a polarized state along the c axis toward the one of a polarized state along the b axis.

Under magnetic field along the c axis, the magnetoresistance of URhGe S3 decreases with field up to a broad minimum around 5 T and then increases with magnetic field. It does not show the two anomalies H_k and $H^\star$ observed in the two other samples. This difference

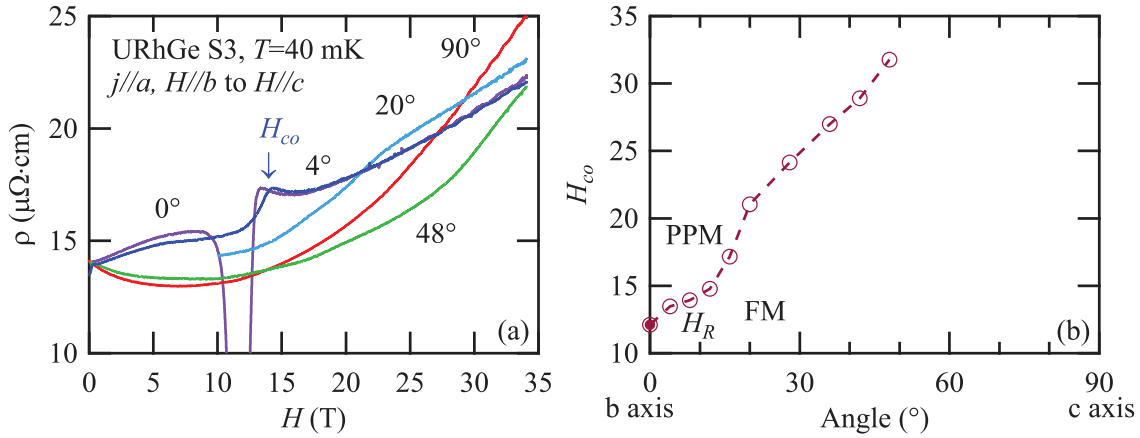

FIG. 5.10 (a) Magnetoresistance of sample 3 at 40 mK as a function of magnetic field applied in the *bc* plane. The crossover between the ferromagnetic state (FM) with a spontaneous magnetization along *c* axis and polarized paramagnetic state (PPM) is denoted by the arrow on the 4° curve. (b) Angular dependence of the crossover field H_{co}. It was defined at the maximum of $d\rho/dH$. The full circle at $H//b$ correspond to the first order transition at H_R defined as the maximum of 450 mK resistivity and measured on the same sample.

may be due to a lower sample quality or to the difference of current direction. Electrical current was applied along the *b* axis in sample S1 and S2 and along the *a* axis in URhGe S3.

5.4 Quantum oscillations study in URhGe

5.4.1 Quantum oscillations in a superconducting magnet ($H < 13.4$ T)

Shubnikov-de Haas oscillations were detected in URhGe S1 between 40° and 65° from the *c* axis toward the *a* axis. They are represented as a function of inverse magnetic field in figure 5.11(a) for different field directions. The angular dependence of their frequency is represented in figure 5.11(b). The detected pocket is relatively small with a frequency increasing with angle from 200 T to 270 T on this angle interval. This pocket will be referred as the γ branch. The quantum-oscillation frequency does not show any abrupt change when H_k anomaly moves in the FFT interval and no field dependence of quantum oscillations was observed even when H_k is at the middle of quantum-oscillation signal. Thus H_k is not related to some change in the observed Fermi surface pocket in difference to measurements on UCoGe reported in section 4.2.2. If a Fermi surface change occurs at H_k, it does not affect this pocket. Thus H_k may be related to a change in the magnetic correlations without a clear Fermi surface change.

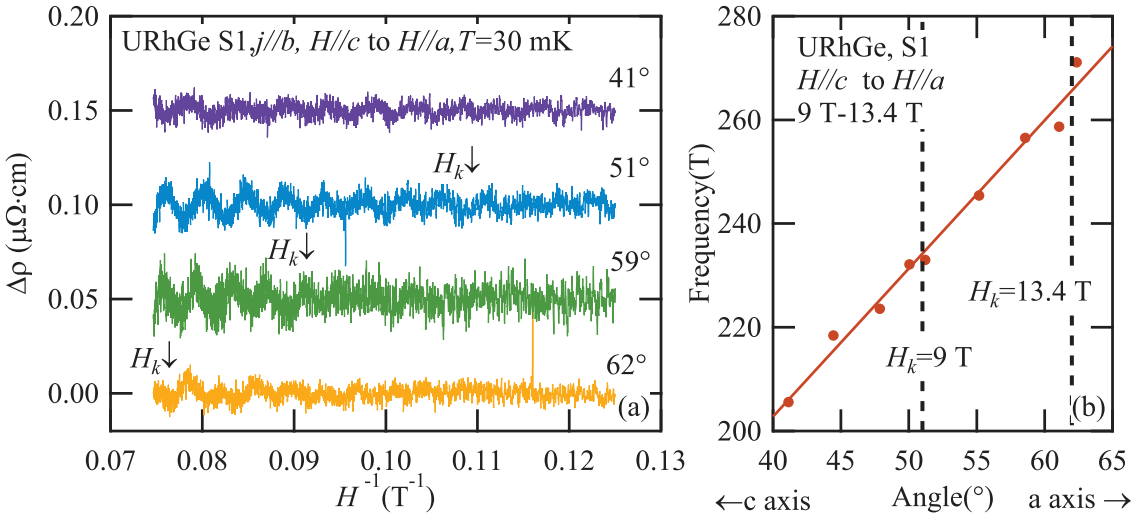

FIG. 5.11 (a)Shubnikov de Haas signal on URhGe S1 as a function of inverse magnetic field for different field directions in the *ac* plane. The arrows indicate the field H_k, where an anomaly was observed on the resistivity data. (b) Angular dependence of the quantum oscillations frequency calculated with FFT on a 9 T-13.4 T interval. The solid line is a guide to the eye. The dashed lines represent the angle where H_k anomaly enters the FFT interval and the angle where it goes above it.

5.4.2 Quantum oscillations under high magnetic field.

Quantum oscillations were also detected under high field magnetic field along the *b* and the *c* axis in the magnetoresistance of sample S3 represented in figure 5.10. Similar oscillations were observed in sample S1 under magnetic field along the *c* axis. The oscillating part of the magnetoresistance is represented as a function of inverse magnetic field in figure 5.12(a) for both samples and different field directions. The signal from sample S1 is more noisy than for sample S3. This is partially due to a less favorable sample geometry. The frequency of these quantum oscillations observed under magnetic field along the *c* axis is around 1150 T. This branch will be referred as α branch. The α branch was not detected in the Kelvinox system with ($H < 13.4$ T). However it was detected between 12 T and 17 T by a simultaneous study with a frequency around 1200 T [Lithgow (2015)]. Another Fermi surface pocket was observed for magnetic field along the *b* axis with $F_\beta \approx 600$ T. This branch will be referred as β branch. Quantum oscillations with the same frequency were also observed in the Seebeck effect on the same sample and are represented in figure 5.12(b) [Gourgout et al. (2016)]. The Seebeck effect shows a good agreement with SdH results and the oscillations appear already above 22 T.

The angular dependence of the quantum oscillation frequencies in the *bc* and *ac* plane is represented in figure 5.13. It is determined in samples S3 and S1 respectively. The

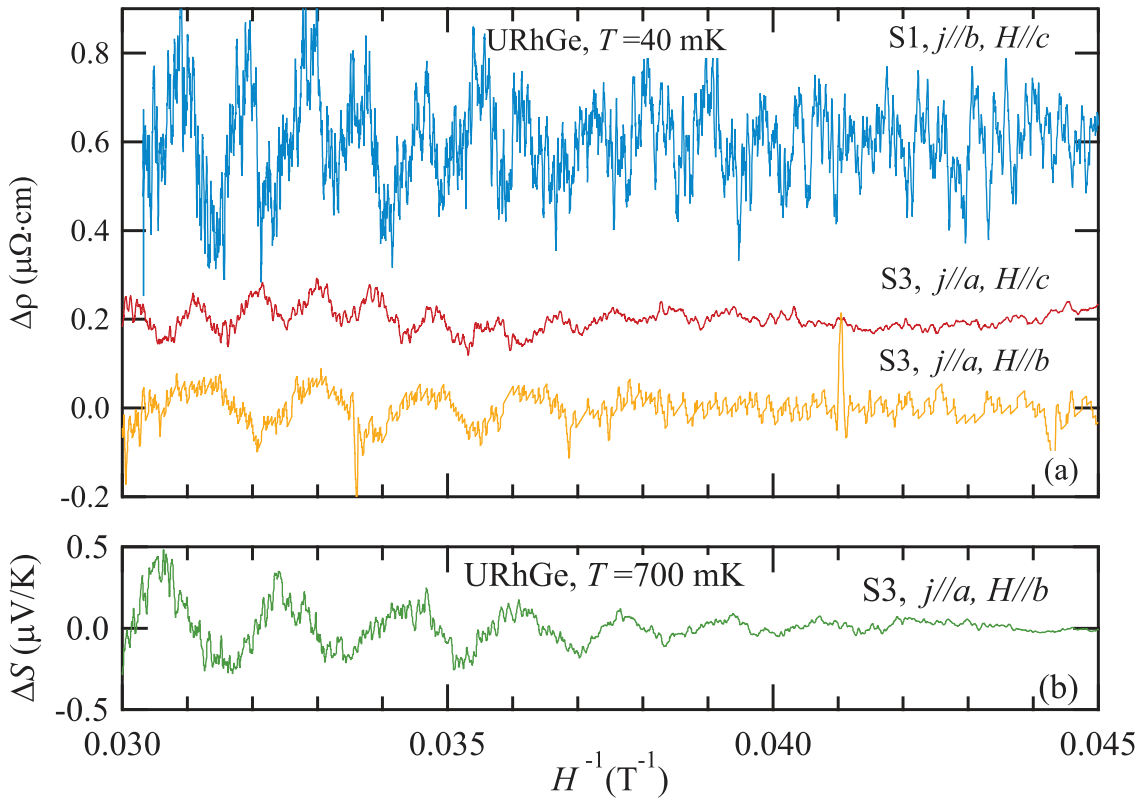

FIG. 5.12 (a) Oscillating part of the resistivity as a function of inverse magnetic field at 40 mK for different sample, current and field directions. (b) Oscillating part of the Seebeck effect as a function of inverse magnetic field at 700 mK.

frequency of the α branch-quantum oscillation increases with angle when the magnetic field is tilted from the c axis toward the a or the b axis. The signal was lost around 20° for both directions. The α branch must be an ellipsoid or a cylinder along the c direction. The β frequency increases when the magnetic field is tilted from the b axis toward the c axis and the oscillation signal disappears above 16°.

A cylinder along the c axis around the S point was predicted by band calculations and observed in ARPES as reported in figure 5.6 [Fujimori et al. (2014)]. The radius of this cylinder along S-Y-S is $k_F = 1$ nm^{-1} from band calculations and $k_F = 1.8$ nm^{-1} from ARPES. Assuming that the α orbit is circular, quantum oscillations experiment gives : $k_F = 1.9$ nm^{-1} in agreement with ARPES results. bandstructure calculations and ARPES experiments were both performed at zero field in the paramagnetic state. This agreement suggests that the Fermi surface of the polarized state below the Curie temperature and under a magnetic field along the c axis far above $H_S = 5$ T would be similar to the Fermi surface of the paramagnetic state.

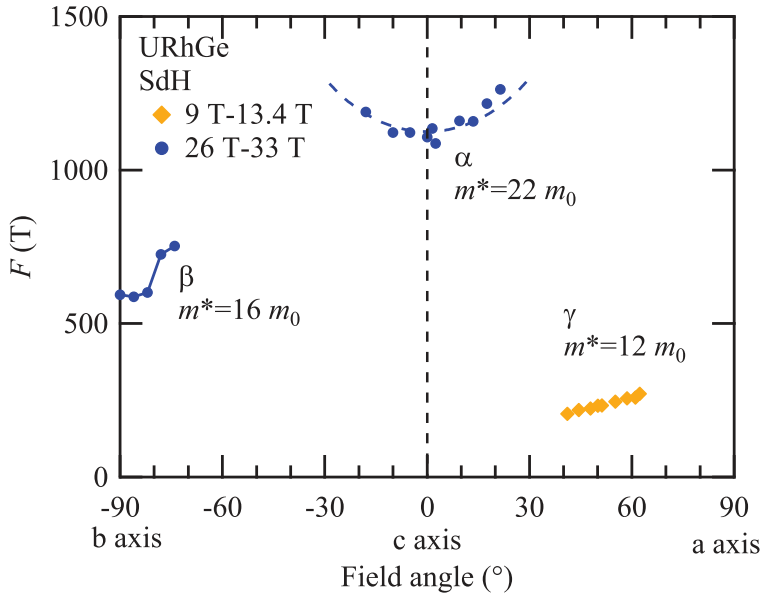

FIG. 5.13 Angular dependence of quantum oscillations frequencies in URhGe. The blue and orange symbols correspond respectively to data points obtained in the LNCMI Grenoble resistive magnet on the field interval 26 T<H<33 T and in the Kelvinox system on the interval 9 T<H<13.4 T. The dashed line for α branch is a fit assuming a cylindrical Fermi surface pocket.

The β branch is observed in the polarized state above the magnetic reorientation H_R. Its frequency is similar to the frequency of oscillations observed below H_R and represented in figure 5.7 [Yelland et al. (2011)]. While the Fermi surface observed below H_R is nearly spherical, the quantum oscillation frequency F_β observed above H_R increases with angle from the b axis. The Fermi surface of the polarized state along the b axis may be similar to the Fermi surface computed in the paramagnetic state and represented in figure 5.6. In this case the β branch could come from the orbit around the Y point of the hole Fermi surface pocket FS70.

5.4.3 Effective mass of the detected Fermi surface pockets

The temperature dependence of the quantum oscillations amplitude of the α branch at the c axis, the β branch at the b axis and the γ branch at 50° from the c axis toward the a axis are represented in figure 5.14. FFT were performed on the interval 26 T-34 T for the α and the β branch and 9 T-13.4 T for the γ branch. The amplitude of quantum oscillations renormalized by its extrapolation down to zero temperature is plotted as a function of the ratio of temperature and effective magnetic field H_{eff}. While the fits for α and γ branches are good, the temperature dependence of the amplitude of β branch quantum oscillations

is very noisy, due to the low signal-noise ratio and the small number of periods in the oscillation signal. The results of the fits are $m^\star_\alpha = 22 \pm 1 m_0$, $m^\star_\beta = 16 \pm 5 m_0$, $m^\star_\gamma = 12 \pm 1 m_0$. So the Fermi surface of URhGe would consist of heavy Fermi surface pockets. However a fit of the temperature dependence of the thermopower-oscillation amplitude gives a much lower effective mass value for the β branch : $m^\star = 7 m_0$ [Gourgout (2017)]. The difference of the effective mass seems to be bigger than the uncertainty of both measurements. The difference might be due to a temperature dependence of the effective mass, since the SdH was measured up 200 mK and the thermopower was only measured down to 450 mK.

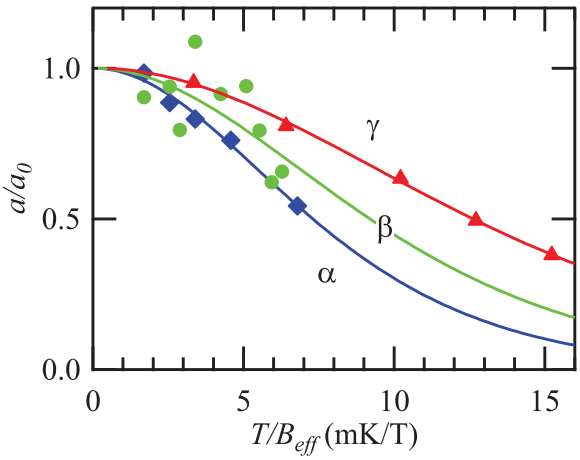

FIG. 5.14 Renormalized amplitude of the quantum oscillations as a function of the ratio between the temperature and the effective magnetic field. The magnetic field was applied along the c axis for the α branch, along the b axis for the β branch and at at 50° from the c axis toward the a axis for the γ branch. Solid lines are fits from the Lifshitz-Kosevic formula (1.35), they give $m^\star_\alpha = 22 \pm 1 m_0$, $m^\star_\beta = 16 \pm 5 m_0$ and $m^\star_\gamma = 12 \pm 1 m_0$.

The contribution to the specific heat of these bands can be estimated as explained in section 1.7.7. Assuming a spherical Fermi surface pocket with the frequency F=250 T for the γ branch, its contribution to the specific heat is $\gamma_\gamma \approx 2$ mJ.mol^{-1}.K^{-2}. Assuming that the α and β Fermi surface pockets are cylinders and comes only from one spin projection, their contributions to the specific heat can be estimated at $\gamma_\alpha = 9$ mJ.mol^{-1}.K^{-2} and $\gamma_\beta =$ 10 mJ.mol^{-1}.K^{-2}. These values are small compared to the Sommerfeld coefficient : $\gamma =$ 160 mJ.mol^{-1}.K^{-2}. Thus many parts of the Fermi surface of URhGe are still not detected.

5.4.4 Field dependence of quantum oscillations frequencies

The oscillations from the α and the β branches are not exactly periodic in $1/H$. FFT spectrum of α branch quantum oscillations in sample 3 for two different field intervals: 21 T$< H <$ 27 T and 24 T$< H <$ 31 T are represented in figure **??**(a). The field dependence of the quantum-oscillation frequency was drawn by performing FFT on a sliding window of 0.01T^{-1}. The FFT frequency is represented as a function of the inverse effective magnetic field $1/H_{eff}$ in figure **??**(b). $1/H_{eff}$ is defined at the center of FFT interval as discussed in section 1.7.3. The quantum oscillation frequency from the α Fermi surface pocket decreases

with magnetic field from 1180 T at 23 T down to 1100 T at 29 T. A field dependence of the quantum oscillation frequency was also observed for the β branch. Under magnetic field along the b axis FFT were performed on a 0.006 T^{-1} sliding window. The frequency is plotted as a function of the effective magnetic field in figure **??**(c). Both probes show that this quantum oscillation frequency decreases with magnetic field. The Seebeck effect oscillations were detected in a broader field range. Their frequency decreases from 670 T at 25 T down to 540 T at 31 T.

The reductions of the quantum oscillation frequencies with magnetic field is too small to be explained by the internal field in URhGe. It may come from the reduction of the Zeeman effect of a minority spin pocket or from the reinforcement of the Zeeman effect of a majority spin pocket as explained in section 1.7.2. The non linear Zeeman effect for the α pocket under magnetic field along the c axis must be a consequence of the strong polarization of the bands under high magnetic field. It confirms that the Fermi surface of URhGe can be easily affected by an external parameter such as the magnetic field. Thus the strong polarization of the Fermi surface under magnetic field along c axis leads to different consequences in UCoGe and URhGe. While it induces Lifshitz transitions in UCoGe, it leads to non linear Zeeman effect in URhGe.

On the contrary the non linear Zeeman effect for the β pocket under magnetic field along the b axis must be related to the proximity of the magnetic moment reorientation at $H_R = 12$ T. A similar non linear Zeeman effect was observed below $H_R = 12$ T [Yelland et al. (2011)]. This non linear Zeeman effect shows, that the Fermi surface change is not only localized at H_R but it is continuous. A similar continuous decrease of the quantum oscillation frequency with magnetic field was observed in UCoGe for the same field direction b [Aoki et al. (2011c)] and it could be due to the same mechanism.

5.5 Conclusion on URhGe

Under magnetic field along the easy magnetization axis c, the ferromagnetic fluctuations are suppressed at $H_S \approx 5$ T. Two anomalies were observed in the resistivity at $H_k = 5.5$ T and $H^\star = 11.5$ T and a Fermi surface pocket α is observed above 20 T. It shows a non linear Zeeman effect. The anomalies in the resistivity and this non linear Zeeman effect must be due to the strong polarization of the bands under high magnetic field along the c axis. Under magnetic field along the b axis, a magnetic moment reorientation with a Fermi surface reconstruction occurs at $H_R = 12$ T. A Fermi surface pocket β was observed above the magnetic moment reorientation. The first order magnetic phase transition at H_R becomes

a crossover when the magnetic field is tilted toward the *c* axis and is rapidly shifted to higher magnetic field.

Chapter 6

Microscopic study of the g factor anisotropy in URu_2Si_2

Résumé en français

URu_2Si_2 s'ordonne en dessous de $T_0 = 17.5$ K et devient supraconducteur à $T_{sc} = 1.3$ K. La nature de sa phase ordonnée est toujours inconnue et cette phase a été nommée : l'ordre caché. Ce chapitre discute seulement une propriété singulière de l'ordre caché, la forte anisotropie du facteur gyromagnétique g. Cette anisotropie a été étudiée macroscopiquement à partir du champ critique supérieur et microscopiquement à parir des oscillations quantiques pour les poches de surfaces de Fermi α, β et γ. Les deux techniques montrent une forte anisotropie entre l'axe c et le plan basal. Les oscillations quantiques montrent également une anisotropie dans le plan basal pour la poche α. L'effet Zeeman de la poche β est non linéaire et l'anisotropie du facteur g observée en est réduite sous champ. La poche légère λ de la surface de Fermi d'URu_2Si_2, qui a été découverte récemment est aussi caractérisée dans ce chapitre.

Abstract

URu_2Si_2 shows a hidden order state below $T_0 = 17.5$ K and unconventional superconductivity below $T_{sc} = 1.3$ K. The nature of the hidden order is still under debate. This chapter is focused on one specific property of the hidden order state, the strong g factor anisotropy. It was studied macroscopically from upper critical field measurements and microscopically from Shubnikov-de Haas experiments for the α, β and γ Fermi surface pockets. Both techniques show a strong g factor anisotropy between the c axis and the basal plane. The

Shubnikov-de Haas oscillations shows an additional anisotropy in the basal plane for the α Fermi surface pocket. The β branch shows non linear Zeeman effect leading to a reduction of the observed g factor anisotropy under magnetic field. The light Fermi surface pocket λ recently discovered in URu_2Si_2 is also characterized in this chapter.

6.1 Brief introduction to URu_2Si_2

6.1.1 Hidden order state and unconventional superconductivity

URu_2Si_2 shows a second order phase transition at 17.5 K with a clear signature in specific heat indicating a reduction of the entropy [Palstra et al. (1985)]. From early neutron-scattering experiment an antiferromagnetic ordered phase with small magnetic moments of $0.03\mu_B$ has been concluded [Broholm et al. (1987)]. However, the large entropy loss at T_0 is in contrast to a small moment antiferromagnetic order. Furthermore, an early muon spectroscopy experiment excluded the antiferromagnetic order [MacLaughlin et al. (1988)]. The present understanding is that the small magnetic moment is not intrinsic to the hidden order phase, but related to the antiferromagnetic state, which appears for $p > 0.5$ GPa. Despite intense research since its discovery, the microscopic nature and the order parameter of the hidden order are still not identified. The investigation of the hidden order during these thirty years is discussed in [Mydosh and Oppeneer (2011)] and a recent review is presented in [Mydosh and Oppeneer (2014)]. URu_2Si_2 shows also unconventional superconductivity inside the hidden order state with $T_{sc} \approx 1.3$ K [Palstra et al. (1985)]. The paring mechanism and the gap symmetry in this superconducting state are also unclear. A recent specific heat study suggested a chiral d-wave superconductivity [Kittaka et al. (2016)].

The temperature pressure phase diagram of URu_2Si_2 is represented in figure 6.1 [Motoyama et al. (2003), Hassinger et al. (2008b)]. The hidden order temperature T_0 increases with pressure. At zero temperature a first order quantum phase transition occurs at $p_x = 0.5$ GPa toward an antiferromagnetic state with a magnetic moment of 0.4 μ_B/U. The superconducting transition T_{sc} decreases with pressure and vanishes at p_x. The transition temperature between the hidden order and the antiferromagnetic state T_x increases with pressure and reaches the hidden order temperature T_0 at $p^\star = 1.4$ GPa. Above $p^\star$ the Néel temperature T_N increases with pressure. Thus the hidden order state appears in the border of an antiferromagnetic region. Bulk superconductivity is excluded from the antiferromagnetic state [Amitsuka et al. (2007)].

URu_2Si_2 crystallizes in the tetragonal $ThCr_2Si_2$ structure with space group I4/mmm. Its unit cell is represented in figure 3.1. The uranium atoms are arranged in a body center

tetragonal structure and they are all equivalent. The antiferromagnetic order above p_x was characterized with elastic neutron scattering and it is also represented in figure 3.1 [Amitsuka et al. (1999)]. The magnetic moment of the atom at the center of the tetragonal unit cell is opposite to the magnetic moments of uranium atoms at the corner of the unit cell. Thus the magnetic Brillouin zone is two times smaller than the crystallographic one. It is obtained by folding along the [001] direction [Hassinger et al. (2010a)].

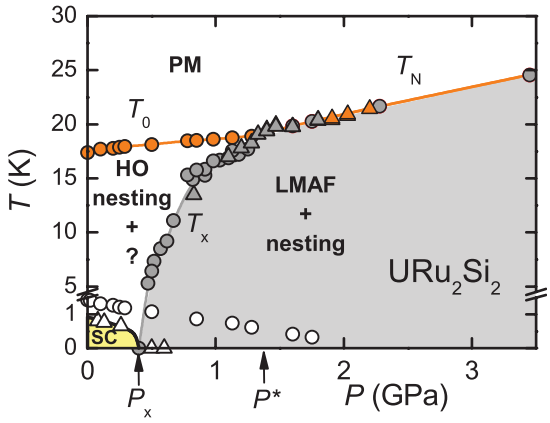

FIG. 6.1 Pressure temperature phase diagram of URu_2Si_2. This phase diagram is taken from reference [Hassinger et al. (2008b)]. Circles and triangles were respectively measured by resistivity and ac calorimetry. Open circles represent the onset of the superconducting transition in the electrical resistivity. HO and LMAF stands for hidden order state and low moment antiferromagnetic state.

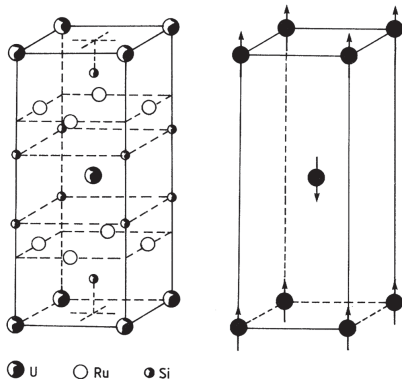

FIG. 6.2 Tetragonal unit cell of URu_2Si_2 on the left. The right panel shows the antiferromagnetic order determined above p_x in [Amitsuka et al. (1999)]. This figure is taken from reference [Mydosh and Oppeneer (2011)].

The observation of strong variations in transport and thermodynamic properties suggested a considerable Fermi-surface reconstruction occurring at the hidden order transition [Palstra et al. (1985), Maple et al. (1986)]. At the transition an electronic gap opens. It was measured by scanning tunnel microscopy (STM) in detail [Schmidt et al. (2010), Aynajian et al. (2010)] and the the charge carrier number decreases strongly [Schoenes et al. (1987)]. A Shubnikov-de Haas study in URu_2Si_2 under hydrostatic pressure shows the similarity of the Fermi surface of the hidden order and the antiferromagnetic state [Hassinger et al. (2010c)]. The folding of the Fermi surface between the paramagnetic and the hidden order state was observed at T_0 with ARPES measurements [Meng et al. (2013)] and with Shubnikov-de Haas effect by suppressing the hidden order with a magnetic field of 40 T along the c axis [Harrison et al. (2013)].

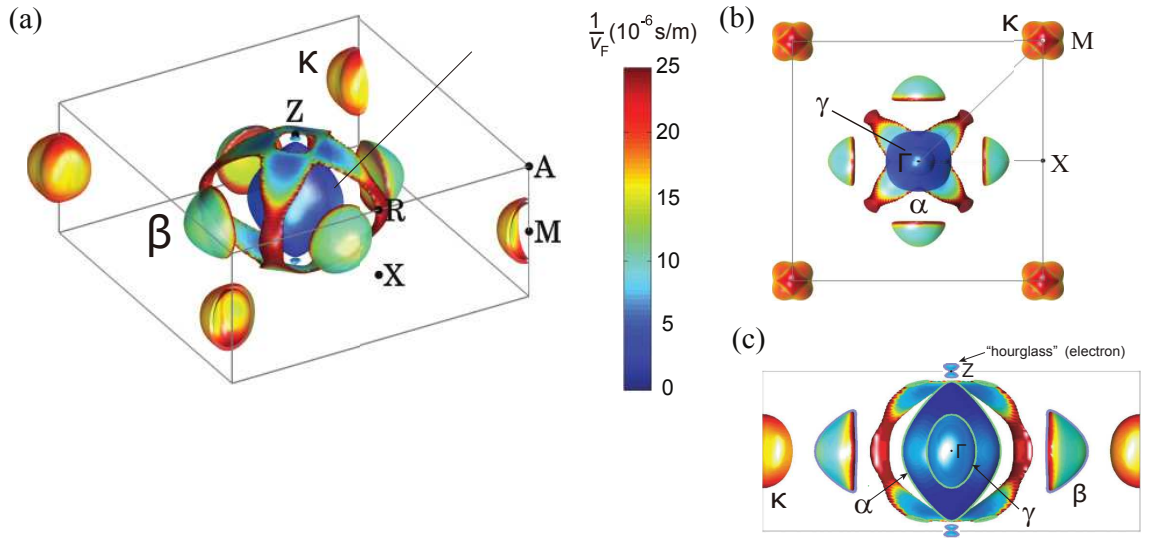

FIG. 6.3 (a) 3D view of the Fermi surface in URu_2Si_2 in the antiferromagnetic and hidden order states calculated by DFT [Tonegawa et al. (2013)]. The color scale gives the inverse Fermi velocity $1/v_F$. The Greek letters give the correspondence with quantum oscillation experiment reported in figure 6.4 proposed in reference [Tonegawa et al. (2013)]. (b) Cross section of the Fermi surface in the ΓMX plane. (c) Cross section of the Fermi surface in the ΓMZ plane.

6.1.2 Bandstructure calculations

The bandstructure in the hidden order state of URu_2Si_2 was calculated with DFT by considering the symmetry of the antiferromagnetic state in the absence of magnetic moments [Elgazzar et al. (2009)]. Later, a DFT electronic structure calculation was performed in the hidden order state taking into account the gap opening and considering different multipole correlations allowed in URu_2Si_2. From this calculation a rank 5 multipole order parameter has been proposed. However the Fermi surface topology is only slightly affected by the different order parameters [Ikeda et al. (2012)]. These results were in good agreement with reference [Elgazzar et al. (2009)] and they recovered the strong similarity between the Fermi surfaces in the hidden order and in the antiferromagnetic states. Other bandstructure calculation studies showing different results and a less good agreement with the experimental results presented below have been reported in [Ohkuni et al. (1999), Yamagami (2011)]. The results of the bandstructure calculation from H. Ikeda et al. are reported in figure 6.3 and were taken from reference [Tonegawa et al. (2013)]. The calculation of the Fermi surface was performed in the antiferromagnetic ordered state and it is expected to be very similar from those of the hidden order state. The calculated Fermi surface shows a relatively light and nearly spherical hole pocket at the center of the Brillouin with a smaller ellipsoidal pocket inside and small electron like hourglass above and below it. A cage structure is

represented around this hole pocket. However this cage structure was not predicted by the calculation from [Elgazzar et al. (2009)]. This difference can be explained by a small Fermi level shift between the two calculations [Tonegawa et al. (2013), Werwiński et al. (2014)]. A four fold electron Fermi surface pocket would be localized between the Γ point and the X point. An heavy Fermi surface pocket with an other electron pocket inside is predicted at the corner of the Brillouin zone.

6.1.3 Fermi surface measurements

The Fermi surface in URu_2Si_2 in the hidden order state was measured by Shubnikov-de Haas (SdH) experiments [Bergemann et al. (1997)] and de Haas-van Alphen (dHvA) experiments [Ohkuni et al. (1999)]. The angular dependence of the quantum oscillation frequencies in URu_2Si_2 from SdH is represented in figure 6.4 [Aoki et al. (2012)]. Four closed Fermi surface pockets η, γ, β and α were measured. While the measurements under magnetic field out of the basal plane were performed both at low field below 13.4 T and under magnetic field up to 30 T, the measurements under magnetic field in the basal plane were performed only under high magnetic field up to 30 T because of the high value of the upper critical field in the basal plane $H_{c2} = 12$ T. The α Fermi surface pocket is nearly spherical with a frequency around $F = 1000$ T and an effective mass around $m^\star \approx 10\ m_0$. Its oscillation frequency is split in three quantum oscillation frequencies under magnetic field in the basal plane. By turning the field from [001] to [100], the β branch splits in β and β', so it must correspond to the fold electron Fermi surface pocket localized between the Γ point and the X point of the Brillouin zone in figure 6.3. This band is heavier with $m^\star = 24m_0$ along the c axis and $m^\star = 13m_0$ in the basal plane. The γ Fermi surface pocket is a small ellipsoid with the c axis as smallest axis. Its frequency and effective mass are $F_\gamma = 200$ T, $m^\star_\gamma = 10\ m_0$ under magnetic field along the c axis and $F_\gamma = 70$ T, $m^\star_\gamma = 7\ m_0$ in plane. A small and heavy orbit η with $F_\eta = 90$ T and $m^\star_\eta = 21m_0$ is also observed under magnetic field along the c axis.

A big ellipsoidal pocket ε with $F_\varepsilon = 1300$ T at the c axis and $F\varepsilon = 2600$ T at the a axis was observed in only one study of quantum oscillations in the resistivity and the Hall effect in URu_2Si_2 [Shishido et al. (2009)]. It comes from a light band with $m^\star_\varepsilon = 2.7m_0$. Two other light orbits λ_1 and λ_2 were detected under pulsed magnetic field applied along the a axis with $F_{\lambda 1} = 1325$ T and $F_{\lambda 2} = 1400$ T [Scheerer et al. (2014)]. The effective mass of λ_1 was estimated at $m^*_{\lambda_1} = 1.0m_0$. The Fermi surface pockets β, the one at the center of the Brillouin zone and the pocket at its corner were also detected by ARPES experiments [Meng et al. (2013), Bareille et al. (2014)]. A cyclotron resonance experiment showed the signature of the different bands measured by quantum oscillations studies and predicted an

heavier band κ with $m^\star_\kappa \approx 60m_0$ and several light bands [Tonegawa et al. (2013)]. This very heavy pocket is also needed to explain the high value of the Sommerfeld coefficient in URu_2Si_2: $\gamma = 65$ mJ.mol^{-1}.K^{-2} [Maple et al. (1986)].

There are discrepancies in the literature about the correspondence between Fermi surface pockets predicted by bandstructure calculations and measured by quantum oscillations. One possibility is, that α and γ Fermi surface pocket are at the center of the Brillouin zone and the κ pocket is at the corner. It is proposed in references [Hassinger et al. (2010c), Aoki et al. (2012), Tonegawa et al. (2013)]. The splitting of α branch under magnetic field in the basal plane was explained by a magnetic breakdown with the two neighboring hourglass in figure 6.3 [Tonegawa et al. (2013)]. A second possibility with the ε pocket at the center of the Brillouin zone and α and γ at the corner is proposed in [Elgazzar et al. (2009), [Harrison et al. (2013), Mydosh and Oppeneer (2014)]. It is important to notice that both scenarios did not predict the light band λ and assigned the ellipsoidal pocket γ with c as smallest axis to ellipsoidal pockets with c as longest axis.

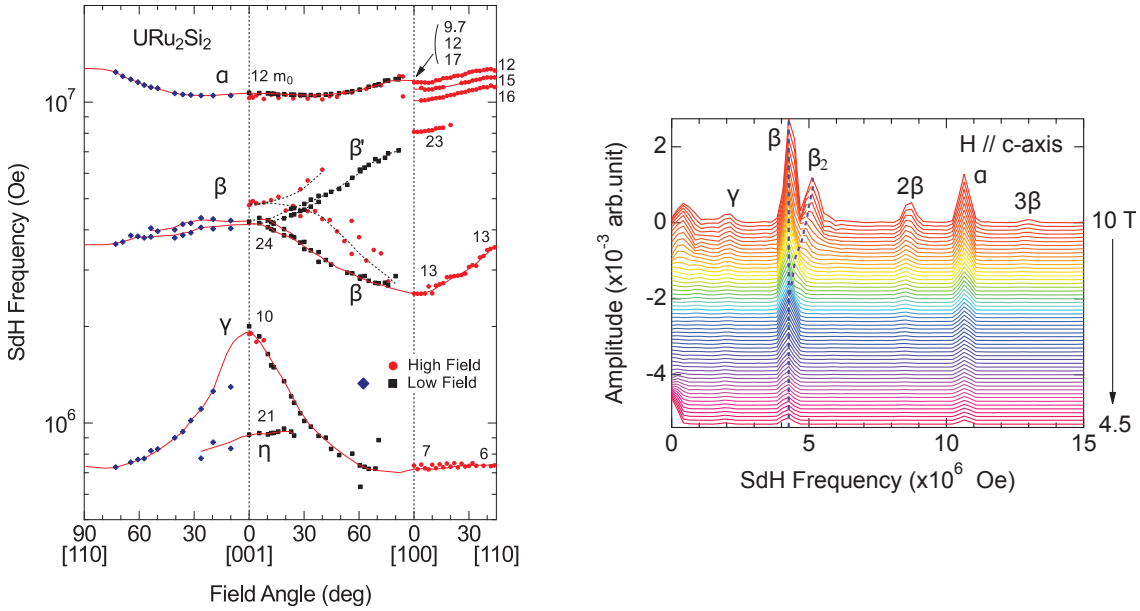

FIG. 6.4 (Left panel) Angular dependence of the SdH frequency in URu2Si2. Red circles are the results at a high field up to 33 T. Dark-blue diamonds and black squares are the results at a low field below 13 T. Cyclotron effective masses are written in the graph for magnetic field along [110], [001] and [100] [Aoki et al. (2012)]. (right panel) FFT spectra in different field ranges from 10 T to 4.5 T under magnetic field along the c axis [Aoki et al. (2012)].

The β and β' branches get split in two peaks under magnetic field in the vicinity of the c axis [Hassinger et al. (2010c)]. The field dependence of the FFT spectrum from the effective field 4.5 T to the effective field 10 T is reported in figure 6.4(b) [Aoki et al. (2012)]. Clearly,

the β peak splits into two peaks β_1 and β_2. While the β_1 frequency is field independent, the β_2 frequency increases strongly with magnetic field. A strong effective mass difference was also observed between β_1 and β_2 with $m^\star_{\beta 1} = 24m_0$ and $m^\star_{\beta 2} = 40m_0$. Further Fermi surface changes were observed inside the hidden order state above 15 T with Hall effect, thermopower and Shubnikov-de Haas experiments [Shishido et al. (2009), Malone et al. (2011), Altarawneh et al. (2011)]. They are discussed and compared to Lifshitz transitions in UCoGe in section 4.2.3. The present chapter is focused on the Fermi surface properties of the hidden order state in URu_2Si_2 below 15 T.

To conclude several bandstructure calculations in the hidden order state of URu_2Si_2 show a good agreement between them and with experimental results. The numerous quantum oscillation studies are also in good agreement with each other except for the light bands ε and λ, which were detected in only one experiment, each. However there are discrepancies about the correspondence between the Fermi surface pockets from band calculations or ARPES studies and the Fermi surface pockets measured in quantum oscillations. New experiments are needed to detect the heavy band κ, to confirm the occurrence of the light bands ε and λ and to study the microscopic properties of α and γ branches to conclude about their localization in k space.

6.1.4 Anisotropy of the magnetic properties

The gyromagnetic factor or g factor measures the response of electrons to an applied magnetic field (see section 1.5.2). In a strongly correlated system such as URu_2Si_2, we should consider the effective g factor of the quasiparticles. It takes into account the screening by other electrons. In an itinerant ferromagnet, the magnetic susceptibility is proportional to the square of the effective g factor: $\chi \propto g^2$. A strong anisotropy of this effective g factor corresponds to an Ising behavior of the magnetic moment. The strong Ising type anisotropy is one of the important characteristics of the hidden order state and different theoretical models of the hidden order state are based on a strong g factor anisotropy such as the hastatic order and the chiral density wave. The hastatic order is a state, which breaks the double time reversal symmetry [Chandra et al. (2013)]. This state is only possible with a huge anisotropy of the g factor. The chiral density wave was proposed for the hidden order from Raman-spectroscopy experiments [Kung et al. (2015)]. In this case a strong anisotropy of the g factor is also needed [Mineev (2015b)].

The magnetic susceptibility in URu_2Si_2 was measured at 2 T under magnetic field along the a and the c axis and is reported in figure 6.5 [Palstra et al. (1985)]. While the magnetic susceptibility along the a axis is almost constant with temperature, the magnetic susceptibility along the c axis shows a maximum around 50 K. At low temperature deep inside

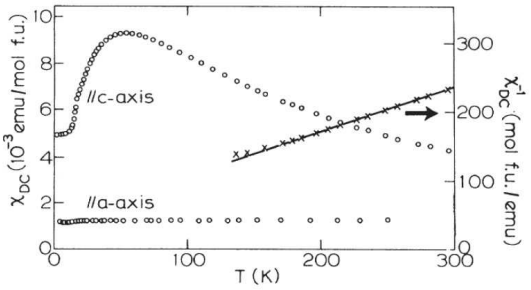

FIG. 6.5 dc magnetic susceptibility, and inverse susceptibility of URu2Si2, measured in a field of 2 T, parallel to the a and c axes [Palstra et al. (1985)]. The crosses represent the inverse susceptibility along the c axis, the solid line is a fit with the Curie-Weiss law $\chi = \chi_0/(T - T_{CW})$ yielding $T_{CW} = -65$ K.

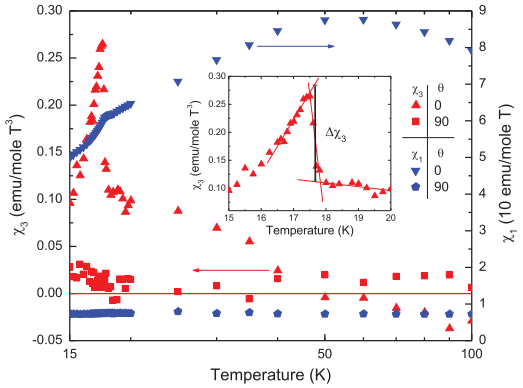

FIG. 6.6 dc magnetic susceptibility χ_1 and non linear magnetic susceptibility χ_3 as a function of temperature for magnetic field along the c axis (0°) and in the basal plane (90°) [Trinh et al. (2016)]. The inset a zoom on the hidden order transition at $T_0 = 17.5$ K to show the non linear magnetic susceptibility jump $\Delta\chi_3$.

the hidden order state, the magnetic susceptibility shows a relatively small anisotropy with $\chi_c/\chi_a = (g_c/g_a)^2 \approx 3.5$. The linear and non linear magnetic susceptibility in URu_2Si_2 were measured more recently and their coefficient χ_1 and χ_3 are represented in figure 6.6 as a function of temperature [Trinh et al. (2016)]. These coefficients are defined from the free energy F by :

$$F = -\frac{\chi_1}{2}H^2 - \frac{\chi_3}{4!}H^4 \tag{6.1}$$

At the hidden order transition at $T_0 = 17.5$ K, a kink occurs in χ_1 and a strong jump in χ_3 under magnetic field along the c axis. On the contrary under magnetic field along the a axis χ_1 and χ_3 are nearly temperature independent. The angular dependence of $\chi - \chi_a$ at 18 K was found to be proportional to $\cos^2(\theta)$, where θ is the angle from the c axis. The jump of χ_3 at the hidden order transition shows a stronger anisotropy and is proportional to $\cos^4(\theta)$. The authors claim, that the angular dependence of χ and χ_3 show the Ising behavior of the quasiparticles in URu_2Si_2.

A relativistic DFT calculation predicted an Ising behavior for the $5f$ bands in URu_2Si_2 [Werwiński et al. (2014)]. The bandstructure and the magnetic moment on the uranium site were calculated for different polarization directions. The authors conclude, that the $5f$ bands show an unusual Ising behavior with magnetic moments along the c axis and no anisotropy was predicted in the basal plane.

The analysis of the upper critical field in URu_2Si_2 revealed a strong g factor anisotropy for the electrons responsible for superconductivity [Brison et al. (1995)]. The upper critical field as a function of temperature for magnetic field applied along the a and c axes are represented in figure 6.10. The experimental upper critical field was compared with numerically computed solutions of the Éliashberg equations. Both the Pauli and the orbital limitation of the upper critical field were taken into account (see section 1.4.2). For magnetic field applied along the c axis this procedure gave a g factor close to 2 : $g_c = 1.9$. However for magnetic field applied along the a axis, the Pauli paramagnetic limit is nearly absent and H_{c2} can be fitted with a very low value of the g factor: $g_c = 0.2$. Thus the analysis of the upper critical field suggests also a strong g factor anisotropy. A recent NMR measurement shows the absence of knight-shift change at the superconducting transition under magnetic field along the a axis [Hattori et al. (2016)]. This results confirms, that the g factor of the quasiparticles along the a axis is very small.

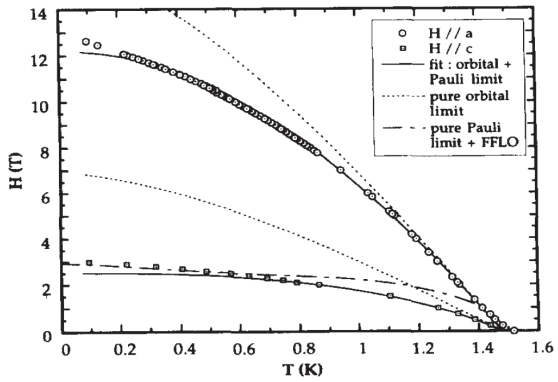

FIG. 6.7 Upper critical field H_{c2} along the a and c axes as a function of temperature [Brison et al. (1995)].

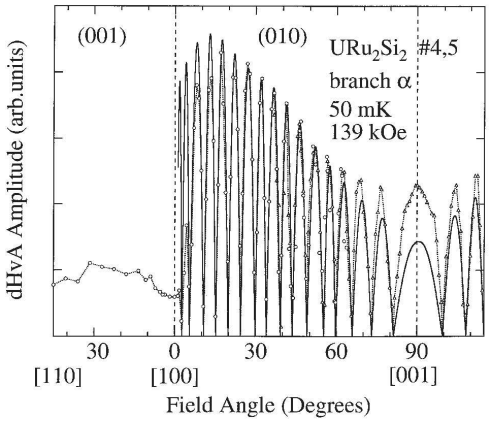

FIG. 6.8 Angular dependence of the dHvA amplitude from the α Fermi-surface pocket at 50 mK [Ohkuni et al. (1999)].

Finally the observation of spin zero in the dHvA angular dependence from the α branch suggests a strong anisotropy of the g factor for this branch. The angular dependence of the amplitude of the quantum oscillations is reported in figure 6.8 [Ohkuni et al. (1999)] and it was fitted by equation (see section 1.7.5):

$$a(\theta) = a_0(\theta)\,|\cos(\pi g(\theta) m^\star(\theta)/2m_0)| \tag{6.2}$$

Where $a_0(\theta)$ is expected to vary slowly with the field angle θ. This method gives access to the variation of the g factor $g_c - g_a \approx 2.6$. These results were compared to the upper critical field anisotropy in URu_2Si_2 in reference [Altarawneh et al. (2012)]. Their analysis assumes that the g factor anisotropy is homogeneous on the Fermi surface of URu_2Si_2 and

that the upper critical field along the c axis is in the pure paramagnetic limit. The authors conclude, that the anisotropy of g factor is very big: $g_c/g_a > 30$.

6.1.5 Aim of this chapter

The aim of this chapter is to study the g factor anisotropy macroscopically from the upper critical field and microscopically from Shubnikov-de Haas experiments, to discuss the role of the different bands for the hidden order state and the unconventional superconductivity.

6.2 Resistivity and magnetoresistance

In the following the two a axis of the tetragonal unit cell will be called [100] and [010], and the c axis is called [001]. Two URu_2Si_2 sample S1 and S2 were used. They were respectively grown by the Czochralski and the flux method and their RRR are 275 and 350, respectively. The resistivity was measured in both samples with electrical current along [010] in the top loading dilution. Details about sample growth and low temperature measurements are given in chapter 2. The resistance of both samples as a function of temperature is represented in figure 6.9(a). While the superconducting transition is clearly resolved in S1 with R=0 at 1.33 K, it is very broad on the flux sample S2. The magnetoresistance was measured in both samples under magnetic field applied from [001] to [100] and the magnetoresistance of the sample S1 was also measured between [001] and [110]. The magnetoresistance of both samples for magnetic field applied along [001] axis is represented in figure 6.9(b). Sample 2 shows a much stronger magnetoresistance suggesting a higher sample quality. The Shubnikov-de Haas oscillations were observed in both samples with a bigger amplitude in sample S2. Thus the sample S2 grown in indium flux has a higher average mean free path, but it is less homogeneous regarding superconductivity than the sample S1 grown by the Czochralski method.

6.3 g factor anisotropy studied by upper critical field measurements

The magnetoresistance of sample S1 at $T = 22$ mK is represented for electric current along [010] and magnetic field in different directions from [001] to [100] and along [110] in figure 6.10(a). The upper critical field H_{c2} under magnetic field along [001] is around 2.5 T with a relatively sharp transition. When the magnetic field is tilted toward [100], H_{c2} increases,

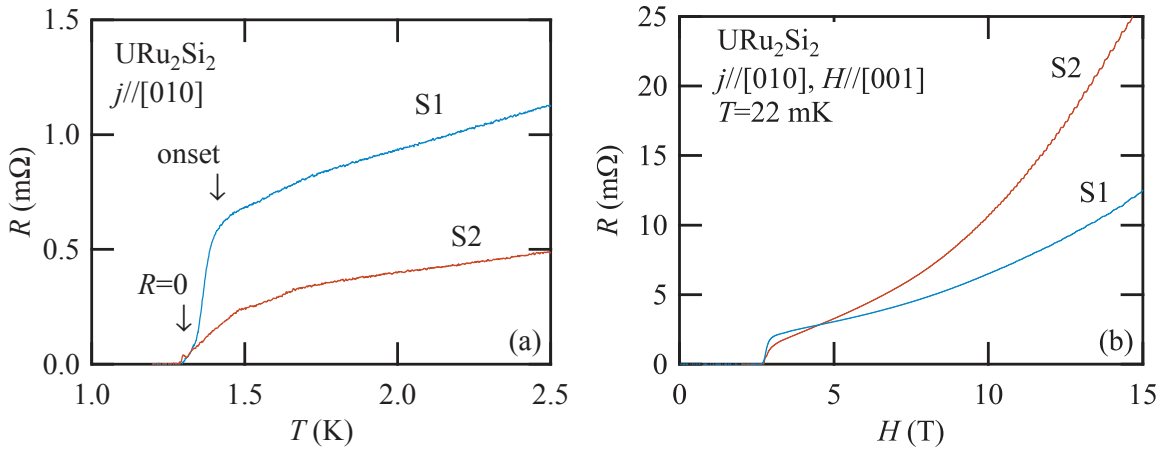

FIG. 6.9 (a) Resistivity in URu_2Si_2 as a function of temperature in sample S1 in blue and sample S2 in brown. (b) Magnetoresistance at 22 mK in URu_2Si_2 under magnetic field applied along [001].

the transition gets broader and the onset of the superconducting transition becomes difficult to define. Under magnetic field along [100] the resistivity becomes non zero at 12 T and the onset of the superconducting transition is above 15 T. The magnetoresistance under magnetic field along [110] is smaller than the magnetoresistance along [100] because the angle between the magnetic field and the electric current is only 45°. The anisotropy of the upper critical field in plane is very small $|H_{c2}[100] - H_{c2}[110]| < 0.1$ T. The second sample S2 shows even broader transitions with step-like anomalies inside, so its upper critical field is not discussed here. A thermal conductivity study in URu_2Si_2 shows, that the bulk upper critical field would be slightly higher than the resistive one [Okazaki et al. (2008)]. This results were interpreted with the occurrence of a vortex liquid phase. This effect is not considered here and the difference between the resistive and the bulk upper critical field will be neglected in the discussion.

The upper critical field H_{c2} with the criterion $R = 0$ is represented as a function of temperature for different field directions between [001] and [100] in figure 6.10(b). The H_{c2} temperature dependence at [001] and [100] shows a good agreement with previous studies [Brison et al. (1995), Ohkuni et al. (1999)]. The angular dependence of its initial slope $-dH_{c2}/dT_{sc}(T = T_sc)$ and its low temperature value $H_{c2}(T = 22$ mK) are represented in figure 6.10(c). Both are higher along [001] and the anisotropy of the low temperature value is stronger than the anisotropy of the initial slope. As discussed in section 1.4.2, the initial slope of the upper critical field is given by the orbital limit and its anisotropy shows the anisotropy of the Fermi velocity :

$$v_F^c / v_F^a = \left(\frac{dH_{c2}^c}{dT_{sc}} / \frac{dH_{c2}^a}{dT_{sc}}\right)^{-1} = 1.5 \tag{6.3}$$

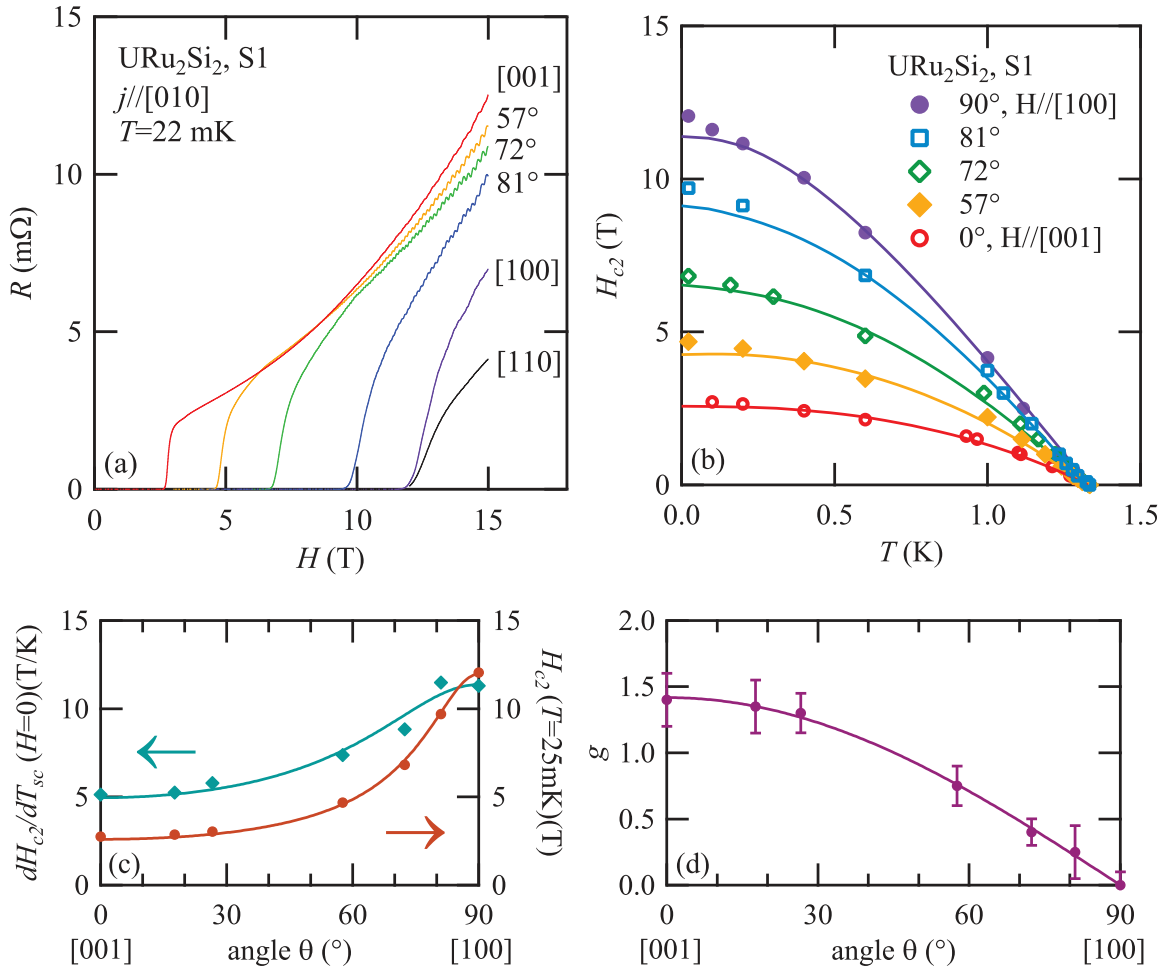

FIG. 6.10 (a) Resistivity at 22 mK in URu_2Si_2 as a function of magnetic field for different field angle from [001] to [100] and along [110]. Electrical current is along [010]. (b) Temperature dependence of the upper critical field H_{c2} with the criterion $R = 0$. The solid lines are fits from the WHH theory [Werthamer et al. (1966)]. (c) Angular dependence of the initial slope $-dH_{c2}/dT_{sc}(T = T_{sc})$ and the low temperature value $H_{c2}(T = 22$ mK$)$ of the upper critical field. Solid lines are guides to the eye. (d) Angular dependence of the g factor deduced from the fits of the temperature dependence of H_{c2}. The solid line is a fit assuming an uniaxial g factor : $g(\theta) = g_c \cos(\theta)$, with $g_c = 1.4$.

Where v_F^c and v_F^a are the average Fermi velocity in the plane perpendicular to c and a respectively. The low temperature value of H_{c2} comes both from the paramagnetic and orbital limit. Its strong anisotropy shows, that the paramagnetic limit is also strongly anisotropic. The temperature dependence of H_{c2} was fitted by taking into account both from the paramagnetic and orbital limit and the resulting fit are plotted in figure 6.10(b). The fits were performed from numerical calculations based on the WHH theory within the weak coupling limit and the clean limit [Werthamer et al. (1966)]. The experimental data are well fitted by this model. The angular dependence of the g factor extracted from these fits is represented

in figure 6.10(d). Under magnetic field along [100], the best fit is in absence of any paramagnetic limitation : $g_a = 0$ although it shows some deviations from the experimental points at low temperature. However in this direction the transition is broad and the bulk transition could be lower than the resistive one. The g factor along [001] axis obtained by the fit is $g_c = 1.4$. These results are in relatively good agreement with a previous similar study which gave $g_a = 0.2$ and g_c=1.9 [Brison et al. (1995)] and a smaller agreement with a study based only on $H_{c2}(T = 25$ mK) measurements assuming a pure paramagnetic limit which gave g_c=2.5 [Altarawneh et al. (2012)]. The angular dependence of g factor in figure 6.10(d) can be well fitted with a uniaxial g factor : $g(\theta) = g_c \cos(\theta)$. So the band responsible for superconductivity shows an Ising behavior as shown by NMR [Hattori et al. (2016)] and predicted by band calculations for all the $5f$ bands [Werwiński et al. (2014)]. Another interpretation of the anisotropy of the upper critical field in URu_2Si_2 was proposed [Kusunose (2012)]. It is based on the field dependence of the pairing interaction. This interpretation needs a very low value of the coupling constant $\lambda = 0.05$. This value would imply a difference of several order of magnitude between the characteristic temperature of fluctuations responsible for superconductivity and the superconducting temperature which seems unrealistic.

6.4 Fermi surface measurement from quantum oscillations

The Shubnikov-de Haas oscillations in both samples are represented as a function of inverse magnetic field applied along [001] in figure 6.11(a). The FFT of these oscillations for the interval 9 T−15 T are represented in figure 6.11(b). The orbits η, γ, β and α were observed in both samples with a higher signal noise ratio in sample S2. The angular dependence of the quantum oscillations frequencies from [001] to [100] and from [001] to [110] are represented in figure 6.12. A good agreement can be observed for α, β, β', γ and η branches between both samples and with the previous experiment reported in figure 6.4 [Aoki et al. (2012)]. The orbits λ_1 and λ_2 are detected in both samples. They were previously observed only under pulsed magnetic field above 20 T [Scheerer et al. (2014)]. Our measurement shows, that these branches are also present below 15 T. They can be observed both on samples grown by Czochralski method and indium flux method. So these oscillations does not come from inclusions of a lighter material in URu_2Si_2.

The FFT of oscillations in sample 2 on the interval 7 T-15 T under magnetic field along 72° from to [001] toward [100] for different temperatures are represented in figure 6.13(a). The magnetic field was tilted from [100] to reduce the upper critical field. At the lowest temperature two small peaks corresponding to λ_1 and λ_2 with $F_{\lambda 1} = 1350$ T and $F_{\lambda 2} = 1430$ T are observed close to the large peak from the α Fermi-surface pocket. The temperature

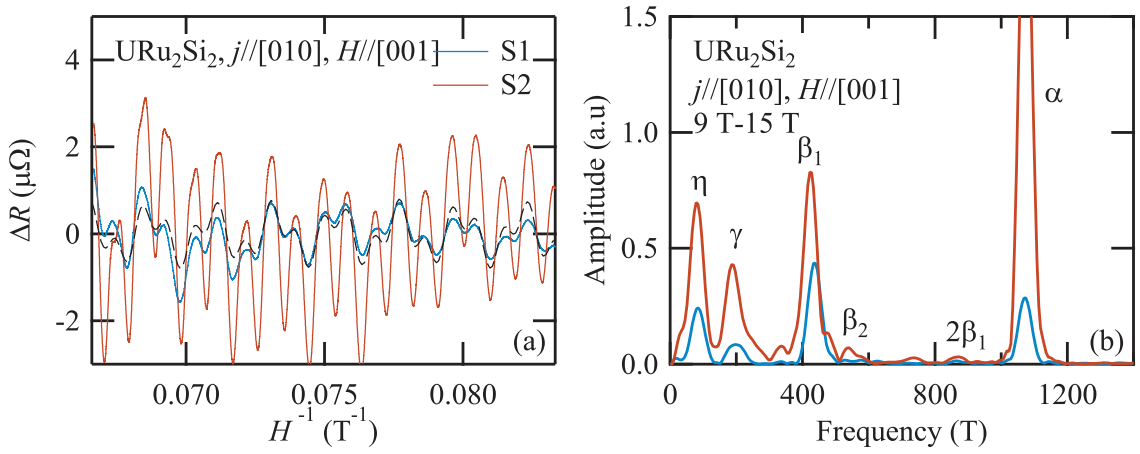

FIG. 6.11 (a) Shubnikov-de Haas oscillations are represented as a function of inverse magnetic field from 12 T to 15 T for S1 in blue and S2 in brown. The black dashed line is a fit by two sinusoids corresponding to the two main frequencies α and β. (b) FFT spectrum of these oscillations performed on the field interval 9 T-15 T.

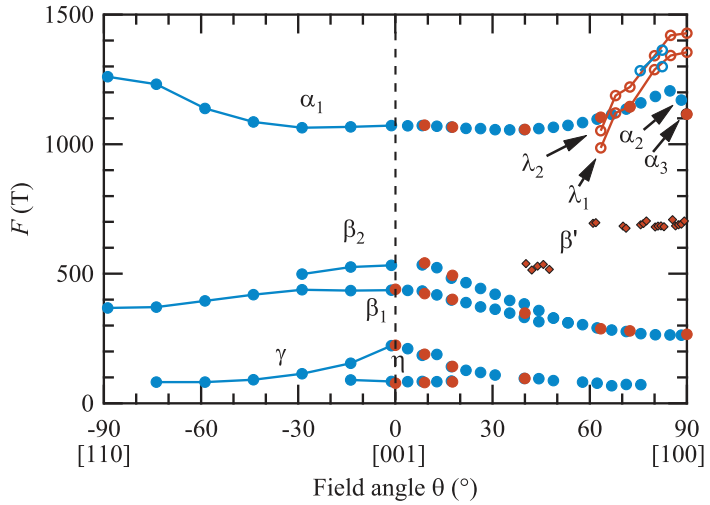

FIG. 6.12 Angular dependence of quantum oscillation frequencies in URu_2Si_2 between [001] and [110] and between [001] and [100]. Blue and brown symbols stand respectively for samples S1 and S2. η, γ, β and α branches were drawn from FFT on the interval 9 T-15 T at 22 mK. The heavy branch β' was drawn from FFT on the interval 12 T-15 T at 22 mK and the light branches λ_1 and λ_2 were observed with FFT on the interval 9 T-15 T at 600 mK.

dependence of quantum oscillation amplitudes of α, λ_1 and λ_2 are represented in figure 6.13(b). While α branch signal is rapidly suppressed, the oscillations from the λ_1 and λ_2 branches can be observed up to 1 K. Fits from Lifshitz-Kosevic equation (see section 1.7.4) give the effective mass values $m^\star_{\lambda_1} = 1.4\ m_0$ and $m^\star_{\lambda_2} = 2.1\ m_0$. The value for λ_1 is slightly

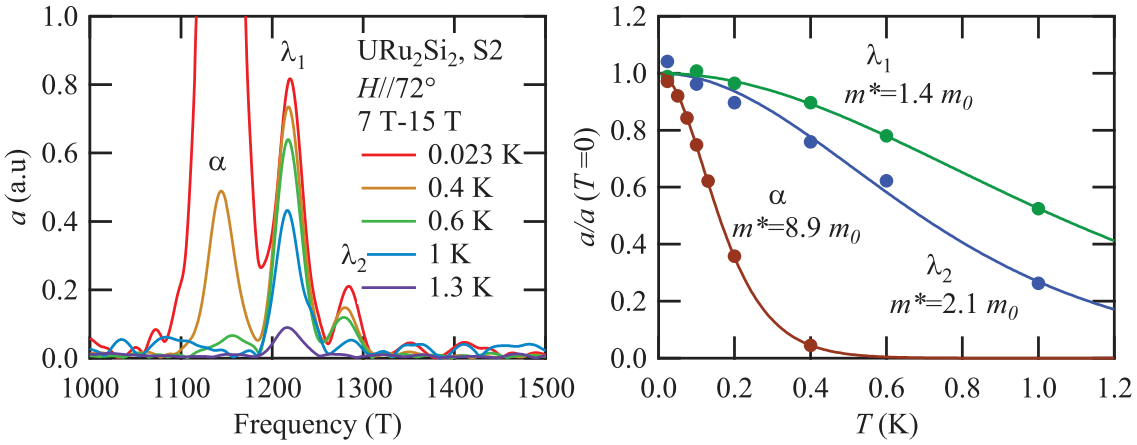

FIG. 6.13 (a) FFT spectrum of SdH oscillations on the interval from 7 T to 15 T for field angle 72° from [001] toward [100]. (b) Temperature dependence of the amplitude of quantum oscillations from α, λ_1 and λ_2 orbits. Fits from Lifshitz-Kosevic formula introduced in section 1.7.4 give the effective mass values $m^\star_\alpha = 8.9\ m_0$ $m^\star_{\lambda_1} = 1.4\ m_0$ and $m^\star_{\lambda_2} = 2.1\ m_0$.

higher that the value obtained at [100] under pulsed magnetic field : $m^\star_{\lambda_1} = 1.0\, m_0$ [Scheerer et al. (2014)]. The effective mass of λ_2 could not be extracted in the pulsed field experiment. The angular dependence of λ_1 and λ_2 frequencies was measured at 600 mK to suppress the quantum oscillations from the heavy band α and it was reported in figure 6.12. Both quantum oscillations frequencies decrease when the magnetic field is tilted from [100] axis toward [001] and the signal was lost around 30° from [100] like in the pulsed field experiment. Our experiment shows, that the light band λ exists also at low field down to 7 T. It gives a higher precision on frequency values, angular dependence and effective mass values, thanks to a higher number of periods in our experiment. These bands may correspond to the light bands F and G observed by cyclotron resonance experiments [Tonegawa et al. (2013)]. The bandstructure calculations did not predict these light bands and must be refined to take them into account.

6.5 Microscopic study of g factor anisotropy

6.5.1 Angular dependence of the quantum oscillation amplitude

The magnetoresistance at 22 mK in URu_2Si_2 S2 is represented for different field angles from [001] to [100] in figure 6.14. The Shubnikov-de Haas oscillations from the α branch are clearly resolved. The quantum oscillation amplitude decreases below 16° and then increases again. A phase shift of 180° can be observed between oscillations observed for angle slightly

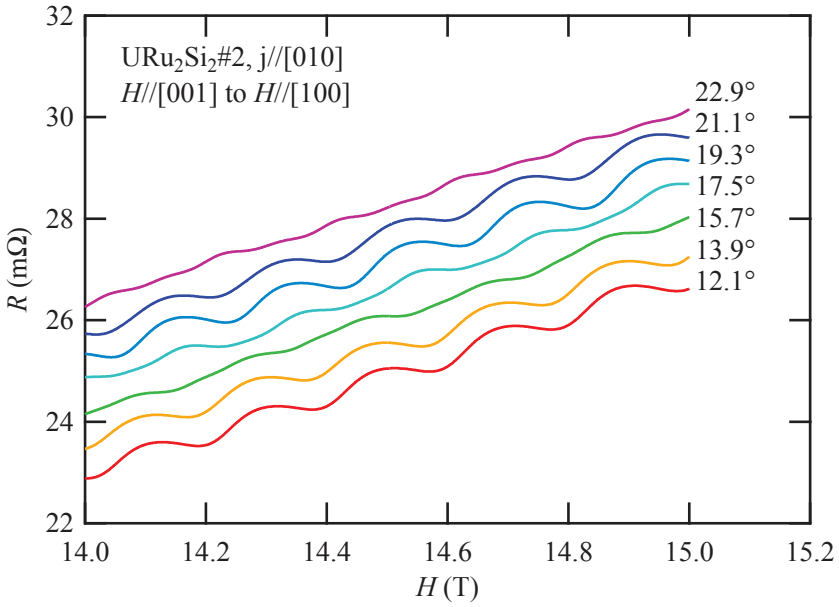

FIG. 6.14 Resistivity in URu_2Si_2 S2 at 22 mK as a function of magnetic field applied in different field directions from [001] to [100]. The curves are vertically shifted of 0.5 $m\Omega$ for clarity. Quantum oscillations coming from the α Fermi surface pocket are clearly resolved. At 16° the oscillations vanish and a phase shift of 180° occurs indicating a spin zero.

below and slightly above 16°. It is the indication of a spin zero of the quantum oscillations as discussed in sections 1.7.5 and 6.1.4. A second spin zero is observed around 22°. The angular dependence from [001] to [100] of quantum oscillation amplitude for α Fermi-surface pocket in both samples is represented in figure 6.15 for the interval 12 T-15 T. Both samples show several spin zero at the same angles. The amplitude of quantum oscillations between these spin zero increases with angle in S1 and is constant in S2. The measurement of dHvA amplitude from the α pocket on a field interval centered at 13.9 T from reference [Ohkuni et al. (1999)] was added in figure 6.15. While Ohkuni et al. measured 16 spin zero between [001] and [100], both samples in our measurements show 17 spin zero. The discrepancy may be due to a slight misalignment of Ohkuni et al. sample around an axis transverse to the rotation axis. Shubnibkov-de Haas measurements between [001] and [110] show only 12 spin zero so 5 spin zero less than between [001] and [100]. The oscillations from the α pocket could not be resolved in the vicinity of [100] and [110] due to the splitting of the α branch in three orbits and thus appearance of the oscillations from the α_2 and α_3 orbits.

The angular dependence of quantum oscillations amplitude from [001] to [100] was studied on two different field intervals 6 T-9 T and 12 T-15 T. The measurement on the interval 6 T-9 T was stopped at 65° because of the increase of H_{c2} with angle. The angular

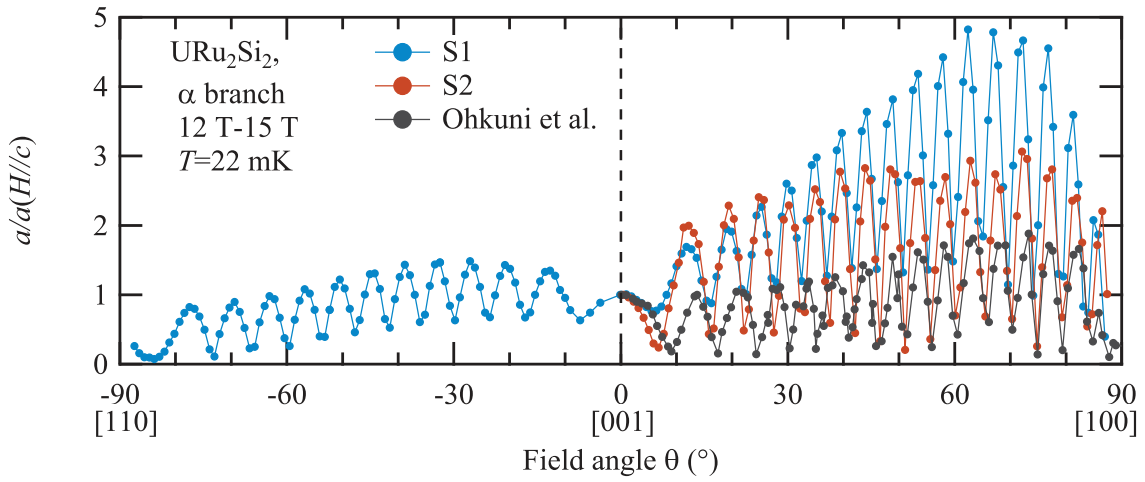

FIG. 6.15 Amplitude of Shubnikov-de Haas oscillations from α orbit in samples S1 and S2 as a function of the field direction. The magnetic field is swept between 12 T and 15 T at $T = 22$ mK. The amplitude is renormalized by its value at $H//[001]$. Green points were taken from reference [Ohkuni et al. (1999)]. They were measured by dHvA on a field interval centered at 13.9 T.

dependence of quantum oscillations amplitude in S2 for α, β, β' and γ orbits are represented in figure 6.16. Spin zero are observed for all these pockets. For the α orbit the same spin zero are observed for both field intervals. They are slightly shifted to higher angle, when the magnetic field is increased. On the contrary, the amplitude of the β orbit quantum oscillations in figure 6.16(b) shows very different pictures in the two field intervals. The spin zero are closer to each other in the lower field interval 6 T-9 T with 8 spin zero between 30 and 65 degrees against 7 for the field interval 12 T-15 T. The amplitude of β' orbit quantum oscillations is represented as a function of angle between [001] and [100] in figure 6.16(c). It could be measured only in sample S2 in the interval 12 T-15 T and it could not be resolved below 40° due to the proximity with β_2 signal neither between 50° and 60° due to the proximity with the signal of the second harmonic from β_1 orbit. It shows three spin zero between 40° and 50° and seven from 60° to 90°. The small pocket γ could be studied only in the interval 6 -9 T, because its frequency is too small to be resolved in the interval 12 T-15 T. Its oscillation amplitude in S2 is represented as a function of angle from [001] toward [100] in figure 6.16(d). Twelve spin zero are observed up to 65°.

The analysis of β branch on the field interval 12 T-15 T should take into account the splitting in two frequencies β_1 and β_2 under magnetic field in the vicinity of [001]. The frequency, amplitude and effective mass of β, β_1 and β_2 oscillations are represented as a function of the field direction in figure 6.17. The signal from the β branch was separate in two peaks for both samples from [001] to 15° toward [100] and from [001] to 40° toward

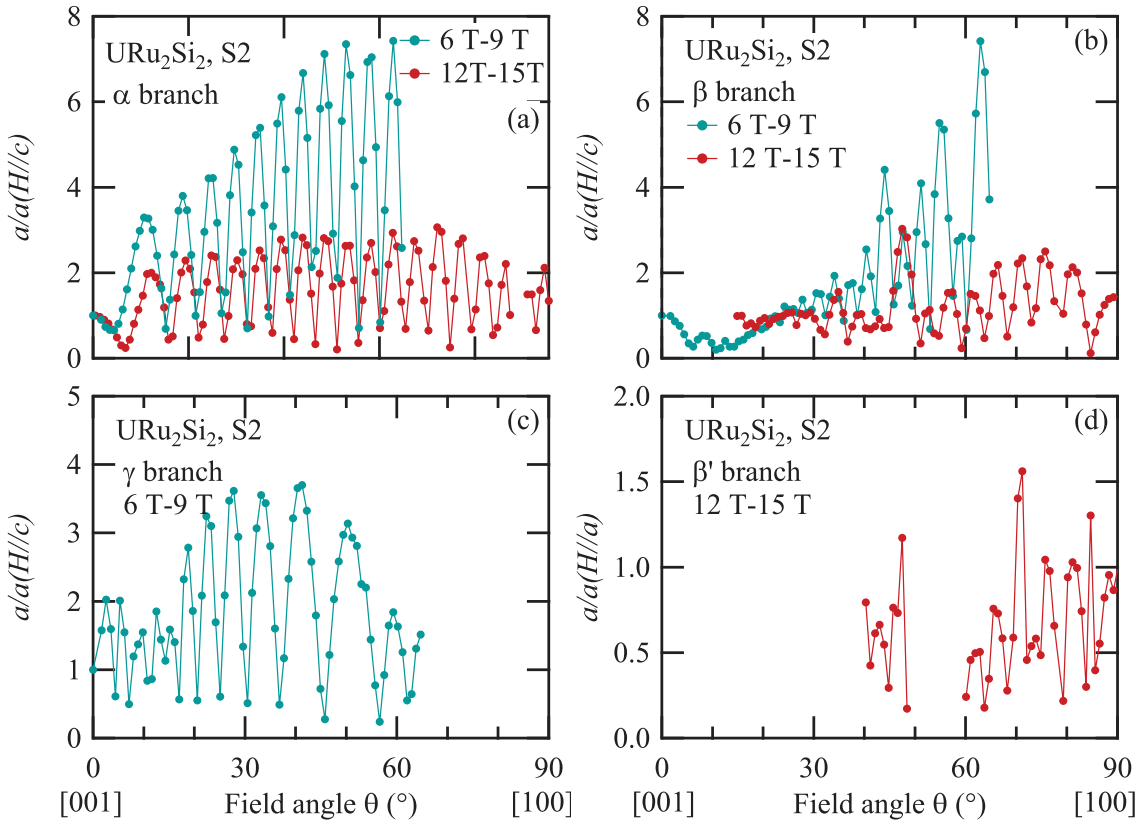

FIG. 6.16 Amplitude of quantum oscillations from α orbit in (a), β orbit in (b), β' orbit in (c) and γ orbit in (d) as a function of the field direction. It is measured at 22 mK in S2 on the field intervals 6 T-9 T and 12 T-15 T. The amplitudes are renormalized by their value at $H//[001]$ except for β' orbit, whose amplitude is renormalized by its value at $H//[100]$.

[110]. In the vicinity of [001] the quantum oscillations frequencies of β_1 and β_2 are respectively $F_{\beta 1} = 450$ T and $F_{\beta 2} = 600$ T. The angular dependence of the amplitude of quantum oscillations from β_1 and β_2 branches are represented in figure 6.17(b) with the angular dependence of the amplitude of quantum oscillations from the β branch in the range where the two peaks are not separate. While the amplitude of β_1 oscillations is maximum at [001], the amplitude of β_2 oscillations is much smaller and nearly constant with angle. No spin zero was observed on the signal from β_1 and β_2 branches. On the contrary the amplitude of β branch quantum oscillations shows a modulation as a function of angle in all the range where the two peaks are not separate. It must come from the interferences between oscillations from the β_1 and the β_2 branches. It confirms that the splitting of the signal from β branch is a spin splitting. The amplitude of the β oscillations shows 11 spin zero between [110] and 40° from [001] and 13 spin zero between [100] and 15° from [001]. Between [001] and [100] both samples show the same spin zero, however they are more clear in S1

the sample with the lowest quantum oscillation amplitude than in S2. The oscillation amplitude in both samples does not vanish completely at the spin zero. It must come from the incomplete cancellation of spin up and spin down oscillations due to their amplitude difference and their small frequency difference.

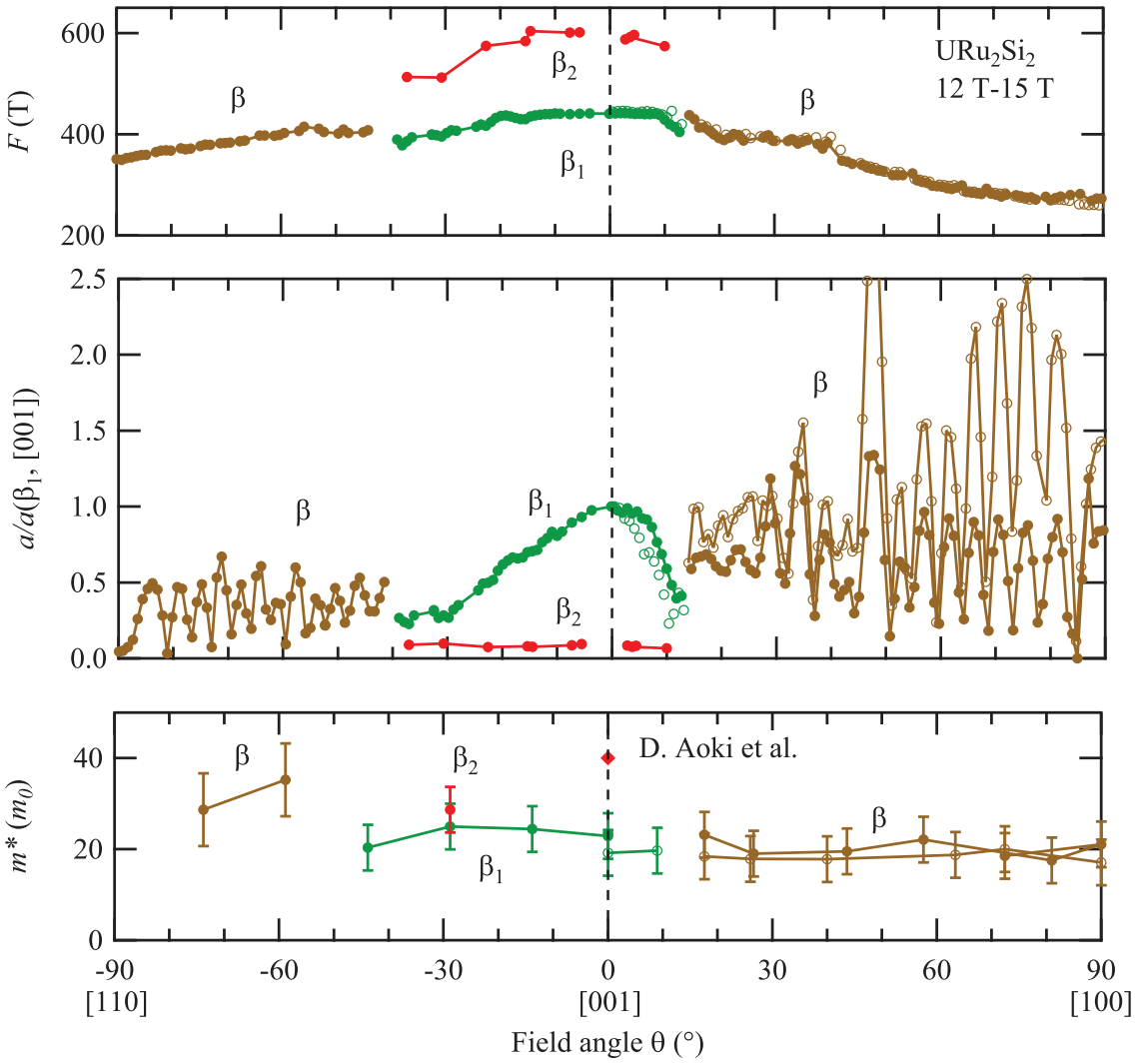

FIG. 6.17 (a) Quantum oscillation frequency from β branch at $T = 22$ mK in the interval 12 T-15 T as a function of the field direction. The signal is split into two frequencies β_1 and β_2 in the vicinity of [001]. The close and open symbols stand for sample S1 and sample S2. (b) Quantum oscillation amplitude of β, β_1 and β_2 as a function of the field direction. (c) Effective mass of β, β_1 and β_2 orbits as a function of the field direction. The results for β_2 orbit was taken from reference [Aoki et al. (2012)].

The angular dependence of the effective mass extracted from the temperature dependence of β_1 and β_2 and β quantum oscillation signal is represented in figure 6.17(c). The

effective mass of β_1 branch is around $m^\star_\beta = 21.5\ m_0$. It is nearly constant with angle, when the magnetic field is tilted toward [110]. The effective mass of β_2 branch could not be resolved in this study, however it was estimated at $m^\star_{\beta_2} = 40\ m_0$ at [001] in reference [Aoki et al. (2012)], so it is much heavier than that of the β_1 branch. This difference explains the amplitude difference between oscillations from β_1 and β_2 branches reported in figure 6.17(b). The effective mass extracted from the β peak above 40° is around $m^\star_\beta \approx 30\ m_0$. On the contrary between [001] and [100] the effective mass of β branch is similar to the effective mass of β_1 and independent of field angle with $m^\star_\beta = 21.5\ m_0$ for both samples. This result is in contradiction with the measurement of β branch effective mass at [100] on the interval 15 T-30 T reported in figure 6.4 [Aoki et al. (2012)]. It gave $m^\star_\beta = 13 m_0$. The strong difference may be due to a field dependence of β branch effective mass for a magnetic field applied along the hard axis magnetization axis [100].

6.5.2 Anisotropy of the g factor for the α branch.

As shown by equation (6.2), the number of spin zero between two directions is related to the variation of the product $m^\star g$. It does not give the sign of this variation. Each band showing a g factor anisotropy will be assumed to undergo the maximum of its g factor along the [001] direction as the global g factor. The anisotropy of the effective mass $m^\star$ was studied on the same field interval 12 T-15 T from the temperature dependence of the quantum oscillations amplitude as explained in section 1.7.4. Its angular dependence is represented in figure 6.18(a). It decreases slowly with angle from $m^\star_\alpha = 13\ m_0$ at [001] to $m^\star_\alpha = 10\ m_0$ at [100]. When the magnetic field is tilted toward [110], the effective mass decreases with angle up to 45° and it could not be resolved precisely above.

The quantity $m^\star g/2m_0$ is an integer number at each maximum of amplitude in the angular dependence of quantum oscillations. Let us define the integer number r_α as the value of $m^\star g/2m_0$ at the closest amplitude maximum from [100]. Then the anisotropy of the g factor for different values of the integer r_α is represented in figure 6.18(b). For its lowest value $r_\alpha = 1$ a huge g factor anisotropy $g_\alpha([001])/g_\alpha([100])$ is observed. In this case the g factor can be fitted from [001] to [100] by the law : $g_\alpha(\theta) = g_\alpha([001])\cos(\theta)$ corresponding to an Ising behavior of the quasiparticles from α Fermi surface pocket. The main difference between the curves for the different values of r_α is a vertical shift, so the variation of the effective mass with angle gives only a small correction. Thus this study gives without ambiguity the g factor difference $g_\alpha([001]) - g_\alpha([100])$=2.5 and $g_\alpha([001]) - g_\alpha([110])$=1.4.

This result implies a big g factor anisotropy in the basal plane between [100] and [110] for the α Fermi surface pocket: $g_\alpha([110]) - g_\alpha([100])$=1.1. The previous experiment reported in figure 6.8 did not observe any spin zero under a magnetic field in plane [Ohkuni

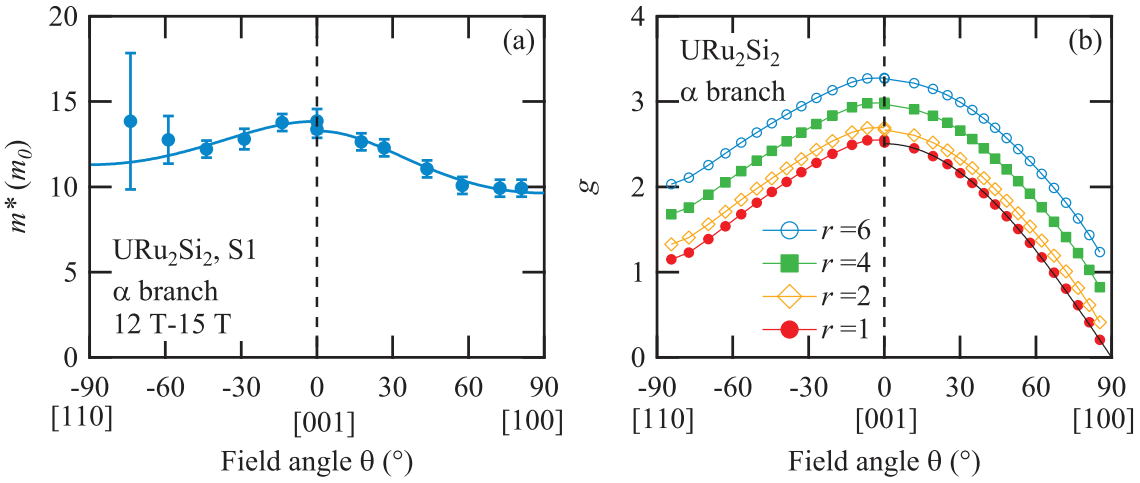

FIG. 6.18 Angular dependence of the effective mass of α branch on the field interval 12 T-15 T. Solid lines are guide to the eye. (b) Angular dependence of g factor for different values of the integer number r_α defined as the value of $m^\star g/2m_0$ at the closest amplitude maximum from [100]. The black line is a fit for $r_\alpha = 1$ from [001] to [100] by the law : $g_\alpha(\theta) = g_\alpha([001])\cos(\theta)$.

et al. (1999)]. However the splitting of the α branch in three orbits was not resolved in the field interval used to study the spin zero. Assuming these three orbits are spin degenerated, the oscillations amplitude would come the interferences between oscillations from the six orbits. It explains why it is nearly constant with the magnetic field angle between [100] and [110]. The quantum oscillations under magnetic field in the basal plane were studied on a broader interval 15 T-30 T in reference [Aoki et al. (2012)]. The three orbits α, α_2 and α_3 were separate and the α_2 branch has one amplitude cancellation between the [100] and the[110] directions, which must be a spin zero. On the contrary our measurement suggests the occurrence of five spin zero between these directions. The discrepancy must come from the field interval difference. Indeed the effective mass may depend on the magnetic field.

The comparison between the two field intervals 6 T-9 T and 12 T-15 T in figure 6.16(a) shows an increase of the product $m^\star g$ under magnetic field along [001]. An increase of the effective mass under magnetic field was also observed between these two intervals as previously reported in reference [Aoki et al. (2012)]. Thus the studies of g factor anisotropy in the two different field intervals show a good agreement.

6.5.3 Anisotropy of the g factor for the γ branch.

To analyze the g factor anisotropy of the γ branch, the strong anisotropy of its effective mass must be taken into account. It is represented in figure 6.19(a). It decreases strongly with angle from $m^\star_\gamma = 11.5\ m_0$ at [001] to $m^\star_\gamma = 3.7\ m_0$ at 40°. The quantity $m^\star g/2m_0 - r$

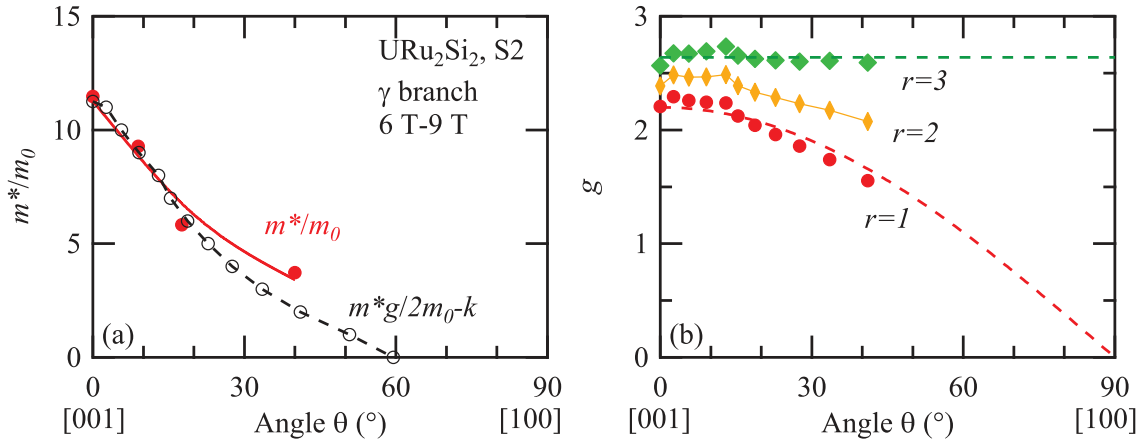

FIG. 6.19 (a) The close red symbols represent the effective mass $m^\star/m_0$ for the γ branch as a function of angle from [001] to [100]. The open symbols and the dashed line represent the quantity $m^\star g/2m_0 - k$ extracted from the analysis of the spin zero by equation (6.2). (b) Angular dependence of the g factor for different values of the integer number r_γ. The dashed line for $r_\gamma = 1$ is a fit with $g_\gamma(\theta) = g_\gamma([001])\cos(\theta)$ and $g_\gamma([001]) = 2.2$. The dashed line for $r_\gamma = 3$ corresponds to the constant g factor case with $g_\gamma = 2.6$.

was extracted from the angular dependence of quantum oscillations from the γ pocket by equation (6.2) and it is also represented on figure 6.19(a). Like for the α branch, the integer number r_γ is defined as the value of $m^\star g/2m_0$ at the closest amplitude maximum from [100]. It decreases strongly with angle like $m^\star$. The angular dependence of the g factor for the γ branch is represented in figure 6.19(b) for three different values of the integer r. For $r = 3$ the g factor is constant with angle up to 40° from [001] toward [100] with $g_\gamma = 2.6$. In this case the numerous spin zero in the signal from the γ Fermi surface pocket would come only from the anisotropy of the effective mass. On the contrary for the scenario $r = 1$ the g factor decreases with angle and could be fitted by $g_\gamma(\theta) = g_\gamma([001])\cos(\theta)$ with $g_\gamma([001]) = 2.2$. Thus our measurement could not prove neither exclude a g factor anisotropy for the γ pocket.

6.5.4 Anisotropy of the g factor for the β branch.

The angular dependence of the effective mass of the β branch in the field interval 12 T-15 represented in figure 6.17(c) shows, that the effective mass for the β branch is constant within the error bars from [001] to [100]. It was taken at its average value $m^\star_\beta = 21.5\ m_0$ between [001] and [100] and at $m^\star_\beta \approx 30\ m_0$ between [001] and [100] for the extraction of the g factor. In the case of a constant effective mass, the solution for the different values of the integer r_β are just shifted vertically with each other. Thus the g factor variation Δg of the g factor with angle is determined and represented in figure 6.20(b). It shows a variation

of $\Delta g_\beta = 1.4$ between [100] and 15° from [001] and a variation of $\Delta g_\beta = 0.8$ between [110] and 40° from [001].

In the vicinity of of [001], the g factor anisotropy for β_1 can be deduced from the phase of quantum oscillations as explained in section 1.7.5. This phase was extracted by fitting the quantum oscillations by the sum of two sinusoids corresponding to oscillations from the β_1 and α orbits as represented in figure 6.11(a). The angular dependence of the phase of quantum oscillations from the β_1 branch is represented in figure 6.20(a). It increases continuously with angle from [001]. It confirms that the β_1 signal comes from a single spin. Otherwise jumps of the phase of π would occur as they can be observed for the α branch in figure 6.14. This phase ϕ is defined from the first harmonic of quantum oscillations by:

$$\Delta R = a \sin(\frac{2\pi F}{B} + \phi) \tag{6.4}$$

As discussed in section 1.7.5, this phase must follow equation:

$$\phi = \phi_0 \pm \frac{mg}{2m_0} \tag{6.5}$$

The g factor is expected to decrease with angle from [001] and the effective mass for β_1 is considered as angle independent at $m^\star_{\beta 1} = 21.5\, m_0$, so the sign represented by $\pm$ in equation (6.5) must be a minus sign. As a consequence β_1 corresponds to the minority band. The g factor variation $\Delta g_{\beta 1}$ is deduced from equation (6.5) and it is represented in figure 6.20(b). It decreases faster with angle than the g factor extracted from the β branch.

In the field interval 6 T - 9 T, no splitting of the β frequency was observed. The effective mass is also angle independent within the error bars and was taken at its average value $m^\star_\beta = 20\, m_0$. The variation Δg_β for this field interval from [001] to [100] is also represented in figure 6.20(b). Its extrapolation up to [100] gives the g factor variation $g_\beta([001]) - g_\beta([100]) \approx 2.4$. It is much stronger than the variation of g factor for the field interval 12 T-15 T : $g_\beta([001]) - g_\beta([100]) \approx 1.5$ and similar to the variation of g factor for the α branch $g_\alpha([001]) - g_\alpha([100]) = 2.5$. Thus the Zeeman effect of the β branch gets weaker and weaker under magnetic field. It explains the increase of the quantum oscillation frequency of the majority band pocket β_2 with magnetic field reported in figure 6.4(b) (see section 1.7.2). No field dependence of the quantum oscillation frequency has been observed for the minority band β_1. It explains why in the interval 12 T - 15 T the variation of g factor of the minority branch β_1 appears bigger than the one extracted from the signal coming both from β_1 and β_2. To conclude the Fermi surface pocket β shows at low magnetic field a g factor anisotropy comparable to the g factor anisotropy of α Fermi surface pocket and this

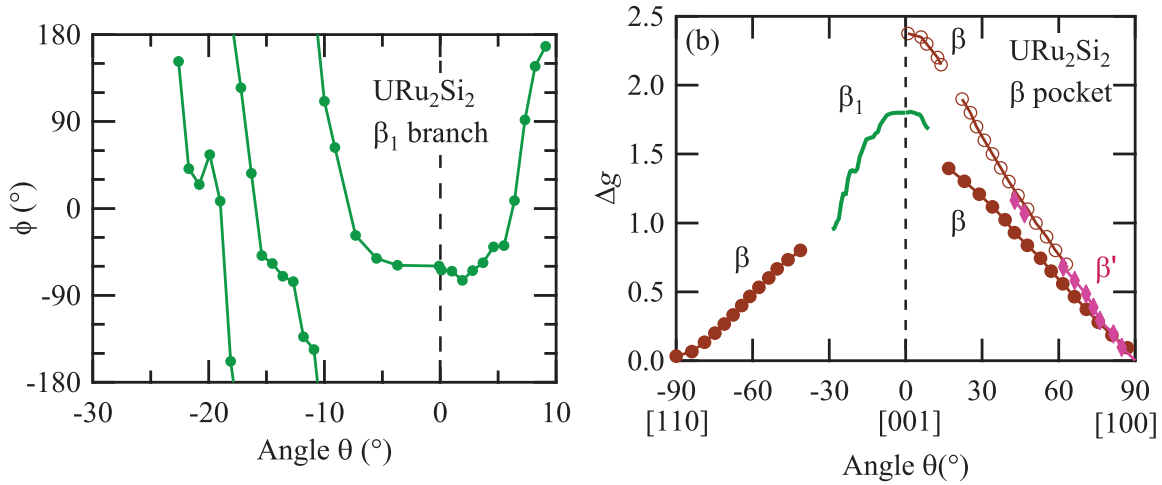

FIG. 6.20 (a) Phase of quantum oscillations from β_1 branch. (b) g factor variation Δg as a function of the field direction for β branch in brown, β_1 in green and β' in pink. Open and full symbols correspond respectively to the field intervals 6 T-9 T and 12 T-15 T. The different curves represent variations with angle and are shifted arbitrary in the vertical direction.

anisotropy is reduced under magnetic field due to the reduction of the Zeeman effect of the majority band.

The variation of the g factor for β' branch on the field interval 12 T-15 T with angle from [001] to [100] was extracted from quantum oscillation interferences. The effective mass for β' could have been measured only under magnetic field along [100] at $m^\star_\beta = 20.6\, m_0$. This mass is considered as angle independent. The resulting g factor variation is represented in figure 6.20(b). It is slightly stronger than the variation of the g factor of the β branch on the same field interval. The spin splitting of β' quantum oscillation frequency was reported in reference [Hassinger et al. (2010c)]. Thus the g factor anisotropy for β' orbit must get reduced under magnetic field as observed for the β orbit.

6.6 Discussion of the g factor anisotropy in URu_2Si_2

The spin zero measurement for the α pocket from reference [Ohkuni et al. (1999)] was analyzed in reference [Altarawneh et al. (2012)]. The value of the unknown integer number r was chosen in their analysis such that the g factor along [001] corresponds to the g factor value extracted from the upper critical field H_{c2} value assuming a pure Pauli limit. However the analysis of the H_{c2} reported in this thesis and the one which had been reported before in [**?**] show, that the orbital limit must also be taken into account. Moreover while the g factor from quantum oscillations is an average along an extremal orbit on a single Fermi surface pocket, the g factor from the upper critical field is an average on the whole Fermi

surface as pointed out in reference [Mineev (2015b)]. The other heavy bands of the Fermi surface such as the β branch must also contribute to the superconductivity, so the analysis in reference [Altarawneh et al. (2012)] assumes the homogeneity of the g factor in URu_2Si_2 Fermi surface. The experiment reported here shows a g factor anisotropy between [001] and [100] for the α and β Fermi surface pockets and the possibility of a g factor anisotropy for the γ Fermi surface pocket. The g factor anisotropy observed for the α pocket and the one estimated for the β pocket at low magnetic field are much stronger than the one extracted from the H_{c2} analysis.

The upper critical field study suggests a very small value of the g factor along [001] in good agreement with the previous bandstructure calculation and NMR studies reported in section 6.1.4 [Werwiński et al. (2014), Hattori et al. (2016)]. Thus we can consider the most anisotropic case for the g factor values between the different possibilities corresponding to different values of the integer r. For both γ and α branch the g factor can in this case be fitted by the law $g(\theta) = g([001])\cos(\theta)$ like the g factor extracted from the upper critical field. This fit corresponds to an uniaxial g factor, so an Ising behavior for the quasiparticles. It was noticed in reference [Trinh et al. (2016)], that the angular dependent part of the magnetic susceptibility $\chi - \chi_a$ at 18 K would be proportional to $\cos^2(\theta)$ giving also a g factor anisotropy proportional to $\cos(\theta)$.

The behavior of the heavy band β under magnetic field is different from the behavior of α and γ branch. Indeed under magnetic field along [001] the Zeeman effect of the majority band for β pocket gets weaker and weaker under magnetic field. Thus the g factor anisotropy gets smaller and smaller under magnetic field. The g factor anisotropy at zero field seems to be similar to the g factor anisotropy for the α branch. The effective mass of the majority spin pocket increases with the magnetic field.

The majority spin β Fermi surface pocket shows a reduction of the Zeeman effect and a strong increases of the effective mass under magnetic field. This Fermi surface change can be compared to the field induced Fermi surface instabilities in UCoGe discussed in chapter 4.2.2. It must also be due to the strong polarization of the small and heavy electron Fermi surface pocket under magnetic field along the easy magnetization axis c. Thermopower measurements in URu_2Si_2 under magnetic field along the c axis shows a minimum at $H_m = 11$ T at low temperature [Malone et al. (2011), Pourret et al. (2013b)]. It indicates also an evolution of the Fermi surface with magnetic field. However while anomalies in thermopower in UCoGe were not shifted with temperature as expected for a Fermi surface instabilities, the anomaly at $H_m = 11$ T in URu_2Si_2 is shifted to higher magnetic field with temperature. It suggests an interplay between the hidden order and the Fermi surface instabilities in URu_2Si_2. The increase of the effective masses of the majority spin β Fermi surface pocket in

URu_2Si_2 with magnetic field is in contradiction with the field dependence of effective mass predicted for an Hubbard model discussed in section 1.5.2 [Korbel et al. (1995)]. However URu_2Si_2 is a complex multiband system and the evolution of Fermi surface properties with magnetic field depends on the detail of the Fermi surface. Further field induced Fermi surface changes inside the hidden order state were observed above $H_m = 11$ T by Hall effect [Shishido et al. (2009)], thermopower [Malone et al. (2011), Pourret et al. (2013b)] and quantum oscillations [Altarawneh et al. (2011), Aoki et al. (2012), Scheerer et al. (2014)].

An anisotropy of the g factor in the basal plane was also observed for the α branch. The upper critical field does not show any anisotropy in the basal plane, however it corresponds to an average on the whole Fermi surface. The Fermi surface of URu_2Si_2 represented in figure 6.3 is far to be invariant in the basal plane. Thus it allows an anisotropy of microscopic properties in the basal plane, even if macroscopic properties such as magnetic susceptibility and upper critical field do not show this anisotropy. The anisotropy in the basal plane was also excluded by DFT bandstructure calculation [Werwiński et al. (2014)].

6.7 Conclusion on URu_2Si_2

The quantum oscillation experiments in URu_2Si_2 performed in this thesis are in full agreement with previous reports. In particular, the experiments show the characteristics of a light band λ of the Fermi surface of URu_2Si_2. This light band was not predicted by the band calculation studies [Elgazzar et al. (2009), Ikeda et al. (2012), Werwiński et al. (2014)]. A strong macroscopic g factor anisotropy was deduced from the analysis of the upper critical field. The microscopic study from quantum oscillations shows a g factor anisotropy for α and β branches and does not exclude any g factor anisotropy for the γ branch. This g factor anisotropy allows the possibilities of a chiral density wave and a hastatic order in the hidden order state [Mineev (2015b), Chandra et al. (2013)]. These results should be compared to new band calculation studies to complete the microscopic study of the g factor anisotropy. The contribution of the different bands to the hidden order state and the superconductivity could be discussed from this analysis. The β pocket in URu_2Si_2 shows a non linear Zeeman effect and a spin dependence of the effective mass, showing the effect of the magnetic polarization on the Fermi surface of URu_2Si_2. A bandstructure calculation under magnetic field is also needed for a better understanding of the causes of these Fermi surface reconstructions induced under magnetic field in URu_2Si_2. Finally the analysis of the g factor for the α branch suggests an additional g factor anisotropy in the basal plane, which is not observed in the macroscopic measurements. More experiments under magnetic field in the basal plane are needed to conclude about the in plane anisotropy.

Conclusion

The measurement of the pressure–temperature phase diagram of UCoGe revealed a broad superconducting dome around the critical pressure $p_c \approx 1$ GPa up to 4 GPa. The analysis of the upper critical under hydrostatic pressure confirms, that superconductivity in the ferromagnetic and in the paramagnetic state is induced by ferromagnetic fluctuations. The study of the temperature dependence of the resistivity and of the study of the upper critical field show both, that strong magnetic fluctuations are present in the entire pressure range of the superconducting dome. They also show, that these fluctuations are strongly suppressed under the application of a magnetic field along the easy magnetization axis c. A quantum oscillation experiment under high pressure shows no Fermi surface change at the critical pressure between the ferromagnetic and the paramagnetic states.

The quantum oscillation study in UCoGe and URhGe reveal several heavy Fermi surface pockets, with some agreement with bandstructure calculations. Two field induced Lifshitz transitions and two other Fermi surface changes were observed in UCoGe under magnetic field along the easy magnetization axis c. Similar anomalies in the resistivity and a non linear Zeeman effect were also observed in the other ferromagnetic superconductor URhGe. These Fermi surface instabilities would come from the strong polarization of the Fermi surface under magnetic field. New bandstructure-calculation studies, ARPES measurements and quantum oscillation study in higher quality samples are needed to characterize the Fermi surface of these two ferromagnetic superconductors. A challenge would be to calculate the bandstructure under magnetic field to characterize these field induced Fermi-surface instabilities in UCoGe and URhGe.

The Fermi surface in URu_2Si_2 was characterized by Shubnikov-de Haas oscillations. A strong g factor anisotropy was observed macroscopically from the upper critical field and microscopically for the α and β Fermi surface pocket. The α branch shows an additional g factor anisotropy in the basal plane. The β Fermi surface pocket shows non linear Zeeman effect and a strong field dependence of the effective mass under magnetic field along the easy magnetization axis. It indicates a strong polarization of the heavy Fermi surface pocket β. This measurement also confirms the existence of a light band λ in the Fermi surface

of URu_2Si_2. These results could allow new band calculation studies to discuss the role of the different pockets for the occurrence of the hidden order state, the unconventional superconductivity and the field induced Fermi-surface reconstructions.

Conclusion en français

L'étude du diagramme de phase pression–température d'UCoGe a montré que la supraconductivité peut être observée sur une grande gamme de champ autour de la pression critique $p_c \approx 1$ GPa jusqu'à 4 GPa. L'analyse du champ critique supérieur sous pression hydrostatique confirme, que les fluctuations magnétiques sont responsables de la supraconductivité aussi bien dans l'état ferromagnétique que dans l'état paramagnétique. La résistivité électrique et le champ critique supérieur montrent la présence de fortes fluctuations magnétiques sur une grande gamme de pression autour de la pression critique, qui peuvent être réduite par l'application d'un champ magnétique selon l'axe facile d'aimantation c. Enfin les mesures d'oscillations quantiques sous pression ne montrent pas de changement de surface de Fermi à la pression critique entre la phase ferromagnétique et la phase paramagnétique.

Plusieurs poches des surfaces de Fermi d'UCoGe et URhGe ont été détectées par les mesures d'oscillations quantiques. Elles montrent certaines similarités avec le calcul de structure de bandes. Deux transitions de Lifshitz et deux autres changements de surface de Fermi sont induits dans UCoGe, lorsqu'un champ magnétique est appliqué selon l'axe facile d'aimantation c. Des anomalies dans la magnétorésistance d'URhGe peuvent correspondre à des changements de surface de Fermi similaires à ceux qui ont été observés dans UCoGe. Les oscillations quantiques dans URhGe montrent également un effet Zeeman non linéaire. Toutes ces instabilités de surface de Fermi sont surement des conséquences d'une forte polarisation des bandes sous champ magnétique. De nouveaux calculs de structure de bandes, de nouvelles mesures d'ARPES et des mesures d'oscillations quantiques dans des échantillons d'une qualité supérieure sont nécessaire pour décrire de manière plus précise ces deux supraconducteurs ferromagnétiques. Un défi pour le calcul de bande serait de calculer la structure de bandes sous champ magnétique afin de caractériser les instabilités de surface de Fermi dans UCoGe et URhGe.

La surface de Fermi d'URu_2Si_2 a été caractérisée par des oscillations Shubnikov-de Haas. L'étude du champ critique supérieur a montré une forte anisotropie du facteur gyromagnétique g macroscopique. Les oscillations quantiques ont confirmé que les poches α et β de la surface de Fermi d'URu_2Si_2 présente cette anisotropie. La branche α présente

une anisotropie supplémentaire dans le plan basal. L'effet Zeeman de la poche de surface de Fermi β est non linéaire et sa masse effective dépend fortement du champ. Ces résultats indique une forte polarisation de la poche de surface de Fermi lourde β. La mesure d'oscillations quantiques dans URu_2Si_2 confirme également l'existence d'une poche légère λ, qui remet en cause l'interprétation des calculs de bandes dans URu_2Si_2. Tous ces résultats combinés avec de nouveaux calculs de bandes pourraient dévoiler le rôle des différentes poches de la surface de Fermi pour l'ordre caché, la supraconductivité non conventionnelle et les reconstructions de surface de Fermi induites sous champ magnétique.

References

Abdul-Jabbar, G., Sokolov, D. A., O'Neill, C. D., Stock, C., Wermeille, D., Demmel, F., Kruger, F., Green, A. G., Levy-Bertrand, F., Grenier, B., and Huxley, A. D. (2015). Modulated magnetism in PrPtAl. *Nat Phys*, 11(4):321–327.

Adamska, A. M., Havela, L., Surble, S., Heathman, S., Pospíšil, J., and Daniš, S. (2010). Pressure effect on the crystal lattice of unconventional superconductor UCoGe. *J. Phys.: Condens. Matter*, 22(27):275603.

Akazawa, T., Hidaka, H., Fujiwara, T., Kobayashi, T. C., Yamamoto, E., Haga, Y., Settai, R., and Ōnuki, Y. (2004). Pressure-induced superconductivity in ferromagnetic UIr without inversion symmetry. *J. Phys.: Condens. Matter*, 16(4):L29–L32.

Altarawneh, M. M., Harrison, N., Li, G., Balicas, L., Tobash, P. H., Ronning, F., and Bauer, E. D. (2012). Superconducting Pairs with Extreme Uniaxial Anisotropy in URu_2Si_2. *Phys. Rev. Lett.*, 108:066407.

Altarawneh, M. M., Harrison, N., Sebastian, S. E., Balicas, L., Tobash, P. H., Thompson, J. D., Ronning, F., and Bauer, E. D. (2011). Sequential Spin Polarization of the Fermi Surface Pockets in URu_2Si_2 and Its Implications for the Hidden Order. *Phys. Rev. Lett.*, 106:146403.

Amitsuka, H., Matsuda, K., Kawasaki, I., Tenya, K., Yokoyama, M., Sekine, C., Tateiwa, N., Kobayashi, T., Kawarazaki, S., and Yoshizawa, H. (2007). Pressure-temperature phase diagram of the heavy-electron superconductor. *J. Magn. Magn. Mater.*, 310(2, Part 1):214–220.

Amitsuka, H., Sato, M., Metoki, N., Yokoyama, M., Kuwahara, K., Sakakibara, T., Morimoto, H., Kawarazaki, S., Miyako, Y., and Mydosh, J. A. (1999). Effect of Pressure on tiny Antiferromagnetic Moment in the Heavy-Electron Compound URu_2Si_2. *Phys. Rev. Lett.*, 83:5114–5117.

Aoki, D., Bourdarot, F., Hassinger, E., Knebel, G., Miyake, A., Raymond, S., Taufour, V., and Flouquet, J. (2010). Field re-entrant hidden-order phase under pressure in URu_2Si_2. *J. Phys.: Condens. Matter*, 22(16):164205–.

Aoki, D. and Flouquet, J. (2014). Superconductivity and ferromagnetic quantum criticality in uranium compounds. *J. Phys. Soc. Jpn.*, 83(6):061011.

Aoki, D., Gourgout, A., Pourret, A., Bastien, G. B., Knebel, G., and Flouquet, J. (2014a). Spin fluctuation and fermi surface instability in ferromagnetic superconductors. *C. R. Phys.*, 15(7):630 – 639. Emergent phenomena in actinides.

Aoki, D., Hardy, F., Miyake, A., Taufour, V., Matsuda, T. D., and Flouquet, J. (2011a). Properties of ferromagnetic superconductors. *C. R. Phys.*, 12(5):573 – 583.

Aoki, D., Huxley, A., Ressouche, E., Braithwaite, D., Flouquet, J., Brison, J.-P., Lhotel, E., and Paulsen, C. (2001). Coexistence of superconductivity and ferromagnetism in URhGe. *Nature*, 413(6856):613–616.

Aoki, D., Knebel, G., and Flouquet, J. (2014b). Fermi Surface Instabilities in Ferromagnetic Superconductor URhGe. *J. Phys. Soc. Jpn.*, 83(9):094719–.

Aoki, D., Knebel, G., Sheikin, I., Hassinger, E., Malone, L., D. Matsuda, T., and Flouquet, J. (2012). High-Field Fermi Surface Properties in the Low-Carrier Heavy-Fermion Compound URu_2Si_2. *J. Phys. Soc. Jpn.*, 81(7):074715–.

Aoki, D., Matsuda, T. D., Hardy, F., Meingast, C., Taufour, V., Hassinger, E., Sheikin, I., Paulsen, C., Knebel, G., Kotegawa, H., and Flouquet, J. (2011b). Superconductivity reinforced by magnetic field and the magnetic instability in uranium ferromagnets. *J. Phys. Soc. Jpn.*, 80(Suppl.A):SA008.

Aoki, D., Matsuda, T. D., Taufour, V., Hassinger, E., Knebel, G., and Flouquet, J. (2009). Extremely Large and Anisotropic Upper Critical Field and the Ferromagnetic Instability in UCoGe. *J. Phys. Soc. Jpn.*, 78(11):113709.

Aoki, D., Seyfarth, G., Pourret, A., Gourgout, A., McCollam, A., Bruin, J. A. N., Krupko, Y., and Sheikin, I. (2016). Field-Induced Lifshitz Transition without Metamagnetism in $CeIrIn_5$. *Phys. Rev. Lett.*, 116:037202.

Aoki, D., Sheikin, I., Matsuda, T. D., Taufour, V., Knebel, G., and Flouquet, J. (2011c). First Observation of Quantum Oscillations in the Ferromagnetic Superconductor UCoGe. *J. Phys. Soc. Jpn.*, 80(1):013705.

Aoki, D., Wiśniewski, P., Miyake, K., Watanabe, N., Inada, Y., Settai, R., Yamamoto, E., Haga, Y., and Ōnuki, Y. (2000). Cylindrical Fermi surfaces formed by a fiat magnetic Brillouin zone in uranium dipnictides. *Philosophical Magazine Part B*, 80(8):1517–1544.

Aoki, H., Uji, S., Albessard, A., and Ōnuki, Y. (1993). dHvA Effect Study of Metamagnetic Transition in $CeRu_2Si_2$. *J. Phys. Soc. Jpn.*, 62(9):3157–3171.

Araki, S., Hayashida, M., Nishiumi, N., Manabe, H., Ikeda, Y., Kobayashi, T. C., Murata, K., Inada, Y., Wiśniewski, P., Aoki, D., Ōnuki, Y., Yamamoto, E., and Haga, Y. (2015). Pressure–Temperature–Field Phase Diagram in the Ferromagnet U_3P_4. *J. Phys. Soc. Jpn.*, 84(2):024705.

Araki, S., Nakashima, M., Nakawaki, H., Settai, R., Harima, H., and Ōnuki, Y. (2002). De Haas-van Alphen effect in $CeRh_2Si_2$ under pressure. *Physica B*, 312–313:435 – 436. The International Conference on Strongly Correlated Electron Systems.

Aynajian, P., da Silva Neto, E. H., Parker, C. V., Huang, Y., Pasupathy, A., Mydosh, J., and Yazdani, A. (2010). Visualizing the formation of the Kondo lattice and the hidden order in URu_2Si_2. *Proceedings of the National Academy of Sciences*, 107(23):10383–10388.

Bareille, C., Boariu, F. L., Schwab, H., Lejay, P., Reinert, F., and Santander-Syro, A. F. (2014). Momentum-resolved hidden-order gap reveals symmetry breaking and origin of entropy loss in URu_2Si_2. *Nat Commun*, 5:–.

Bastien, G., Braithwaite, D., Aoki, D., Knebel, G., and Flouquet, J. (2016). Quantum criticality in the ferromagnetic superconductor UCoGe under pressure and magnetic field. *Phys. Rev. B*, 94:125110.

Bauer, E., Bühler-Paschen, S., and Prokofiev, A. (2007). The Kondo Problem to Heavy Fermions.

Baumbach, R., Fisk, Z., Ronning, F., Movshovich, R., Thompson, J., and Bauer, E. (2014). High purity specimens of URu_2Si_2 produced by a molten metal flux technique. *Philos. Mag. B*, 94(32-33):3663–3671.

Bay, T. V., Nikitin, A. M., Naka, T., McCollam, A., Huang, Y. K., and de Visser, A. (2014). Angular variation of the magnetoresistance of the superconducting ferromagnet UCoGe. *Phys. Rev. B*, 89:214512.

Belitz, D., Kirkpatrick, T. R., and Rollbühler, J. (2005). Tricritical behavior in itinerant quantum ferromagnets. *Phys. Rev. Lett.*, 94:247205.

Belitz, D., Kirkpatrick, T. R., and Vojta, T. (1999). First order transitions and multicritical points in weak itinerant ferromagnets. *Phys. Rev. Lett.*, 82:4707–4710.

Bennemann, K. H. and Ketterson, J. B. (2014). *Novel Superfluids*, volume Vol. 2. Oxford University Press.

Bercx, M. and Assaad, F. F. (2012). Metamagnetism and lifshitz transitions in models for heavy fermions. *Phys. Rev. B*, 86:075108.

Bergemann, C., Julian, S., McMullan, G., Howard, B., Lonzarich, G., Lejay, P., Brison, J., and Flouquet, J. (1997). Quantum oscillations in URu_2Si_2. *Physica B*, 230:348–350.

Bireckoven, B. and Wittig, J. (1988). A diamond anvil cell for the investigation of superconductivity under pressures of up to 50 GPa: Pb as a low temperature manometer. *J. Phys. E: Sci. Instrum.*, 21(9):841–.

Blanter, Y., Kaganov, M., Pantsulaya, A., and Varlamov, A. (1994). The theory of electronic topological transitions. *Physics Reports*, 245(4):159 – 257.

Blundell, S. (2001). *Magnetism in condensed matter*. Oxford University Press.

Brando, M., Belitz, D., Grosche, F. M., and Kirkpatrick, T. R. (2016). Metallic quantum ferromagnets. *Rev. Mod. Phys.*, 88:025006.

Brison, J. P., Keller, N., Vernière, A., Lejay, P., Schmidt, L., Buzdin, A., Flouquet, J., Julian, S., and Lonzarich, G. (1995). Anisotropy of the upper critical field in URu_2Si_2 and FFLO state in antiferromagnetic superconductors. *Physica C: Superconductivity*, 250(1):128–138.

Broholm, C., Kjems, J. K., Buyers, W. J. L., Matthews, P., Palstra, T. T. M., Menovsky, A. A., and Mydosh, J. A. (1987). Magnetic excitations and ordering in the heavy-electron superconductor URu_2Si_2. *Phys. Rev. Lett.*, 58:1467–1470.

Bruin, J. A. N., Sakai, H., Perry, R. S., and Mackenzie, A. (2013). Similarities of Scattering Rates in Metals Showing T-linear Resistivity. *Science*, 339:804.

Buhmann, J. M. and Sigrist, M. (2013). Thermoelectric effect of correlated metals: Band-structure effects and the breakdown of Mott's formula. *Phys. Rev. B*, 88:115128.

Bulaevskii, L. N., Dolgov, O. V., and Ptitsyn, M. O. (1988). Properties of strong-coupled superconductors. *Phys. Rev. B*, 38:11290–11295.

Butchers, M. W., Duffy, J. A., Taylor, J. W., Giblin, S. R., Dugdale, S. B., Stock, C., Tobash, P. H., Bauer, E. D., and Paulsen, C. (2015). Determination of spin and orbital magnetization in the ferromagnetic superconductor UCoGe. *Phys. Rev. B*, 92:121107.

Chandra, P., Coleman, P., and Flint, R. (2013). Hastatic order in the heavy-fermion compound URu2Si2. *Nature*, 493(7434):621–626.

Clogston, A. M. (1962). Upper limit for the critical field in hard superconductors. *Phys. Rev. Lett.*, 9:266–267.

Coleman, P. (2012). *Introduction to Many Body Physics*.

Coleman, P., Pépin, C., Si, Q., and Ramazashvili, R. (2001). How do fermi liquids get heavy and die? *J. Phys.: Condens. Matter*, 13(35):R723–.

Cooper, R. A., Wang, Y., Vignolle, B., Lipscombe, O. J., Hayden, S. M., Tanabe, Y., Adachi, T., Koike, Y., Nohara, M., Takagi, H., Proust, C., and Hussey, N. E. (2009). Anomalous criticality in the electrical resistivity of $La_{2-x}Sr_xCuO_4$. *Science (New York, N.Y.)*, 323(5914):603–607.

Daou, R., Bergemann, C., and Julian, S. R. (2006). Continuous Evolution of the Fermi Surface of $CeRu_2Si_2$ across the Metamagnetic Transition. *Phys. Rev. Lett.*, 96:026401.

Daou, R., Doiron-Leyraud, N., LeBoeuf, D., Li, S. Y., Laliberte, F., Cyr-Choiniere, O., Jo, Y. J., Balicas, L., Yan, J.-Q., Zhou, J.-S., Goodenough, J. B., and Taillefer, L. (2009). Linear temperature dependence of resistivity and change in the Fermi surface at the pseudogap critical point of a high-Tc superconductor. *Nat. Phys.*, 5(1):31–34.

de la Mora, P. and Navarro, O. (2009). Magnetic stripes in the UCoGe superconductor. *Journal of Physics: Conference Series*, 167(1):012015.

de Nijs, D. E., Huy, N. T., and de Visser, A. (2008). Simultaneous suppression of ferromagnetism and superconductivity in UCoGe by Si substitution. *Phys. Rev. B*, 77:140506.

de Visser, A., Huy, N. T., Gasparini, A., de Nijs, D. E., Andreica, D., Baines, C., and Amato, A. (2009). Muon Spin Rotation and Relaxation in the Superconducting Ferromagnet UCoGe. *Phys. Rev. Lett.*, 102:167003.

Deguchi, K., Osaki, E., Ban, S., Tamura, N., Simura, Y., Sakakibara, T., Satoh, I., and K. Sato, N. (2010). Absence of Meissner State and Robust Ferromagnetism in the Superconducting State of UCoGe: Possible Evidence of Spontaneous Vortex State. *J. Phys. Soc. Jpn.*, 79(8):083708–.

Diviš, M. (2008). Electronic structure and magnetism of UCoGe from first principles. *Physica B*, 403(13-16):2505–2508.

Dmowski, L. H. and Litwin-Staszewska, E. (1999). The variation of the pressure coefficient of manganin sensors at low temperatures. *Meas. Sci. Technol.*, 10(5):343–.

Doiron-Leyraud, N., Auban-Senzier, P., René de Cotret, S., Bourbonnais, C., Jérome, D., Bechgaard, K., and Taillefer, L. (2009). Correlation between linear resistivity and T_c in the Bechgaard salts and the pnictide superconductor $Ba(Fe_{1-x}Co_x)_2As_2$. *Phys. Rev. B*, 80:214531.

Doniach, S. (1977). The Kondo lattice and weak antiferromagnetism. *Physica B+C*, 91:231 – 234.

Edwards, D. and Green, A. (1997). Heavy fermions in high magnetic fields. *Zeitschrift fur Physik B*.

Elgazzar, S., Rusz, J., Amft, M., Oppeneer, P. M., and Mydosh, J. A. (2009). Hidden order in URu_2Si_2 originates from Fermi surface gapping induced by dynamic symmetry breaking. *Nat. Mater.*, 8(4):337–341.

Éliashberg, G. M. (1960). Interactions between electrons and lattice vibrations in a superconductor. *Soviet Physics JETP*.

Fay, D. and Appel, J. (1980). Coexistence of *p*-state superconductivity and itinerant ferromagnetism. *Phys. Rev. B*, 22:3173–3182.

Fernandez Pañella, A. (2012). PhD thesis, Université Joseph Fourrier.

Flouquet, J. (2005). On the Heavy Fermion Road. In Halperin, W., editor, *Progress Low Temperature Physics*, volume 15 of *Progress in Low Temperature Physics*, pages 139 – 281. Elsevier.

Fujimori, S.-i., Kawasaki, I., Yasui, A., Takeda, Y., Okane, T., Saitoh, Y., Fujimori, A., Yamagami, H., Haga, Y., Yamamoto, E., and Ōnuki, Y. (2014). Itinerant magnetism in URhGe revealed by angle-resolved photoelectron spectroscopy. *Phys. Rev. B*, 89:104518.

Fujimori, S.-i., Ohkochi, T., Kawasaki, I., Yasui, A., Takeda, Y., Okane, T., Saitoh, Y., Fujimori, A., Yamagami, H., Haga, Y., Yamamoto, E., and Ōnuki, Y. (2015). Electronic structures of ferromagnetic superconductors UGe_2 and UCoGe studied by angle-resolved photoelectron spectroscopy. *Phys. Rev. B*, 91:174503.

Fujimori, S.-i., Ohkochi, T., Kawasaki, I., Yasui, A., Takeda, Y., Okane, T., Saitoh, Y., Fujimori, A., Yamagami, H., Haga, Y., Yamamoto, E., Tokiwa, Y., Ikeda, S., Sugai, T., Ohkuni, H., Kimura, N., and Ōnuki, Y. (2011). Electronic Structure of Heavy Fermion Uranium Compounds Studied by Core-Level Photoelectron Spectroscopy. *J. Phys. Soc. Jpn.*, 81(1):014703–.

Gegenwart, P., Custers, J., Geibel, C., Neumaier, K., Tayama, T., Tenya, K., Trovarelli, O., and Steglich, F. (2002). Magnetic-field induced quantum critical point in $YbRh_2Si_2$. *Phys. Rev. Lett.*, 89(5):056402.

Glémot, L., Brison, J. P., Flouquet, J., Buzdin, A. I., Sheikin, I., Jaccard, D., Thessieu, C., and Thomas, F. (1999). Pressure Dependence of the Upper Critical Field of the Heavy Fermion Superconductor UBe_{13}. *Phys. Rev. Lett.*, 82:169–172.

Gourgout, A. (2017). *Fermi surface instatbilities with and without magnetic transition*. PhD thesis, Université Grenoble Alpes.

Gourgout, A., Pourret, A., Knebel, G., Aoki, D., Seyfarth, G., and Flouquet, J. (2016). Collapse of Ferromagnetism and Fermi Surface Instability near Reentrant Superconductivity of URhGe. *Phys. Rev. Lett.*, 117:046401.

Hardy, F., Aoki, D., Meingast, C., Schweiss, P., Burger, P., v. Löhneysen, H., and Flouquet, J. (2011). Transverse and longitudinal magnetic-field responses in the Ising ferromagnets URhGe, UCoGe, and UGe_2. *Phys. Rev. B*, 83:195107.

Hardy, F., Huxley, A., Flouquet, J., Salce, B., Knebel, G., Braithwaite, D., Aoki, D., Uhlarz, M., and Pfleiderer, C. (2005). Phase diagram of the ferromagnetic superconductor URhGe. *Physica B: Condensed Matter*, 359–361:1111 – 1113. Proceedings of the International Conference on Strongly Correlated Electron Systems.

Hardy, F. and Huxley, A. D. (2005). p-Wave Superconductivity in the Ferromagnetic Superconductor URhGe. *Phys. Rev. Lett.*, 94:247006.

Harrison, N., Moll, P. J. W., Sebastian, S. E., Balicas, L., Altarawneh, M. M., Zhu, J.-X., Tobash, P. H., Ronning, F., Bauer, E. D., and Batlogg, B. (2013). Magnetic field-tuned localization of the $5f$-electrons in URu_2Si_2. *Phys. Rev. B*, 88:241108.

Hassinger, E., Aoki, D., Bourdarot, F., Knebel, G., Taufour, V., Raymond, S., Villaume, A., and Flouquet, J. (2010a). Suppression of hidden order in URu_2Si_2 under pressure and restoration in magnetic field. *Journal of Physics: Conference Series*, 251(1):012001.

Hassinger, E., Aoki, D., Knebel, G., and Flouquet, J. (2008a). Pressure-temperature phase diagram of polycrystalline UCoGe studied by resistivity measurement. *J. Phys. Soc. Jpn.*, 77(7):073703.

Hassinger, E., Aoki, D., Knebel, G., and Flouquet, J. (2010b). Pressure-phase diagram of UCoGe by ac-susceptibility and resistivity measurements. *J. Phys.: Conf. Series*, 200(1):012055.

Hassinger, E., Knebel, G., Izawa, K., Lejay, P., Salce, B., and Flouquet, J. (2008b). Temperature-pressure phase diagram of URu_2Si_2 from resistivity measurements and ac calorimetry: Hidden order and Fermi-surface nesting. *Phys. Rev. B*, 77:115117.

Hassinger, E., Knebel, G., Matsuda, T. D., Aoki, D., Taufour, V., and Flouquet, J. (2010c). Similarity of the Fermi Surface in the Hidden Order State and in the Antiferromagnetic State of URu_2Si_2. *Phys. Rev. Lett.*, 105:216409.

Hattori, T., Ihara, Y., Nakai, Y., Ishida, K., Tada, Y., Fujimoto, S., Kawakami, N., Osaki, E., Deguchi, K., Sato, N. K., and Satoh, I. (2012). Superconductivity Induced by Longitudinal Ferromagnetic Fluctuations in UCoGe. *Phys. Rev. Lett.*, 108:066403.

Hattori, T., Karube, K., Ishida, K., Deguchi, K., Sato, N. K., and Yamamura, T. (2014). Relationship between Ferromagnetic Criticality and the Enhancement of Superconductivity Induced by Transverse Magnetic Fields in UCoGe. *J. Phys. Soc. Jpn.*, 83(7):073708.

Hattori, T., Sakai, H., Tokunaga, Y., Kambe, S., Matsuda, T. D., and Haga, Y. (2016). No Detectable Change in In-Plane ^{29}Si Knight Shift in the Superconducting State of URu_2Si_2. *J. Phys. Soc. Jpn.*, 85(7):073711–.

Hegger, H., Petrovic, C., Moshopoulou, E. G., Hundley, M. F., Sarrao, J. L., Fisk, Z., and Thompson, J. D. (2000). Pressure-Induced Superconductivity in Quasi-2D $CeRhIn_5$. *Phys. Rev. Lett.*, 84:4986–4989.

Holmes, A. T., Jaccard, D., and Miyake, K. (2004). Signatures of valence fluctuations in $CeCu_2Si_2$ under high pressure. *Phys. Rev. B*, 69(2):024508.

Hoshino, S. and Kuramoto, Y. (2013). Itinerant versus localized heavy-electron magnetism. *Phys. Rev. Lett.*, 111:026401.

Huy, N. T., de Nijs, D. E., Huang, Y. K., and de Visser, A. (2008). Unusual Upper Critical Field of the Ferromagnetic Superconductor UCoGe. *Phys. Rev. Lett.*, 100:077002.

Huy, N. T., Gasparini, A., de Nijs, D. E., Huang, Y., Klaasse, J. C. P., Gortenmulder, T., de Visser, A., Hamann, A., Görlach, T., and Löhneysen, H. v. (2007a). Superconductivity on the Border of Weak Itinerant Ferromagnetism in UCoGe. *Phys. Rev. Lett.*, 99:067006.

Huy, N. T., Gasparini, A., Klaasse, J. C. P., de Visser, A., Sakarya, S., and van Dijk, N. H. (2007b). Ferromagnetic quantum critical point in URhGe doped with Ru. *Phys. Rev. B*, 75:212405.

Ikeda, H., Suzuki, M.-T., Arita, R., Takimoto, T., Shibauchi, T., and Matsuda, Y. (2012). Emergent rank-5 nematic order in URu_2Si_2. *Nat. Phys.*, 8(7):528–533.

Imada, M., Misawa, T., and Yamaji, Y. (2010). Unconventional quantum criticality emerging as a new common language of transition-metal compounds, heavy-fermion systems, and organic conductors. *Journal of Physics: Condensed Matter*, 22(16):164206–.

Izawa, K., Yamaguchi, H., Matsuda, Y., Shishido, H., Settai, R., and Ōnuki, Y. (2001). Angular Position of Nodes in the Superconducting Gap of Quasi-2D Heavy-Fermion Superconductor $CeCoIn_5$. *Phys. Rev. Lett.*, 87:057002.

Jaccard, D., Behnia, K., and Sierro, J. (1992). Pressure induced heavy fermion superconductivity of cecu2ge2. *Physics Letters A*, 163(5):475–480.

Jarlborg, T. and Bianconi, A. (2016). Breakdown of the Migdal approximation at Lifshitz transitions with giant zero-point motion in the H_3S superconductor. *Sci. Rep.*, 6:24816–.

Jian, X., Zhang, J., Gu, Q., and Klemm, R. A. (2009). Enhancement of ferromagnetism by *p*-wave cooper pairing in superconducting ferromagnets. *Phys. Rev. B*, 80:224514.

Jiao, L., Chen, Y., Kohama, Y., Graf, D., Bauer, E. D., Singleton, J., Zhu, J.-X., Weng, Z., Pang, G., Shang, T., Zhang, J., Lee, H.-O., Park, T., Jaime, M., Thompson, J. D., Steglich, F., Si, Q., and Yuan, H. Q. (2015). Fermi surface reconstruction and multiple quantum phase transitions in the antiferromagnet $CeRhIn_5$. *Proceedings of the National Academy of Sciences*, 112(3):673–678.

Joseph, A. S. and Thorsen, A. C. (1964). Low-Field de Haas-van Alphen Effect in Copper. *Phys. Rev.*, 134:A979–A980.

Kabeya, N., Maekawa, H., Deguchi, K., Kimura, N., Aoki, H., and Sato, N. K. (2012). Non-Fermi Liquid State Bounded by a Possible Electronic Topological Transition in $ZrZn_2$. *J. Phys. Soc. Jpn.*, 81(7):073706.

Kadowaki, K. and Woods, S. (1986). Universal relationship of the resistivity and specific heat in heavy-fermion compounds. *Solid State Communications*, 58(8):507–509.

Karahasanovic, U., Krüger, F., and Green, A. G. (2012). Quantum order-by-disorder driven phase reconstruction in the vicinity of ferromagnetic quantum critical points. *Phys. Rev. B*, 85:165111.

Khan, S. N. and Johnson, D. D. (2014). Lifshitz Transition and Chemical Instabilities in $Ba_{1-x}K_xFe_2As_2$ Superconductors. *Phys. Rev. Lett.*, 112:156401.

Kittaka, S., Shimizu, Y., Sakakibara, T., Haga, Y., Yamamoto, E., Ōnuki, Y., Tsutsumi, Y., Nomoto, T., Ikeda, H., and Machida, K. (2016). Evidence for Chiral d-Wave Superconductivity in URu_2Si_2 from the Field-Angle Variation of Its Specific Heat. *J. Phys. Soc. Jpn.*, 85(3):033704–.

Knafo, W., Matsuda, T. D., Aoki, D., Hardy, F., Scheerer, G. W., Ballon, G., Nardone, M., Zitouni, A., Meingast, C., and Flouquet, J. (2012). High-field moment polarization in the ferromagnetic superconductor UCoGe. *Phys. Rev. B*, 86:184416.

Knebel, G., Aoki, D., Brison, J.-P., and Flouquet, J. (2008). The Quantum Critical Point in $CeRhIn_5$: A Resistivity Study. *J. Phys. Soc. Jpn.*, 77(11):114704.

Knebel, G., Braithwaite, D., Lapertot, G., Canfield, P., and Flouquet, J. (2001). Magnetically ordered Kondo lattice in $YbNi_2Ge_2$ at high pressure. *J. Phys.: Condens. Matter*, 13:10935.

Kobayashi, T. C., Hanazono, N., Tateiwa, N., Amaya, K., Haga, Y., Settai, R., and Ōnuki, Y. (2002). Pressure-induced superconductivity in a ferromagnet , UGe_2 : resistivity measurements in a magnetic field. *J. Phys. Condens. Matter*, 14:10779.

Korbel, P., Spałek, J., Wójcik, W., and Acquarone, M. (1995). Spin-split masses and metamagnetic behavior of almost-localized fermions. *Phys. Rev. B*, 52:R2213–R2216.

Kotegawa, H., Fukumoto, K., Toyama, T., Tou, H., Harima, H., Harada, A., Kitaoka, Y., Haga, Y., Yamamoto, E., Ōnuki, Y., Itoh, K. M., and Haller, E. E. (2015). ^{73}Ge-Nuclear Magnetic Resonance/Nuclear Quadrupole Resonance Investigation of Magnetic Properties of URhGe. *J. Phys. Soc. Jpn.*, 84(5):054710.

Kubo, K. (2013). Ferromagnetism and Fermi surface transition in the periodic Anderson model: Second-order phase transition without symmetry breaking. *Phys. Rev. B*, 87:195127.

Kubo, K. (2015). Lifshitz Transitions in Magnetic Phases of the Periodic Anderson Model. *Journal of the Physical Society of Japan*, 84(9):094702.

Kung, H.-H., Baumbach, R. E., Bauer, E. D., Thorsmølle, V. K., Zhang, W.-L., Haule, K., Mydosh, J. A., and Blumberg, G. (2015). Chirality density wave of the "hidden order" phase in URu_2Si_2. *Science*, 347(6228):1339–1342.

Kusunose, H. (2012). Magnetic Exciton Mediated Superconductivity in the Hidden-Order Phase of URu_2Si_2. *J. Phys. Soc. Jpn.*, 81(2):023704–.

Landau, L. D. (1957). The Theory of a Fermi Liquid. *Soviet Physics JETP*.

LeBoeuf, D., Doiron-Leyraud, N., Vignolle, B., Sutherland, M., Ramshaw, B. J., Levallois, J., Daou, R., Laliberté, F., Cyr-Choinière, O., Chang, J., Jo, Y. J., Balicas, L., Liang, R., Bonn, D. A., Hardy, W. N., Proust, C., and Taillefer, L. (2011). Lifshitz critical point in the cuprate superconductor $YBa_2Cu_3O_y$ from high-field Hall effect measurements. *Phys. Rev. B*, 83:054506.

Lee, P. A., Nagaosa, N., and Wen, X.-G. (2006). Doping a Mott insulator: Physics of high-temperature superconductivity. *Rev. Mod. Phys.*, 78:17.

Leggett, A. J. (1975). A theoretical description of the new phases of liquid ^{3}He. *Rev. Mod. Phys.*, 47:331–414.

Lévy, F., Sheikin, I., Grenier, B., and Huxley, A. D. (2005). Magnetic Field-Induced Superconductivity in the Ferromagnet URhGe. *Science*, 309(5739):1343–.

Lévy, F., Sheikin, I., Grenier, B., Marcenat, C., and Huxley, A. (2009). Coexistence and interplay of superconductivity and ferromagnetism in URhGe. *J. Phys.: Condens. Matter*, 21(16):164211.

Lifshitz, I. M. and Kaganov, M. I. (1963). Some problems of the electron theory of metals II. Statistical mechanichs and thermodynamics of electrons in metals . *Soviet Physics Uspekhi*, 5(6):878.

Lithgow, C. (2015). Poster at icm conference in barcelona.

Liu, C.-C., Zhou, J.-J., Yao, Y., and Zhang, F. (2016). Weak Topological Insulators and Composite Weyl Semimetals: β-Bi_4X_4 ($X = $ Br, I). *Phys. Rev. Lett.*, 116:066801.

MacLaughlin, D. E., Cooke, D. W., Heffner, R. H., Hutson, R. L., McElfresh, M. W., Schillaci, M. E., Rempp, H. D., Smith, J. L., Willis, J. O., Zirngiebl, E., Boekema, C., Lichti, R. L., and Oostens, J. (1988). Muon spin rotation and magnetic order in the heavy-fermion compound URu_2Si_2. *Phys. Rev. B*, 37:3153–3158.

Malone, L., Howald, L., Pourret, A., Aoki, D., Taufour, V., Knebel, G., and Flouquet, J. (2012). Thermoelectricity of the ferromagnetic superconductor UCoGe. *Phys. Rev. B*, 85:024526.

Malone, L., Matusda, T. D., Antunes, A., Knebel, G., Taufour, V., Aoki, D., Behnia, K., Proust, C., and Flouquet, J. (2011). Thermoelectric evidence for high-field anomalies in the hidden order phase of URu_2Si_2. *Phys. Rev. B*, 83:245117.

Maple, M. B., Chen, J. W., Dalichaouch, Y., Kohara, T., Rossel, C., Torikachvili, M. S., McElfresh, M. W., and Thompson, J. D. (1986). Partially gapped Fermi surface in the heavy-electron superconductor URu_2Si_2. *Phys. Rev. Lett.*, 56:185–188.

Mathur, N. D., Grosche, F. M., Julian, S. R., Walker, I. R., Freye, D. M., Haselwimmer, R. K. W., and Lonzarich, G. G. (1998). Magnetically mediated superconductivity in heavy fermion compounds. *Nature*, 394(6688):39–43.

McMillan, W. L. (1968). Transition Temperature of Strong-Coupled Superconductors. *Phys. Rev.*, 167:331–344.

McMullan, G. J., Rourke, P. M. C., Norman, M. R., Huxley, A. D., Doiron-Leyraud, N., Flouquet, J., Lonzarich, G. G., McCollam, A., and Julian, S. R. (2008). The Fermi surface and f-valence electron count of UPt_3. *New Journal of Physics*, 10(5):053029–.

Meng, J.-Q., Oppeneer, P. M., Mydosh, J. A., Riseborough, P. S., Gofryk, K., Joyce, J. J., Bauer, E. D., Li, Y., and Durakiewicz, T. (2013). Imaging the Three-Dimensional Fermi-Surface Pairing near the Hidden-Order Transition in URu_2Si_2 Using Angle-Resolved Photoemission Spectroscopy. *Phys. Rev. Lett.*, 111:127002.

Millis, A. J. (1993). Effect of a nonzero temperature on quantum critical points in itinerant fermion systems. *Phys. Rev. B*, 48(10):7183–7196.

Mineev, V. P. (1999). *Introduction to Unconventional Superconductivity*. Gordon and Breach Science.

Mineev, V. P. (2002). Superconducting states in ferromagnetic metals. *Phys. Rev. B*, 66:134504.

Mineev, V. P. (2008). Pressure-Temperature Phase Diagram of Ferromagnetic Superconductors. *J. Phys. Soc. Jpn.*, 77(10):103702–.

Mineev, V. P. (2010). Paramagnetic limit in ferromagnetic superconductors with triplet pairing. *Phys. Rev. B*, 81:180504.

Mineev, V. P. (2011). Magnetic field dependence of pairing interaction in ferromagnetic superconductors with triplet pairing. *Phys. Rev. B*, 83:064515.

Mineev, V. P. (2015a). Reentrant superconductivity in urhge. *Phys. Rev. B*, 91:014506.

Mineev, V. P. (2015b). Uru_2si_2: hidden order and amplitude of quantum oscillations. *arxiv*:1504.05020.

Miyake, A., Aoki, D., and Flouquet, J. (2008). Field Re-entrant Superconductivity Induced by the Enhancement of Effective Mass in URhGe. *J. Phys. Soc. Jpn.*, 77(9):094709.

Miyake, A., Aoki, D., and Flouquet, J. (2009). Pressure Evolution of the Ferromagnetic and Field Re-entrant Superconductivity in URhGe. *J. Phys. Soc. Jpn.*, 78(6):063703–.

Miyake, K. and Watanabe, S. (2014). Unconventional quantum criticality due to critical valence transition. *J. Phys. Soc. Jpn.*, 83(6):061006.

Monthoux, P. and Lonzarich, G. G. (2001). Magnetically mediated superconductivity in quasi-two and three dimensions. *Phys. Rev. B*, 63:054529.

Monthoux, P. and Lonzarich, G. G. (2002). Magnetically mediated superconductivity: Crossover from cubic to tetragonal lattice. *Phys. Rev. B*, 66:224504.

Moriya, T. (1985). *Spin Fluctuations in Itinerant Electron Magnetism*. Springer-Verlag.

Moriya, T. (2003). *Acta Phys. Pol.*, B34:287.

Motoyama, G., Nishioka, T., and Sato, N. K. (2003). Phase Transition between Hidden and Antiferromagnetic Order in URu_2Si_2. *Phys. Rev. Lett.*, 90:166402.

Mydosh, J. and Oppeneer, P. (2014). Hidden order behaviour in URu_2Si_2 (A critical review of the status of hidden order in 2014). *Philos. Mag.*, 94(32-33):3642–3662.

Mydosh, J. A. and Oppeneer, P. M. (2011). *Colloquium* : Hidden order, superconductivity, and magnetism: The unsolved case of URu_2Si_2. *Rev. Mod. Phys.*, 83:1301–1322.

Nagaosa, N., Sinova, J., Onoda, S., MacDonald, A. H., and Ong, N. P. (2010). Anomalous hall effect. *Rev. Mod. Phys.*, 82:1539–1592.

Nakamura, S. e. a. (2016). to be published.

Niklowitz, P., Beckers, F., Lonzarich, G., Knebel, G., Salce, B., Thomasson, J., Bernhoeft, N., Braithwaite, D., and Flouquet, J. (2005). Spin-fluctuation-dominated electrical transport of Ni_3Al at high pressure. *Phys. Rev. B*, 72(2):1–10.

Ohkuni, H., Inada, Y., Tokiwa, Y., Sakurai, K., Settai, R., Honma, T., Haga, Y., Yamamoto, E., Ōnuki, Y., Yamagami, H., Takahashi, S., and Yanagisawa, T. (1999). Fermi surface properties and de Haas–van Alphen oscillation in both the normal and superconducting mixed states of URu_2Si_2. *Philosophical Magazine Part B*, 79(7):1045–1077.

Ohta, T., Hattori, T., Ishida, K., Nakai, Y., Osaki, E., Deguchi, K., Sato, N. K., and Satoh, I. (2010). Microscopic Coexistence of Ferromagnetism and Superconductivity in Single-Crystal UCoGe. *J. Phys. Soc. Jpn.*, 79(2):023707.

Okazaki, R., Kasahara, Y., Shishido, H., Konczykowski, M., Behnia, K., Haga, Y., Matsuda, T. D., Ōnuki, Y., Shibauchi, T., and Matsuda, Y. (2008). Flux Line Lattice Melting and the Formation of a Coherent Quasiparticle Bloch State in the Ultraclean URu_2Si_2 Superconductor. *Phys. Rev. Lett.*, 100:037004.

Ōnuki, Y., Won Yun, S., Ukon, I., Umehara, I., Satoh, K., Sakamoto, I., Hunt, M., Meeson, P., Probst, P.-A., and Springford, M. (1991). High Field Magnetoresistance and de Haas-van Alphen Effect in UGe_2. *J. Phys. Soc. Jpn.*, 60(7):2127–2130.

Ott, H. R., Rudigier, H., Fisk, Z., and Smith, J. L. (1983). UBe_{13}: An Unconventional Actinide Superconductor. *Phys. Rev. Lett.*, 50:1595–1598.

Palacio Morales, A., Pourret, A., Knebel, G., Bastien, G., Taufour, V., Aoki, D., Yamagami, H., and Flouquet, J. (2016). Thermoelectric power quantum oscillations in the ferromagnet UGe_2. *Phys. Rev. B*, 93:155120.

Palstra, T. T. M., Menovsky, A. A., Berg, J. v. d., Dirkmaat, A. J., Kes, P. H., Nieuwenhuys, G. J., and Mydosh, J. A. (1985). Superconducting and Magnetic Transitions in the Heavy-Fermion System URu_2Si_2. *Phys. Rev. Lett.*, 55:2727–2730.

Pantsulaya, A. and Varlamov, A. (1989). Possibility of observation of giant oscillations of thermoelectric power in normal metal. *Physics Letters A*, 136(6):317 – 320.

Park, T., Sidorov, V. A., Ronning, F., Zhu, J.-X., Tokiwa, Y., Lee, H., Bauer, E. D., Movshovich, R., Sarrao, J. L., and Thompson, J. D. (2008). Isotropic quantum scattering and unconventional superconductivity. *Nature*, 456:366.

Paul, I., Pépin, C., and Norman, M. R. (2013). Equivalence of Single-Particle and Transport Lifetimes from Hybridization Fluctuations. *Phys. Rev. Lett.*, 110(6):066402.

Paulsen, C., Hykel, D. J., Hasselbach, K., and Aoki, D. (2012). Observation of the Meissner-Ochsenfeld Effect and the Absence of the Meissner State in UCoGe. *Phys. Rev. Lett.*, 109:237001.

Petrovic, C., Movshovich, R., Jaime, M., Pagliuso, P. G., Hundley, M. F., Sarrao, J. L., Fisk, Z., and Thompson, J. D. (2001a). A new heavy-fermion superconductor $CeIrIn_5$: A relative of the cuprates? *EPL (Europhysics Letters)*, 53(3):354.

Petrovic, C., Pagliuso, P. G., Hundley, M. F., Movshovich, R., Sarrao, J. L., Thompson, J. D., Fisk, Z., and Monthoux, P. (2001b). Heavy-fermion superconductivity in $CeCoIn_5$ at 2.3 K. *J. Phys.: Condens. Matter*, 13(17):L337–.

Pfau, H., Daou, R., Lausberg, S., Naren, H. R., Brando, M., Friedemann, S., Wirth, S., Westerkamp, T., Stockert, U., Gegenwart, P., Krellner, C., Geibel, C., Zwicknagl, G., and Steglich, F. (2013). Interplay between Kondo Suppression and Lifshitz Transitions in $YbRh_2Si_2$ at High Magnetic Fields. *Phys. Rev. Lett.*, 110:256403.

Pfau, H., Hartmann, S., Stockert, U., Sun, P., Lausberg, S., Brando, M., Friedemann, S., Krellner, C., Geibel, C., Wirth, S., Kirchner, S., Abrahams, E., Si, Q., and Steglich, F. (2012). Thermal and electrical transport across a magnetic quantum critical point. *Nature*, 484(7395):493–7.

Pfleiderer, C. and Huxley, A. D. (2002). Pressure Dependence of the Magnetization in the Ferromagnetic Superconductor UGe_2. *Phys. Rev. Lett.*, 89:147005.

Pfleiderer, C., Julian, S. R., and Lonzarich, G. G. (2001). Non-Fermi-liquid nature of the normal state of itinerant-electron ferromagnets. *Nature*, 414(6862):427–30.

Pikul, A. P. and Kaczorowski, D. (2012). Search for quantum criticality in a ferromagnetic system $UNi_{1-x}Co_xSi_2$. *Phys. Rev. B*, 85:045113.

Pippard, A. (1989). *Magnetoresistance in Metals*. Cambridge university press.

Pourret, A., Knebel, G., Matsuda, T. D., Lapertot, G., and Flouquet, J. (2013a). Magnetic Polarization and Fermi Surface Instability: Case of $YbRh_2Si_2$. *J. Phys. Soc. Jpn.*, 82(5):053704.

Pourret, A., Palacio-Morales, A., Krämer, S., Malone, L., Nardone, M., Aoki, D., Knebel, G., and Flouquet, J. (2013b). Fermi Surface Reconstruction inside the Hidden Order Phase of URu_2Si_2 Probed by Thermoelectric Measurements. *Journal of the Physical Society of Japan*, 82(3):034706.

Pratt, D. K., Tian, W., Kreyssig, A., Zarestky, J. L., Nandi, S., Ni, N., Bud'ko, S. L., Canfield, P. C., Goldman, A. I., and McQueeney, R. J. (2009). Coexistence of Competing Antiferromagnetic and Superconducting Phases in the Underdoped $Ba(Fe_{0.953}Co_{0.047})_2As_2$ Compound Using X-ray and Neutron Scattering Techniques. *Phys. Rev. Lett.*, 103:087001.

Press, W. H., Teukolsky, S. H. Vetterling, W. T., and Flanney, B. P. (1986). *Numerical recipes*. Cambridge university press.

Rajput, S. S., Prasad, R., Singru, R. M., Triftshauser, W., Eckert, A., Kogel, G., Kaprzyk, S., and Bansil, A. (1993). A study of the Fermi surfaces of lithium and disordered lithium-magnesium alloys: theory and experiment. *J. Phys.: Condens. Matter*, 5(35):6419.

Rosch, A., Schröder, A., Stockert, O., and Löhneysen, H. v. (1997). Mechanism for the Non-Fermi liquid behavior in $CeCu_{1-x}Au_x$. *Phys. Rev. Lett.*, 79:159.

Rourke, P. M. C., McCollam, A., Lapertot, G., Knebel, G., Flouquet, J., and Julian, S. R. (2008). Magnetic-Field Dependence of the $YbRh_2Si_2$ Fermi Surface. *Phys. Rev. Lett.*, 101:237205.

Rueff, J.-P., Raymond, S., Taguchi, M., Sikora, M., Itié, J.-P., Baudelet, F., Braithwaite, D., Knebel, G., and Jaccard, D. (2011). Pressure-Induced Valence Crossover in Superconducting $CeCu_2Si_2$. *Phys.Rev.Lett.*, 106(18) : 186405.

Salce, B., Thomasson, J., Demuer, A., Blanchard, J. J., Martinod, J. M., Devoille, L., and Guillaume, A. (2000). Versatile device for low temperature in situ generation of forces up to 25 kN: Application to hydrostatic pressure experiments. *Rev. Sci. Instrum.*, 71(6):2461–2466.

Samsel-Czekała, M., Elgazzar, S., Oppeneer, P. M., Talik, E., Walerczyk, W., and Troć, R. (2010). The electronic structure of UCoGe by ab initio calculations and XPS experiment. *J. Phys.: Condens. Matter*, 22(1):015503.

Sandeman, K. G., Lonzarich, G. G., and Schofield, A. J. (2003). Ferromagnetic Superconductivity Driven by Changing Fermi Surface Topology. *Phys. Rev. Lett.*, 90:167005.

Saxena, S. S., Agarwal, P., Ahilan, K., Grosche, F. M., Haselwimmer, R. K. W., Steiner, M. J., Pugh, E., Walker, I. R., Julian, S. R., Monthoux, P., Lonzarich, G. G., Huxley, A., Sheikin, I., Braithwaite, D., and Flouquet, J. (2000). Superconductivity on the border of itinerant-electron ferromagnetism in UGe_2. *Nature*, 406(6796):587–592.

Scheerer, G. W., Knafo, W., Aoki, D., Ballon, G., Mari, A., Vignolles, D., and Flouquet, J. (2012). Interplay of magnetism, Fermi surface reconstructions, and hidden order in the heavy-fermion material URu_2Si_2. *Phys. Rev. B*, 85:094402.

Scheerer, G. W., Knafo, W., Aoki, D., Nardone, M., Zitouni, A., Béard, J., Billette, J., Barata, J., Jaudet, C., Suleiman, M., Frings, P., Drigo, L., Audouard, A., Matsuda, T. D., Pourret, A., Knebel, G., and Flouquet, J. (2014). Fermi surface in the hidden-order state of URu_2Si_2 under intense pulsed magnetic fields up to 81 T. *Phys. Rev. B*, 89:165107.

Schirber, J. E. and Van Dyke, J. P. (1971). Pressure-Induced "Electron Transition" in As. *Phys. Rev. Lett.*, 26:246–249.

Schlottmann, P. (2011). Lifshitz transition with interactions in high magnetic fields. *Phys. Rev. B*, 83:115133.

Schlottmann, P. (2013). Calculation of electric transport close to a lifshitz transition in a high magnetic field. *The European Physical Journal B*, 86(3):1–7.

Schmidt, A. R., Hamidian, M. H., Wahl, P., Meier, F., Balatsky, A. V., Garrett, J. D., Williams, T. J., Luke, G. M., and Davis, J. C. (2010). Imaging the Fano lattice to 'hidden order' transition in URu_2Si_2. *Nature*, 465(7298):570–576.

Schoenberg, D. (1984). *Magnetic oscillations in metals*. Cambridge university press.

Schoenes, J., Schönenberger, C., Franse, J. J. M., and Menovsky, A. A. (1987). Hall-effect and resistivity study of the heavy-fermion system URu_2Si_2. *Phys. Rev. B*, 35:5375–5378.

Schulze Grachtrup, D., Bleckmann, M., Willenberg, B., Süllow, S., Bartkowiak, M., Skourski, Y., Rakoto, H., Sheikin, I., and Mydosh, J. A. (2012). Field-induced phases in UPt_2Si_2. *Phys. Rev. B*, 85:054410.

Sebastian, S. E., Harrison, N., Batista, C. D., Trugman, S. A., Fanelli, V., Jaime, M., Murphy, T. P., Palm, E. C., Harima, H., and Ebihara, T. (2009). Heavy holes as a precursor to superconductivity in antiferromagnetic $CeIn_3$. *Proceedings of the National Academy of Sciences*, 106(19):7741–7744.

Senthil, T. (2008). Critical Fermi surfaces and non-Fermi liquid metals. *Phys. Rev. B*, 78(3):035103.

Settai, R., Nakashima, M., Araki, S., Haga, Y., Kobayashi, T. C., Tateiwa, N., Yamagami, H., and Ōnuki, Y. (2002). A change of the Fermi surface in UGe_2 across the critical pressure. *J. Phys.: Condens. Matter*, 14(1):L29.

Shick, A. B. (2002). Electronic and magnetic structure of URhGe. *Phys. Rev. B*, 65:180509.

Shimizu, Y., Braithwaite, D., Salce, B., Combier, T., Aoki, D., Hering, E. N., Ramos, S. M., and Flouquet, J. (2015). Unusual strong spin-fluctuation effects around the critical pressure of the itinerant Ising-type ferromagnet URhAl. *Phys. Rev. B*, 91:125115.

Shishido, H., Hashimoto, K., Shibauchi, T., Sasaki, T., Oizumi, H., Kobayashi, N., Takamasu, T., Takehana, K., Imanaka, Y., Matsuda, T. D., Haga, Y., Ōnuki, Y., and Matsuda, Y. (2009). Possible Phase Transition Deep Inside the Hidden Order Phase of Ultraclean URu_2Si_2. *Phys. Rev. Lett.*, 102:156403.

Shishido, H., Settai, R., Harima, H., and Ōnuki, Y. (2005). A Drastic Change of the Fermi Surface at a Critical Pressure in $CeRhIn_5$: dHvA Study under Pressure. *J. Phys. Soc. Jpn.*, 74(4):1103–1106.

Si, Q., Rabello, S., Ingersent, K., and Smith, J. L. (2003). Local fluctuations in quantum critical metals. *Phys. Rev. B*, 68:115103.

Sidorov, V. A., Krasnorussky, V. N., Petrova, A. E., Utyuzh, A. N., Yuhasz, W. M., Lograsso, T. A., Thompson, J. D., and Stishov, S. M. (2011). High-pressure study of the phase transition in the itinerant ferromagnet CoS_2. *Phys. Rev. B*, 83:060412.

Sidorov, V. A., Nicklas, M., Pagliuso, P. G., Sarrao, J. L., Bang, Y., Balatsky, A. V., and Thompson, J. D. (2002). Superconductivity and Quantum Criticality in CeCoIn_{5}. *Phys. Rev. Lett.*, 89(15):157004.

Silaev, M. A., Thuneberg, E. V., and Fogelström, M. (2015). Lifshitz Transition in the Double-Core Vortex in ^{3}He-B. *Phys. Rev. Lett.*, 115:235301.

Sinha, S. K., Crabtree, G. W., Hinks, D. G., and Mook, H. (1982). Study of Coexistence of Ferromagnetism and Superconductivity in Single-Crystal $ErRh_4B_4$. *Phys. Rev. Lett.*, 48:950–953.

Skomski, R. (2008). *Simple models of magnetism*. Oxford university press.

Slooten, E., Naka, T., Gasparini, A., Huang, Y. K., and de Visser, A. (2009). Enhancement of Superconductivity near the Ferromagnetic Quantum Critical Point in UCoGe. *Phys. Rev. Lett.*, 103:097003.

Spałek, J. (2006). Spin-split masses and a critical behavior of almost localized narrow-band and heavy-fermion systems. *Physica B: Condensed Matter*, 378-380:654–660.

Steglich, F., Aarts, J., Bredl, C. D., Lieke, W., Meschede, D., Franz, W., and Schäfer, H. (1979). Superconductivity in the Presence of Strong Pauli Paramagnetism: $CeCu_2Si_2$. *Phys. Rev. Lett.*, 43:1892–1896.

Steven, E., Kiswandhi, A., Krstovska, D., Brooks, J. S., Almeida, M., Gonçalves, A. P., Henriques, M. S., Luke, G. M., and Williams, T. J. (2011). Robust properties of the superconducting ferromagnet UCoGe. *Applied Physics Letters*, 98(13).

Stewart, G. R., Fisk, Z., Willis, J. O., and Smith, J. L. (1984). Possibility of Coexistence of Bulk Superconductivity and Spin Fluctuations in UPt_3. *Phys. Rev. Lett.*, 52:679–682.

Tada, Y., Fujimoto, S., Kawakami, N., Hattori, T., Ihara, Y., Ishida, K., Deguchi, K., Sato, N. K., and Satoh, I. (2013). Spin-Triplet Superconductivity Induced by Longitudinal Ferromagnetic Fluctuations in UCoGe: Theoretical Aspect. *J. Phys. Conf. Ser.*, 449(1):012029.

Tateiwa, N. and Haga, Y. (2009). Evaluations of pressure-transmitting media for cryogenic experiments with diamond anvil cell. *Review of Scientific Instruments*, 80(12).

Tateiwa, N., Kobayashi, T. C., Hanazono, K., Amaya, K., Haga, Y., Settai, R., and Ōnuki, Y. (2001). Pressure-induced superconductivity in a ferromagnet uge 2. *Journal of Physics: Condensed Matter*, 13(1):L17–.

Taufour, V., Aoki, D., Knebel, G., and Flouquet, J. (2010). Tricritical Point and Wing Structure in the Itinerant Ferromagnet UGe_2. *Phys. Rev. Lett.*, 105:217201.

Taupin, M., Howald, L., Aoki, D., and Brison, J.-P. (2014a). Superconducting gap of UCoGe probed by thermal transport. *Phys. Rev. B*, 90:180501.

Taupin, M., Howald, L., Aoki, D., Flouquet, J., and Brison, J. P. (2014b). Existence of anisotropic spin fluctuations at low temperature in the normal phase of the superconducting ferromagnet UCoGe. *Phys. Rev. B*, 89:041108.

Taupin, M., Sanchez, J.-P., Brison, J.-P., Aoki, D., Lapertot, G., Wilhelm, F., and Rogalev, A. (2015). Microscopic magnetic properties of the ferromagnetic superconductor UCoGe reviewed by x-ray magnetic circular dichroism. *Phys. Rev. B*, 92:035124.

Terashima, T., Matsumoto, T., Terakura, C., Uji, S., Kimura, N., Endo, M., Komatsubara, T., and Aoki, H. (2001). Evolution of Quasiparticle Properties in UGe_2 with Hydrostatic Pressure Studied via the de Haas–van Alphen Effect. *Phys. Rev. Lett.*, 87:166401.

Tinkham, M. (1975). *Introduction to Superconductivity*. Robert E. Krieger Publishing Company.

Tokunaga, Y., Aoki, D., Mayaffre, H., Krämer, S., Julien, M.-H., Berthier, C., Horvatić, M., Sakai, H., Kambe, S., and Araki, S. (2015). Reentrant Superconductivity Driven by Quantum Tricritical Fluctuations in URhGe: Evidence from ^{59}Co NMR in $URh_{0.9}Co_{0.1}Ge$. *Phys. Rev. Lett.*, 114:216401.

Tonegawa, S., Hashimoto, K., Ikada, K., Tsuruhara, Y., Lin, Y.-H., Shishido, H., Haga, Y., Matsuda, T. D., Yamamoto, E., Ōnuki, Y., Ikeda, H., Matsuda, Y., and Shibauchi, T. (2013). Cyclotron resonance study of quasiparticle mass and scattering rate in the hidden-order and superconducting phases of URu_2Si_2. *Phys. Rev. B*, 88:245131.

Trinh, J., Brück, E., Siegrist, T., Flint, R., Chandra, P., Coleman, P., and Ramirez, A. P. (2016). Thermodynamic Measurement of Angular Anisotropy at the Hidden Order Transition of URu_2Si_2. *Phys. Rev. Lett.*, 117:157201.

van Loon, E. G. C. P., Katsnelson, M. I., Chomaz, L., and Lemeshko, M. (2016). Interaction-driven Lifshitz transition with dipolar fermions in optical lattices. *Phys. Rev. B*, 93:195145.

Wang, Y., Gastiasoro, M. N., Andersen, B. M., Tomić, M., Jeschke, H. O., Valentí, R., Paul, I., and Hirschfeld, P. J. (2015). Effects of Lifshitz Transition on Charge Transport in Magnetic Phases of Fe-Based Superconductors. *Phys. Rev. Lett.*, 114:097003.

Werthamer, N. R., Helfand, E., and Hohenberg, P. C. (1966). Temperature and Purity Dependence of the Superconducting Critical Field, H_{c2}. III. Electron Spin and Spin-Orbit Effects. *Phys. Rev.*, 147:295–302.

Werwiński, M., Rusz, J., Mydosh, J. A., and Oppeneer, P. M. (2014). Exceptional Ising magnetic behavior of itinerant spin-polarized carriers in URu_2Si_2. *Phys. Rev. B*, 90:064430.

Wu, B. (2016). *Unconventional superconductivity in Uranium compounds*. PhD thesis, Université Grenoble Alpes.

Wu, B., Bastien, G., Taupin, M., Paulsen, C., Howald, L., Aoki, D., and Brison, J. (2016). Pairing mechanism in the ferromagnetic superconductor UCoGe. *to be published*.

Yamagami, H. (2011). Theoretical reconsideration of antiferromagnetic Fermi surfaces in URu_2Si_2. *J. Phys. Conf. Ser.*, 273(1):012064–.

Yamaji, Y., Misawa, T., and Imada, M. (2006). Quantum and Topological Criticalities of Lifshitz Transition in Two-Dimensional Correlated Electron Systems. *J. Phys. Soc. Jpn.*, 75(9):094719.

Yelland, E. A., Barraclough, J. M., Wang, W., Kamenev, K. V., and Huxley, A. D. (2011). High-field superconductivity at an electronic topological transition in URhGe. *Nat Phys*, 7(11):890–894.

Yu, J. X., Cheng, Y., Zhu, B., and Yang, H. (2011). *Physica B*, 406:2788.

Zwicknagl, G. (2011). Field-induced suppression of the heavy-fermion state in $YbRh_2Si_2$. *J. Phys.: Condens. Matter*, 23(9):094215.

Abstract

This thesis is concentrated on the ferromagnetic superconductors UCoGe and URhGe and on the hidden order state in URu_2Si_2. In the first part the pressure–temperature phase diagram of UCoGe was studied up to 10.5 GPa. Ferromagnetism vanishes at the critical pressure $p_c \approx 1$ GPa. Unconventional superconductivity and non Fermi liquid behavior can be observed in a broad pressure range around p_c. The superconducting upper critical field properties were explained by the suppression of the magnetic fluctuations under field. In the second part the Fermi surfaces of UCoGe and URhGe were investigated by quantum oscillations. In UCoGe four Fermi surface pockets were observed. Under magnetic field successive Lifshitz transitions of the Fermi surface have been detected. The observed Fermi surface pockets in UCoGe evolve smoothly with pressure up to 2.5 GPa and do not show any Fermi surface reconstruction at the critical pressure p_c. In URhGe, three heavy Fermi surface pockets were detected by quantum oscillations. In the last part the quantum oscillation study in the hidden order state of URu_2Si_2 shows a strong g factor anisotropy for two Fermi surface pockets, which is compared to the macroscopic g factor anisotropy extracted from the upper critical field study.

Résumé

Cette thèse montre de nouveaux résultats sur les supraconducteurs ferromagnétiques UCoGe et URhGe et sur l'ordre caché dans URu_2Si_2. Le diagramme de phase pression température d'UCoGe a été étudié jusqu'à 10.5 GPa. L'ordre ferromagnétique subsiste jusqu'à la pression critique $p_c \approx 1$ GPa et la supraconductivité non conventionnelle jusqu'à $p = 4$ GPa. Les fluctuations magnétiques responsables de la supraconductivité peuvent être réduites par l'application d'un champ magnétique. Les surfaces de Fermi d'UCoGe et d'URhGe ont été mesurées grace aux oscillations quantiques. Quatre poches ont été détectées dans UCoGe, elles subissent une succession de transition de Lifshitz sous champ magnétique. Les poches détectées évoluent continument avec la pression jusqu'à 2.5 GPa, sans montrer de reconstruction de la surface de Fermi à la pression critique p_c. Dans URhGe, trois poches lourdes de la surface de Fermi ont aussi été découvertes. Enfin dans la phase d'ordre caché d'URu_2Si_2, les oscillations quantiques ont révélé une forte anisotropie du facteur gyromagnétique g pour deux poches de la surface de Fermi, qui est comparable à l'anisotropie macroscopique. Cette dernière a été étudiée à partir du champ critique supérieur de la supraconductivité.